Use of a Seven-Hole Pressure Probe in Highly Turbulent Flow-Fields

Kevin Pisterman

Thesis submitted to the faculty of the Virginia Polytechnic Institute and State University in partial fulfillments of the requirements for degree of

Master of Science
In
Aerospace Engineering

Dr. Roger L. Simpson (Chair)
Dr. William J. Devenport
Dr. James Marchman

June, 8th 2004
Blacksburg, Virginia

Keywords: Multi-hole probe, Seven-hole probe, Pressure measurements, Turbulent flow, Subsonic, Pressure correlation, Pressure uncertainties

Use of a Seven-Hole Pressure Probe in Highly Turbulent Flow-Fields

Kevin Pisterman

Abstract

This work presents the experimental study of the flow generated in the wakes of three three-dimensional bumps in the Virginia Polytechnic Institute and State University Boundary Layer Wind Tunnel. The three bumps examined are named bump 1, small bump 3, and large bump 3, and are the same test cases studied by Byun et *al.* (2004) and Ma and Simpson (2004) with a LDV system and a quad-wire hot-wire probe, respectively. Various experimental methods are used in this work: For measuring the mean velocity component in the planes examined, a seven-hole pressure probe is used with the data reduction algorithm developed by Johansen et *al.* (2001). A sixteen-hole pressure rake is used for boundary layer data on the sidewalls and ceiling of the test section and a Pitot-static probe is used to obtain mean velocity magnitude in the centerline of the test section. Specific techniques are developed to minimize the uncertainties due to the apparatus used, and an uncertainty analysis is used to confirm the efficiency of these techniques.

Measurements in the wake of bump 1 reveal a strong streamwise vorticity creating large amounts of high moment fluid entrained close to the wall. In the wake of small bump 3, the amount of high momentum fluid entrained close to the wall is small as well as the streamwise vorticity. The flow in the wake of large bump 3 incorporate the characteristics of the two previous bumps by having a relatively large entrainment of high momentum fluid close to the wall and a low generation of streamwise vorticity. In the wakes of the three bumps, a pair of counter rotating vortices is created. The influence of large bump 3 on the incoming flow-field is found to be significant and induces an increase of the boundary layer thickness.

By comparing LDV data and quad-wire hot-wire data with seven-hole probe data in the wakes of the bumps at the same locations, it is shown that uncertainties defined for

a quasi-steady, non-turbulent flow-field without velocity gradient are bad indicators of the magnitude of the uncertainties in a more complex flow-field. A theoretical framework is discussed to understand the effects of the velocity gradient and of turbulence on the pressures measured by the seven-hole probe. In this fashion, a model is proposed and validated to explain these effects. It is observed that the main contribution to the uncertainties in seven-hole probe measurements due to the velocity gradient and to the turbulence comes from the velocity gradient.

To correct for the effects of the velocity gradient on seven-hole probe measurements in an unknown flow-field, a technique is proposed. Using an estimation of the velocity gradient calculated from the seven-hole probe, the proposed model could be used to re-evaluate non-dimensional pressure coefficients used in the data reduction algorithm therefore correcting for the effects of the velocity gradient on seven-hole probe measurements.

Acknowledgements

First, I want to thank my family who encouraged me, supported me in difficult times, and allowed me to be able to complete this work.

My advisor, Dr. Roger Simpson, who guided me, assisted me, and shared his knowledge and enthusiasm through the project. The members of my committee: Dr. William Devenport, for his insights, and Dr. Jim Marchman, who gave me insights and help me when I first arrived at Virginia Tech.

My co-workers Jeremy Bennington, Dr. Ruolong Ma, Gwibo Byun, Todd Lowe, Devin Stewart, Edgar Orsi, Genglin Tang, Qing Tian, Shereef Sadek, and Kenneth Granlund who helped me when I needed, answered my questions when I was backed against a wall and that I now consider as friends. The shop technicians, Bruce Stanger, Mike Vaught, James Lambert, and Steve Edwards without whom this project could not have even begun.

Aeroprobe Corp, and particularly its C.E.O., Matthew Zeiger who calibrated the probe, provided the data reduction code and took time to collaborate with me and answer my questions.

The Kendo club at Virginia Tech, its members and my friends, Peter Park, Philip Hwang, Sean Tzeng, Julia Yang, Justin Marcus, Aurelien Borgoltz, Julien Pierru, Steve, and Jason Alvesteffer, who were always there for me whenever I needed.

Finally, I want to thank the sponsors of this project, NASA and the Office of Naval Research for their support under grant NAG-3-2733 and N00014-01-1-0421, respectively.

Table of Content

Nomenclature

Roman

a_1, b_1	Bump 1, rectangular base length and width , respectively
a_3	Small and large bump 3 radius
A, B	Coefficients defined in equation 2.10
A_u, B_n	Coefficients defined in equation 1.1
$A_{stagnation}$, $B_{stagnation}$	Coefficients defined in equation 4.11
b_1, b_2	b_α, b_β for low angle of incidence, b_θ, b_ϕ , for high angle of incidence
b_α, b_β, A_t, A_S	Low angle of incidence non-dimensional pressure coefficients
b_θ, b_ϕ , A_t, A_S	High angle of incidence non-dimensional pressure coefficients
b_{α_model}, b_{β_model}	Low angle of incidence non-dimensional pressure coefficients calculated from model equation (equation 4.17 to 4.19)
$B_{i\ measured}$, $B_{i\ calculated}$	Pressure transducer offset measured and calculated, respectively
c_{0j}, c_{1j}, c_{2j}	Coefficients defined in equation 2.6
C_{i1}, C_{i2}, C_{i3}	Coefficients defined in equation 4.6
C_u, C_{vw}	Coefficients defined in equation 4.10
d	Probe diameter
G	Magnitude of non-dimensional velocity gradient
G_s	Non-dimensional velocity gradient in the s direction
H	Bump height
H_{factor}	Shape factor
$\vec{i}$	Unit vector in positive streamwise direction
J_0, I_0	Bessel function of the first kind and Modified Bessel function of the first kind, respectively
K_i	Local dynamic pressure coefficient of the i^{th} pressure port
LDV	Laser Doppler Velocimeter
m, b	Coefficients defined in equation 2.12
$p_1, p_2, p_3, p_4, p_5, p_6, p_7$	Pressured of seven pressure ports of seven-hole probe
p^+, p^-	Pressure next to i^{th} port in clockwise and counter clockwise direction, respectively
$p_{i\ max}$	Maximum pressure read by seven ports of seven-hole probe

p_i	Pressure measured by the i^{th} pressure port
p_r, V_r	Pressure read by pressure transducer and corresponding voltage output, respectively
P_{total}, P_{static}	Total and static pressure, respectively
P_m, P_t	Measured and true static pressures, respectively
$P_{dynamic\_true}$	True dynamic pressure
$P_{dynamic\_port\_i}$	Dynamic pressure measured by the i^{th} pressure port
q	Pseudo-dynamic pressure
r	Rectangular coordinate for small and large bump 3
R	Gas constant
R_p	Seven-hole probe tip radius
$R_{LDV/hot\text{-}wire}$	Correction factor for differences in incoming flow conditions
Re_θ	Reynolds number based on momentum thickness
Re_d	Reynolds number based on probe diameter
t	Time variable
T	Flow temperature
T_i	Pressure transducer temperature
T_{ref}	Reference temperature
TKE	Turbulent Kinetic Energy
$\overline{u^2}$, $\overline{v^2}$, $\overline{w^2}$	Turbulent normal stresses measured by hot-wire probe or LDV
U	Magnitude of velocity vector
$\overline{U}$, $\overline{V}$, $\overline{W}$	Mean velocity components
U_e	Boundary layer edge velocity
$U_{indicated}$	Mean velocity magnitude indicated by a pressure probe
$U_{hot\text{-}wire\ or\ LDV}$	Mean velocity magnitude measured by hot-wire or LDV
U_{ref}	Reference velocity
U_{true}	True velocity magnitude measured by hot-wire or LDV
$\overline{U}_{negative\_z}$, $\overline{U}_{positive\_z}$	Mean streamwise velocity component in negative spanwise coordinates and positive spanwise coordinates, respectively
U^+	Non-dimensional streamwise velocity, $U^+ = \overline{U} / U_\tau$
U_τ	Friction velocity

$\overline{v_n^2}$	Cross-flow turbulent normal stress
$\vec{V}$	Velocity vector
x, y, z	Coordinates in the streamwise, normal and spanwise direction, respectively
x_1, x_2	First and second streamwise positions used in equation 3.2
y^+	Non-dimensional vertical position, $y^+ = y \cdot U_\tau / \nu$

Greek

α	Pitch angle
α_0, β_0	Offsets in pitch and yaw angle, respectively
α_i, β_i	Pitch and yaw angle in local coordinate of i^{th} pressure port, respectively
β	Yaw angle
δ	Uncertainty with 20:1 odds
$\delta_{stagnation}$	Displacement of stagnation point due to velocity gradient
δ^*	Displacement thickness
δ_{99}	Boundary layer thickness
δB	Uncertainty in the offset pressure of the pressure transducers
δU	Uncertainty in mean velocity magnitude
$\delta\overline{U}_{symmetry}, \delta\overline{V}_{symmetry}, \delta\overline{W}_{symmetry}$	Uncertainty quantifying the symmetry of the mean streamwise, normal and spanwise components of the velocity in the wake of the bumps, respectively
$\delta(\Delta U)$	Uncertainty in absolute bias-error ΔU
$\Delta b_\alpha, \Delta b_\beta$	Bias-error in non-dimensional pressure coefficients
ΔB	Absolute error defined
$\Delta P_{dynamic\_port\_i}$	Bias-error of the dynamic pressure at the i^{th} pressure port
ΔU	Absolute bias-error in mean velocity magnitude
$\Delta U_{LDV/hot\text{-}wire}$	Bias-error in mean velocity magnitude
$\Delta\alpha_{LDV/hot\text{-}wire}$	Bias-error in pitch angle
$\Delta\beta_{LDV/hot\text{-}wire}$	Bias-error in yaw angle
γ	Specific heat ratio
Λ	Constant for small and large bump 3
κ_i	Local dynamic pressure coefficient of the i^{th} pressure port

	including velocity gradient effects
ν	Kinematic viscosity
Ω_x	Streamwise vorticity
ϕ	Roll angle
ϕ_p	Velocity potential
ρ	Density
σ	Standard Deviation
θ	Momentum thickness

Symbols

$\lvert\ \rvert$	Absolute value of enclosed variable
$(\ )_{average}$	Average value of enclosed variable
$(\ )_{ceiling}$	Enclosed variable is measured on ceiling of test section
$(\ )_{left\_sidewall}$	Enclosed variable is measured on left sidewall of test section
$(\ )_{right\_sidewall}$	Enclosed variable is measured on right sidewall of test section

List of Figure

List of Table

1 Introduction

The use of multi-hole pressure probes such as the seven-hole pressure probe or the five-hole pressure probe has become more common with the increasing capabilities of multi-hole probes to measure flow data in three-dimensional flow. The easiness of operation of such probes as well as their durability and relatively low cost make them preferable to Laser Doppler Velocimeter (LDV) systems or hot-wire probes. LDV systems are complex to operate, require a laborious alignment procedure with extremely careful manipulation, are limited in measurement locations, necessitate the seeding of particles into the flow under particular conditions, and are relatively expensive. On the other hand, LDV systems produce non-intrusive measurements and can have a spatial resolution of the order of tens of microns with extremely small uncertainties in the measurements. Hot-wire measurement techniques are much easier to use than a LDV system but require delicate operation to prevent the wires from snapping and are particularly sensitive to velocity gradients in a flow field. Furthermore, hot-wire techniques necessitate repetitive calibration to reduce uncertainties of the measurements.

1.1 Previous studies on pressure probes

Two of the main calibration algorithms for multi-hole pressure probe were developed by Gallington (1980) and Zilliac (1989) for subsonic steady uniform flow-fields. Both methods use non-dimensional pressure coefficients and apply an interpolation scheme from a set of calibration data to get information on the velocity vector in an unknown flow-field. Gallington (1980) performed a third-order polynomial fit on the calibration data on a specific sector of the flow defined by which pressure port of the multi-hole probe reads the maximum pressure leading to uncertainties of ±2.5 deg. for flow angles and ±5% for velocity magnitude. Zilliac (1989) used an Akima (1978) interpolation (IMSL subroutine) of the calibration data to obtain the velocity vector information in the unknown flow resulting in uncertainties of ±0.5 deg. for flow angles and ±1% for velocity magnitude. Devenport and Wenger (1998) improved Gallington's method by adding to the third order polynomial fit a set of error coefficients, therefore decreasing the uncertainties to ±0.4 deg. for flow angles and ±0.7% for velocity magnitude. The work by Johansen et *al*. (2001) produced lower uncertainties than

Devenport and Wenger (1998) by using another data reduction method. Instead of interpolating on a wide sector of the calibration data to obtain the flow conditions in an unknown flowfield, they applied a low order polynomial fit using a least square fit for a few calibration data points selected from similar conditions as the one measured in the unknown flow field, leading to uncertainties of ±0.4 deg. for the flow angles and ±0.6% for the velocity magnitude. The data reduction algorithm used in this work is the one developed by Johansen et *al.* (2001) chosen for having the best capabilities.

The principal problem in these methods of determining the mean flow velocity in an unknown flow-field is that they are calibrated for a steady, non-turbulent uniform flow-field. Of course, such an ideal situation is rare to find in flow-fields, and one may wonder as to what response these techniques offer in most situations with unsteadiness, turbulence, and velocity gradient in the flow-field. Siddon (1969) studied the effect of unsteadiness and turbulences on the static pressure measurements performed by Pitot-static pressure probe in various turbulent flow-fields. He found an empirical formula (equation 1.1) to account for the difference between the static pressure measured and the true static pressure in the wind tunnel as well as bounds where this difference becomes significant.

$$P_m - P_t = A_u \cdot \rho\left(\overline{U}^2 + \overline{u^2}\right) + B_n \cdot \rho\left(\overline{V_n}^2 + \overline{v_n^2}\right) \qquad \textbf{(1.1)}$$

where $\overline{V_n}^2 = \overline{V}^2 + \overline{W}^2$ and $\overline{v_n^2} = \overline{v^2} + \overline{w^2}$

P_m and P_t are the measured and the true mean static pressure, respectively, $\overline{U}^2$, $\overline{V}^2$, and $\overline{W}^2$ are the streamwise, normal, and spanwise components of the mean velocity vector, respectively, and $\overline{u^2}$, $\overline{v^2}$, and $\overline{w^2}$ are the streamwise, vertical, and spanwise turbulent normal stresses, respectively. The coefficients A_u and B_n prescribe the magnitude of the errors due to the axial flow and crossflow effects, respectively.

Hooper and Musgrove (1993) tested the response of a four-hole cobra probe in a turbulent swirling jet flow and found that for a turbulence intensity greater than 20%, large errors are introduced in the velocity measurements. Hooper and Musgrove (1997) used an improved version of their four-hole probe (enhanced in dynamic response) with the calibration data from a steady flow to determine the mean velocity as well as the Reynolds stresses. From a comparison with hot-wire anemometer results, they found a

20% discrepancy error between hot-wire data and four-hole probe data for high axial turbulence intensity. By using a steady calibration algorithm with a four-hole cobra probe, Guo and Wood (2001) measured instantaneous velocity components and velocity spectra in a two-dimensional turbulent mixing layer, and compared their pressure probe data to X-wire anemometer results. They found that the pressure probe over-estimates the mean velocity normal to the flow in the high turbulence intensity region.

The question that has to be asked from these studies is if the errors found in the mean velocity measurements in high turbulence intensity regions are actually due to the poor response of pressure probes in a high turbulence intensity flow or to the steady calibration data used for unsteady flow measurements. To answer this question, Takahashi (1997) used an unsteady potential flow analysis to evaluate the errors in measurements introduced by an unsteady flow on the surface of a conical head seven-hole probe and compared his data with X-wire probe data in the wake of a circular cylinder. He found that the pressure probe overestimates the velocity measurements when immersed in the vortex street of a cylinder wake. Johansen and Rediniotis (2002) used a similar unsteady potential flow analysis on a hemispherical head five-hole probe and found that flow angles smaller than ±30 deg. did not affect the five-hole probe measurements due to the unsteady effects but that the velocity magnitude measured was significantly affected by the unsteady effects if a steady calibration was used.

These studies reveal that the use of a steady calibration database for measuring the velocity in an unsteady flowfield with a multi-hole probe induces uncertainties in the magnitude of the velocity measured and in large flow angles ($\geq \pm 30$ deg). The work by Guo and Wood (2001) and Takahashi (1997) suggests that the turbulent kinetic energy induces uncertainty in multi-hole probe measurements but no detailed analysis was done to understand these effects. Furthermore, no study was found to understand how velocity gradient may affect multi-hole probe pressure measurements.

1.2 Motivations for the present study

While recent studies correct for the errors induced by the unsteadiness in the flow field on the time dependent velocity measurements by a multi-hole probe, they do not account for the effects of the flow characteristics on the multi-hole probe measurements as it was done by Siddon (1969) on a Pitot-static probe. Consequently, the effects of the

turbulence or of the velocity gradient on multi-hole pressure probe measurements are still unknown. To answer these questions, seven-hole probe mean velocity measurements were made in the unsteady, turbulent, shear flow generated in the wakes of three three-dimensional bumps. By comparing the seven-hole probe measurements with LDV measurements by Byun et *al.* (2004) and with quad-wire hot-wire measurements by Ma and Simpson (2004) in the wakes of the same three bumps, quantitative comparisons of the three measuring methods can be discussed. Using the calibration database of the seven-hole probe, a model is proposed to calculate the pressures at each pressure port of the seven-hole probe in a steady, non-turbulent, uniform flow-field. Moreover, to account for the effects of turbulence (as discussed by Siddon (1959)) and of the velocity gradient on the pressure measurements of the seven-hole probe, a modified version of the model is examined and tested.

The other goal of this study is to improve initial and boundary conditions information as well as wake data around the three bumps that can be used to enhance CFD simulations. The seven-hole probe was used to measure the mean velocity vector at several spanwise planes upstream and downstream of the bumps. A sixteen-hole pressure rake as well as a Pitot-static tube were used to provide information on the sidewalls and ceiling boundary layer of the wind tunnel, and on the mean velocity magnitude in the centerline on the test section.

1.3 Organization of the thesis

The remainder of the thesis is organized as follow: Chapter 2 describes the experimental apparatus and techniques used in this research. A description of the wind-tunnel facility, the three three-dimensional bumps, and the equipment used are presented as well as a description of the theory and of the techniques utilized to obtain measurements with the seven-hole pressure probe.

Chapter 3 presents a description of the mean velocity vector measurements obtained with the seven-hole pressure probe, the sixteen-hole pressure rake and the Pitot-static probe around the three bumps. Descriptions of the variations of the flow-field in the positive streamwise direction in the wakes of the three bumps are examined as well as comparisons between the flow-fields measured in the wakes of the three bumps. Qualitative and quantitative comparisons between the seven-hole probe measurements

and the experimental work of Byun et al. (2004) with LDV measurements and the work of Ma and Simpson (2004) with quad-wire hot-wire anemometer measurements are analyzed.

Chapter 4 quantitatively compares the seven-hole probe data with LDV data and hot-wire data from Byun et *al.* (2004) and Ma and Simpson (2004), respectively. The effects of turbulence and of the velocity gradient on the seven pressures measured by the seven-hole probe are discussed, and a model for the seven pressures of the seven-hole probe in a turbulent flow-field with velocity gradient is proposed and tested. Finally, the discussions from the previous sections are recapitulated in a conclusion, and a prescription for correcting for the effect of the velocity gradient on seven-hole probe measurements is proposed.

2 Apparatus and Technique

2.1 Apparatus

2.1.1 The seven-hole pressure probe

The seven-hole pressure probe manufactured by Aeroprobe Corporation (Figure 2.1) has a 6" long stem and a 2 mm diameter with seven tubes of internal diameter of 0.5 mm imbedded in the stem. The probe has a conical tip with a half angle of 30 deg. and six of the pressure ports (numbered two to six) are distributed with an angle of 60 deg. with respect to each other. The first pressure port is located at the tip of the probe. The calibration of the seven-hole probe was performed in Aeroprobe Corp. facilities and the software used to reduce the seven-hole probe data was MultiProbe v.3.3.1.240 developed by Aeroprobe Corp. and, using the data reduction algorithm developed by Johansen et *al*. (2001). To connect the pressure ports to the pressure transducers, tygon tubing was used. Seven, five meters long tubes were used with an internal diameter of 1/16 inch.

2.1.2 Pressure transducers

To read the pressure sensed by the pressure ports of the seven-hole pressure probe, two systems were considered. The first system consists of a scanivalve model CTLR2P/S2-S6 manufactured by Scanivalve Corp., a Setra 239 pressure transducer with a ± 5 in. of water range, and a 286 IBM PC with a DT2801 A/D board for acquiring data. The second system consists of seven Data Instruments pressure transducers model XPCL04DTC. Each transducer has a ±2.5 in. of water range and is temperature compensated over a range of 0-50°C. The transducer volume of the differential pressure ports are 0.004303 inch³ and 0.003908 inch³. The output signal is of ±25mV and is amplified to an appropriate range for data acquisition. In this fashion, a 100-gain amplifier model INA131AP manufactured by Burr-Brown is used as well as a low-pass filter with a cutoff frequency of 200Hz in order to reduce the noise of the signals. The data acquisition system consists of a PC with a Data Instruments PCI-6013 data acquisition card and the corresponding CB-68LP connector bloc allowing up to eight simultaneous inputs with a total sampling rate of 200k samples per seconds. To limit temperature variations of the seven-pressure transducer device, the device is coated with

a one-inch thick layer of Styrofoam. The temperature inside the device was read using a HH21 thermocouple manufactured by Omega with an uncertainty of $\pm 0.1^{\circ}C$. The two systems measure pressures in differential mode and were nulled with respect to the atmospheric pressure measured by a Kahlsico precision aneroid barometer Model MK2 type M2236 with an uncertainty of $\pm 0.05\,mbars$.

2.1.3 Pressure rake

A pressure rake was used to measure the boundary layer on the sidewalls and on the ceiling of the wind tunnel while large bump 3 was set in place. It has sixteen pressure ports aligned in a row on a one-inch length (Figure 2.2). The pressure rake was set in the test section with a manual traverse set on a support on top of the test section as shown in Figure 2.3 (the automatic traverse system described previously was not used so as not to modify the existing set-up). The traverse allowed vertical motion of the pressure rake by rotating a knob; the horizontal motion was obtained by laterally sliding the traverse on the support. Since the pressure rake only measured total pressures, a Pitot-static probe described in the next section was used to measure the static pressure at a location in the boundary layer under the assumption that the static pressure stayed constant in the boundary layer. The scanivalve system was first intended to be used for the pressure rake measurements but, due to technical problems, a digital manometer Model 474-FM mark III from Dwyer Instruments Inc. with an uncertainty of ±0.01 inch of water was used. In order to have statistically ergodic measurements and to account for the time lags due to the tubing system, recording of the total and static pressures were made when the pressures indicated by the digital manometer approached an asymptotic value.

2.1.4 Pitot-static probe

A Pitot-static probe model 160 manufactured by Dwyer Instruments Inc. was used to measure the velocity magnitude at various streamwise locations along the centerline of the test section with large bump 3 set in place. The Pitot-static probe was fixed in inclination and height to a wooden plate via a bearing and was displaced along the centerline of the test section by sliding the wooden plate along the centerline slot of the test section ceiling (Figure 2.11). Since the alignment of the probe with the velocity vector was important to read the correct magnitude of the velocity vector, it was rotated

in yaw angle until the maximum total pressure was read at which point, the static pressure was read and the magnitude of the velocity vector was obtained using Bernoulli's equation,

$$U = \sqrt{2\frac{\left(P_{total} - P_{static}\right)}{\rho}} \qquad \textbf{(2.1)}$$

where U is the magnitude of the velocity vector, ρ is the density of the flow, P_{total}, and P_{static} are the mean total and static pressures, respectively. To perform these measurements, a digital manometer Model 474-FM mark III from Dwyer Instruments Inc. with an accuracy of ±0.01 inch of water was used. The measurements were read such that statistically ergodic data were measured as described in the previous section.

2.1.5 Boundary Layer Wind Tunnel

The Virginia Polytechnic Institute and State University Boundary Layer Wind Tunnel in the Aerospace and Ocean Engineering Department is an open-circuit type low speed wind tunnel. It is powered by a 19kW centrifugal blower that draws air from an air filter and blows it through a flow damper used for speed variations. To reduce the turbulence intensity and the mean swirl of the flow, the air passes through a section of honeycomb, a 4:1 contraction ratio section and seven wire-mesh screens before going through the test section. The flow entering the test section is tripped by a 6.3 mm high step and passes through a 1.5:1 contraction with a 25.1 cm throat height, where the reference velocity and temperature are measured, located 1.63 m downstream of the test section entrance. The test section has a 0.91 m wide rectangular cross section with a variable height to allow for the growth of the boundary layer and to maintain a streamwise zero pressure gradient.

At the reference velocity of 27.5 m /s and a reference temperature of 25°C (±1°C), the turbulence intensity in the freestream is 0.1 % and the potential core is uniform within 0.5% and 1% in the spanwise and vertical direction respectively. The Reynolds number based on the momentum thickness produced at these conditions, located 120 inches downstream of the beginning of the test-section, is $\mathrm{Re}_\theta = 7300$ that corresponds to similar conditions as the one observed by Byun et *al.* (2004) and Ma and Simpson (2004). The reference velocity U_{ref} , was measured via a digital manometer

Model 474-FM mark III from Dwyer Instruments Inc. with an uncertainty of ±0.01 inch of water connected to a Pitot-static probe by Dwyer Instruments. The reference temperature, T_{ref} was read by a thermocouple model 72-2065 manufactured by TENMA with an uncertainty of $\pm 1 \deg .C$.

2.1.6 Test Flows Geometries

The test cases utilized for this study are three three-dimensional symmetric bumps referred as bump 1, small bump 3 and large bump 3. Byun et *al.* (2004) describe these bumps and the flow behavior in one wake plane of each bump.

2.1.6.1 Coordinate system

The coordinate system which origin is located at the center of the bumps has the x, y, and z coordinates in the positive streamwise, normal to the tunnel floor, and spanwise directions, respectively (Figure 2.4).

2.1.6.2 Bump 1

Bump 1 (Figure 2.5 and Figure 2.7) is a symmetric bump with its axis of symmetry along the streamwise axis. It is defined by equation 2.2 from Willits and Boger (1999). Its height is $H = 78mm$ and it has a rectangular base of length and width, $a_1 = 4H$ and $b_1 = 2H$, respectively.

$$\frac{y(x,z)}{H} = \frac{1}{1.1329^2}\left[\cos\left(4.73\frac{x}{a_1}\right) + 0.1329\cosh\left(4.73\frac{x}{a_1}\right)\right] \times \left[\cos\left(4.73\frac{z}{b_1}\right) + 0.1329\cosh\left(4.73\frac{z}{b_1}\right)\right] \quad \textbf{(2.2)}$$

2.1.6.3 Small and large bumps 3

The small and large bumps 3 (Figure 2.5 and Figure 2.7) are axisymmetric Gaussian bumps defined by equation 2.3 from Willits and Boger (1999).

$$\frac{y(r)}{H} = -\frac{1}{6.04844}\left[J_0(\Lambda)I_0\left(\Lambda\frac{r}{a_3}\right) - I_o(\Lambda)J_0\left(\Lambda\frac{r}{a_3}\right)\right] \quad \textbf{(2.3)}$$

where $\Lambda = 3.1962$, $H = 78mm$ is the large bump 3 height and $H = 39mm$ is the small bump 3 height. For both, $a_3 = 2H$ is the radius of the circular base of the bumps, J_0 is the Bessel function of the first kind, and I_0 the modified Bessel function of the first kind.

2.1.7 The traverse system

The traverse system was developed to provide horizontal and vertical displacements of a probe in a plane at a specific streamwise position. The horizontal displacements were obtained by two HL46D0M223001 Techno-Isel carriages moving along two one-meter long HL4222M0011000 Techno-Isel rails themselves fixed to a one-meter long HL4720M1012-1000 Techno-Isel base plate. Two similar carriages moving along a sixty centimeters long HL4222M0010600 Techno-Isel rail fixed to the horizontal displacement carriages produced the vertical displacements. A photo of the traverse is shown in Figure 2.8. A circular shaft going through three mountings fixed to the vertical displacement carriages had a triangular L joint attached at its end from which a rod extended to a probe holder (Figure 2.9). Extra vibration from the drag induced by the shaft and probe in the flow was reduced using a bearing attached at the end of the vertical rail and the traverse was fixed to the wind tunnel structure via C-clamps.

To provide the displacements of the carriages along the rails, two S/QM-57-83-S Compumotors (one for each direction) and their corresponding PDX-13 drivers from Parker Automation were used. The motors speed range, acceleration range, rotor-inertia and maximum resolution are *0.01* to *50* rps, *0.01* to *999* rps^2, *0.201* kg-cm^2, and *4000* steps/revolution, respectively. The motions of the carriages were obtained from the rotation of lead screws going from the motors to a bearing in a plate fixed on the carriages. The lead screws have a *16* threads/inch resolution. A photo of the traverse arm is seen in Figure 2.9. Figure 2.8 is a photo of the whole traverse and a photo of the seven-hole probe set on the traverse when measuring small bump 3 is in Figure 2.10. The motors were controlled using a Labview interface allowing modification of speed and position of the shaft with respect to an initial position defined as the surface of the wind-tunnel test section. The traverse movements were used with an uncertainty of $\pm 10^{-2}$ inch.

2.1.8 Wind tunnel ceiling

To allow for movements of the traverse shaft through the ceiling, two ceiling sections for the test section were designed with six spanwise slots and one streamwise slot (Figure 2.11 and Figure 2.12). The ceiling sections were made out of a quarter inch thick transparent Plexiglas and were reinforced with aluminum channels for structural purposes. Two ceiling sections were used, one section on top of the bumps (Figure 2.11) and the other downstream of the bumps (Figure 2.12). The ceiling downstream of the bumps was set on top of a quarter inch thick transparent Plexiglas fixed against the sidewalls of the test section. The ceiling on top of the bumps was partly supported by the Plexiglas used to support the downstream ceiling and partly by a set of ceiling supporters, shown in Figure 2.13, on either sidewall at the beginning of the test section.

2.1.9 Wind tunnel surface

To set the bumps in the wind tunnel, a hole with a ledge around the edge (stepped cutout) was cut in the floor of the wind tunnel to allow a base plate to fit in it. The dimensions of the hole as well as its position in the wind tunnel test section are shown in Figure 2.13. The base plates used are smaller than the hole to allow for changing the base plate position and therefore, bumps positions in the wind tunnel. Figure 2.14, Figure 2.15, and Figure 2.16 show the base plates used for bump 1, small bump 3, and large bump 3 with their dimensions, respectively. A discussion of their position on the hole is done later. The bumps were fixed to the base plate with screws and, to produce smooth joints, scotch tape was used.

2.2 Technique

2.2.1 Seven-hole probe data reduction algorithm description

The data reduction algorithm used for this study to reduce the seven-hole probe pressure data was developed and discussed by Johansen et *al.* (2001). An overview of this method is presented next.

Because of the wide range of flow angles the seven-hole probe can perform measurements (up to 75 deg., Johansen et *al.* (2001)), it is obvious that at high flow angles the flow will be separated on the lee side of the probe. Since the pressure ports located in the separated flow regions cannot be used, two sets of incidence angles are

defined. For low incidence angles, when the port located on the tip of the probe reads the maximum pressure, the flow is attached everywhere on the surface of the probe and all the pressure ports are used in the data reduction algorithm. For large incidence angles, the maximum pressure is read by one of the circumferential port, and only the pressure ports located in non-separated flow regions are used in the data reduction algorithm. For low angles of incidence, when the maximum pressure is read by the tip pressure port, a pseudo-dynamic pressure q and a set of non-dimensional pressure coefficients are defined (Johansen et *al.* (2001)).

$$
\begin{aligned}
q &= p_1 - \frac{p_2 + p_3 + p_4 + p_5 + p_6 + p_7}{6} \\
b_\alpha &= \frac{p_5 + p_4 - p_7 - p_2}{q\sqrt{3}}, \quad b_\beta = \frac{p_4 + p_2 - p_5 - p_7}{2q} + \frac{p_3 - p_6}{q}, \\
A_t &= \frac{p_1 - P_{total}}{q}, \quad A_S = \frac{q}{P_{total} - P_{static}}
\end{aligned}
\qquad \textbf{(2.4)}
$$

where P_{total} and P_{static} are the total and static pressure, respectively. For large angles of incidence, when the maximum pressure is read by one of the circumferential pressure port, a set of non-dimensional pressure coefficients are defined (Johansen et *al.* (2001)).

$$
\begin{aligned}
q &= p_{i\max} - \frac{p^+ - p^-}{2} \\
b_\theta &= \frac{p_{i\max} - p_1}{q}, \quad b_\phi = \frac{p^+ - p^-}{q} \\
A_t &= \frac{p_{i\max} - P_{total}}{q}, \quad A_S = \frac{q}{P_{total} - P_{static}}
\end{aligned}
\qquad \textbf{(2.5)}
$$

where $p_{i\ max}$ is the pressure read by port *"i"*, the maximum pressure reading port, and p^+ and p^- are the pressure ports next to the i^{th} pressure port in the clockwise and counter clockwise direction, respectively. The coordinate system of the data reduction algorithm with its origin at the tip of the probe is represented on Figure 2.17 with the corresponding angle definitions. For simplicity, the coefficients b_α and b_β for low angles of incidence, and b_θ and b_ϕ for high angles of incidence are referred as b_1 and b_2, respectively.

In order to obtain a calibration database for the seven-hole probe, the seven-hole probe was placed in a low turbulence intensity steady uniform known flow-field. By

changing the flow angles of the probe with respect to the known flowfield, a table of calibration data consisting of the seven pressures from each of the seven pressure ports, the flow angles α and β, the total and static pressures, and the calculated non-dimensional pressure coefficients b_1, b_2, A_t and A_S were obtained. The sets of non-dimensional pressure coefficients b_1 and b_2 from the calibration database similar to the set of non-dimensional pressure coefficients calculated in an unknown flowfield are used to interpolate the flow properties in the unknown flow field using a first order polynomial fit.

$$\begin{aligned}
\alpha &= \alpha(b_1, b_2) = c_{0\alpha} + c_{1\alpha} b_1 + c_{2\alpha} b_2 \\
\beta &= \beta(b_1, b_2) = c_{0\beta} + c_{1\beta} b_1 + c_{2\beta} b_2 \\
A_S &= A_S(b_1, b_2) = c_{0As} + c_{1As} b_1 + c_{2As} b_2 \\
A_t &= A_t(b_1, b_2) = c_{0At} + c_{1At} b_1 + c_{2At} b_2
\end{aligned} \qquad \textbf{(2.6)}$$

where c_{0j}, c_{1j}, and c_{2j} are the polynomial coefficients (j = α, β, A_S, or A_t). Using the pressure coefficients A_S and A_t, the total and static pressures are calculated (equation 2.4 and 2.5) and the magnitude of the velocity vector can be evaluated. The data reduction algorithm developed by Johansen et *al.* (2001) accounts for compressibility effects for calculating the velocity magnitude (equation 2.7). Using the total and static pressure calculated, the Bernoulli's equation was used and similar results as the ones using equation 2.7 were obtained. This observation reveals that the flow at the reference velocity, $U_{ref} = 27.5\ m/s$, is incompressible and using Bernoulli's equation or equation 2.7 leads to similar results.

$$U = \sqrt{5 \cdot \left(\left(\frac{P_{total}}{P_{static}} \right)^{2/7} - 1 \right) \cdot \gamma \cdot R \cdot T} \qquad \textbf{(2.7)}$$

where P_{total} and P_{static} are computed with,

$$P_{total} = p_i - A_t \cdot q \quad and \quad P_{static} = P_{total} - \frac{q}{A_S} \qquad \textbf{(2.8)}$$

With the flow angles and the magnitude of the velocity vector known, the components of the mean velocity vector are calculated.

$$\begin{aligned}\overline{U} &= U \cdot \cos(\alpha) \cdot \cos(\beta) \\ \overline{V} &= U \cdot \sin(\beta) \\ \overline{W} &= U \cdot \sin(\alpha) \cdot \cos(\beta)\end{aligned} \qquad \textbf{(2.9)}$$

where, $\overline{U}$, $\overline{V}$, and $\overline{W}$ are the streamwise, vertical and spanwise components of the mean velocity vector respectively. The uncertainties with 20:1 odds obtained by the algorithm described from the MultiProbe software are presented in Table 2.1.

Table 2.1: Uncertainty analysis results from data reduction algorithm for the seven-hole probe

Pitch (deg)	±0.64
Yaw (deg)	±0.46
Velocity Magnitude (%)	±0.58

The uncertainties calculated are smaller than those observed by Gallington (1980), Zilliac (1989) or Wenger and Devenport (1999). However, the uncertainties induced by the apparatus (principally the pressure transducers) are not included in the calculated uncertainties presented in Table 2.1.

2.2.2 Choice of the Pressure transducer system and its calibration

A pressure transducer transforms a pressure to a voltage through a linear relation of the form:

$$V_r = A \cdot p_r + B \qquad \textbf{(2.10)}$$

where V_r is the voltage emitted by a pressure transducer, p_r the pressure read, A and B the coefficients of the linear relationship. The main disadvantage of a pressure transducer comes from its offset B known to drift as function of time and temperature, therefore inducing a bias in the pressures read. Since the seven-hole probe results are obtained from pressure measurements, it is obvious that a bias in the pressure readings will lead to significant errors in the seven-hole probe results. It is therefore essential to minimize this bias induced by the drift of the transducer offset.

Using the first system described in section 2.1.2, with one pressure transducer and the scanivalve system, the value of the offset of the linear relation is not important since it is cancelled in the subtraction and quotient of the pressure readings. Consequently, as long as a linear relationship exists between the pressures felt and the voltages produced

by the transducers, the bias error is cancelled. With the second system and its seven different pressure transducers, the drift of the offset voltages if not carefully monitored becomes a major source of uncertainty. At this point, it would seem that using the scanivalve system would be the best choice to use since the errors due to the offset drift are cancelled. The problem comes from the need to acquire data for a long time to measure statistically ergodic data with the seven-hole probe. For the Virginia Polytechnic Institute and State University Boundary Layer Wind Tunnel, it was determined in previous studies that the statistical ergodicity of the flow is obtained by acquiring data for a minimum time of 40 seconds. Using the seven pressure transducers, the pressures would be obtained in 40 seconds simultaneously but, if the scanivalve system was used, the time required to obtain the seven pressures is 4 minutes and 40 seconds. Since the grids of data points selected to perform measurements in the wake of the bumps often ranges between 300 and 400 data points, using the scanivalve system would require a tremendous amount of time for a limited amount of data. Consequently, a study of the seven transducers was performed to determine if the bias induced by the drift of the offset could be minimized.

2.2.2.1 Pressure transducer offset drift investigation

First, the time dependency of the drift of the offset voltage was examined. Figure 2.18 shows the data obtained for the time dependency investigation of the offset voltage of the pressure transducers; the abscissa corresponds to the time when data were obtained and the ordinate shows the voltage output from the seven pressure transducers. The data were obtained in a period of two days and the pressure transducers stayed turned on for the whole time. It can be seen that the values of the offsets for each of the seven pressure transducers vary in a relatively similar manner at the same times implying that time is not the main factor driving the drift of the offsets. For this reason the investigation of the temperature dependence of the drift of the offset was done.

Three different time cases were studied, the temperature dependence of the drift of the transducers on the data taken on the first day, on the second day, and over the two days period as can be seen in Figure 2.19. It appears that a linear relationship between the temperature around the transducers and the value of their offsets exists. Consequently, a linear fit was applied to the data as can be seen in Figure 2.19

$$B = m \cdot T_i + b \qquad \textbf{(2.11)}$$

In equation 2.11, m and b are the coefficients of the linear relationship, respectively, T_i is the temperature indicated by the thermometer, and B is the offset pressure of the transducers. In order to test the accuracy of the linear fit, the uncertainties with 20:1 odds in the offset pressure of each transducer, δB, are calculated with equation 2.12 and presented in Table 2.2.

$$\delta B = 1.96 \cdot \sqrt{\frac{1}{N}\sum \left(m \cdot T_i + b - B\right)^2} \qquad \textbf{(2.12)}$$

Table 2.2: U**ncertainty analysis in the offset pressure calculations**

Transducer # →	**1**	**2**	**3**	**4**	**5**	**6**	**7**
	δB [Pa]						
Day 1 and 2	0.0016	0.0010	0.0009	0.0007	0.0008	0.0024	0.0005
Day 1	0.0004	0.0009	0.0009	0.0005	0.0007	0.0014	0.0002
Day 2	0.0002	0.0011	0.0009	0.0005	0.0009	0.0007	0.0005

The uncertainties calculated on a one-day period are smaller than the uncertainties calculated on a two-day period, and the uncertainties calculated on the two one-day periods are different one from the other. Moreover, for the three time cases, the uncertainties calculated are small. These observations reveal that the temperature variations of the pressure transducers are indeed affecting the value of the offset voltage. The time also affects the offset voltage value but to a lesser extent than the temperature variations.

The two sources of error responsible for the drift of the offset voltage of the pressure transducers utilized were identified as the temperature variations of the pressure transducers and the time. A method was proposed to predict the value of the offset voltage and was tested with an uncertainty analysis. Small uncertainties of the offset voltage predictions were calculated confirming the validity of the model proposed and, it was found that smaller uncertainties were observed on a one-day period than on a two-day period.

2.2.3 Method to acquire data

2.2.3.1 Monitoring of the offset drift

As discussed in the previous section, using the linear fit approximation to monitor the drift of the offset voltage, the use of the second system with the seven pressure transducers reading the seven pressure ports from the seven-hole probe is now possible since the bias due to the drift of the transducer offset is minimized. A technique to monitor the offset and obtain the linear fit coefficients is presented in this section.

To read the offsets of the seven pressure transducers when the seven-hole probe was set up in the wind tunnel test section, the wind tunnel was turned off with no air circulating in it. At this point, a measurement of the pressure transducers output was done and the temperature of the pressure transducers was recorded. It was decided that every time the probe vertical position was modified, a measurement of the offsets along with the transducers temperature was done. The discussion from the previous section shows that the uncertainties due to the drift of the transducers are minimized if the linear fit is calculated on a one-day period. Consequently, the monitoring of the offset was done and the coefficients for the linear fit were obtained everyday that data were being recorded.

2.2.3.2 Sampling time determination

As briefly stated previously, the sampling time for acquiring data has to be chosen long enough to allow the data to be statistically ergodic. From previous experimental work in the Virginia Polytechnic Institute and State University Boundary Layer Wind Tunnel, it was shown that a 40 seconds sampling time was enough to allow the flow to be statistically ergodic and therefore, it was chosen as the sampling time for the measurements upstream and in the wake of large bump 3. A mistake was done in this since the statistical ergodicity of the data was assumed to be obtained with the 40 seconds sampling time without being checked but, as it will be shown later in this work, the sampling time chosen was too short for statistical ergodicity of the data. As a result, an error was introduced in the measurements over large bump 3 particularly in regions of high turbulence intensity.

For small bump 3, the sampling time used to record data was studied by measuring several sets of data with an increasing sampling time. The three components

of the mean velocity vector measured with the seven-hole probe using a sampling time of 50 seconds and of 60 second are presented in Figure 2.20. The differences between the two sets of data are small confirming that the data were statistically ergodic for the two sampling times studied (a sampling time of 2 minutes was studied using a quad-wire hot-wire probe by Ma and Simpson (2004) and it was found that the data measured were the same than the one measured with a sampling time of 60 seconds). Consequently, the sampling time chosen for acquiring data on small bump 3 was 60 seconds. A similar investigation on the sampling time to acquire data for statistically ergodic data was done for bump 1 and the results are shown in Figure 2.21. The data were measured over bump 1 at $x/H = 3.455$ at $y = 0.1 inch$ in two cases, one with a sampling time of 50 seconds and one with a sampling time of 60 seconds. The two sets of data are identical proving the statistical ergodicity of the data with a sampling time of 50 seconds.

When acquiring data the number of samples was chosen to be 10,000 samples, leading to sampling rate of 200 samples/seconds, 167 samples/seconds, and 250 samples/seconds for measurements in the wakes of bump 1, small bump 3, and large bump 3, respectively. The sampling times used for each of the three three-dimensional bumps are summarized in Table 2.3.

Table 2.3: **Sampling rate used to measure statistical ergodic data for bump 1, small and large bump 3**

	Sampling time for statistically ergodic data
Bump 1	50 seconds
Small bump 3	60 seconds
Large bump 3	unknown, 40 seconds is used

A 10 seconds delay was used at each measurement locations to account for the time delay induced by the long tubing system and the response of the pressure transducers.

2.2.3.3 Symmetry of the flow field in the wake of the bumps

To obtain a symmetric flowfield at the streamwise planes measured with the seven-hole probe in the wakes of the bumps, the position of the bumps had to be adjusted in the wind-tunnel test section. In this fashion, a study of the flow symmetry in the wakes of the bumps at specific location was made.

Two positions were used for bump1; position 1 corresponds to the base plate set against the left side of the stepped cutout (looking at Figure 2.13) and position 2 corresponds to the base plate set against the right side of the stepped cutout that is, 0.125 inch to the right of position 1. Figure 2.22 represents the sets of data obtained at these two positions. Note that the heights of the two sets of data were slightly different due to a mistake in the input of the vertical position in the acquisition code. For the two cases, the symmetry of the flowfield at $x/H = 3.455$ in the wake of bump 1 is qualitatively good. For a quantitative analysis of the symmetry of the flow in the wake of bump 1, an uncertainty analysis quantifying the symmetry of the mean velocity components is made.

$$\delta\overline{U}_{symmetry} = 1.96 \cdot \sigma\left|\left|\overline{U}\right|_{negative\_z} - \left|\overline{U}\right|_{positive\_z}\right| \qquad \textbf{(2.13)}$$

In equation 2.13, $\left|\overline{U}\right|_{negative\_z}$ and $\left|\overline{U}\right|_{positive\_z}$ are the absolute value of the mean streamwise velocity component in negative spanwise coordinates and positive spanwise coordinates, respectively, σ is the symbol for the standard deviation of the absolute difference and, $\delta\overline{U}_{symmetry}$ is an uncertainty quantifying the symmetry of the mean streamwise velocity component with 20:1 odds. Similarly, uncertainties for the normal and streamwise mean velocity components are calculated and the results are presented in Table 2.4.

Table 2.4: Uncertainty analysis quantifying the symmetry of the flowfield in the wake of bump 1

Bump 1	$\delta\overline{U}_{symmetry}$ [m/s]	$\delta\overline{V}_{symmetry}$ [m/s]	$\delta\overline{W}_{symmetry}$ [m/s]
Position 1: *Base plate set against the left side of the stepped cutout*	±0.57	±0.25	±0.30
Position 2: *Base plate set against the right side of the stepped cutout*	±0.62	±0.10	±0.20

The uncertainties quantifying the symmetry of the mean streamwise velocity component are of the same order of magnitude at both positions. However, the uncertainties quantifying the symmetry of the normal and spanwise mean velocity components are smaller when the base plate is set in position 2. Consequently, it was concluded that when the base plate is set in position 2, on the right side of the stepped cutout, a better symmetry of the flowfield was observed in the wake of bump 1. Accordingly, position 2 was selected as the position of bump 1 in the test section. The relatively similar

magnitude of the uncertainties calculated for both positions revealed that the symmetry of the flow in the wake of bump 1 is not very sensitive to the position of bump 1 in the test section.

In a similar manner, the position of small bump 3 in the test section was determined and uncertainties quantifying the symmetry of the mean velocity components in the wake of small bump 3 were calculated. Figure 2.23 represents the set of data obtained at two positions in the wake of small bump 3 at $x/H = 3.26$. Position 1 corresponds to the base plate of small bump 3 set against the left side of the stepped cutout (looking at Figure 2.13) and position 2 corresponds to the base plate being 3 mm away from the right side of the stepped cutout. A significant qualitative difference in the mean velocity components is observed suggesting that the position of small bump 3 in the test section significantly affected the symmetry of the flow in its wake. A similar uncertainty analysis as the one performed in the wake of bump 1 was done to quantify the symmetry of the mean velocity components at both positions. The results of this uncertainty analysis are presented in Table 2.5.

Table 2.5: Uncertainty analysis to quantify the symmetry of the flowfield in the wake of bump 1

Small bump 3	$\delta\overline{U}_{symmetry}$ [m/s]	$\delta\overline{V}_{symmetry}$ [m/s]	$\delta\overline{W}_{symmetry}$ [m/s]
Position 1: *Base plate set against the left side of the stepped cutout*	±0.42	±1.48	±0.06
Position 2: *Base plate 3mm away from the right side of the stepped cutout*	±0.18	±1.13	±0.10

The results of the uncertainty analysis reveal that the symmetries of the streamwise and normal mean velocity component are better when small bump 3 was set in position 2. However, the symmetry of the normal mean velocity component is slightly better when small bump 3 was set in position 1. Since the symmetry of the spanwise velocity component is less affected by the position of the bump than the symmetry of the streamwise and normal velocity components, it was decided to set small bump 3 in position 2, that is, 3 mm away from the right side of the stepped cutout.

The verification of the symmetry of the flow-field in the wake of large bump 3 was performed previously using a quad-wire hot-wire probe by Ma and Simpson (2004). The position obtained for the best symmetry of the mean velocity components in the

wake of large bump 3 was with the base plate 4.5 mm away from the right side of the stepped cutout (looking at Figure 2.13). Figure 2.24 shows a summary of the positions of the base plates for each bump with respect to the stepped cutout.

2.2.3.4 Alignment of the seven-hole probe

When the seven-hole probe was set on the traverse, its alignment with the tunnel coordinate system could not be accurately known. As a result, a method to find the alignment of the seven-hole probe was designed. At first, visual alignment of the seven-hole probe was made with respect to the tunnel coordinate. With the bump removed from the test section and a flat plate set instead, a few two-dimensional free-stream measurements were obtained with the seven-hole probe. The free-stream flow was assumed to be two-dimensional; consequently, the freestream velocity vector was a good reference for aligning the probe in the wind tunnel. In this fashion, the mean pitch and yaw angles were calculated from the measurement of the misaligned seven-hole probe. A coordinate transformation was used to rotate the mean velocity vector in the tunnel coordinate system.

An uncertainty analysis of the pitch and yaw angles (Table 2.6) was performed to test the accuracy of the method used for correcting the misalignment of the seven-hole probe with respect to the freestream.

Table 2.6: **Uncertainties in angular misalignment correction**

Pitch angle (deg)	±0.14
Yaw angle (deg)	±0.06

The standard deviations calculated are small giving confidence in the method used for aligning the probe.

2.2.4 Measurement locations

2.2.4.1 Two-dimensional flow

To know the quality of the incoming flow, seven-hole probe measurements of the undisturbed flow were done at $x/H = -4.6$ where information on the incoming boundary

layer properties were obtained and discussed. The grid of data used is represented in Figure 2.25.

2.2.4.2 Bump 1

The first plane examined on bump 1 with the seven-hole probe was $x/H = 3.455$ that has been thoroughly documented by Byun et *al.* (2004) using LDV measurements and quad-wire hot-wire data by Simpson and Ma (2004). The grid of data points used for measuring this plane of data is represented on Figure 2.26. The second plane of data examined in the wake of bump 1 was x/H=11.5. The grid of measurement points at this location is represented in Figure 2.27.

2.2.4.3 Small bump 3

The first plane examined on small bump 3 with the seven-hole probe was $x/H = 3.26$ that has been thoroughly documented by Byun et *al.* (2004) using LDV measurements and quad-wire hot-wire data by Simpson and Ma (2004). The grid of data points used for measuring this plane of data is represented on Figure 2.28. The second plane of data examined in the wake of small bump 3 was $x/H = 11.5$. The grid of measurement points at this location is represented in Figure 2.29.

2.2.4.4 Large bump 3

The first plane of data examined around large bump 3 with the seven-hole probe was x/H=–4.6 that is the same location as the one used to measure the two-dimensional incoming flow. By comparing with the two-dimensional flow, the influence of the bump on the incoming flow was discussed. The grid of measurement locations is the same as the one used for the two-dimensional flow (Figure 2.25). The second plane of data obtained on large bump 3 was x/H=0 that uses the grid of measurement points represented in Figure 2.30. The third plane examined on large bump 3 was x/H=3.629 that has been thoroughly documented by Byun et *al*. (2004) using LDV and Ma and Simpson (2004) with quad-wire hot wire anemometry. The grid of measurement location is shown in Figure 2.31. Finally, the last plane of data examined with the seven-hole probe about large bump 3 as $x/H = 11.5$ that uses the grid of measurement points in Figure 2.32.

The sidewall and ceiling boundary layer measured around large bump 3 were obtained using the sixteen-hole pressure rake. The ceiling boundary layer was measured in the centerline of the test section ($z/H = 0$) at $x/H = -3.81$. The sidewall boundary layers were measured at the same streamwise location ($x/H = -3.81$) at the vertical position of $y/H = 1.71$ for the positive spanwise coordinate sidewall (left sidewall looking at Figure 2.13) and $y/H = 1.77$ for the negative spanwise coordinate sidewall (right sidewall looking at Figure 2.13). With the Pitot-static probe, the streamwise velocity component about large bump 3 in the centerline of the test section ($z/H = 0$) at $y/H = 2.2$ was measured.

2.3 Figures

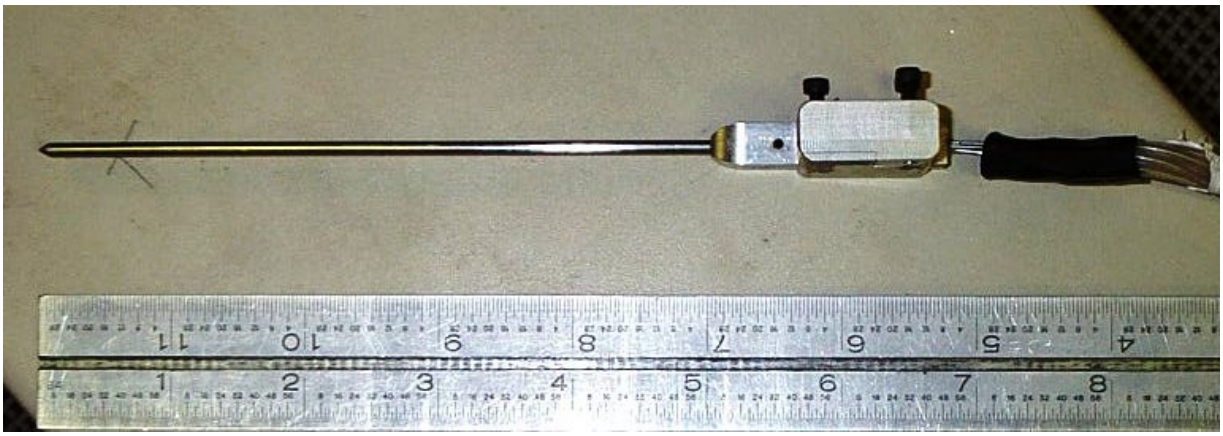

Figure 2.1: **Top view of the seven-hole probe used for this study**

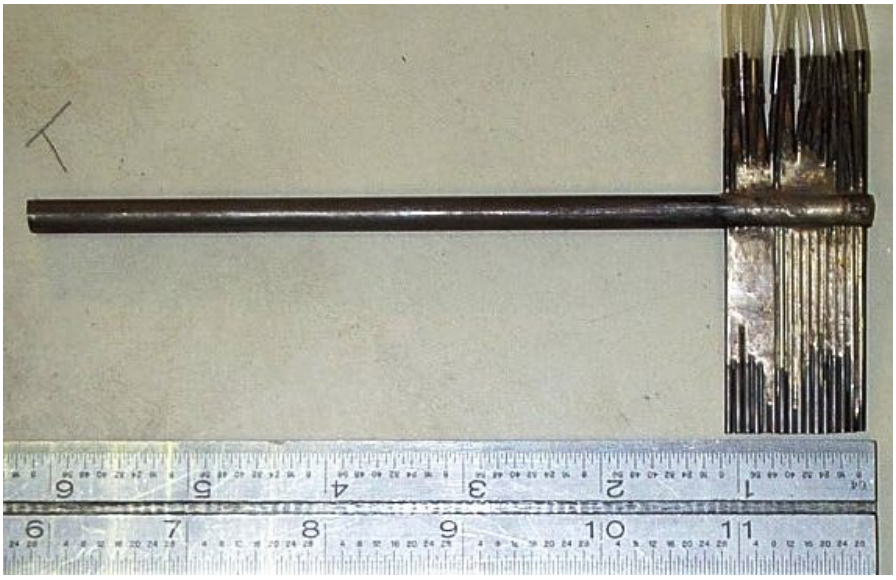

Figure 2.2: The pressure rake

Figure 2.3: The pressure rake set to measure the sidewall boundary layer in the Virginia Polytechnic Institute and State University Boundary Layer Wind Tunnel

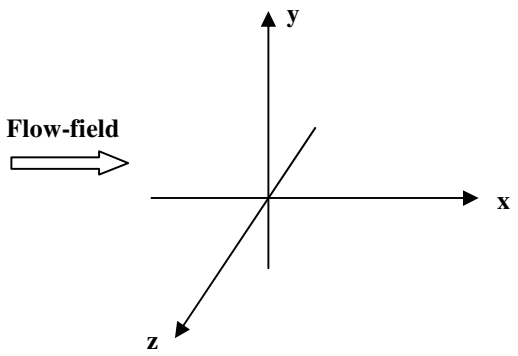

Figure 2.4: coordinate system for the 3 bumps

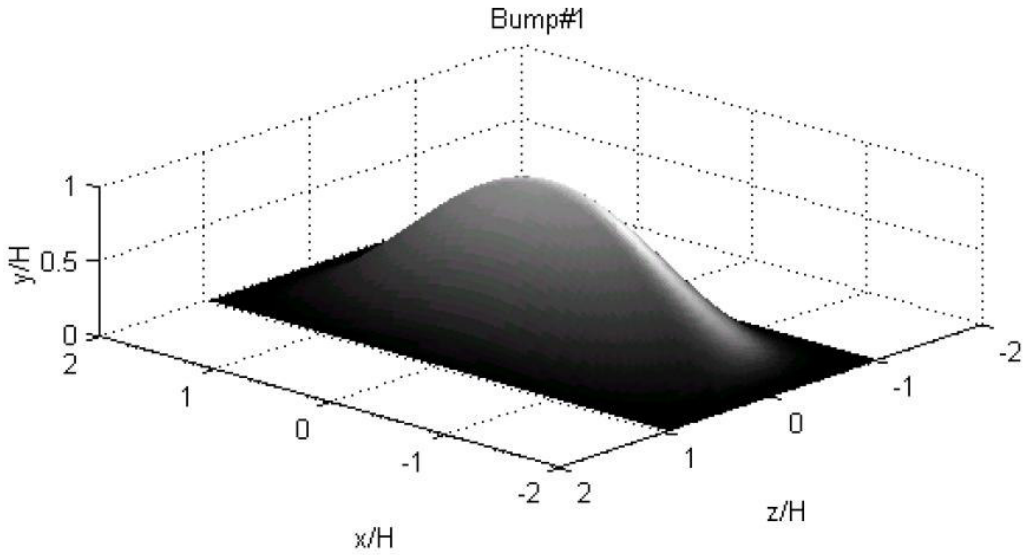

Figure 2.5: 3D representation of bump 1 in its coordinate system, Byun et *al.* (2004)

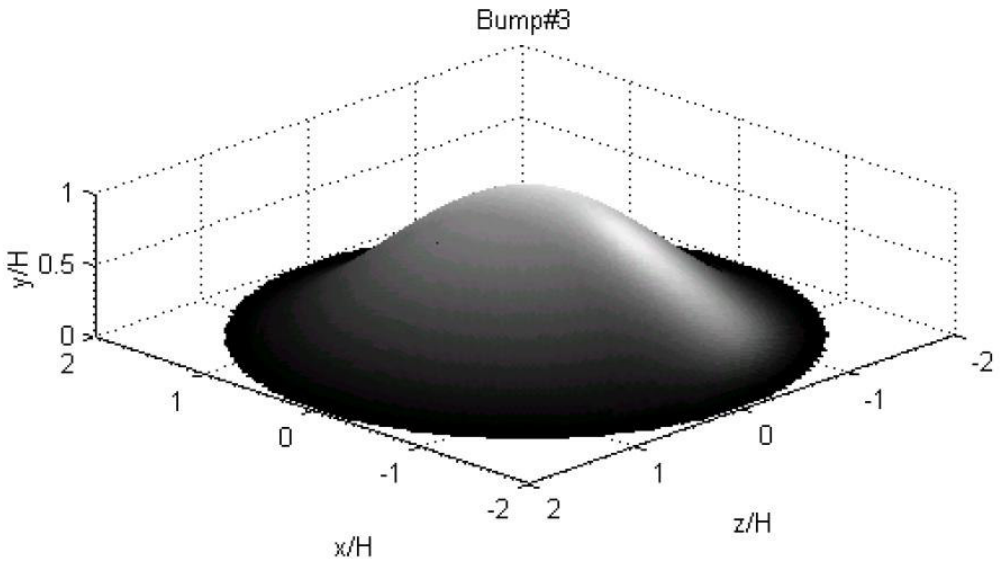

Figure 2.6: 3D representations of small and large bump 3 in their coordinate system, Byun et *al.* (2004)

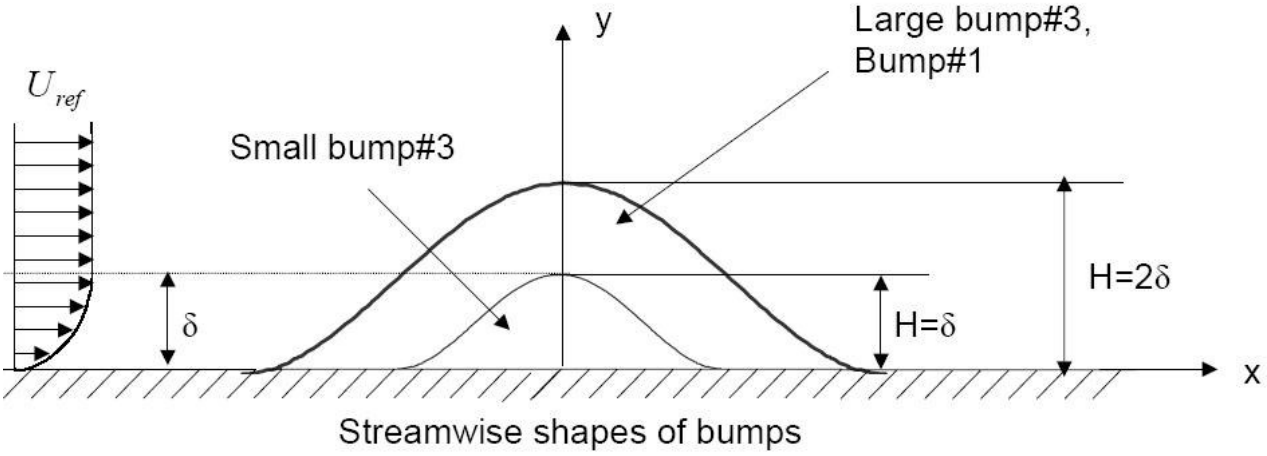

Figure 2.7: Side views representations of bump 1, small and large bump 3, Byun et *al.* (2004)

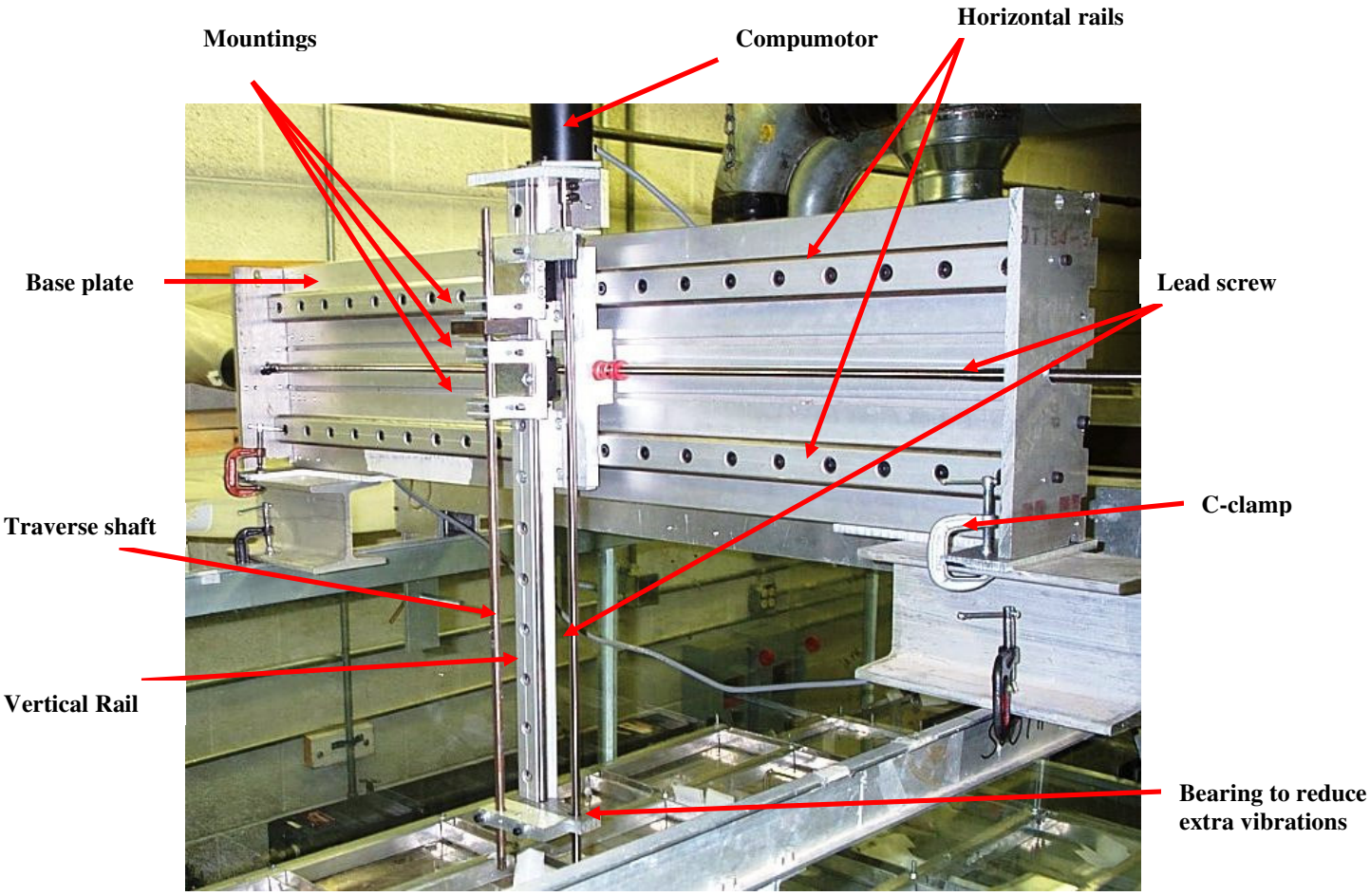

Figure 2.8; Photo of the traverse fixed on top of the Virginia Polytechnic Institute and State University Boundary Layer Wind Tunnel. The blocks under the traverse are only for photography purpose and are not used when data are being taken

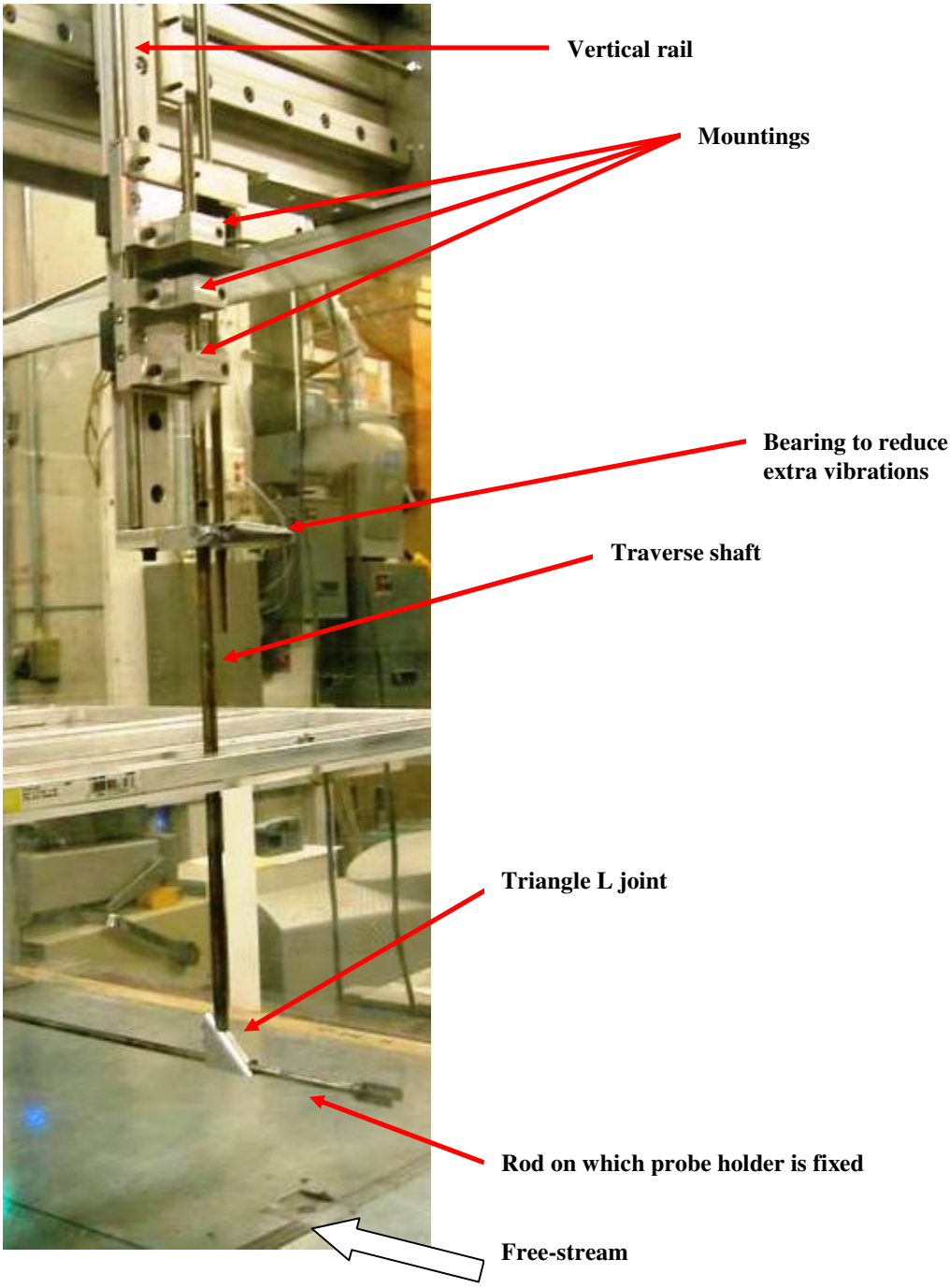

Figure 2.9: Representation of the traverse arm with no probe set on it

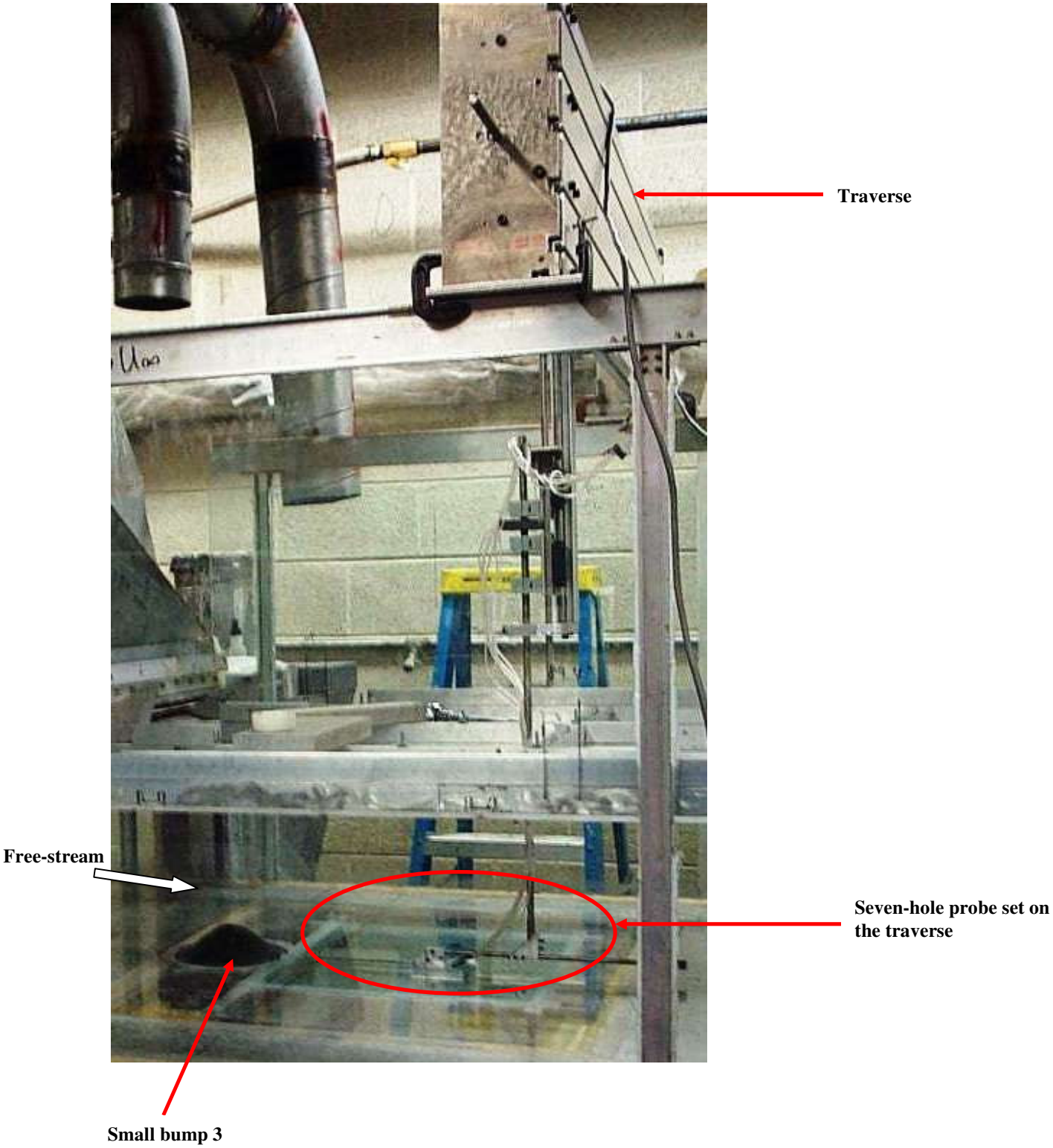

Figure 2.10: Photo of the seven-hole probe set on the traverse in the Virginia Polytechnic Institute and State University Boundary Layer Wind Tunnel with small bump 3 set in the test section

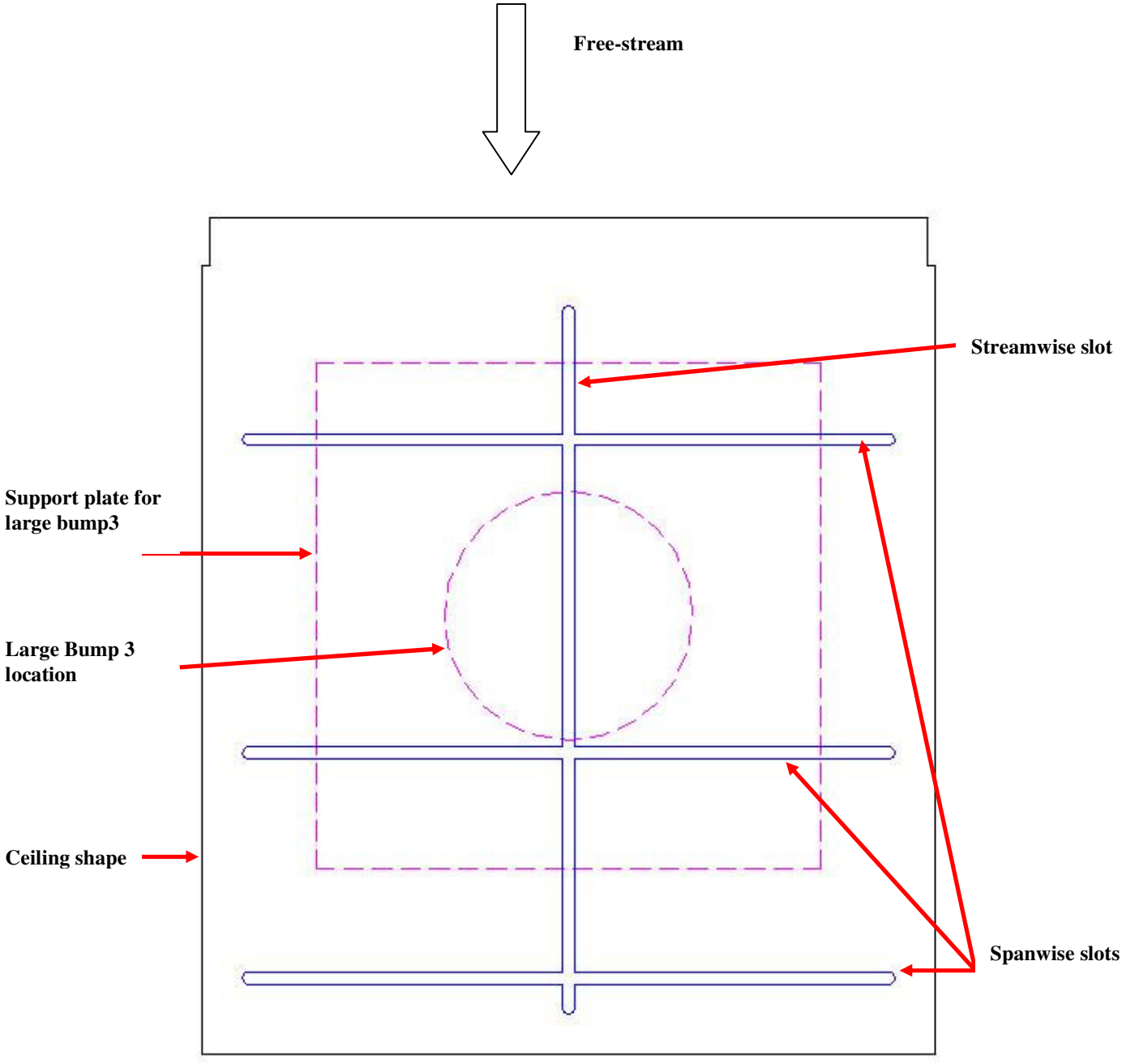

Figure 2.11: Ceiling of test section on top of the bump

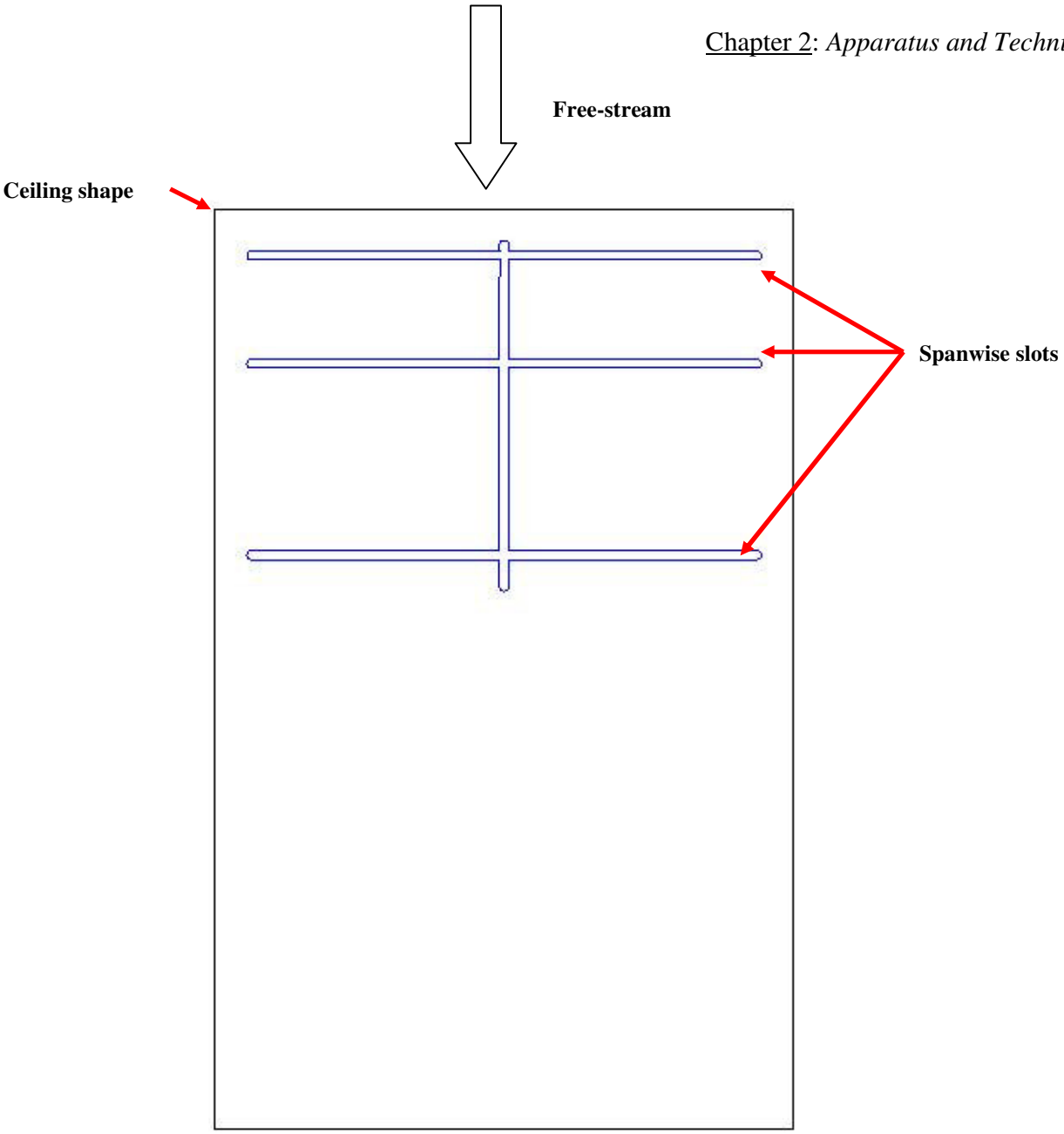

Figure 2.12: Downstream ceiling of test section

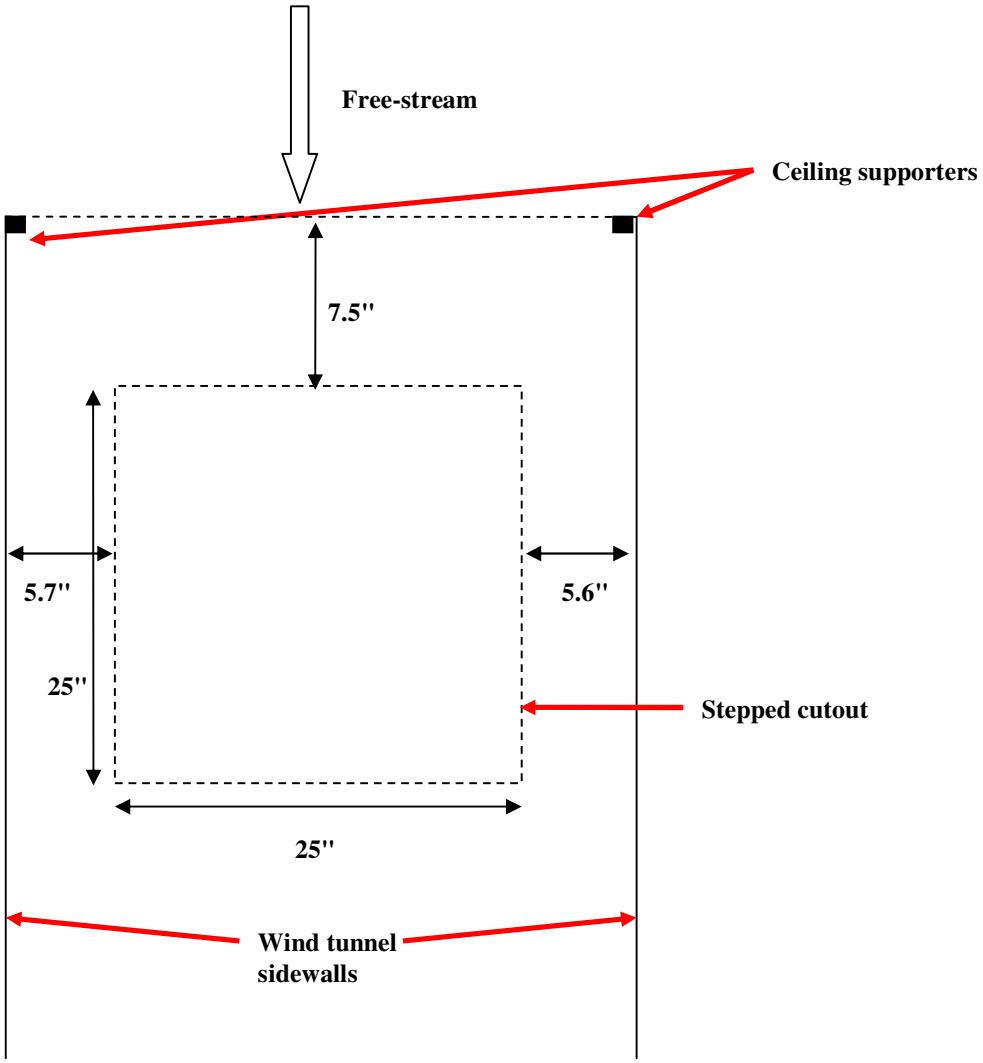

Figure 2.13: Representation of the stepped cutout where the base plate for the bumps is set on (not to scale)

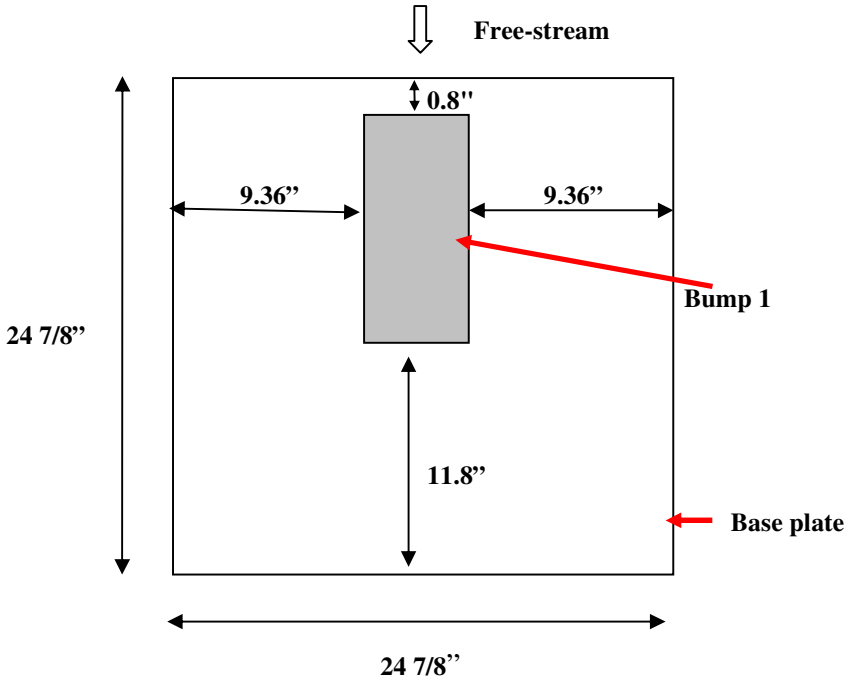

Figure 2.14: Base plate for bump 1 (not to scale)

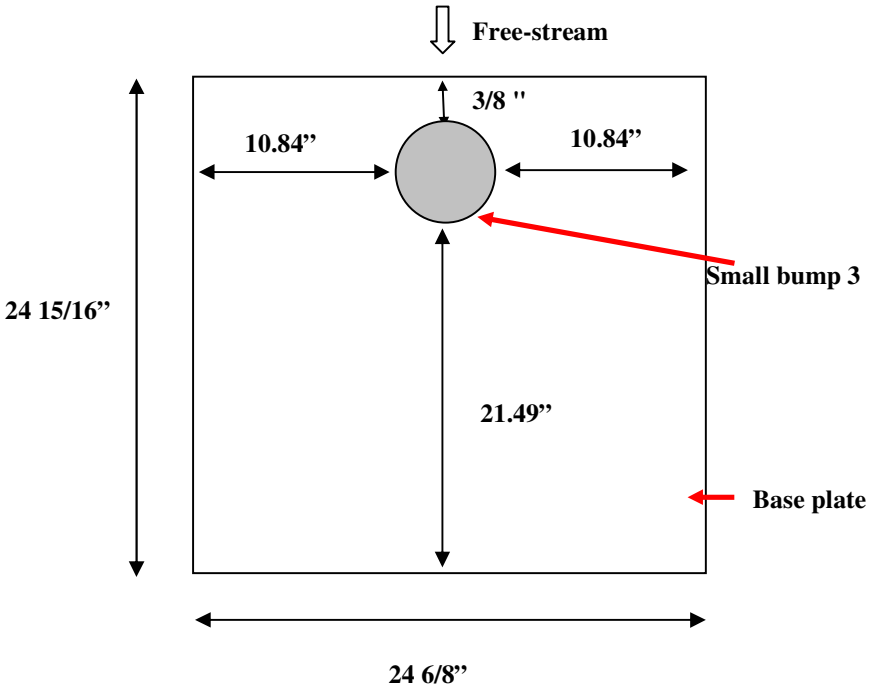

Figure 2.15: Base plate for small bump 3 (not to scale)

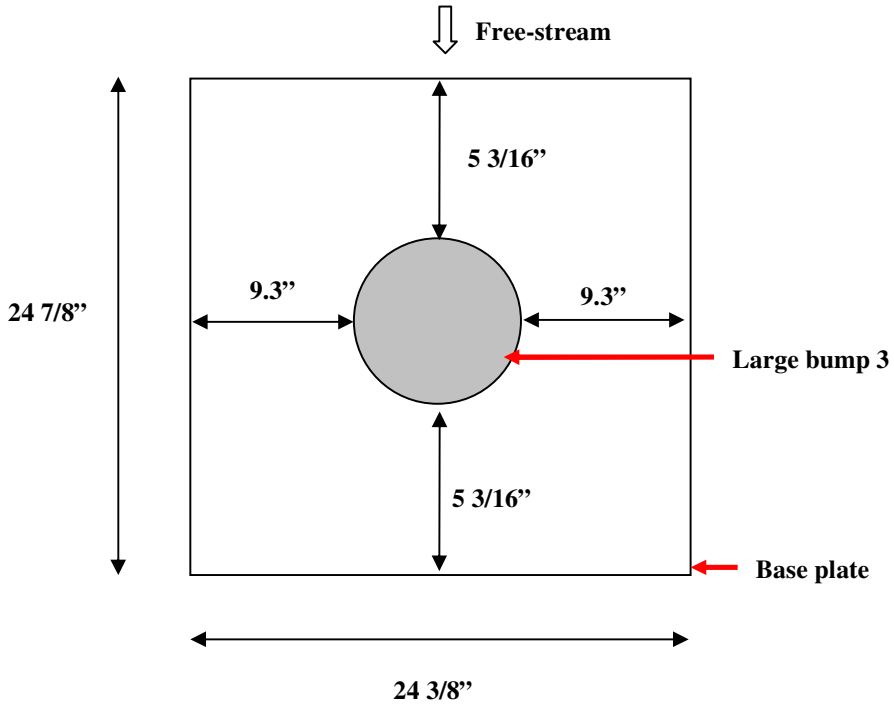

Figure 2.16: Base plate for large bump 3 (not on scale)

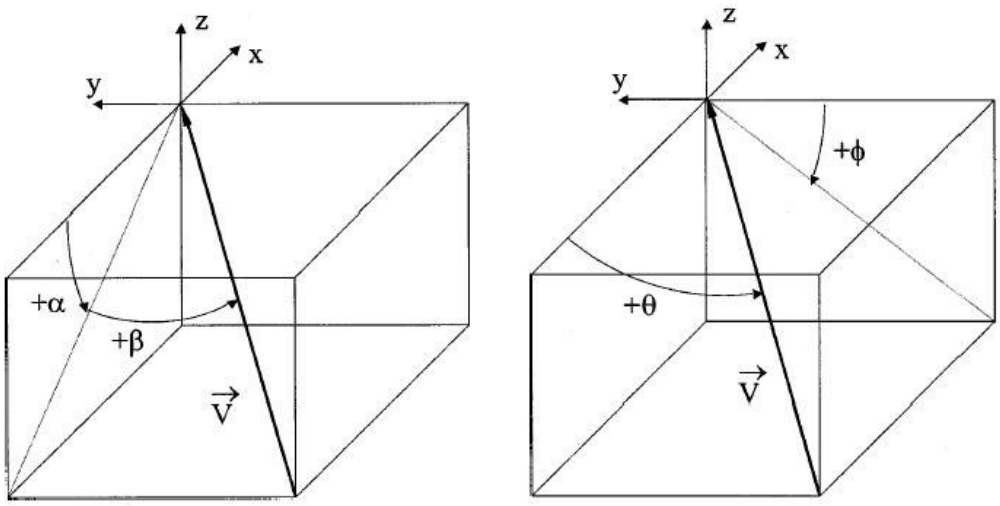

Figure 2.17: Definition of the coordinate systems and of the angles used for the seven-hole probe calibration algorithm, Johansen et *al.* (2001)

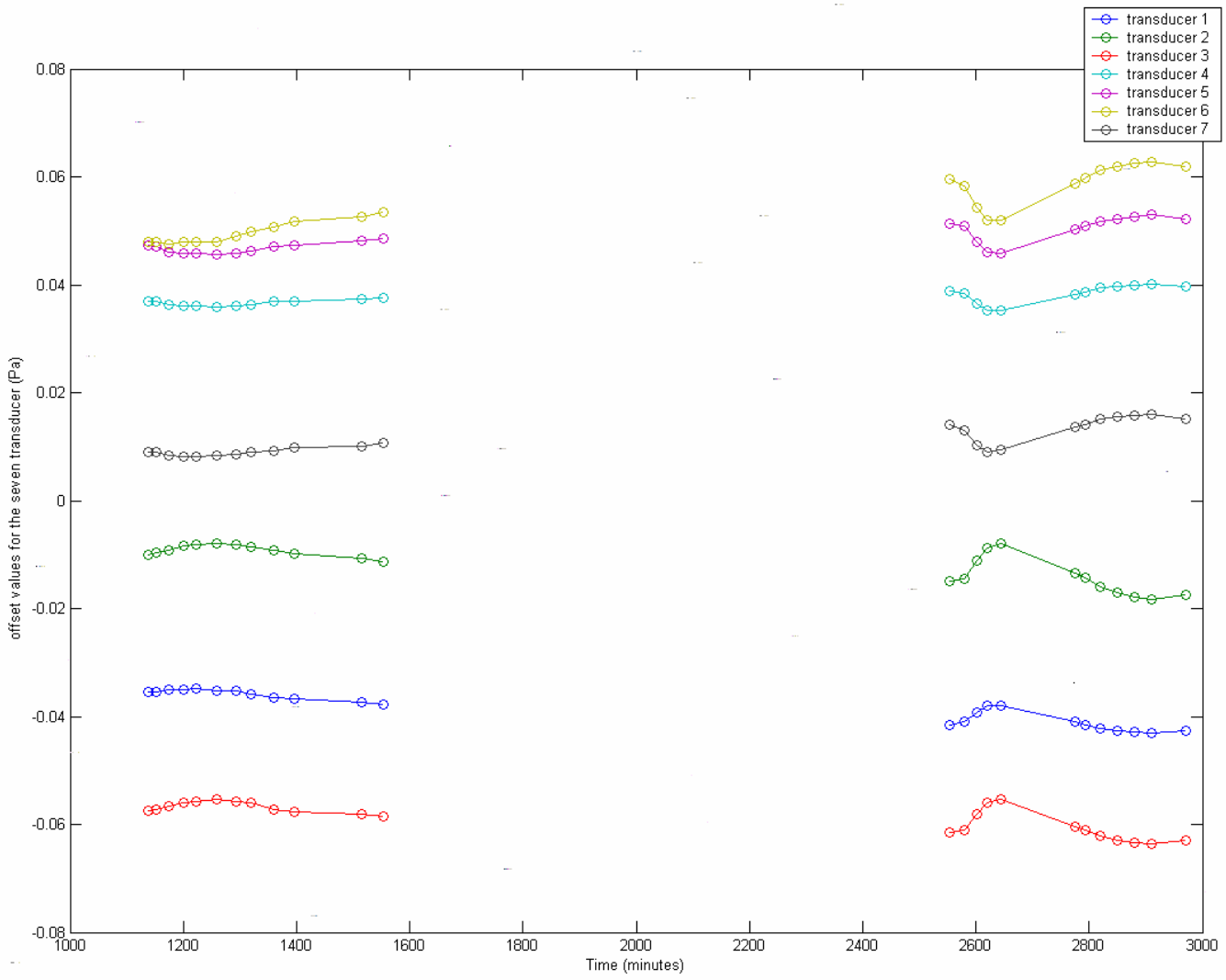

Figure 2.18: Investigation of the pressure transducer drift of the offsets over time. The gap between the data is because no data are measured,

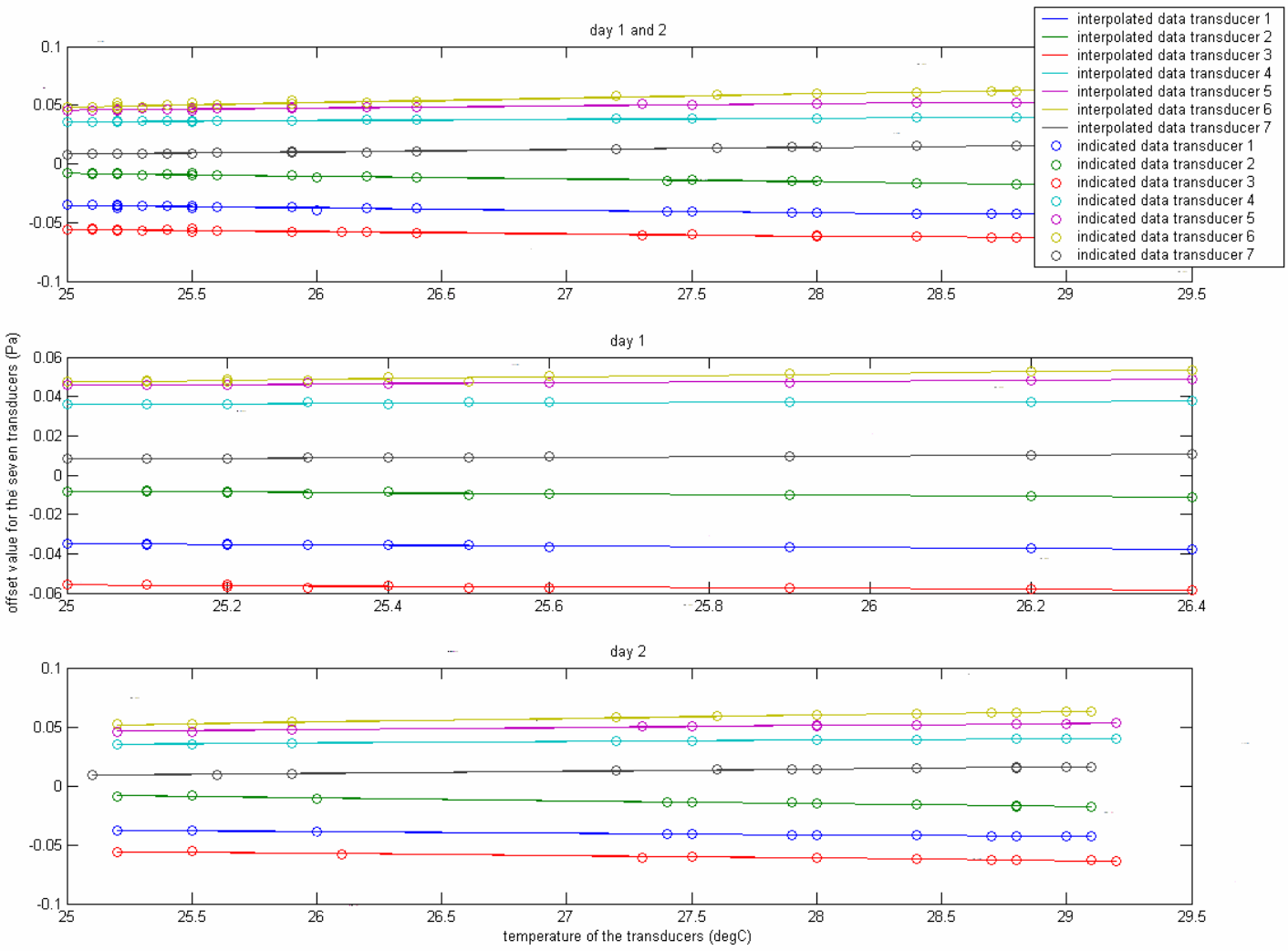

Figure 2.19: Linear fit approximation of the magnitude of the offset of the pressure transducers versus temperature in the transducers,

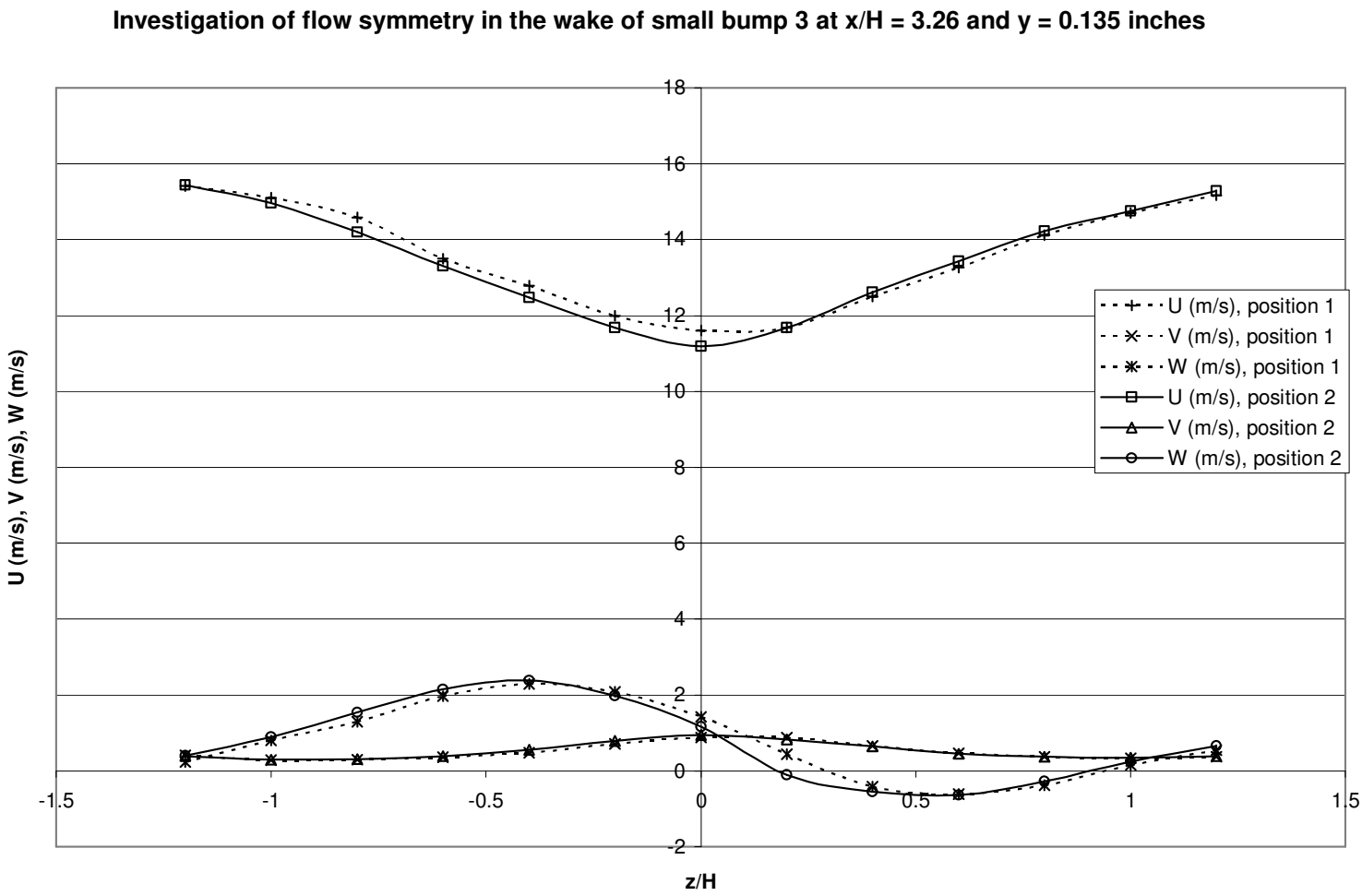

Figure 2.20: Investigation on the sampling time to acquire data necessary to have statistical ergodic data in the wake of small bump 3 at x/H = 3.26 and y = 0.135 inches

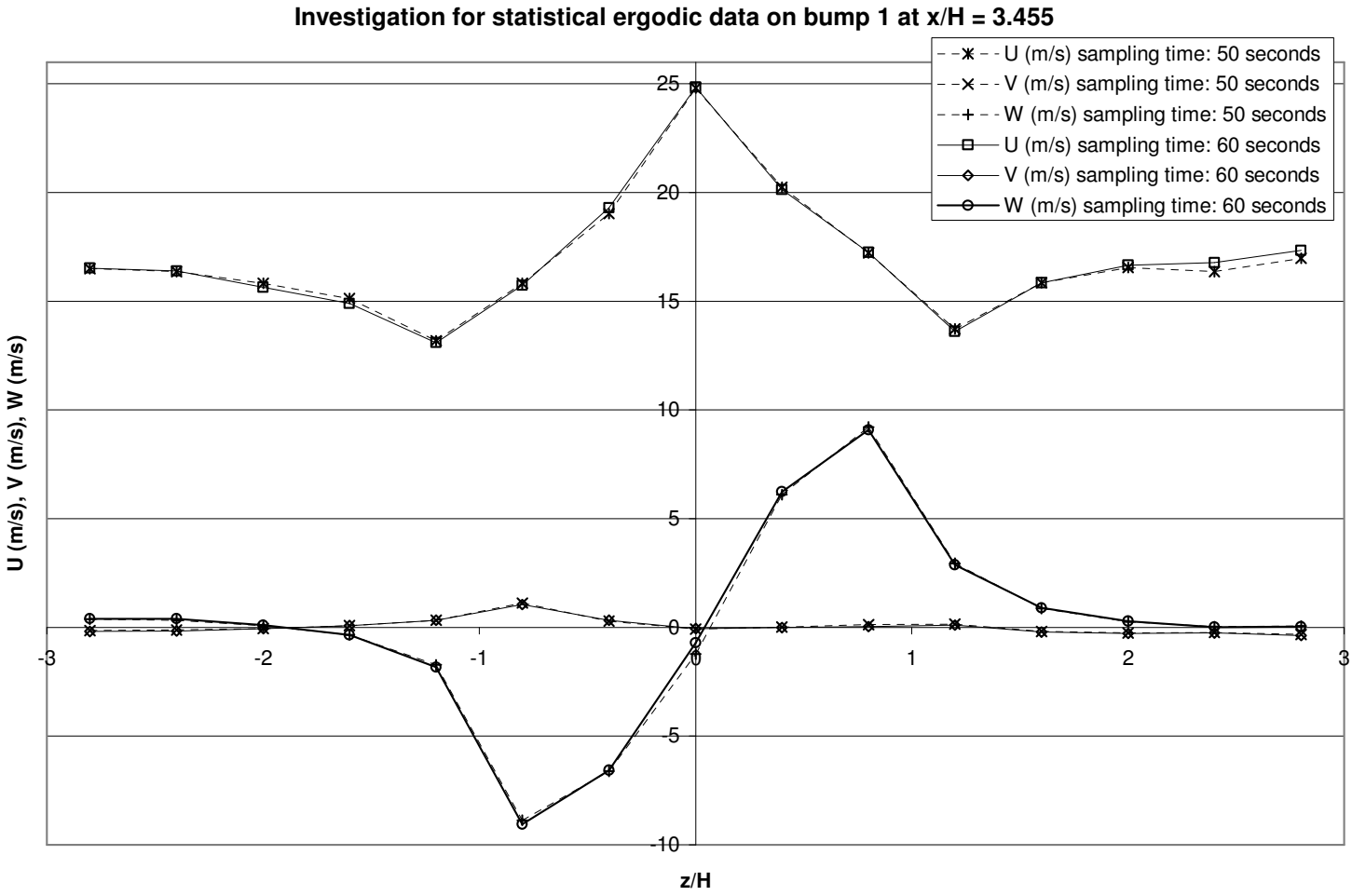

Figure 2.21: Investigation on the sampling time to acquire data necessary to have statistical ergodic data in the wake of bump 1 at x/H = 3.455 and y = 0.1 inches

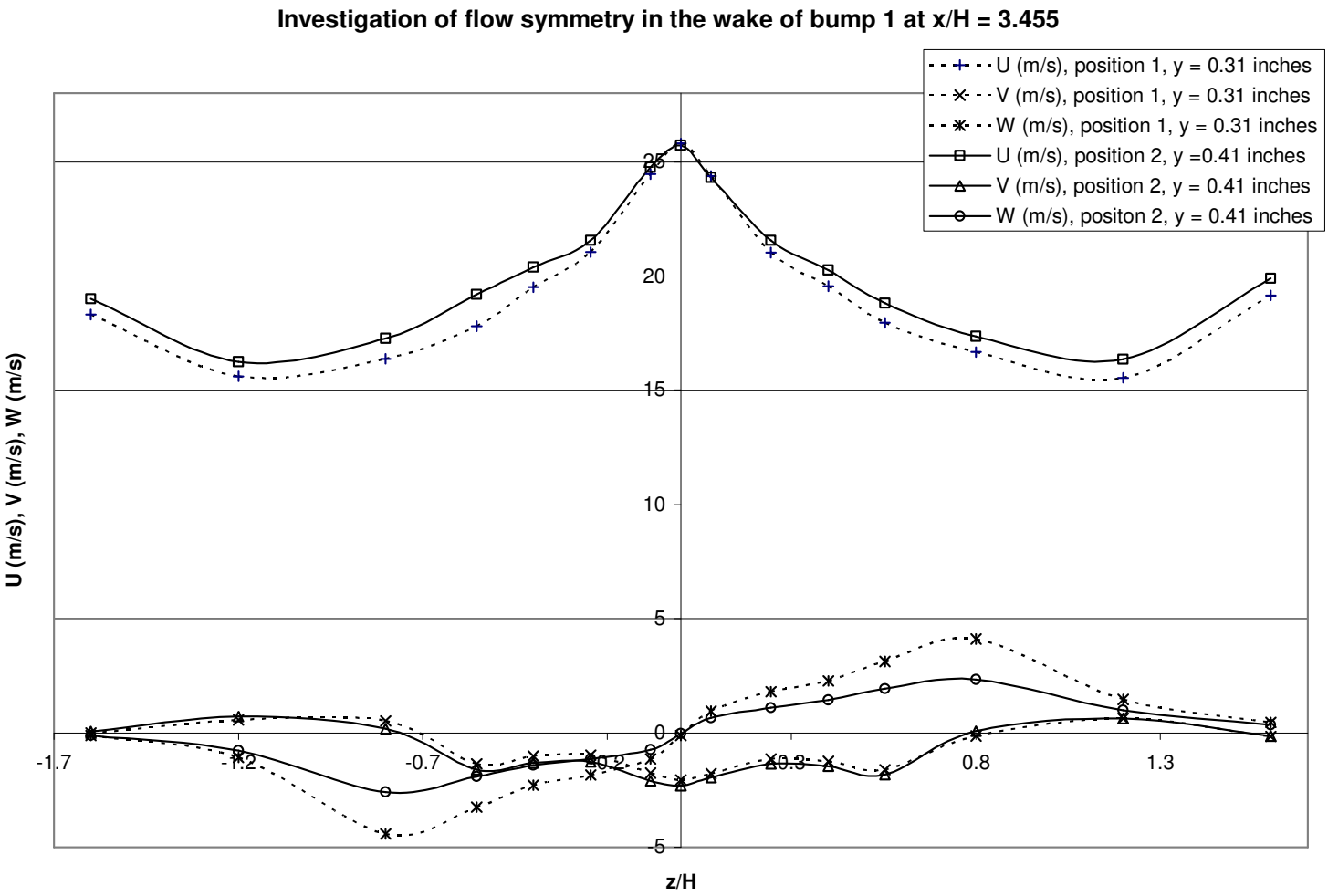

Figure 2.22: Investigation of the position of bump 1 in the test section to have a symmetric flow field at x/H = 3.455

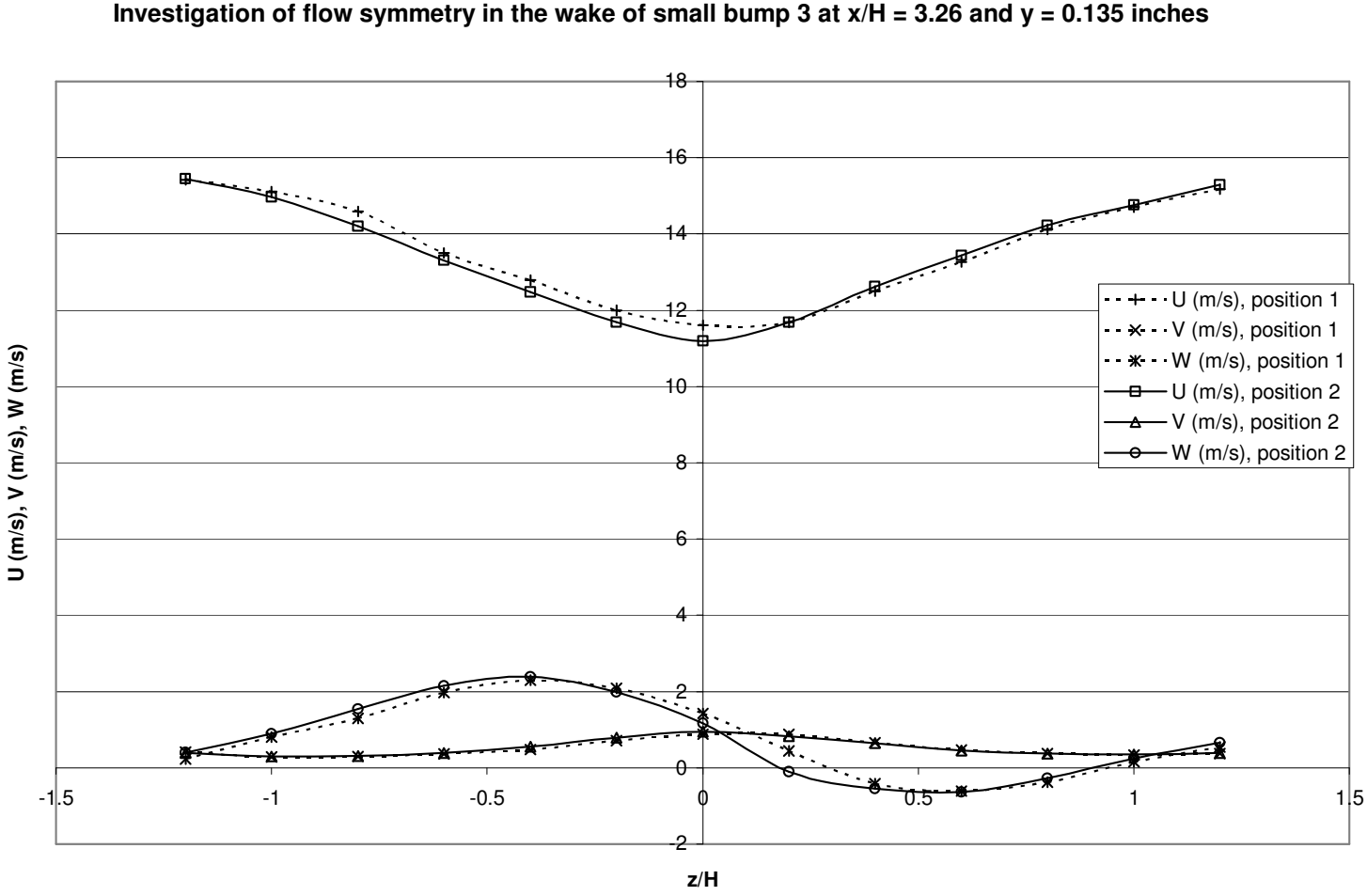

Figure 2.23: Investigation of the position of small bump 3 in the test section to have a symmetry flow field at x/H = 3.26

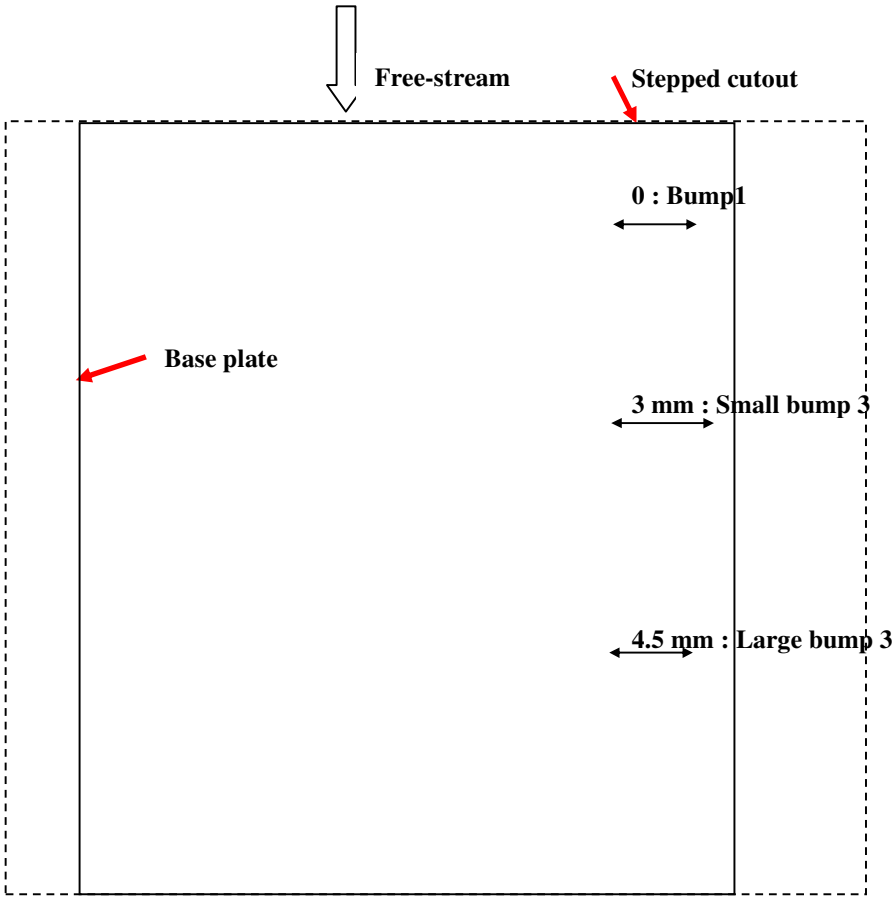

Figure 2.24: Summary of the base plate positions with respect to the stepped cutout (not to scale)

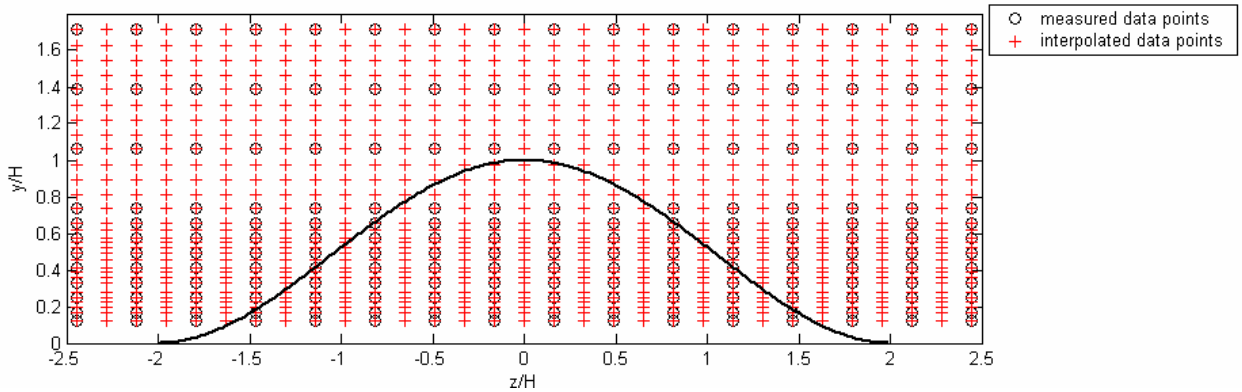

Figure 2.25: Representation of the grid of measured points and interpolated data points for large bump 3 at x/H = -4.6 for the two cases, with and without large bump 3

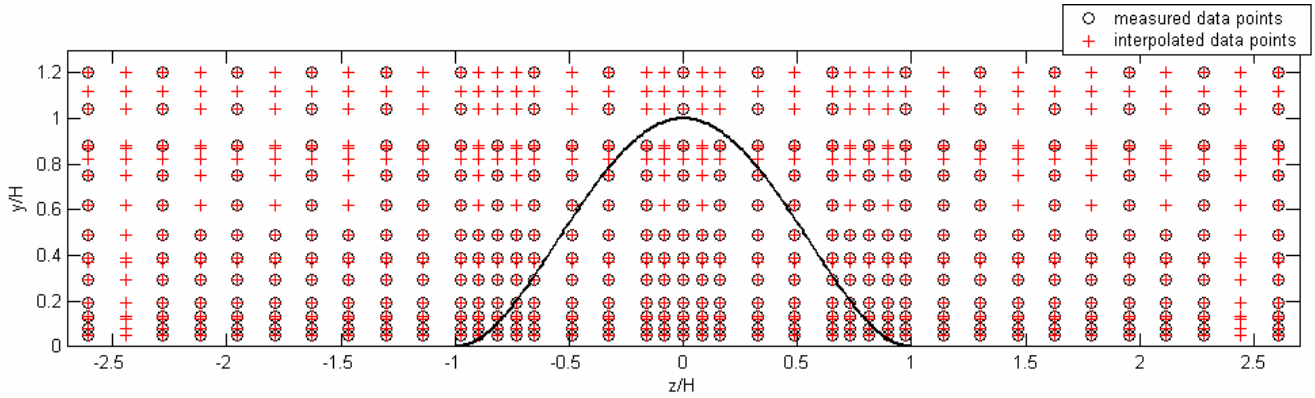

Figure 2.26: Representation of the grid of measured points and interpolated data points for bump 1 at x/H = 3.455

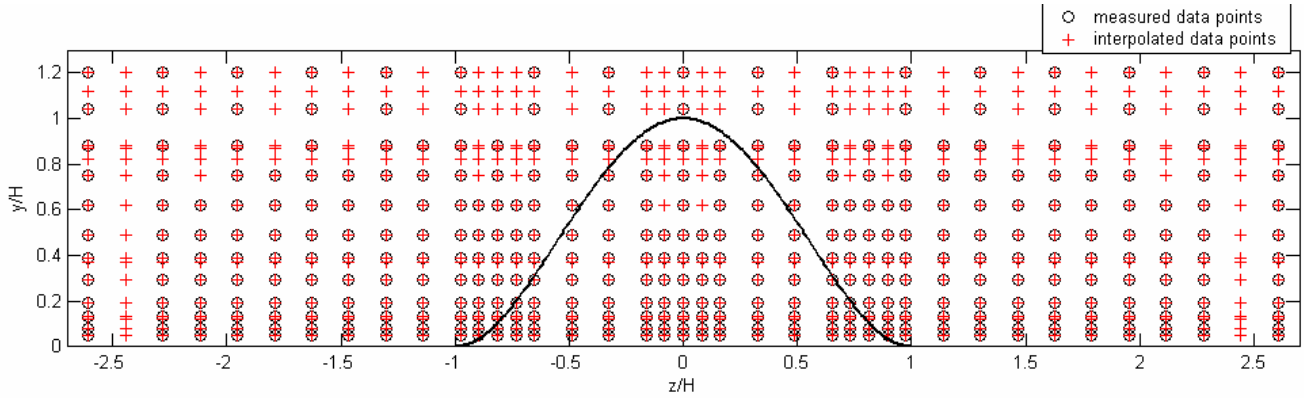

Figure 2.27: Representation of the grid of measured points and interpolated data points for bump 1 at x/H = 11.5

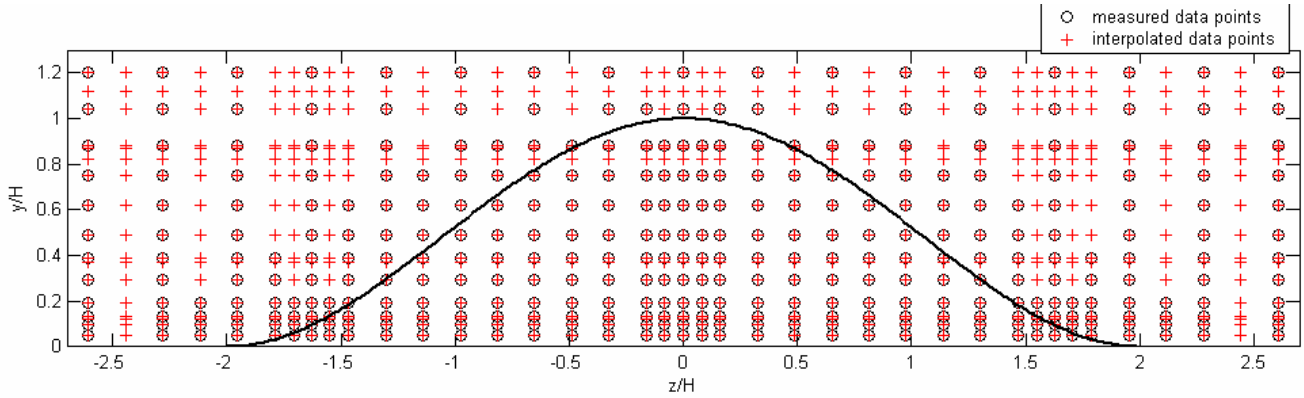

Figure 2.28: Representation of the grid of measured points and interpolated data points for small bump 3 at x/H = 3.26

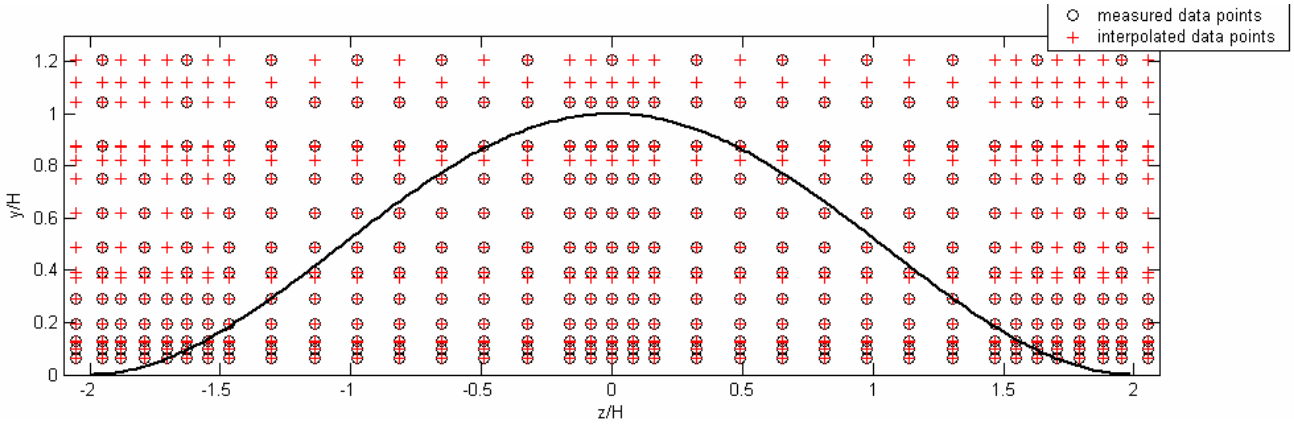

Figure 2.29: Representation of the grid of measured points and interpolated data points for small bump 3 at x/H = 11.5

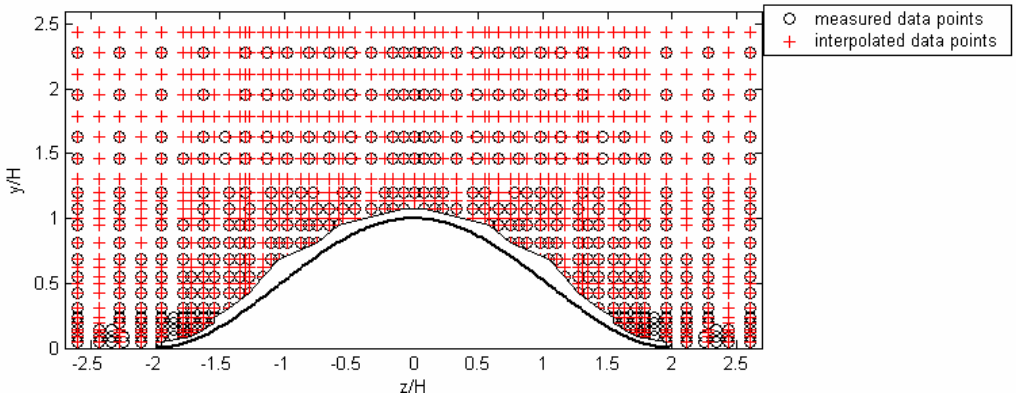

Figure 2.30: Representation of the grid of measured points and interpolated data points for large bump 3 at x/H = 0

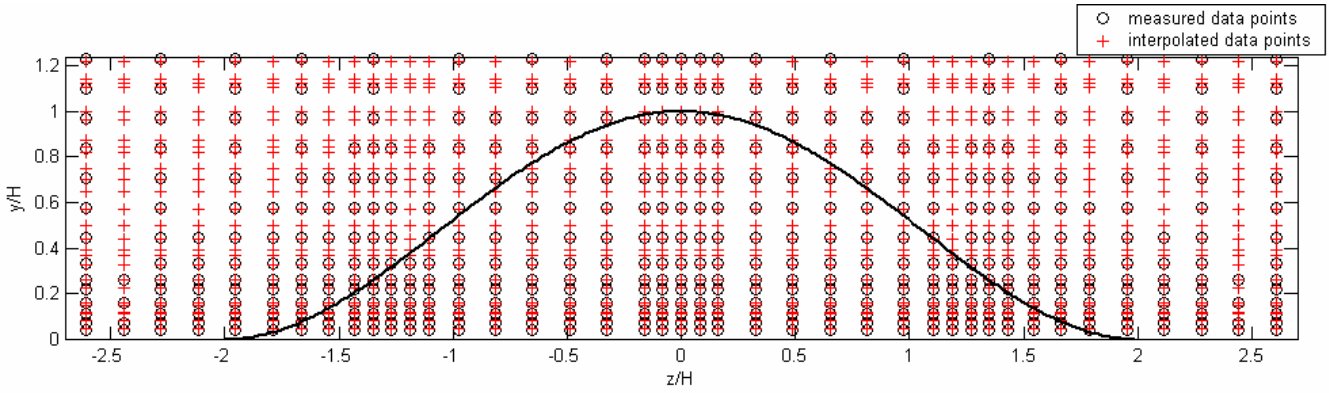

Figure 2.31: Representation of the grid of measured points and interpolated data points for large bump 3 at x/H = 3.629

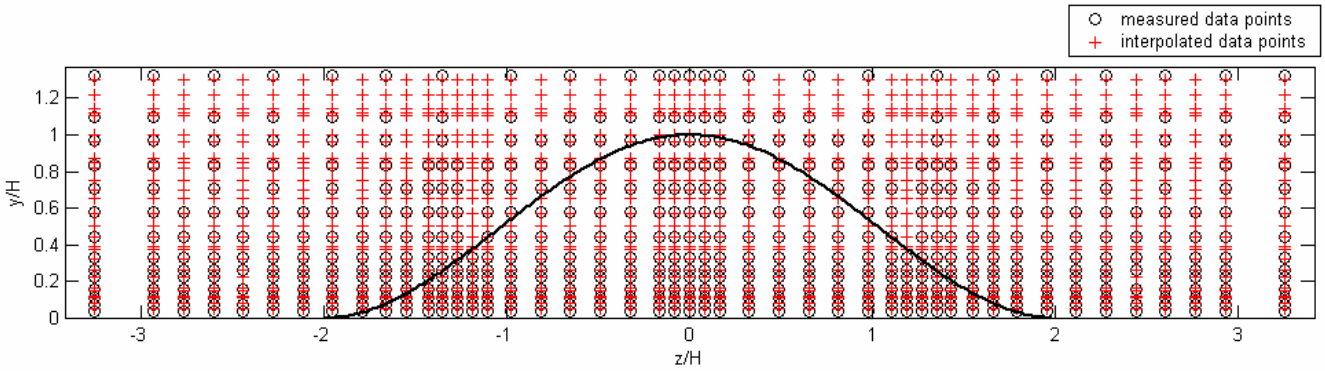

Figure 2.32: Representation of the grid of measured points and interpolated data points for large bump 3 at x/H = 11.5

3 Descriptions of seven-hole probe measurements

The following discussions describe the mean velocity measurements made upstream and downstream of the three three-dimensional bumps with the seven-hole probe, the sixteen-hole pressure rake, and the pitot-static probe. The incoming flow conditions with and without large bump 3 set in place in the test section are described and compared with each other to examine the influence of large bump 3 on the upstream flow field. Descriptions of the mean velocity components measured with the seven-hole probe in the wakes of the bumps are made, and comparisons of the evolutions of the flow fields in the wakes of the three bumps in the positive streamwise direction are examined. As a prologue to chapter 4, qualitative and quantitative comparisons of the seven-hole probe measurements with quad-wire hot-wire measurements by Ma and Simpson (2004) and LDV measurements by Byun et *al.* (2004) are studied.

In the wakes of the three three-dimensional bumps, the range of the Reynolds number based on the probe diameter was calculated to be between $1470 \le \mathrm{Re}_d \le 3300$.

3.1 Two-Dimensional flow at x/H = -4.6 (H=78mm)

Figure 3.1 represents the mean streamwise, normal, and spanwise velocity components, $\overline{U}$, $\overline{V}$, and $\overline{W}$, respectively, measured with the seven-hole probe in the test section at $x/H = -4.6$ for different vertical and spanwise locations when no test case is set in place in the test section. A two-dimensional turbulent boundary layer exists at this location. A scatter of the streamwise velocity component is observed close to the wall in the boundary layer due to the increased amount of probe/flow interactions and to the large velocity gradient in the near wall regions. The normal velocity is relatively large in magnitude close to the wall and decreases in magnitude with increasing vertical locations. The relatively large magnitude observed close to the wall is also due to the increased amount of probe/flow interactions and to the large velocity gradient in the near wall regions. The spanwise velocity component magnitude is relatively small ($\overline{W}/U_{ref} \le \pm 5 \cdot 10^{-3}$) through all the vertical profiles.

The boundary layer thickness at each spanwise position is calculated. The boundary layer thickness is defined as the vertical distance from the wall where

$$\delta_{99} = y \text{ where } \overline{U} = 0.99 \cdot U_e \qquad \textbf{(3.1)}$$

where, $\overline{U}$ is the streamwise velocity component and U_e is the boundary layer edge velocity. To obtain information on the momentum thickness at $x/H = -4.6$, the approximate solution developed by Kays (1966) for mild adverse pressure gradient is used. This method can be used since measurements performed in earlier studies of the mean velocity magnitude in the centerline of the test section as a function of the streamwise position show a mild deceleration of the flow between $x/H = -4.6$ and $x/H = 0$ (Figure 3.2, George (2004)). To obtain an approximate solution for the momentum thickness, Kays (1966) used the momentum integral equation under the assumption that the shape factor stays constant at all streamwise positions. The approximate solution Kays (1966) developed between two streamwise positions x_1 and x_2 is,

$$\left[\theta^{5/4} \cdot U_e^{\frac{5}{4}(H_{factor}+2)}\right]_{x1}^{x2} = 0.016 \cdot \nu^{1/4} \cdot \int_{x1}^{x2} U_e^{\frac{5}{4}(H_{factor}+2)-0.25} dx \qquad \textbf{(3.2)}$$

$$H_{factor} = \frac{\delta^*}{\theta}$$

where, θ is the momentum thickness, δ^* is the displacement thickness, and ν is the kinematic viscosity. In equation 3.2, U_e is shown in Figure 3.2, and was obtained from measurements by George (2004). From equation 3.2, the Reynolds number based on the momentum thickness is computed with,

$$\mathrm{Re}_\theta = \frac{U_e \cdot \theta}{\nu} \qquad \textbf{(3.3)}$$

The boundary layer properties at the x_2 location in equation 3.2 are evaluated at $x/H = -2$ and $z/H = 0$ from the boundary layer profile measured with a LDV system by Byun et *al.* (2004) as see in Figure 3.3. The law of the wall ($U^+ = y^+$ for $y^+ \le 10$, Schetz (1993)) is used to fit the near-wall data with a friction velocity $U_\tau = 0.99$ (Byun et *al.* (2004)), and the momentum and displacement thicknesses are calculated using the following equations.

$$\theta = \int_{y=0}^{\delta_{99}} \left(1 - \frac{\overline{U}}{U_e}\right) \cdot \frac{\overline{U}}{U_e}$$
$$\delta^* = \int_{y=0}^{\delta_{99}} \left(1 - \frac{\overline{U}}{U_e}\right) \cdot \qquad \textbf{(3.4)}$$

The momentum and displacement thicknesses as well as the shape factor calculated from the LDV measurements by Byun et *al.* (2004) are shown in Table 3.1.

Table 3.1: Boundary layer properties at *x/H* = -2 and *z/H* = 0 from LDV measurements by Byun et *al.* (2004)

θ	δ^*	H_{factor}
4.85 *mm*	6.53 *mm*	1.34

The variations of the boundary layer thickness δ_{99} with respect to the spanwise position at $x/H = -4.6$ are represented in Figure 3.4. The boundary layer thickness slightly varies along the span of the test section, a maximum is observed at $z/H = 0.98$ with $\delta_{99}/H = 0.52$, a minimum at $z/H = 1.63$ with $\delta_{99}/H = 0.45$ and the average boundary layer thickness is $(\delta_{99}/H)_{average} = 0.478$.

To calculate the momentum thickness using the method developed by Kays (1966) (equation 3.2) at $x/H = -4.6$ for all spanwise locations, it would be required to assume that the boundary layer properties, and the variation of the free-stream mean velocity magnitude at all spanwise locations stay relatively constant. However, as is seen in Figure 3.4, some variations of the boundary layer thickness are observed in the spanwise direction at $x/H = -4.6$. In this fashion, the assumption that the two-dimensional boundary layer is constant at a streamwise location for various spanwise positions does not hold. Consequently, the momentum thickness at $x/H = -4.6$ is only evaluated at $z/H = 0$ by using the method developed by Kays (1966). Utilizing equation 3.2 and 3.3 with the boundary layer properties of Table 3.1 and the measurements in the centerline of the test-section in Figure 3.2, the Reynolds number based on the momentum thickness at $x/H = -4.6$ and $z/H = 0$ is $\mathrm{Re}_\theta = 7278$. It can be seen that the Reynolds number based on the momentum thickness is slightly smaller than the one referenced at $x/H = 0$ by Byun et *al.* (2004).

3.2 Bump 1

3.2.1 Description of the flow at *x/H = 3.455*

Figure 3.5, Figure 3.6, and Figure 3.7 represent the mean streamwise, normal, and spanwise velocity components, respectively, measured by the seven-hole probe at $x/H = 3.455$ in the wake of bump 1. Figure 3.5 shows two regions of low momentum fluid close to the wall between $\pm 0.4 \le z/H \le \pm 1.5$. High momentum fluid is entrained close to the wall between $z/H \le \pm 0.2$. Figure 3.6 shows a region of relatively strong normal velocity magnitude and negative sign for $z/H \le \pm 0.75$ that is smaller in magnitude close to the wall, and decreases in magnitude with increasing vertical positions. On either side of this region, the normal velocity changes sign at $z/H = \pm 0.75$ and a maximum in the positive normal velocity component is observed at $z/H = \pm 0.9$. For larger spanwise positions ($z/H \ge \pm 0.9$), the normal velocity component magnitude decreases with increasing vertical positions and spanwise positions. Figure 3.7 shows two regions of relatively strong spanwise velocity magnitude and opposite sign close to the wall between $z/H \le \pm 1.25$ that decrease in magnitude with increasing vertical positions until $y/H = 0.18$ where they change sign. The magnitude of the spanwise velocity component then increases with the vertical positions until the regions defined by $\pm 0.3 \le z/H \le \pm 1.1$ and $0.21 \le y/H \le 0.79$, beyond which it decreases with increasing vertical and spanwise positions.

The secondary flow vectors represented in Figure 3.8 show a pair of counter rotating streamwise vortices with their vortex centers located at $(z/H,\ y/H) = (\pm 0.81,\ 0.19)$. The streamwise vorticity, Ω_x of the flow field is computed with,

$$\Omega_x = curl\left(\vec{V}\right) \bullet \vec{i} = \frac{\partial \overline{W}}{\partial y} - \frac{\partial \overline{V}}{\partial z} \qquad \textbf{(3.5)}$$

where $\vec{V}$ is the mean velocity vector measured at the vertical position y and spanwise coordinate z, and $\vec{i}$ is the unit vector in the positive streamwise direction. Figure 3.9 shows the streamwise vorticity computed from seven-hole probe data measured at $x/H = 3.455$ in the wake of bump 1. Two regions of strong magnitude and opposite

sign are observed for $z/H \le \pm 1.1$ and $y/H \le 0.25$. In the rest of the plane, the magnitude of the streamwise vorticity is small.

The boundary layer thickness is calculated using equation 3.1 from the streamwise velocity component and is represented in Figure 3.10. With decreasing spanwise positions ($|z/H| \to 0$), the variations of the boundary layer thickness are relatively small until $z/H = \pm 1$. When approaching $z/H = 0^-$ the boundary layer thickness is observed to be decreasing, and to be increasing when approaching $z/H = 0^+$. The discontinuity observed between $z/H \le \pm 0.25$ and $0.4 \le y/H \le 0.6$ in the boundary layer thickness, and in the mean streamwise velocity profiles measured by the seven-hole probe is also observed but to a lesser extent in the mean streamwise velocity profiles measured with the hot-wire probe by Ma and Simpson (2004). This suggests that imperfections on the surface of bump 1 may cause the discontinuities observed.

3.2.2 Description of the flow at *x/H = 11.5*

Figure 3.11, Figure 3.12, and Figure 3.13 represent the mean streamwise, normal, and spanwise velocity components, respectively, measured by the seven-hole probe at $x/H = 11.5$ in the wake of bump 1. Figure 3.11 shows regions of low momentum fluid close to the wall between $\pm 1.5 \le z/H \le \pm 2.5$. High momentum fluid is entrained close to the wall for $z/H \le \pm 0.1$. Two regions of strong magnitude and negative normal velocity component are observed between $\pm 0.65 \le z/H \le \pm 1.25$ and $0.15 \le y/H \le 0.7$. The normal velocity component changes sign at $z/H = \pm 1.3$ and, next to the two regions of negative normal velocity and relatively strong magnitude, two regions of positive normal velocity with relatively strong magnitude are observed with a maximum found at $z/H = \pm 1.64$ and $y/H = 0.29$. Figure 3.13 shows a similar distribution of the mean spanwise velocity component as the one observed at $x/H = 3.455$. The regions of relatively strong spanwise velocity magnitude and opposite sign are located close to the wall between $\pm 0.05 \le z/H \le \pm 1.8$. In the centerline of the test section, the spanwise velocity magnitude is small and two regions of relatively strong magnitude are observed away from the wall between $\pm 1.05 \le z/H \le \pm 1.75$ and $0.36 \le y/H \le 0.85$.

The secondary flow vectors represented in Figure 3.14 show a pair of counter rotating streamwise vortices with their vortex centers located at $(z/H,\ y/H) = (\pm 1.42,\ 0.34)$. Figure 3.15 shows the streamwise vorticity computed from seven-hole probe data measured at $x/H = 11.5$ in the wake of bump 1. Two regions of relatively strong streamwise vorticity magnitude and opposite sign are observed between $\pm 1.2 \le z/H \le \pm 1.8$ and $y/H \le 0.5$. In the rest of the measurement plane, the streamwise vorticity is small.

The boundary layer thickness is calculated using equation 3.1 from the streamwise velocity component and is represented in Figure 3.16. With decreasing spanwise positions ($|z/H| \to 0$), the boundary layer thickness increases until $z/H = \pm 1.3$. It then significantly decreases when approaching $z/H = 0$ and reaches a minimum height of $\delta_{99}/H = 0.23$. Note that an offset in the spanwise position of the minimum boundary layer thickness is observed when it would have been expected to have this minimum at $z/H = 0$. This offset may be explained by the asymmetry of the mean streamwise velocity component observed in the wake of bump 1 as discussed in section 2.2.3.3 or by the possible imperfections on the surface of bump 1.

3.3 Small Bump 3

3.3.1 Description of the flow at *x/H = 3.26*

Figure 3.17, Figure 3.18, and Figure 3.19 represent the mean streamwise, normal, and spanwise velocity components, respectively, measured by the seven-hole probe at $x/H = 3.26$ in the wake of small bump 3. Figure 3.17 shows regions of low momentum fluid close to the wall for all spanwise positions between $-0.7 \le z/H \le 0.7$ and $y/H \le 0.75$. Figure 3.18 shows a region of relatively strong magnitude and negative normal velocity for $z/H \le \pm 1$ and $y/H \ge 0.1$. A region of positive normal velocity close to the wall is observed between $-0.4 \le z/H \le 0.4$. With increasing spanwise positions, the normal velocity component changes sign and becomes positive with a maximum observed between $\pm 1.5 \le z/H \le \pm 2.5$ and $y/H \le 0.6$. Note that this region of positive normal velocity is smaller in size in the negative spanwise coordinates than in the positive spanwise coordinates due to the asymmetry in the flow

field in the wake of small bump 3 discussed in section 2.2.3.3. Figure 3.19 shows two regions of relatively strong spanwise velocity magnitude and opposite sign between $\pm 0.1 \le z/H \le \pm 0.75$ and $0.1 \le y/H \le 0.42$ that decrease in magnitude with increasing vertical and spanwise positions. Close to the wall, the sign of the spanwise velocity component is different from the sign of the two regions of relatively strong magnitude and opposite sign.

The secondary flow vectors represented in Figure 3.20 show a pair of counter rotating streamwise vortices with their vortex centers located at $(z/H,\ y/H) = (-1.32,\ 0.11)$ and $(z/H,\ y/H) = (1.16,\ 0.14)$. From these observations, it is obvious that the mean velocity components are not symmetric in the wake of small bump 3 as discussed in section 2.2.3.3. Figure 3.21 shows the streamwise vorticity computed from seven-hole probe data measured at $x/H = 3.26$ in the wake of small bump 3. Two regions of relatively strong magnitude and opposite sign are observed close to the wall between $\pm 0.2 \le z/H \le \pm 2$ and $y/H \le 0.2$, and two other regions of opposite sign are observed about the centerline of the test section. In the rest of the plane, the magnitude of the streamwise vorticity is small.

The boundary layer thickness is calculated using equation 3.1 from the streamwise velocity component and is represented in Figure 3.22. Note that more data at higher vertical positions would be needed to map the full profile in the wake of small bump 3. Consequently, quantitative information on the boundary layer thickness cannot be calculated for $z/H \le \pm 1$. With decreasing spanwise positions, the boundary layer thickness increases. The distribution of the streamwise velocity component suggests that the boundary layer thickness would keep in increasing with decreasing spanwise positions and would be maximum at $z/H = 0$.

3.3.2 Description of the flow at *x/H = 11.5*

Figure 3.23, Figure 3.24, and Figure 3.25 represent the mean streamwise, normal, and spanwise velocity components, respectively, measured by the seven-hole probe at $x/H = 11.5$ in the wake of small bump 3. Figure 3.23 shows regions of low momentum fluid close to the wall for $z/H \ge \pm 1.4$ and $y/H \le 0.4$. Figure 3.24 shows a region of negative normal velocity between $z/H \le \pm 1$ and $y/H \ge 0.1$. Two regions of

positive normal velocity are observed between $\pm 1.8 \le z/H \le \pm 2.4$ and $y/H \le 0.7$. Figure 3.25 shows a different distribution of the spanwise velocity component than the one observed at $x/H = 3.26$. Two regions of relatively strong magnitude and opposite sign are observed close to the wall for $\pm 0.1 \le z/H \le \pm 2.4$ and $y/H \le 0.47$. At $y/H = 0.47$, the spanwise velocity component changes sign and its magnitude increases with vertical positions until $z/H = \pm 0.7$ and $y/H = 0.8$, beyond which its magnitude decreases with increasing vertical positions.

The secondary flow vectors represented in Figure 3.26 show a pair of counter rotating streamwise vortices with their vortex centers located at $(z/H,\ y/H) = (-1.69, 0.47)$ and $(z/H,\ y/H) = (1.75, 0.52)$. The locations of the vortex centers show that an asymmetry in the mean flow field is still present at $x/H = 11.5$ but to a lesser extent than the one observed at $x/H = 3.26$. Figure 3.27 shows the streamwise vorticity computed from seven-hole probe data measured at $x/H = 11.5$ in the wake of small bump 3. Two regions of relatively strong magnitude and opposite sign are observed for $\pm 0.15 \le z/H \le \pm 2.4$ and $y/H \le 0.45$. In the rest of the plane of measurement, the streamwise vorticity is small. Similarly as at $x/H = 3.26$, information on the boundary layer thickness require measurements at higher vertical positions than the ones measured and no conclusions can be drawn.

3.4 Large bump 3

3.4.1 Initial conditions at x/H = -4.6

Figure 3.28 represents the mean streamwise, normal, and spanwise velocity components measured in the test section at $x/H = -4.6$ for various spanwise and vertical locations when large bump 3 is set in place. The streamwise velocity component has a similar behavior than when large bump 3 is not set in place. A scatter of the streamwise velocity component is observed close to the wall due to the increased amount of probe/flow interactions and to the large velocity gradients in the near wall regions. Significant variations of the normal and spanwise velocity components are observed close to the wall of the order of $\pm 2\%$ of U_{ref}. In free-stream regions, the variations are less significant and are of the order of to $\pm 0.5\%$ of U_{ref}. These observations reveal that

at $x/H = -4.6$, the influence of large bump 3 on the upstream flow-field is significant, especially for the normal and spanwise velocity components.

The boundary layer thickness at various spanwise locations is calculated using equation 3.1 and is shown in Figure 3.29. The boundary layer thickness is not constant along the span of the test section, it increases with decreasing spanwise coordinates ($|z/H| \to 0$), and a maximum is observed for $z/H \le \pm 0.5$ with $\delta_{99}/H = 0.79$. At $z/H = -1.14$, a peak in the boundary layer thickness is observed that may have been due to wall imperfections or a bad data point. The latter is more logical since in the two-dimensional case, the peak is not present so the wall imperfections cannot be the cause. For increasing spanwise positions, the boundary layer thickness appears to converge to the boundary layer thickness measured in the two-dimensional case.

3.4.2 Boundary conditions at x/H = -3.81

The boundary conditions measured with the pressure rake upstream of large bump 3 at $x/H = -3.81$ on the ceiling and on the sidewalls of the test-section are discussed. The test section ceiling is located at $y/H = 3.42$, and, the measurements on the sidewalls are located at $y/H = 1.71$ for the left sidewall (looking at Figure 2.13) located at $z/H = 5.91$ and at $y/H = 1.77$ for the right sidewall (looking at Figure 2.13) located at $z/H = -5.91$. Figure 3.30 shows the boundary layer profiles for the three cases. The boundary layer thickness computed with equation 3.1 is $(\delta_{99}/H)_{ceiling} = 0.42$. The boundary layer edge velocity of the left sidewall ($z/H = 5.91$) has a lower magnitude than the reference velocity. The right sidewall ($z/H = -5.91$) boundary layer profile shows a boundary layer edge velocity lower than the reference velocity. The sidewalls boundary layer thicknesses calculated using equation 3.1 are $(\delta_{99}/H)_{\text{left\_sidewall}} = 0.44$ and $(\delta_{99}/H)_{\text{right\_sidewall}} = 0.42$.

3.4.3 Velocity measurements at z/H = 0, y/H = 2.2 for various streamwise locations

The measurements of the mean velocity magnitude in the centerline of the test-section at $y/H = 2.2$ (Figure 2.28) were obtained for various streamwise positions at $z/H = 0$ using the Pitot-static probe described in section 2.1.4. In Figure 3.31, the two

gaps in the data correspond to regions where no data could be measured due to the structure bars of the ceiling of the test-section. It can be seen that the flow velocity magnitude stays relatively constant with increasing streamwise positions until $x/H = -0.75$. For $x/H \geq -0.75$, the mean flow accelerates with increasing streamwise positions and a maximum is observed at $x/H = 0$ of $U_{max} = 28.33\, m/s$. After this maximum, the mean velocity magnitude decreases with increasing streamwise positions until $x/H = 1.3$ after which, the mean velocity magnitude stays relatively constant.

3.4.4 Description of the flow at x/H = 0

Figure 3.32, Figure 3.33, and Figure 3.34 represent the mean streamwise, normal, and spanwise mean velocity components, relatively, measured by the seven-hole probe at $x/H = 0$ when large bump 3 is set in place in the test section. Figure 3.32 shows a region of strong streamwise velocity magnitude close to the top of the bump surface that decreases in magnitude with increasing spanwise and vertical positions. Note that at high vertical locations ($y/H \geq 1.5$), the mean streamwise velocity magnitude is still larger than the reference velocity. On either sides of the bump and close to the wall, for $z/H \geq \pm 1.4$ and $y/H \leq 0.4$, the mean streamwise velocity magnitude increases with vertical positions. A region of lower streamwise velocity magnitude is observed between $1.6 \leq z/H \leq 2.5$ and $y/H \geq 2.22$ that may be due to some imperfections on the surface of the ceiling of the test section. The normal velocity component is positive in sign and has a relatively strong magnitude across the surface of the bump and, decreases with increasing vertical and spanwise positions. This observation suggests that the flow on the upstream part of the bump separates before $z/H = 0$. The magnitude of the spanwise velocity component is relatively small in the whole measurement plane.

3.4.5 Description of the flow at *x/H = 3.629*

Figure 3.35, Figure 3.36, and Figure 3.37 represent the mean streamwise, normal, and spanwise velocity components, relatively, measured by the seven-hole probe at $x/H = 3.629$ in the wake of large bump 3. Figure 3.35 shows regions of low momentum fluid close to the wall for $z/H \geq \pm 1.2$ and $y/H \leq 0.2$. High momentum fluid is entrained close to the wall for $z/H \leq \pm 0.5$. Figure 3.36 shows a region of relatively

strong negative normal velocity magnitude between $z/H \le \pm 0.5$ and $0.12 \le y/H \le 0.76$ that decreases in magnitude close to the wall and with increasing vertical position. At $z/H = \pm 1.1$, the normal velocity component changes sign. Its magnitude then increases with increasing spanwise locations until a maximum magnitude is reached in the regions defined by $\pm 1.7 \le z/H \le \pm 2.05$ and $y/H \le 0.3$. Beyond this region, the normal velocity component decreases in magnitude with increasing spanwise and vertical positions. Figure 3.37 shows two regions of strong spanwise velocity magnitude and opposite sign close to the wall between $\pm 0.05 \le z/H \le \pm 2.1$ and $y/H \le 0.25$ that decrease in magnitude with increasing spanwise and vertical positions. At $y/H = 0.25$, the spanwise velocity component changes sign. Its magnitude then increases with vertical positions until a maximum value is reached between $0.4 \le y/H \le 0.69$, beyond which the magnitude of the spanwise velocity component decreases with increasing vertical positions.

The secondary flow vectors represented in Figure 3.38 show a pair of counter rotating streamwise vortices with their vortex centers located at $(z/H,\ y/H) = (-1.4,\ 0.29)$ and $(z/H,\ y/H) = (1.48,\ 0.26)$. The difference of position of the vortex centers indicates an asymmetry in the flow field in the wake of large bump 3. However, this asymmetry is not as pronounced as the one observed in the wake of small bump 3. Figure 3.39 shows the streamwise vorticity computed from seven-hole probe data measured at $x/H = 3.629$ in the wake of large bump 3. Two regions of relatively strong magnitude and opposite sign are observed between $0.25 \le z/H \le \pm 2$ and $y/H \le 0.34$. In the rest of the plane, the magnitude of the streamwise vorticity is small.

The boundary layer thickness is calculated using equation 3.1 from the streamwise velocity component and is represented in Figure 3.40. For $z/H \ge \pm 1$, the boundary layer thickness is relatively constant. For $z/H \le \pm 1$, the boundary layer thickness increases while approaching $z/H = 0$, and reaches a maximum at $z/H = 0.16$ of $\delta_{99}/H = 0.93$. Note that the maximum boundary layer thickness is not found at $z/H = 0$ but at $z/H = 0.16$ indicating some asymmetry in the mean velocity components measured in the wake of large bump 3.

3.4.6 Description of the flow at *x/H = 11.5*

Figure 3.41, Figure 3.42, and Figure 3.43 represent the mean streamwise, normal, and spanwise velocity components, respectively, measured by the seven-hole probe at $x/H = 11.5$ in the wake of large bump 3. Figure 3.41 shows regions of low momentum fluid close to the wall for $\pm 1.8 \le z/H \le \pm 2.7$ and $y/H \le 0.25$. High momentum fluid is entrained close to the wall for $z/H \le \pm 1.8$. Note that the velocity magnitude in the freestream is larger than the reference velocity. This may be due to the low sampling time chosen as discussed in section 2.2.3.2. A region of relatively strong negative normal velocity magnitude is observed between $z/H \le \pm 1.1$ and $0.25 \le y/H \le 1.1$. Under and over this region, the normal velocity magnitude decreases with decreasing vertical positions and with increasing vertical positions. Two regions of relatively strong positive normal velocity magnitude are observed between $\pm 1.9 \le z/H \le \pm 2.5$ and $y/H \le 0.65$. For larger spanwise positions ($z/H \ge \pm 2.5$), the magnitude of the normal velocity component decreases in magnitude with increasing spanwise and vertical positions. Figure 3.43 shows two regions of strong spanwise velocity magnitude and opposite sign close to the wall for $\pm 0.2 \le z/H \le \pm 2.4$ and $y/H \le 0.45$ that decrease in magnitude with increasing spanwise and vertical positions. At $y/H = 0.45$, the spanwise velocity component changes sign and, for $y/H \ge 0.45$, it increases with vertical position until a maximum is reached between $0.65 \le y/H \le 1.05$. Beyond this region, the mean spanwise velocity component decreases in magnitude with increasing vertical positions.

The secondary flow vectors represented in Figure 3.44 show a pair of counter rotating streamwise vortices with their vortex centers located at $(z/H,\ y/H) = (-1.39,\ 0.44)$ and $(z/H,\ y/H) = (1.53,\ 0.47)$. Again, the difference of position of the vortex centers is a sign of an asymmetry in the flow field in the wake of large bump 3. Figure 3.45 shows the streamwise vorticity computed with equation 3.5 from seven-hole probe data measured at $x/H = 11.5$ in the wake of large bump 3. Two regions of relatively strong magnitude and opposite sign are observed for $0.3 \le z/H \le \pm 2.3$ and $y/H \le 0.4$. In the rest of the plane, the magnitude of the streamwise vorticity is small.

The boundary layer thickness is calculated using equation 3.1 from the streamwise velocity component (Figure 3.46). Three local maximum are observed in the boundary layer thickness at $(z/H, \delta_{99}/H) = (-1.95, 0.92)$, $(z/H, \delta_{99}/H) = (0, 0.92)$, and $(z/H, \delta_{99}/H) = (1.95, 0.88)$. The two local maximum located at $z/H = \pm 1.95$ are due to the regions of low momentum fluid observed close to the wall that decrease the velocity magnitude near the wall and induce an increase of the boundary layer thickness. At $z/H = 0$, the high momentum fluid entrained close to the wall constrain the growth of the boundary layer.

3.5 Comparison of bump data at first measurement plane

A comparison of the flow-fields measured in the wakes of the three bumps is discussed at the first downstream measurement plane, $x/H = 3.455$, $x/H = 3.26$, and $x/H = 3.629$, for bump 1, small bump 3, and large bump 3, respectively. Figure 3.47, Figure 3.48, and Figure 3.49 show the three components of the mean velocity vectors for bump 1, small bump 3, and large bump 3, respectively, at different vertical and spanwise positions at the first downstream measurement plane.

The high momentum fluid entrained close to the wall and close to the centerline of the test section in the wake of bump 1, energizes the boundary layer making the boundary layer thickness to stay relatively constant across the span of the test-section. In the wake of large bump 3, less high momentum fluid is entrained close to the wall and close to the centerline of the test section than in the wake of bump 1. Consequently, the boundary layer growth is less constrained than the one in the wake of bump 1. In the wake of small bump 3, no high momentum fluid is observed close to the wall. In the wakes of the three bumps, the normal velocity component is relatively small in magnitude close to the wall. Close to the centerline of the test section, the negative normal velocity component increases in magnitude with increasing vertical positions until a maximum negative normal velocity magnitude is reached. This maximum is largest in the wake of bump 1 with a magnitude of $\overline{V}/U_{ref} = -0.09$, and smallest in the wake of large bump 3 with a magnitude of $\overline{V}/U_{ref} = -0.06$. The vertical locations of these maximum is highest in the wake of small bump 3 with $y/H = 0.5$, and lowest in the

wake of bump 1 with $y/H = 0.1$. A maximum is observed in the positive normal velocity component in the wake of bump 1 at $y/H = 0.07$ for the spanwise positions $z/H = \pm 0.98$, with a magnitude of $\overline{V}/U_{ref} = 0.04$ caused by the recirculating flow of the pair of counter rotating vortices. Similarly, a maximum is observed for both bumps 3 for the spanwise locations $z/H = \pm 1.63$ but with a significantly smaller magnitude ($\overline{V}/U_{ref} \leq 0.01$). At large spanwise positions ($z/H \geq \pm 1.63$), the profiles of the normal velocity component are the same for the three bumps due to the limited influence of the bumps on the flow-field. The spanwise velocity components in the wakes of bump 1 and large bump 3 have similar qualitative characteristics. However, the magnitude of the spanwise velocity component is larger in the wake of bump 1 than in the wake of large bump 3, especially close to the wall. The location where all the spanwise velocity profiles converge to a zero magnitude and change sign is at a higher vertical position in the wake of large bump 3 than in the wale of bump 1. Small bump 3 shows a different distribution of the spanwise velocity component than the ones observed in the wakes of bump 1 and large bump 3. There is no vertical position where all the spanwise velocity component profiles converge to zero and change sign in the wake of small bump 3. Moreover, the spanwise velocity magnitude is not largest close to the wall but at $y/H = 0.2$ and $z/H = \pm 0.32$. The distributions of the streamwise vorticity in the wakes of bump 1 and small bump 3 are similar with a maximum in magnitude observed closest to the wall, and a decrease in magnitude with increasing vertical positions. In the wake of large bump 3, the streamwise vorticity distribution shows a maximum not close to the wall, but at $y/H = 0.13$. The maximum streamwise vorticity magnitude is larger in the wake of bump 1 with $(\Omega_x \cdot H)/U_{ref} = \pm 2.5$ than in the wakes of both bumps 3. In the wakes of both bumps 3, the streamwise vorticity magnitude is of the order of $(\Omega_x \cdot H)/U_{ref} = \pm 0.8$.

At the first measurement planes, the flow fields in the wakes of the three bumps were significantly different one to the other. Significant amounts of high momentum fluid were entrained close to the wall in the wake of bump 1 constraining the boundary layer to stay constant. However, only small amounts of high momentum fluid were entrained close to the wall in the wake of large bump 3, and no high momentum fluid was

found close to the wall in the wake of small bump 3. The normal and velocity component in the wakes of the three bumps showed similar characteristics. However, its magnitude and distribution were different in the wakes of each bump. The spanwise velocity component behavior in the wakes of bump 1 and large bump 3 were similar. In the wake of small bump 3, a different distribution than bump 1 and large bump 3 was observed. The magnitude of the streamwise vorticity in the wake of bump 1 was found to be larger than in the wakes of both bumps 3. Finally, the streamwise vorticity was found to have a similar behavior in the wakes of bump 1 and small bump 3. Large bump 3 exhibited a different distribution of the streamwise vorticity. The magnitude of the streamwise vorticity was found to be similar in the wakes of both bumps 3 and significantly larger in the wake of bump 1.

3.6 Comparison of bump data at x/H = 11.5

A comparison of the flow-field measured in the wakes of the three bumps is made at $x/H = 11.5$. Figure 3.50, Figure 3.51, and Figure 3.52 show the three components of the velocity vectors for bump 1, small bump 3, and large bump 3, respectively, at different vertical and spanwise locations. Large amounts of high momentum fluid are entrained close to the wall and to the centerline of the test section in the wake of bump 1 and, to a lesser extent, in the wakes of both bumps 3. In the wakes of both bumps 3, the high momentum fluid entrained close to the wall energizes the boundary layer and constrains the growth of the boundary layer thickness. In the wake of bump 1, the large amounts of high momentum fluid entrained close to the wall induce a significant decrease of the boundary layer thickness. The distribution and the magnitude of the normal velocity component are similar in the wakes of both bumps 3. The normal velocity component in the wakes of both bumps 3 stays relatively constant with increasing vertical positions and is relatively small ($\overline{V}/U_{ref} \leq \pm 0.02$). In the wake of bump 1, the normal velocity magnitude is relatively large ($\overline{V}/U_{ref} \geq \pm 0.02$) and varies significantly with increasing vertical positions. The spanwise velocity components and the streamwise vorticity show similar distributions and magnitudes in the wakes of the three bumps.

At $x/H = 11.5$, the amount of high momentum entrained close to the wall was significantly larger in the wake of bump 1 than in the wakes of both bumps 3. It induced

a significant reduction in the boundary layer thickness close to the centerline of the test section in the wake of bump 1. In the wakes of both bumps 3, the high momentum fluid constrained the growth of the boundary layer. The normal velocity component had similar distributions and magnitude in the wakes of both bumps 3 but significant differences in the distribution and magnitude of the normal velocity component were observed in the wake of bump 1. The spanwise velocity component and the streamwise vorticity were observed to be relatively similar in the wakes of the three bumps.

3.7 Evolution of the flowfield in the positive streamwise direction in the wake of the bumps

3.7.1 Bump 1

In the wake of bump 1, the mean streamwise velocity component measured at $x/H = 3.455$ and $x/H = 11.5$ presented in Figure 3.47 and Figure 3.50, respectively, indicates that with increasing streamwise positions, the entrainment of high momentum fluid close to the wall and to the centerline of the test section increases inducing a significant decrease in the boundary layer thickness with increasing streamwise positions. At both locations, $x/H = 3.455$ and $x/H = 11.5$, a region of low momentum fluid is observed close to the pair of counter rotating vortices. This region decreases in magnitude with increasing streamwise positions. The peak of negative normal velocity decreases in magnitude, and increases in vertical position with increasing streamwise positions. Its magnitude at $x/H = 3.455$ is $\overline{V}/U_{ref} = 0.09$ and it is located at $y/H = 0.2$. At $x/H = 11.5$, it is $\overline{V}/U_{ref} = 0.03$ and it is located at $y/H = 0.5$. The peak of positive normal velocity component conserves its magnitude with increasing streamwise positions. However, the vertical locations where it is located increases with increasing vertical locations. It is located at $y/H = 0.15$ at $x/H = 3.455$ and at $y/H = 0.3$ at $x/H = 11.5$. The spanwise velocity component decreases in magnitude with increasing streamwise positions. Moreover, the location where the magnitude of the spanwise velocity component converges to zero and changes sign, increases in vertical positions with increasing streamwise position from $y/H = 0.2$ at $x/H = 3.455$ to $y/H = 0.4$ at $x/H = 11.5$.

From Figure 3.8 and Figure 3.14, the position of the vortex centers of the pair of counter-rotating vortices increases in vertical and spanwise position with increasing streamwise positions. The outward motion of the vortex center pair of counter-rotating vortices is due to the mirror image vortices. The increase in vertical position of the vortex centers with increasing streamwise locations is due to the diffusion of the vorticity into the outer flow. The streamwise vorticity magnitude close to the wall decays significantly with increasing streamwise location. The maximum streamwise vorticity magnitude is $\left|\Omega_x \cdot H/U_{ref}\right| = 2.5$ at $x/H = 3.455$, and decays to $\left|\Omega_x \cdot H/U_{ref}\right| = 0.5$ at $x/H = 11.5$.

3.7.2 Small bump 3

The mean streamwise velocity component measured in the wake of small bump 3 at $x/H = 3.26$ and $x/H = 11.5$ in Figure 3.48, and Figure 3.51, respectively, indicates that the region of low momentum fluid close to the wall and to the centerline observed at $x/H = 3.26$ recedes at $x/H = 11.5$ due to the entrainment of high momentum fluid close to the wall at the same locations. The magnitude of the normal velocity component decreases significantly with increasing streamwise direction. The peak of negative normal velocity observed at $x/H = 3.26$ of $\overline{V}/U_{ref} = -0.07$ recedes with increasing streamwise positions. At $x/H = 11.5$, it is $\overline{V}/U_{ref} = -0.02$. However, the vertical position of this peak stays constant with increasing streamwise positions. The magnitude of the spanwise velocity component decreases with increasing streamwise positions for a same vertical position except close to the wall, where the magnitude of the spanwise velocity component is larger at $x/H = 3.26$ than at the downstream plane. Furthermore, the behavior of the spanwise velocity component is significantly different at the two streamwise locations. At $x/H = 3.26$, the maximum magnitude of the spanwise velocity component is observed at $y/H = 0.2$ whereas at $x/H = 11.5$, it is located nearest to the wall.

From Figure 3.20 and Figure 3.26, the locations of the vortex centers of the pair of counter-rotating vortices are observed to increase in vertical and spanwise positions with increasing streamwise positions. The outward motion of the vortex center pair of

counter-rotating vortices is due to the mirror image vortices. The increase in vertical position of the vortex centers with increasing streamwise locations is due to the diffusion of the vorticity into the outer flow. The streamwise vorticity magnitude close to the wall decays significantly with increasing streamwise location. The maximum streamwise vorticity magnitude is $\left|\Omega_x \cdot H/U_{ref}\right| = 0.9$ at $x/H = 3.26$ and decays to $\left|\Omega_x \cdot H/U_{ref}\right| = 0.1$ at $x/H = 11.5$.

3.7.3 Large bump 3

The mean streamwise velocity component measured in the wake of large bump 3 at $x/H = 3.629$ and $x/H = 11.5$ in Figure 3.49 and Figure 3.52, respectively, reveals that with increasing streamwise positions, the entrainment of high momentum fluid close to the wall and close to the centerline of the test section increases. The regions of low momentum fluid observed close to the wall at both streamwise positions diverge from the centerline of the test section with increasing streamwise positions. The boundary layer thickness stays constant for $z/H \le \pm 0.5$ with increasing streamwise positions suggesting that the amount of high momentum fluid entrained close to the wall prevents from further growth of the boundary layer. However, for $z/H \ge \pm 0.5$, the boundary layer increases with increasing streamwise positions since no high momentum fluid is entrained close to the wall at these spanwise locations. The peak of negative normal velocity component significantly decreases in magnitude and its vertical positions increases with increasing streamwise positions. At $x/H = 3.629$, the peak of negative normal velocity is located at $y/H = 0.35$ and is $\overline{V}/U_{ref} = -0.06$. At $x/H = 11.5$ its vertical position increased to $y/H = 0.6$ and its magnitude decreased to $\overline{V}/U_{ref} = -0.015$. The magnitude of the spanwise velocity component decreases with increasing vertical positions however, its behavior is similar at the downstream location. The maximum magnitude at $x/H = 3.629$ is $\overline{W}/.U_{ref} = \pm 0.1$. At $x/H = 11.5$, the maximum magnitude of the spanwise velocity component decreases to $\overline{W}/U_{ref} = \pm 0.08$ Moreover, the location where the spanwise velocity component magnitude converges to zero and changes sign, slightly increases in vertical position with increasing streamwise position from $y/H = 0.3$ at $x/H = 3.629$ to $y/H = 0.45$ at $x/H = 11.5$.

From Figure 3.38 and Figure 3.44, the locations of the vortex centers of the pair of counter-rotating vortices are observed to increase in vertical positions but not in spanwise positions with increasing streamwise position. The fact that no displacement in spanwise position of the vortex centers is observed may be due to erroneous data caused by the low sampling time as discussed in section 2.2.3.2. The increase in vertical position of the vortex centers with increasing streamwise locations is due to the diffusion of the vorticity into the outer flow. The streamwise vorticity magnitude close to the wall decays significantly with increasing streamwise location. The maximum streamwise vorticity magnitude is $\left|\Omega_x \cdot H/U_{ref}\right| = 0.8$ at $x/H = 3.629$ and decays to $\left|\Omega_x \cdot H/U_{ref}\right| = 0.2$ at $x/H = 11.5$.

3.8 Qualitative comparison of the seven-hole probe measurements with quad-wire hot-wire data and LDV data

3.8.1 Bump 1

The mean velocity components in the wake of bump 1 at $x/H = 3.455$ measured with LDV and quad-wire hot-wire anemometer method by Byun et *al.* (2004) and Ma and Simpson (2004), respectively, are plotted in Figure 3.53 and Figure 3.54, respectively. A qualitative comparison is done of the seven-hole probe measurements (Figure 3.47) at the same location with LDV and hot-wire measurements. The qualitative agreement in the streamwise velocity component between the three methods is good. The three sets of data have a similar distribution and the magnitudes measured by the three methods appear similar. The distribution of the normal velocity component is similar for the three methods but its magnitude is significantly underestimated by the seven-hole probe. The peak of negative normal velocity indicated from hot-wire and LDV measurements is $\overline{V}/U_{ref} \geq -0.1$ whereas the seven-hole probe measurements indicates $\overline{V}/U_{ref} \leq -0.1$. A similar observation is observed for the peak of positive normal velocity. The qualitative agreement in the spanwise velocity component as well as in the streamwise vorticity is good. The measurements from the three methods of the spanwise velocity component and of the streamwise vorticity show similar distributions and magnitudes.

3.8.2 Small bump 3

The mean velocity measurements in the wake of small bump 3 at $x/H = 3.26$ measured with LDV and quad-wire hot-wire anemometer method by Byun et *al.* (2004) and Ma and Simpson (2004), respectively, are plotted in Figure 3.55, and Figure 3.56, respectively. A qualitative comparison is done of the seven-hole probe measurements (Figure 3.48) at the same location with LDV and hot-wire measurements. The agreement in the streamwise velocity component between LDV and seven-hole probe measurement is good. The two sets of data have a similar distribution and the magnitudes are comparable. Between hot-wire data and seven-hole probe measurements, the agreement in the distribution of the streamwise velocity component is good however, the magnitude of the streamwise velocity component measured by the seven-hole probe is smaller than the measurements from the hot-wire probe. Away from the wall, the normal velocity component distribution is similar from the three methods' measurements with the peak of negative normal velocity located at the same vertical position and with a similar magnitude. However, close to the wall, seven-hole probe measurements indicate positive normal velocities whereas LDV measurements and hot-wire measurements indicate negative normal velocities. The agreement in the spanwise velocity component for the three measuring methods is good. The magnitudes as well as the distributions of the spanwise velocity component measured by the three methods appear to be similar. A good agreement is observed between the streamwise vorticity magnitudes distributions computed from seven-hole probe data and hot-wire data. However, differences in magnitude are observed between seven-hole probe data and LDV data. Close to the wall, LDV measurements indicate a streamwise vorticity smaller than what is indicated from seven-hole probe measurements and, away from the wall, seven-hole probe measurements indicate a streamwise vorticity smaller than what is indicated by the LDV measurements.

3.8.3 Large bump 3

The mean velocity measurements in the wake of large bump 3 at $x/H = 3.629$ and quad-wire hot-wire anemometer method by Ma and Simpson (2004) are plotted in Figure 3.57. A qualitative comparison is done of the seven-hole probe measurements (Figure 3.49) at the same location with hot-wire measurement. Note that the comparison

with LDV data is not done due to seeding problems in the wake of large bump 3 at large vertical positions. The agreement in the streamwise velocity component between the two methods is poor. The streamwise velocity component measured by the seven-hole probe is larger than what is indicated from hot-wire measurements for all the vertical positions. The normal velocity component distribution is similar for the two methods but, the magnitude measured by the seven-hole probe is significantly smaller than what is indicated by hot-wire measurements. The spanwise velocity component magnitude is similar for the two methods for $y/H \leq 0.2$. However, for $y/H \geq 0.2$, the magnitude of the spanwise velocity component measured by the seven-hole probe is smaller than what is indicted from hot-wire measurements. The distributions of the streamwise vorticity measured by the two methods are similar. However, close to the wall, the streamwise vorticity magnitude calculated from seven-hole probe measurements is smaller than what is indicated from hot-wire measurements. The poor qualitative and quantitative agreements of seven-hole probe measurements and hot-wire measurements, are due to the choice of the sampling time that was too short to obtain statistically ergodic measurements in the wake of large bump 3.

3.9 Quantitative comparison of the seven-hole probe measurements with quad-wire hot-wire data and LDV data

As discussed in section 3.8.3 and in section 2.2.3.2, the measurements performed by the seven-hole probe in the wake of large bump 3 are not statistically ergodic. Consequently, quantitative comparisons of seven-hole probe data to hot-wire data and LDV data are done only in the wakes of bump 1 and of small bump 3. The mean velocity magnitude comparisons are done by defining a non-dimensional bias-error expressed as a percentage of the local velocity magnitude.

$$\Delta U_{LDV/hot-wire} = \frac{U_{7HP} - U_{LDV/hot-wire}}{U_{LDV/hot-wire}} \qquad \textbf{(3.6)}$$

The pitch and yaw angles comparisons by defining two bias-errors,

$$\begin{aligned} \Delta\alpha_{LDV/hot-wire} &= \alpha_{7HP} - \alpha_{LDV/hot-wire} \\ \Delta\beta_{LDV/hot-wire} &= \beta_{7HP} - \beta_{LDV/hot-wire} \end{aligned} \qquad \textbf{(3.7)}$$

3.9.1 Bump 1

The bias-errors (equations 3.6 and 3.7) calculated with respect to quad-wire hot-wire measurements and LDV measurements by Ma and Simpson (2004) and Byun et *al.* (2004), respectively, in the wake of bump 1 at $x/H = 3.455$ are presented in Figure 3.58 and Figure 3.59, respectively.

The bias-errors of the mean velocity magnitude calculated with equation 3.6 with respect to LDV measurements and hot-wire measurements are relatively large ($\Delta U_{LDV/hot-wire} \geq \pm 2\%$ of $U_{LDV/hot-wire}$) close to the wall and decrease in magnitude with increasing vertical positions until $y/H = 0.3$. For $y/H \geq 0.3$, the bias-errors in the mean velocity magnitude stay relatively constant and small ($\Delta U_{LDV/hot-wire} \leq \pm 2\%$ of $U_{LDV/hot-wire}$). It is interesting to note that close to the wall, the magnitudes of $\Delta U_{LDV/hot-wire}$ do not appear correlated to the spanwise positions indicating that the magnitudes of $\Delta U_{LDV/hot-wire}$ are primarily due to the wall effects that is, increased amount of probe/flow interactions and large velocity gradient in near wall regions. Note that for $y/H \geq 0.7$, the seven-hole probe measurements slightly over-predict the hot-wire measurements. However, for the same vertical positions, the seven-hole probe measurements slightly under-predict the LDV measurements. Nevertheless, the differences are small ($\Delta U_{LDV/hot-wire} \leq \pm 0.5\%$ of $U_{LDV/hot-wire}$). The bias-errors of the pitch angles calculated with equation 3.6 with respect to LDV measurements and hot-wire measurements are relatively large and of positive sign ($\Delta\alpha_{LDV/hot-wire} \geq 1\,\text{deg}$) close to the wall and to the centerline of the test-section ($z/H \leq \pm 0.32$). With increasing vertical positions, $\Delta\alpha_{LDV/hot-wire}$ decrease in magnitude until $y/H = 0.7$. For $y/H \geq 0.7$, $\Delta\alpha_{LDV/hot-wire}$ stays relatively constant and small ($\Delta\alpha_{LDV/hot-wire} \leq 1\,\text{deg}$) at all spanwise positions with increasing vertical positions. Note that for $y/H \geq 0.7$, the seven-hole probe slightly ($\Delta\alpha_{LDV} \leq 1\,\text{deg}$) over-predicts the pitch angles measured by the LDV system. However, the quantitative agreement of the pitch angles measured by the seven-hole probe and the hot-wire probe for $y/H \geq 0.7$ is good. Away from the centerline ($z/H \geq \pm 0.32$), the seven-hole probe slightly under-predicts the pitch angles measurements ($\left|\Delta\alpha_{LDV/hot-wire}\right| \leq 1\,\text{deg}$). It is interesting to note that at the vertical

locations closest to the wall and away from the centerline of the test-section, the seven-hole probe slightly over-predicts the pitch angle measurements due to the increased amount of probe/flow interactions and to the large velocity gradient in the near wall regions. It can be seen that near the wall, at $z/H = -0.98$, the magnitude of $\Delta\alpha_{hot-wire}$ is relatively large. The bias-errors of the yaw angles calculated with equation 3.6 with respect to LDV measurements and hot-wire measurements are relatively large ($\Delta\beta_{LDV/hot-wire} \geq \pm 1\,\text{deg}$) close to the wall. With increasing vertical positions, $\Delta\beta_{LDV/hot-wire}$ decrease in magnitude until $y/H = 0.7$. For $y/H \geq 0.7$, $\Delta\beta_{LDV/hot-wire}$ stays relatively constant and small ($\Delta\beta_{LDV/hot-wire} \leq 1\,\text{deg}$) at all spanwise positions with increasing vertical positions. It is interesting to note that for $\pm 0.32 \leq z/H \leq \pm 0.98$ and close to the wall, the bias-errors are smaller ($\Delta\beta_{LDV/hot-wire} \leq 1\,\text{deg}$) than at other spanwise locations. Except for $\pm 0.32 \leq z/H \leq \pm 0.98$, the magnitudes of the bias-errors of the yaw angles close to the wall do not appear to be correlated to the spanwise position.

3.9.2 Small bump 3

The bias-errors (equations 3.6 and 3.7) calculated with respect to quad-wire hot-wire measurements and LDV measurements by Ma and Simpson (2004) and, Byun et *al.* (2004), respectively, in the wake of small bump 3 at $x/H = 3.26$ are presented in Figure 3.60 and Figure 3.61, respectively. With one look at Figure 3.60 and Figure 3.61, it is obvious that the bias-errors calculated with respect to LDV measurements and hot-wire measurements of the mean velocity magnitude are quantitatively and qualitatively different. The bias-errors of the pitch angles and yaw angles calculated with respect to LDV measurements and hot-wire measurements agree qualitatively but not quantitatively. These observations indicate qualitative and quantitative differences between LDV measurements and hot-wire measurements.

With respect to hot-wire measurements (Figure 3.60), the magnitude of the bias-errors in the mean velocity magnitude for $z/H \leq \pm 0.32$ are relatively large and of negative sign ($|\Delta U_{hot-wire}| \geq 5\%$ of $U_{hot-wire}$) close to the wall. With increasing vertical positions, for $z/H \leq \pm 0.32$, the magnitudes of the bias-errors increase until a maximum

of negative sign of $|\Delta U_{hot-wire}| \approx 10\%$ of $U_{hot-wire}$ at $y/H = 0.2$. For $y/H \geq 0.2$ and $z/H \leq \pm 0.32$, the bias-errors of the velocity magnitude decrease and become relatively small ($|\Delta U_{hot-wire}| \leq 1\%$ of $U_{hot-wire}$) for $y/H \geq 0.9$. For $z/H \geq \pm 0.32$, the magnitudes of the bias-errors in the mean velocity magnitude are of the order of 4% of $U_{hot-wire}$ close to the wall, and decrease with increasing vertical positions to relatively small magnitudes ($|\Delta U_{hot-wire}| \leq 1\%$ of $U_{hot-wire}$). It is interesting to note that for $z/H \geq \pm 0.32$, the seven-hole probe over-predicts the magnitudes of the mean velocity magnitude. However, for $z/H \leq \pm 0.32$, the seven-hole probe under-predicts the magnitude of the mean velocity magnitude.

With respect to LDV measurements (Figure 3.61), the magnitudes of the bias-errors in the mean velocity magnitude stay relatively constant with increasing vertical positions for a given spanwise positions until $y/H = 0.4$. A different behavior of the bias errors of the mean velocity magnitude is observed at $z/H = -0.32$; the bias-errors at $z/H = -0.32$ are small close to the wall and increase in magnitude with increasing vertical positions until a maximum magnitude is reached at $y/H = 0.3$ of $\Delta U_{LDV} \approx -5\%$ of U_{LDV}. For $y/H \geq 0.3$, at the spanwise location $z/H = -0.32$, the bias-errors in the mean velocity magnitude decrease with increasing vertical positions. For $y/H \leq 0.4$ and close to the centerline of the test section ($z/H \leq \pm 0.32$), the seven-hole probe measurements of the mean velocity magnitude significantly over-predict ($\Delta U_{LDV} \geq 3\%$ of U_{LDV}) the LDV measurements of the mean velocity magnitude (except for $z/H = -0.32$). Away from the centerline ($z/H \geq \pm 0.32$) and for $y/H \leq 0.4$, the LDV measurements and seven-hole probe measurements of the mean velocity magnitude are in good quantitative agreement. For $y/H \geq 0.4$ the bias-errors close to the centerline of the test section ($z/H \leq \pm 0.32$) increase with increasing vertical positions until a maximum of $\Delta U_{LDV} \approx 10\%$ of U_{LDV} at $y/H = 0.75$. For $y/H \geq 0.75$, the bias-errors decrease with increasing vertical positions. Except for the spanwise position of $z/H = -0.32$, the seven-hole probe always over-predicts the mean velocity magnitude measured by the LDV system.

The bias-errors of the pitch angles calculated with respect to hot-wire and LDV measurements are qualitatively similar. Close to the wall and to the centerline of the test section ($z/H \le \pm 0.32$), the bias-errors in the pitch angles are relatively large ($\Delta\alpha_{LDV/hot-wire} \ge 2\deg$). With increasing vertical positions, the bias-errors in the pitch angles for $z/H \le \pm 0.32$ decrease in magnitude until $y/H \approx 0.35$. For $y/H \ge 0.35$, the magnitudes of the bias-errors in the pitch angles for $z/H \le \pm 0.32$ increase with increasing vertical positions until maximum magnitudes are observed at $y/H = 0.6$ of $\left|\Delta\alpha_{LDV/hot-wire}\right| \ge 1\deg$. Note that the maximum magnitudes of the bias-errors in the pitch angles calculated with respect to LDV measurements are significantly larger than the one calculated with respect to hot-wire measurements. Similarly, close to the wall, for $z/H \le \pm 0.32$, the magnitudes of the bias-errors calculated with respect to LDV measurements are significantly larger than the bias-errors calculated with respect to hot-wire measurements. For $z/H \ge \pm 0.32$, the seven-hole prove slightly over-predicts the measurements of pitch angles ($\Delta\alpha_{LDV/hot-wire} \le 2\deg$) until $y/H = 0.1$. For $y/H \ge 0.1$, the quantitative agreement of the pitch angles measured by the seven-hole probe, the LDV system, and the hot-wire probe is good until $y/H = 0.7$. For $y/H \ge 0.7$, the pitch angles measured by the seven-hole probe are larger than the ones measured by the LDV system or hot-wire probe and the bias-errors in pitch angle appear to collapse on $\Delta\alpha_{LDV/hot-wire} \approx 1\deg$.

The bias-errors in the yaw angles calculated with respect to hot-wire measurements (Figure 3.60) are relatively small ($\Delta\beta_{hot-wire} \le \pm 1\deg$) and constant with increasing vertical positions for $z/H \ge \pm 0.32$. For $z/H \le \pm 0.32$, the yaw angles measured by the seven-hole probe are smaller than the ones measured by the hot-wire probe. Close to the wall, for $z/H \le \pm 0.32$, the bias-errors are relatively large in magnitude and of negative sign ($\left|\Delta\beta_{hot-wire}\right| \ge 1\deg$). With increasing vertical positions, the bias-errors increase in magnitude until a maximum located at $y/H \approx 0.25$. For $y/H \ge 0.25$, the bias-errors in the yaw angle decrease in magnitude with increasing vertical positions until $y/H \approx 0.6$ beyond which, the bias-errors stay relatively constant and small ($\Delta\beta_{hot-wire} \le \pm 1\deg$) with increasing vertical positions. Note that

for $z/H = -0.32$, the seven-hole probe measurements of the yaw angle are significantly smaller ($|\Delta\beta_{hot-wire}| \geq 2\,\text{deg}$) than the hot-wire measurements.

The bias-errors in the yaw angle calculated with respect to LDV measurements (Figure 3.61) away from the centerline of the test section ($z/H \geq \pm 0.32$) are relatively large ($\Delta\beta_{LDV} \geq \pm 1\,\text{deg}$) close to the wall and decrease in magnitude with increasing vertical positions. For $z/H \leq \pm 0.32$, close to the wall, the seven-hole probe measurements of the yaw angles quantitatively agree with the LDV measurements of the yaw angle ($|\Delta\beta_{LDV}| \leq 1\,\text{deg}$). With increasing vertical positions, for $z/H \leq \pm 0.32$, the bias-errors of the yaw angles increase with increasing vertical positions until a maximum of $\Delta\beta_{LDV} \geq 1\,\text{deg}$ located at $y/H = 0.15$. After this maximum, the bias-errors of the yaw angles decrease with increasing vertical positions. As observed with the bias-errors calculated with respect to hot-wire measurements, for $z/H = \pm 0.32$, the yaw angles measured by the seven-hole probe are smaller than the ones measured by the LDV probe. At $z/H = \pm 0.32$, the bias-errors are largest closest to the wall and decrease in magnitude with increasing vertical positions.

3.9.3 Quantitative comparisons with respect to vertical positions

As discussed in the previous sections, the proximity to the wall appears to induce large bias-errors (equation 3.6 and 3.7). To understand where the wall effects become significant, the bias-errors are calculated as a function of the vertical position as shown in Figure 3.62, Figure 3.63, and Figure 3.64 corresponding to the bias-errors in the mean velocity magnitude, the pitch angles, and the yaw angles, respectively, in the wakes of bump 1 and small bump 3. Furthermore, to examine if large flow angles imply larger bias-errors, the bias-errors are plotted for three ranges of flow angles, $|\alpha|, |\beta| \leq 1\,\text{deg}$, $1\,\text{deg} \leq |\alpha|, |\beta| \leq 4\,\text{deg}$, and $|\alpha|, |\beta| \geq 4\,\text{deg}$. In Figure 3.62, Figure 3.63, and Figure 3.64, the bias-errors calculated with respect to hot-wire measurements and with respect to LDV measurements are plotted independently. As discussed in the previous sections, close to the centerline of the test-section ($z/H \leq \pm 0.32$), the bias-errors close to the wall were observed to be significantly larger than for $z/H \geq \pm 0.32$. This observation indicates that other parameters are responsible for the large bias-errors observed for $z/H \leq \pm 0.32$. In

this fashion, to examine the effects of wall proximity on the seven-hole probe measurements, only measurements performed for $z/H \geq \pm 0.32$ are utilized. In Figure 3.62, Figure 3.63, and Figure 3.64, it can be seen that for the larger ranges of flow angles, the bias-errors are of the same order of magnitude than for the smaller ranges of flow angles. This observation indicates that large flow angles do not imply poor performance of the seven-hole probe.

With respect to hot-wire measurements and to LDV measurements, the bias-errors in the mean velocity magnitude (Figure 3.62) are relatively large and scattered close to the wall indicating large uncertainties of the seven-hole probe measurements due to the wall effects. With increasing vertical positions, the bias-errors become relatively small ($\Delta U_{LDV/hot-wire} \leq 2\%$ of $U_{LDV/hot-wire}$) and constant. Furthermore, with increasing vertical positions, the scatter of the bias-errors decreases indicating smaller uncertainties in the seven-hole probe measurements. The magnitudes of the bias-errors as well as the scatter of the bias-errors become relatively small for $y \geq 9$ probe diameters. This observation indicates that the wall effects induce significant uncertainty in the seven-hole probe measurements of the mean velocity magnitude for $y \leq 9$ probe diameters.

The bias-errors in the pitch and yaw angles (Figure 3.63 and Figure 3.64) show similar characteristics as the ones observed in the bias-errors of the mean velocity magnitude. Close to the wall, the magnitudes of the bias-errors are large and significant scatter of the bias-errors is observed. With increasing vertical positions, the magnitude of the bias-errors decreases as well as the scatter of the bias-errors. This observation indicates that close to the wall, the uncertainties in the flow angles measured by the seven-hole probe are large and that they decrease with increase vertical positions. The magnitudes of the bias-errors as well as the scatter of the bias-errors become relatively small and constant for $y \geq 6$ probe diameters. This observation indicates that for $y \leq 6$ probe diameters large uncertainties in the measurements of the flow angles by the seven-hole probe are to be expected due to the wall effects.

3.9.4 Quantitative comparisons with respect to TKE and velocity gradient

As discussed in the previous sections, larger flow angles do not induce larger uncertainties in the seven-hole probe measurements than for smaller ranges of flow angles. Consequently, no distinction of the flow angles is done for this analysis. To examine if the turbulent kinetic energy and the velocity gradients are sources of uncertainty in the measurements performed by the seven-hole probe, the bias-errors (equation 3.6 and 3.7) are plotted as a function of the turbulent kinetic energy and the magnitude of a non-dimensional velocity gradient *G* (defined in equation 4.11) measured from a quad-wire hot-wire probe and a LDV system by Ma and Simpson (2004) and Byun et *al.* (2004), respectively. Figure 3.65, Figure 3.66, and Figure 3.67 represents the bias-errors in the mean velocity magnitude (equation 3.6), the pitch angle (equation 3.7), and the yaw angle (equation 3.7), respectively, as a function of turbulent kinetic energy and the non-dimensional velocity gradient *G* calculated with respect to hot-wire measurements in the wakes of bump 1 and small bump 3 at $x/H = 3.455$ and $x/H = 3.26$, respectively. Figure 3.68, Figure 3.69, and Figure 3.70 represents the bias-errors in the mean velocity magnitude (equation 3.6), the pitch angle (equation 3.7), and the yaw angle (equation 3.7), respectively, as a function of turbulent kinetic energy and the non-dimensional velocity gradient *G* calculated with respect to LDV measurements in the wakes of bump 1 and small bump 3 at $x/H = 3.455$ and $x/H = 3.26$, respectively.

It can be seen Figure 3.65 and Figure 3.68, that for relatively small values of turbulent kinetic energy and of velocity gradients, the bias-errors in the mean velocity magnitude are relatively small and constant. With increasing turbulent kinetic energy and velocity gradients, the magnitudes of the bias-errors increase and a significant scatter of the bias-errors is observed. Similarly, the bias-errors in the pitch and yaw angles in Figure 3.66, Figure 3.67, Figure 3.69, and Figure 3.70 (equation 3.7) show a similar behavior as the bias-errors in the mean velocity magnitude. With increasing magnitude of the velocity gradients and of the turbulent kinetic energy, the magnitudes of the bias-errors in the pitch and yaw angles as well as the scatter of the bias-errors increase. These observations indicate that the turbulent kinetic energy and velocity gradients are a source of uncertainty in seven-hole probe measurements. Note that regions of large turbulent

kinetic energy and regions of large velocity gradient are not necessarily the same. Consequently, to this point, it is difficult to draw conclusion as to what parameter (turbulent kinetic energy or velocity gradient) has the most effect on seven-hole probe measurements.

3.10 Figures

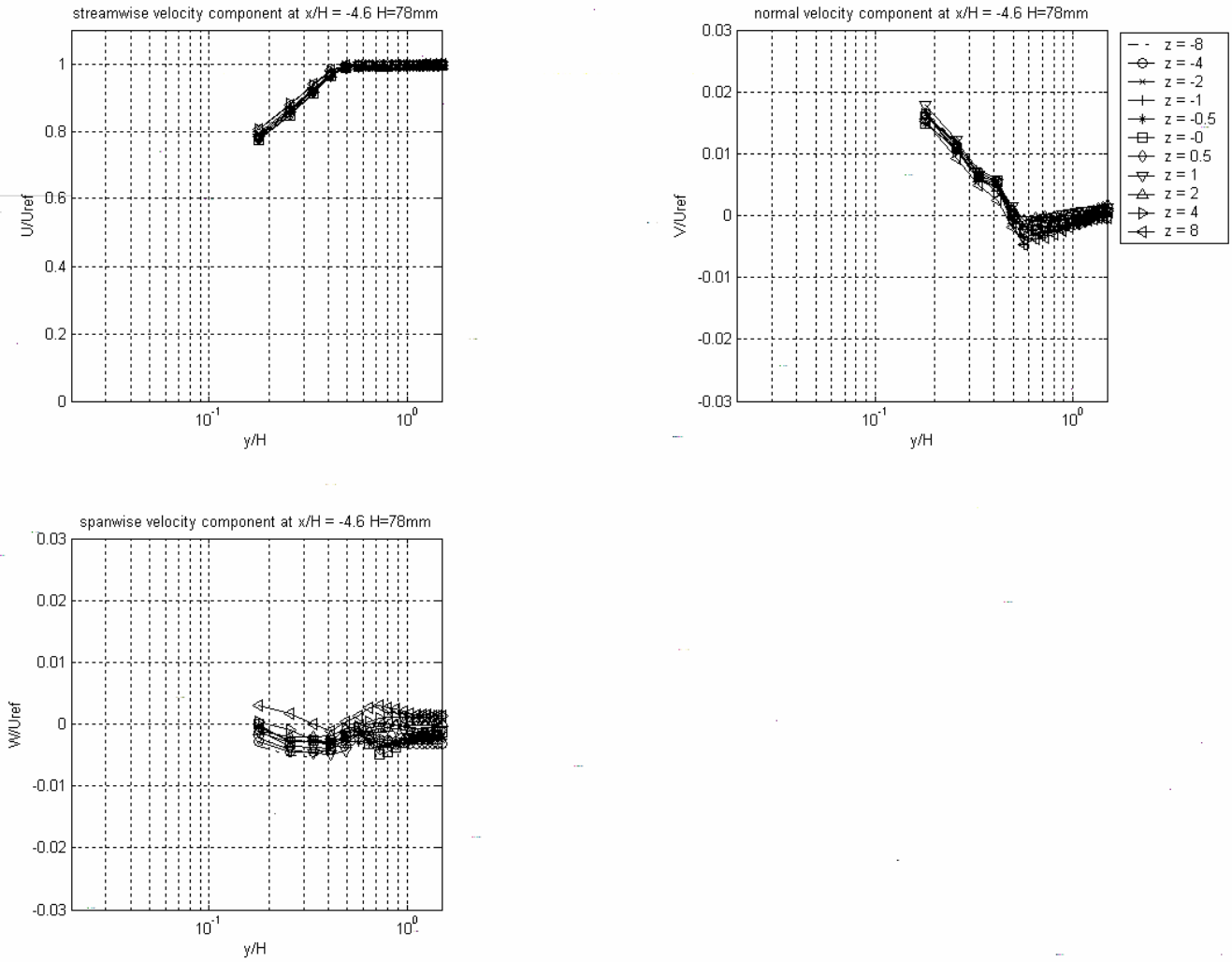

Figure 3.1: Two-dimensional Boundary layer measured with the seven-hole probe at x/H = -4.6 (H=78mm)

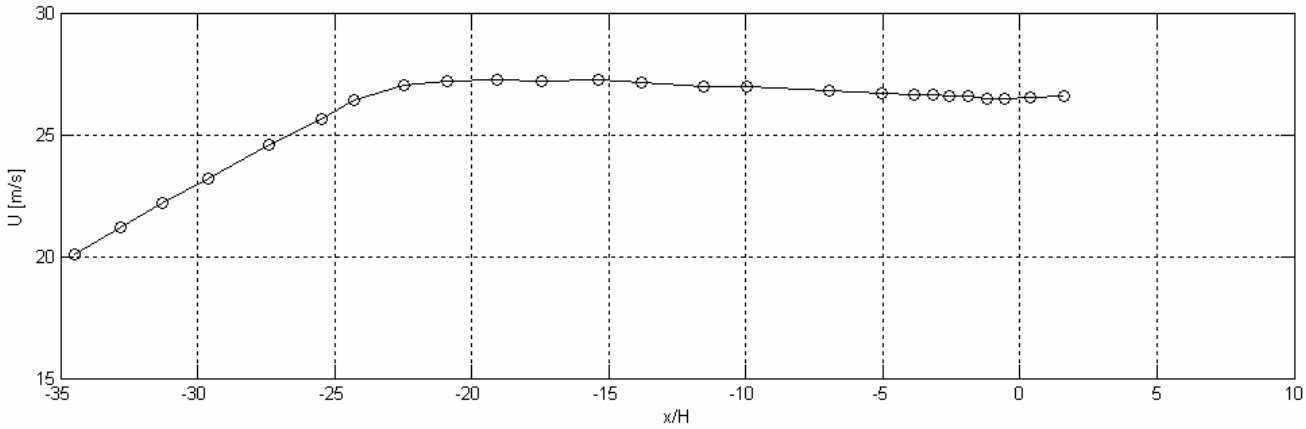

Figure 3.2: Variation of the mean velocity magnitude in the centerline of the test section (no bump set in place) as a function of the streamwise position, George (2004)

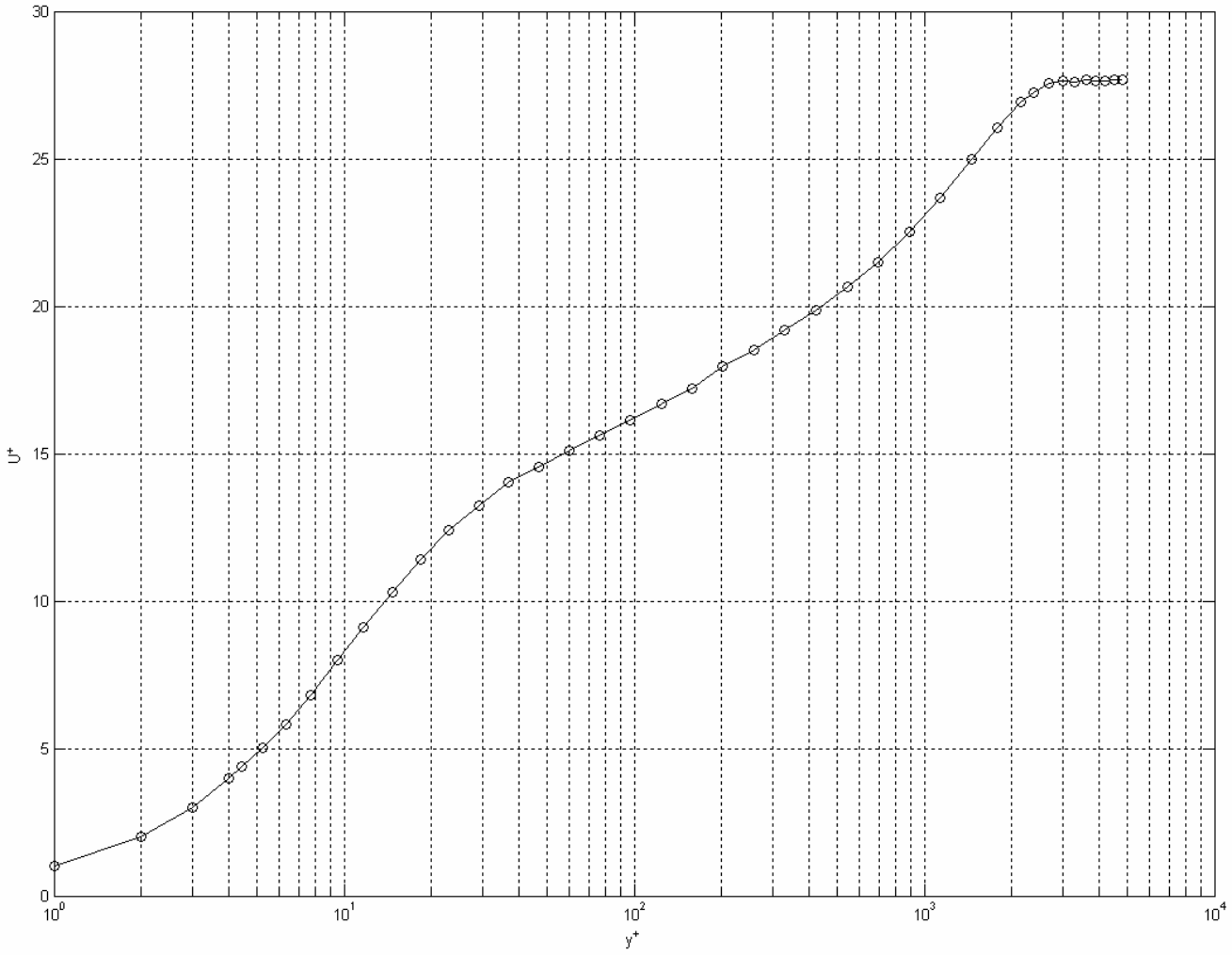

Figure 3.3: Two-dimensional boundary layer profile (U_τ = 0.99) measured with a LDV system at *x/H* = -2 and *z/H* = 0 by Byun et *al.* (2004)

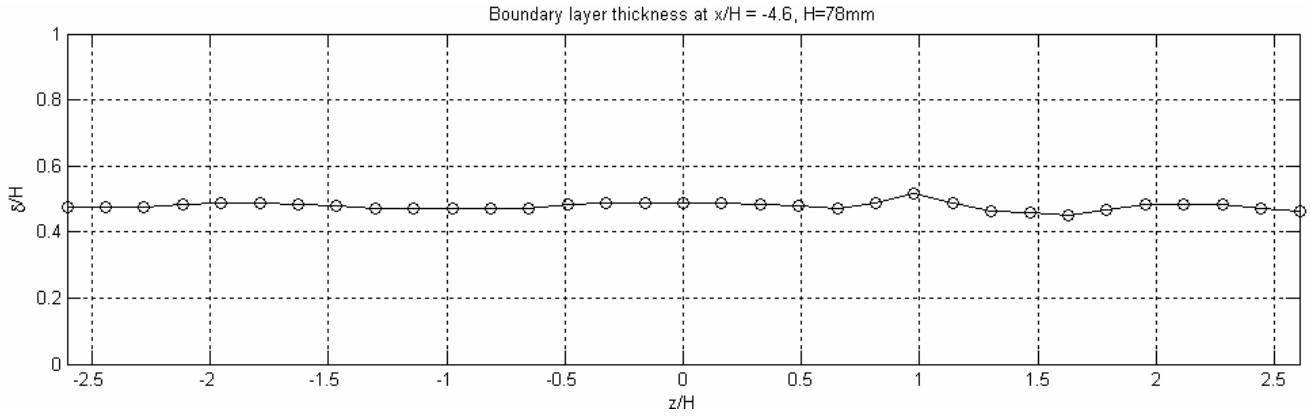

Figure 3.4: Variation of the boundary layer thickness with respect to the spanwise position of the two-dimensional flow at x/H = -4.6 (H = 78mm)

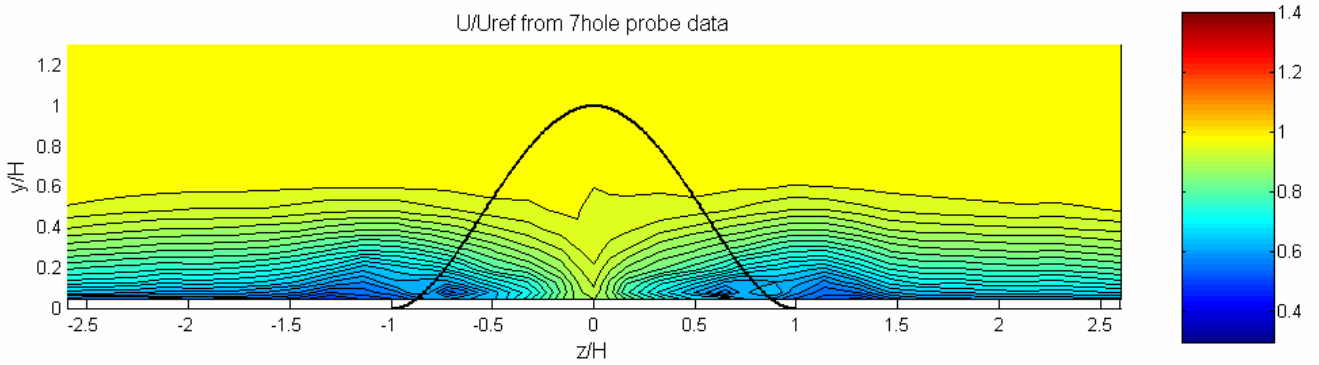

Figure 3.5: Normalized mean streamwise velocity component at x/H= 3.455 in the wake of bump 1 measured with the seven-hole probe

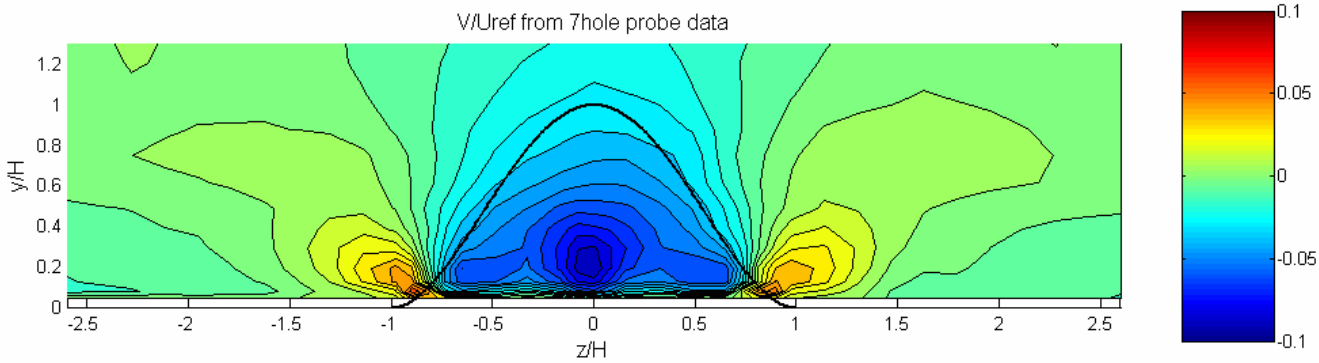

Figure 3.6: Normalized mean normal velocity component at x/H = 3.455 in the wake of bump 1 measured with the seven-hole probe

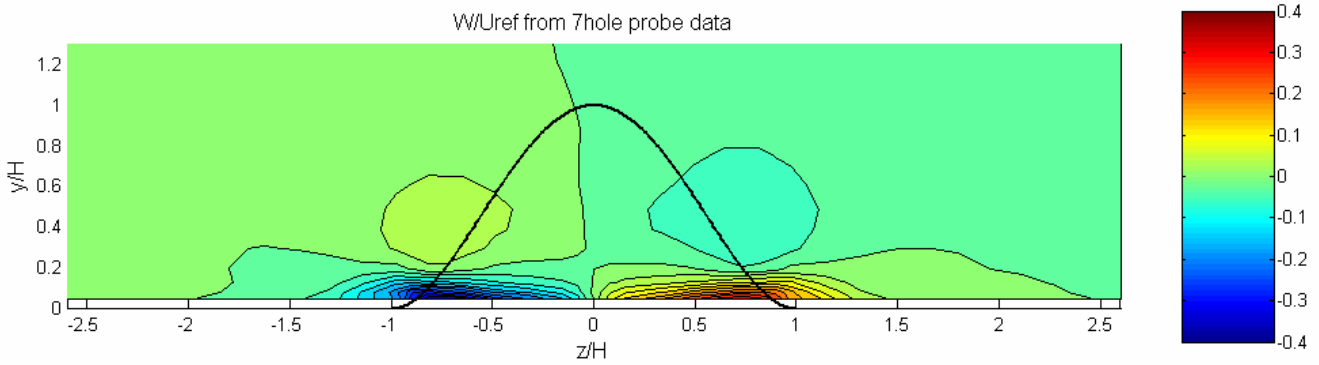

Figure 3.7: Normalized mean spanwise velocity component at x/H = 3.455 in the wake of bump 1 measured with the seven-hole probe

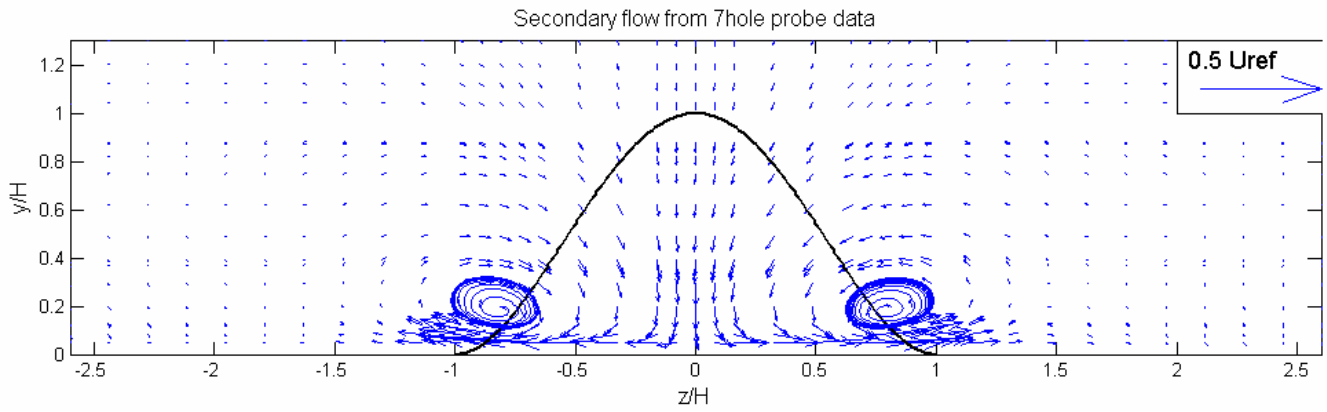

Figure 3.8: Secondary flow vector field at x/H = 3.455 in the wake of bump 1 measured with the seven-hole probe

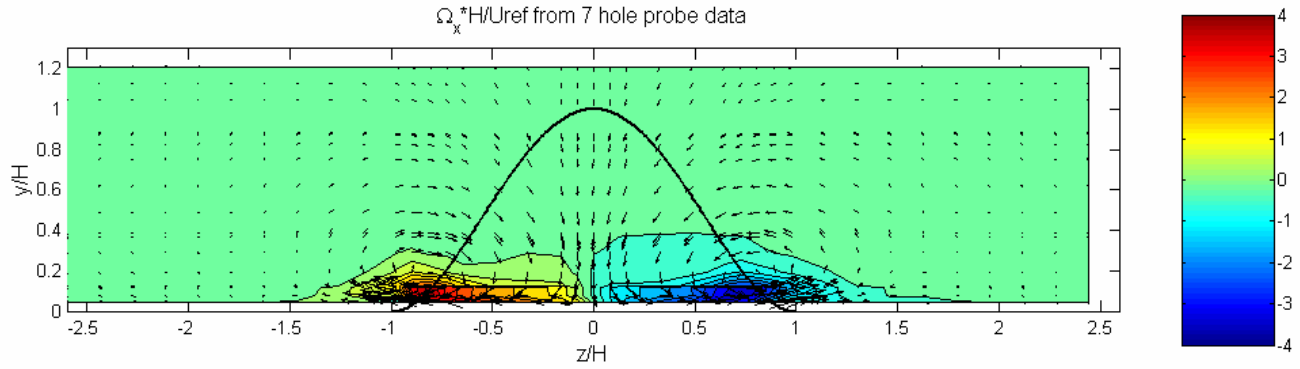

Figure 3.9: Normalized streamwise vorticity at x/H = 3.455 in the wake of bump 1 measured with the seven-hole probe and secondary flow vectors

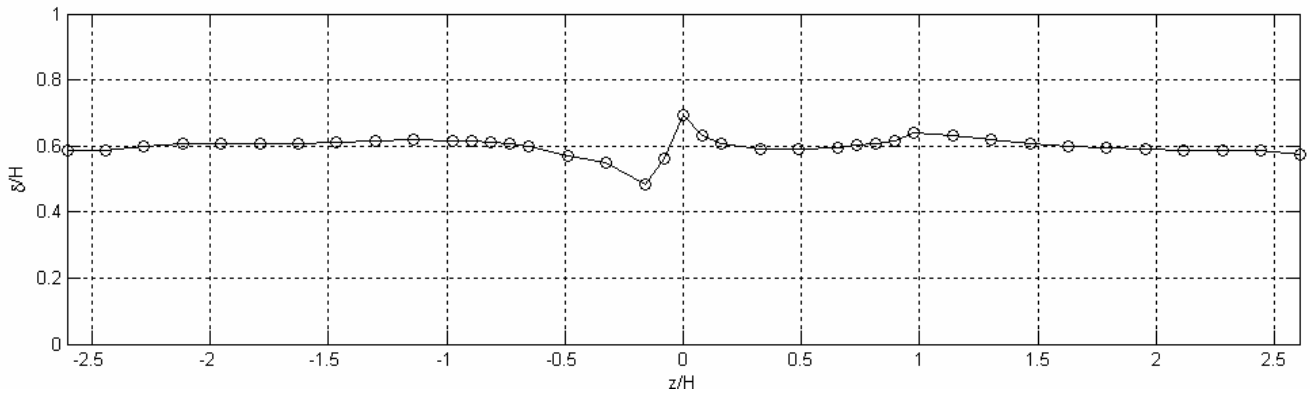

Figure 3.10: Variation of the boundary layer thickness on the span of the test section measured with the seven-hole probe in the wake of bump 1 at x/H = 3.455

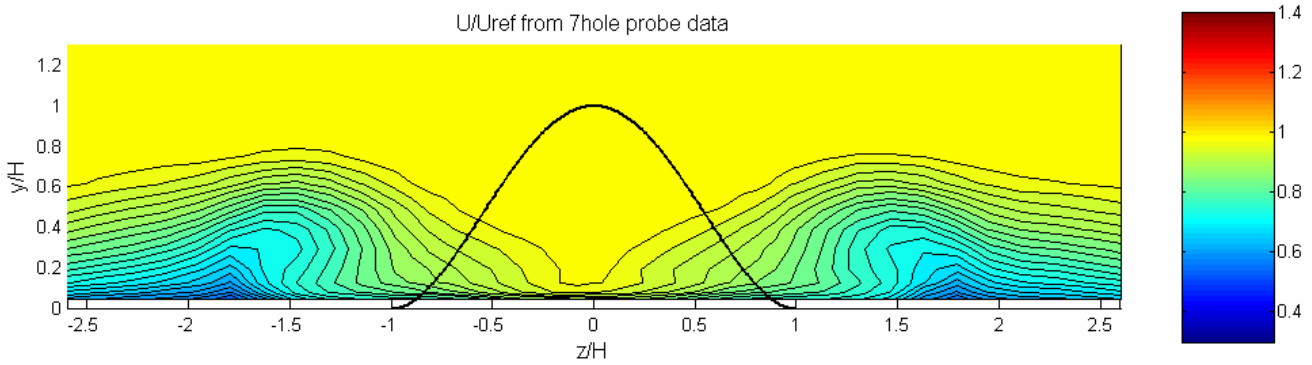

Figure 3.11: Normalized mean streamwise velocity component at x/H= 11.5 in the wake of bump 1 measured with the seven-hole probe

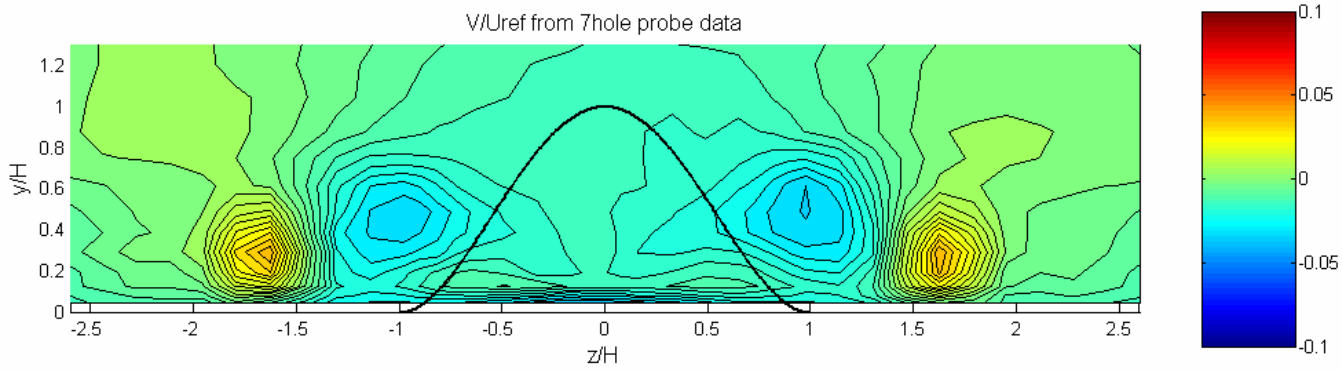

Figure 3.12: Normalized mean normal velocity component at x/H = 11.5 in the wake of bump 1 measured with the seven-hole probe

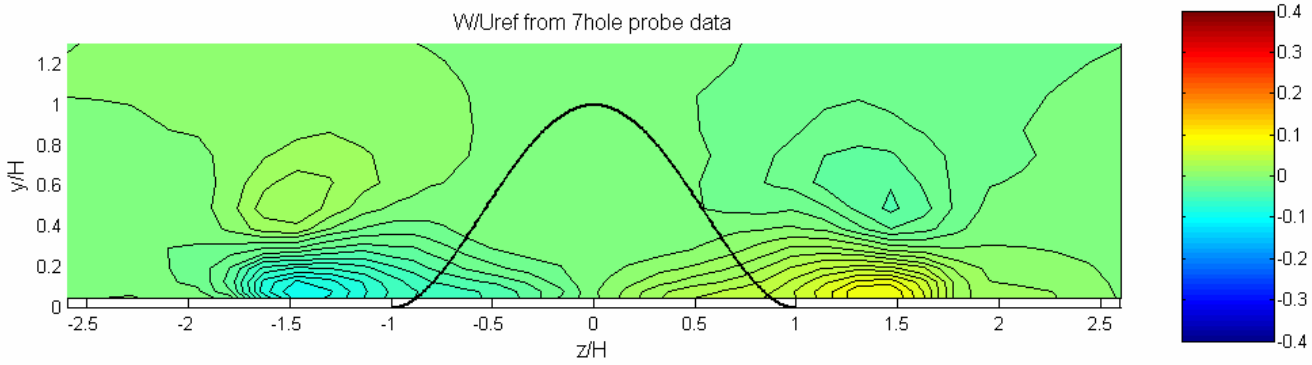

Figure 3.13: Normalized mean spanwise velocity component at x/H = 11.5 in the wake of bump 1 measured with the seven-hole probe

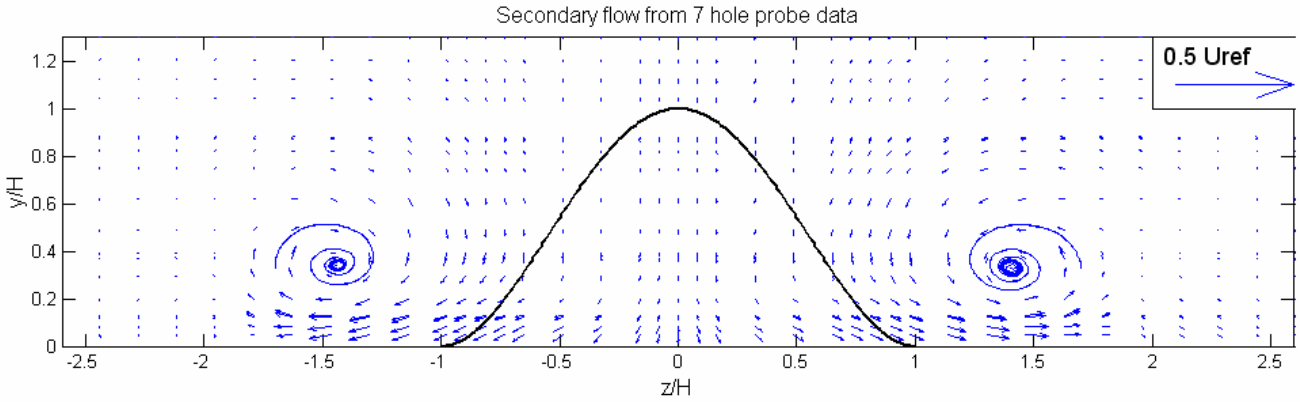

Figure 3.14: Secondary flow vector field at x/H = 11.5 in the wake of bump 1 measured with the seven-hole probe

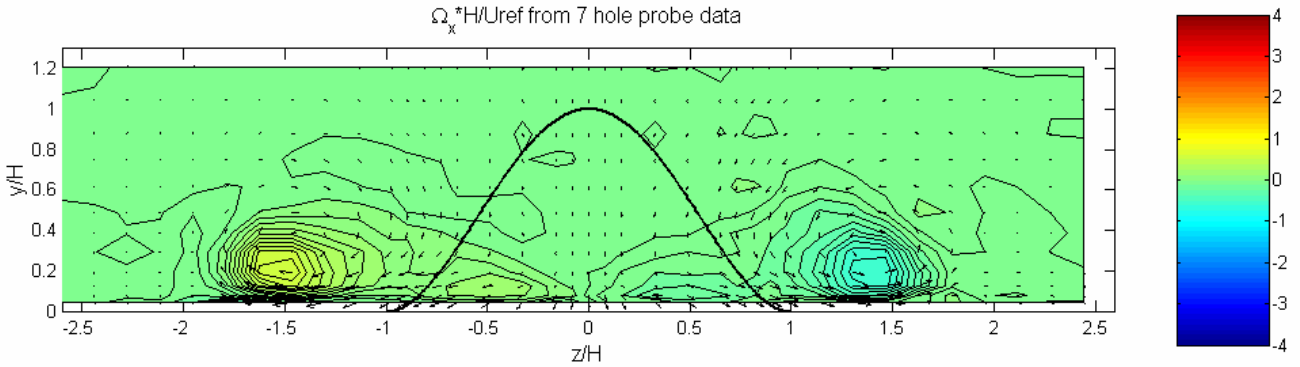

Figure 3.15: Normalized streamwise vorticity at x/H = 11.5 in the wake of bump 1 measured with the seven-hole probe and secondary flow vectors

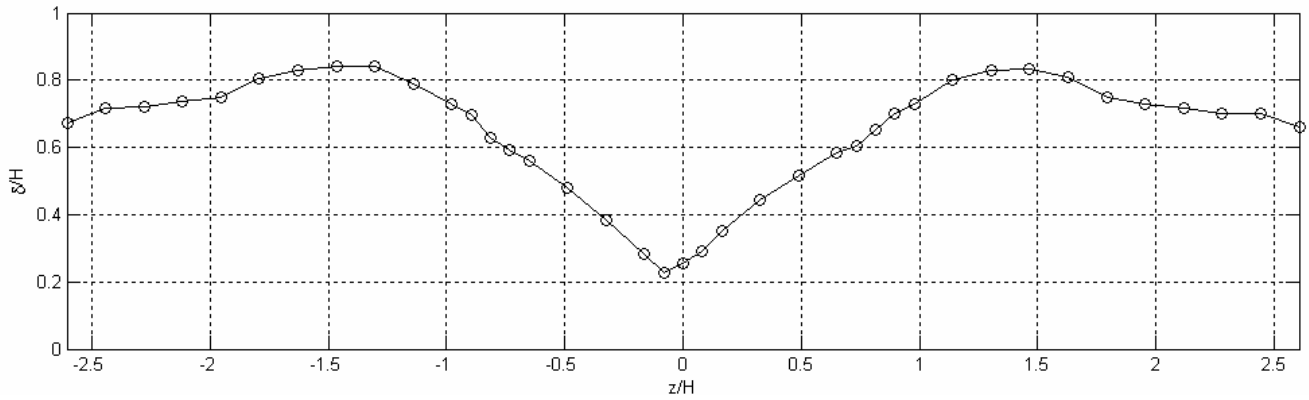

Figure 3.16: Variation of the boundary layer thickness on the span of the test section measured with the seven-hole probe in the wake of bump 1 at x/H = 11.5

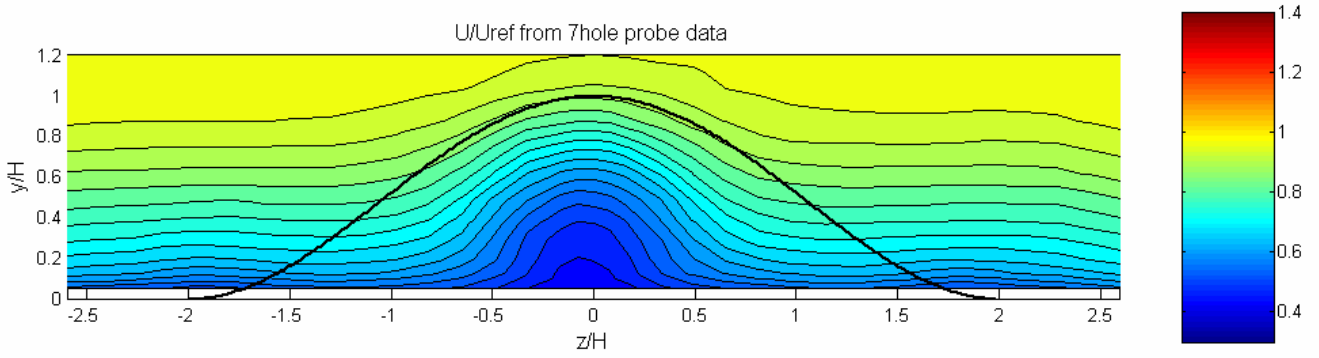

Figure 3.17: Normalized mean streamwise velocity component at x/H= 3.26 in the wake of small bump 3 measured with the seven-hole probe

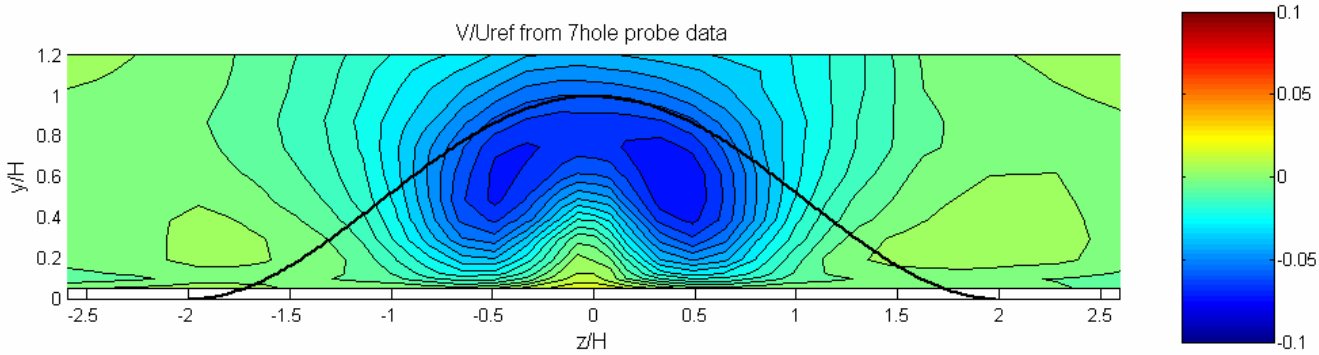

Figure 3.18: Normalized mean normal velocity component at x/H= 3.26 in the wake of small bump 3 measured with the seven-hole probe

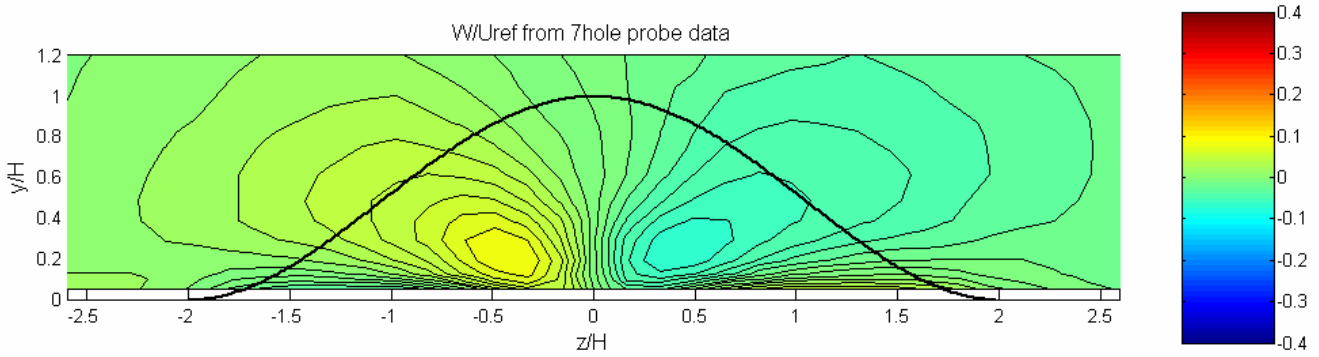

Figure 3.19: Normalized mean spanwise velocity component at x/H= 3.26 in the wake of small bump 3 measured with the seven-hole probe

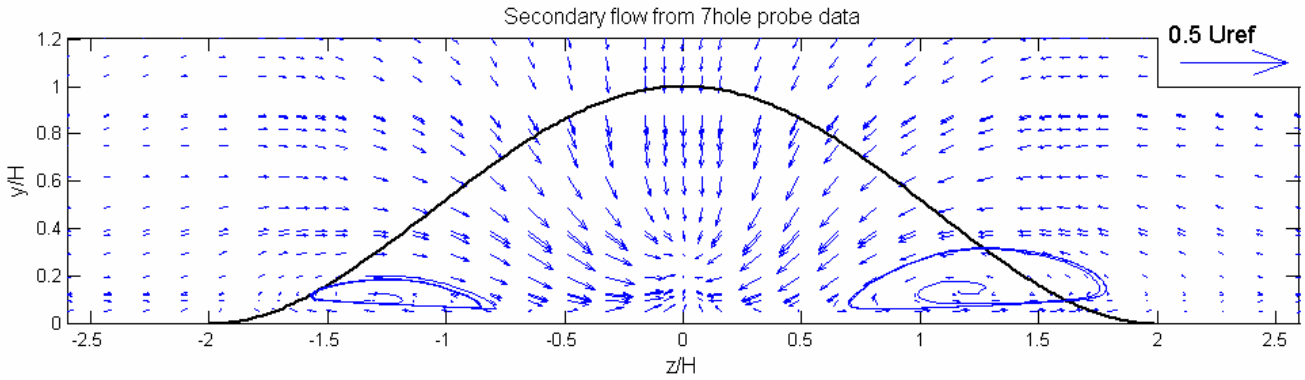

Figure 3.20: Secondary flow vector field at x/H= 3.26 in the wake of small bump 3 measured with the seven-hole probe

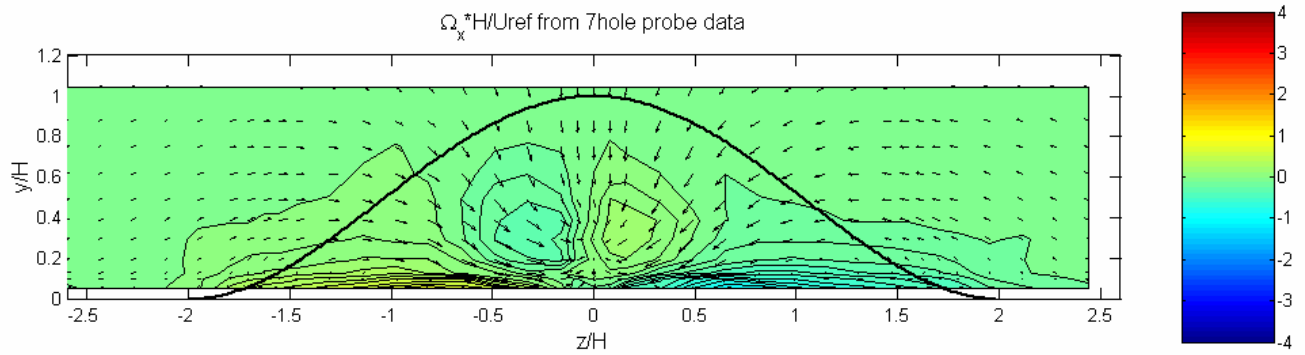

Figure 3.21: Normalized streamwise vorticity at x/H= 3.26 in the wake of small bump 3 measured with the seven-hole probe and secondary flow vectors

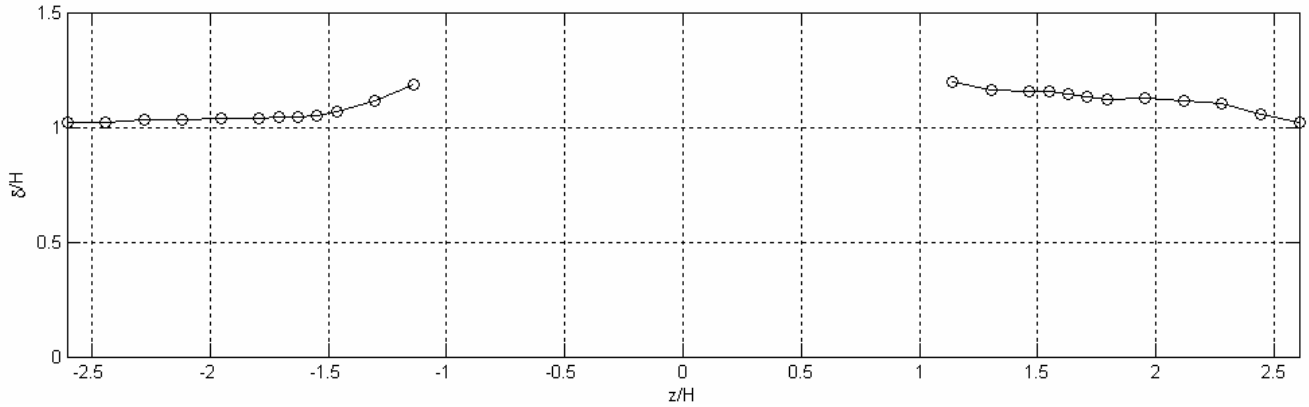

Figure 3.22: Variation of the boundary layer thickness on the span of the test section measured with the seven-hole probe in the wake of small bump 3 at x/H = 3.26

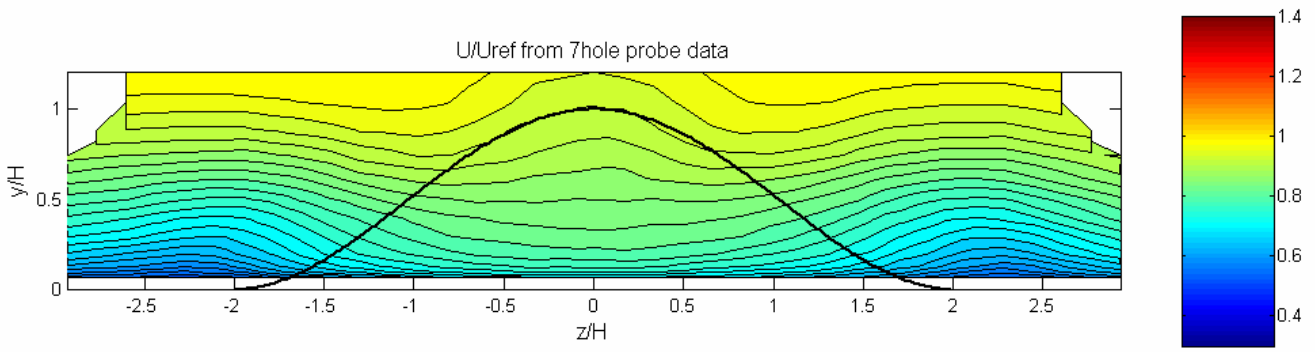

Figure 3.23: Normalized mean streamwise velocity component at x/H= 11.5 in the wake of small bump 3 measured with the seven-hole probe

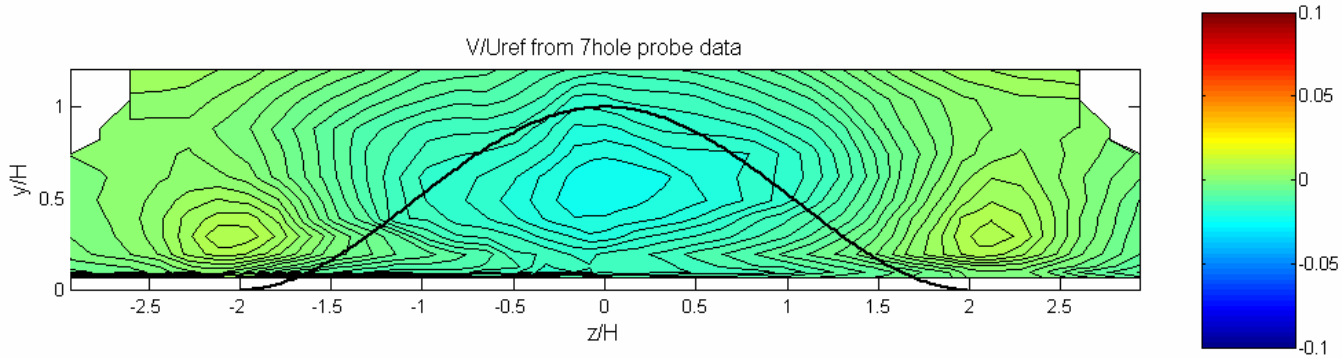

Figure 3.24: Normalized mean normal velocity component at x/H= 11.5 in the wake of small bump 3 measured with the seven-hole probe

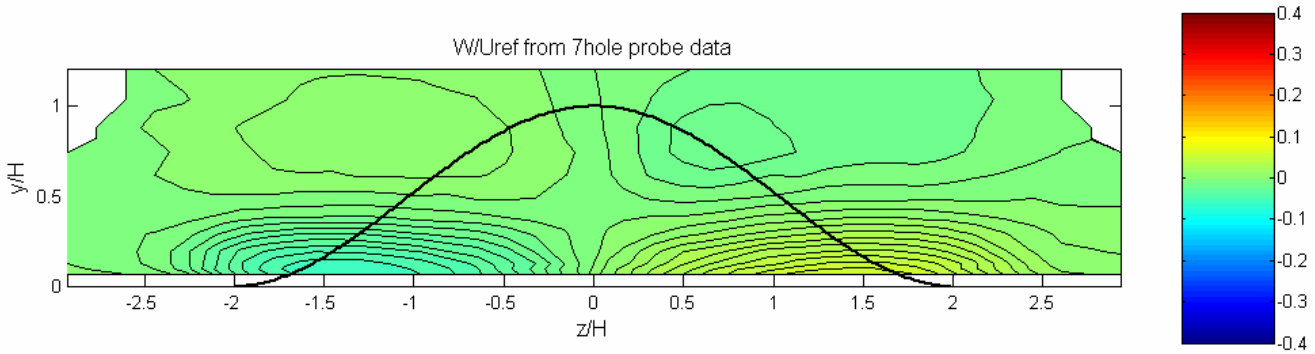

Figure 3.25: Normalized mean spanwise velocity component at x/H= 11.5 in the wake of small bump 3 measured with the seven-hole probe

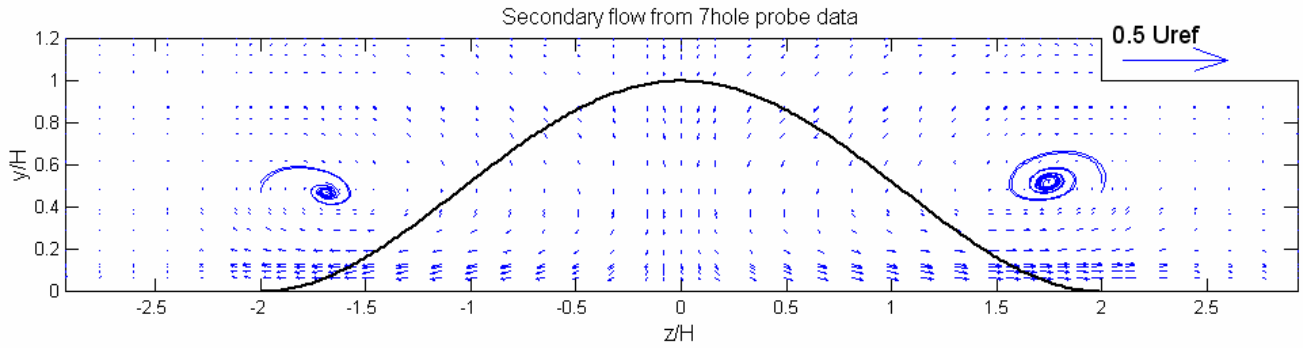

Figure 3.26: Secondary flow vector field at x/H= 11.5 in the wake of small bump 3 measured with the seven-hole probe

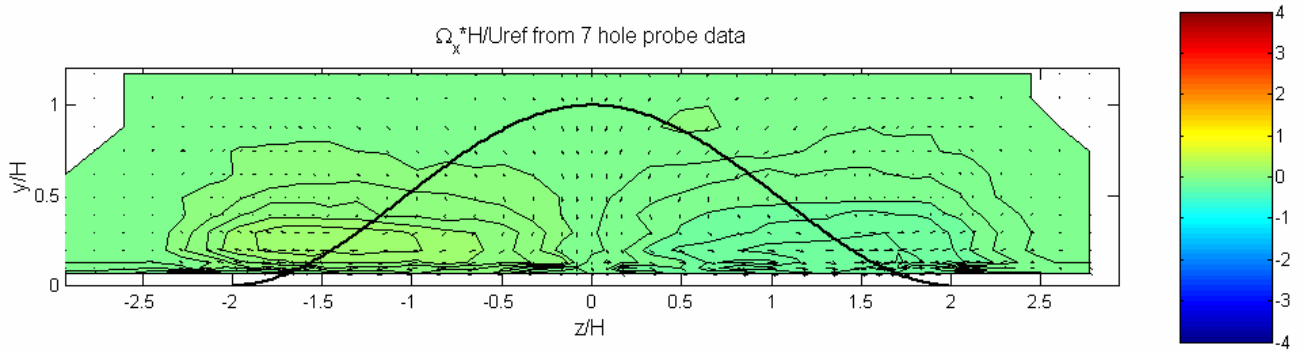

Figure 3.27: Normalized streamwise vorticity at x/H= 11.5 in the wake of small bump 3 measured with the seven-hole probe and secondary flow vectors

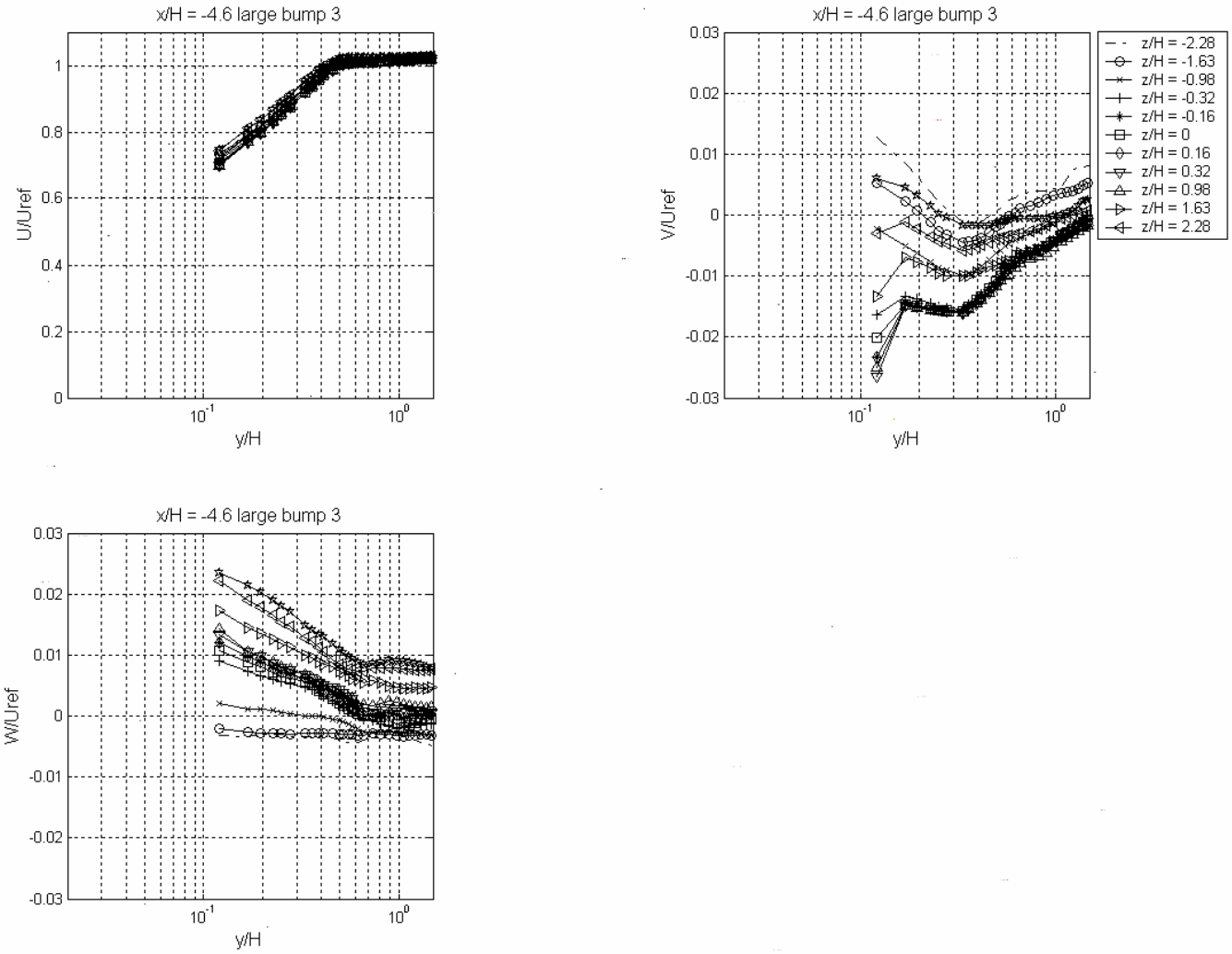

Figure 3.28: Normalized mean velocity components measured with the seven-hole probe at x/H = -4.6 upstream of large bump 3

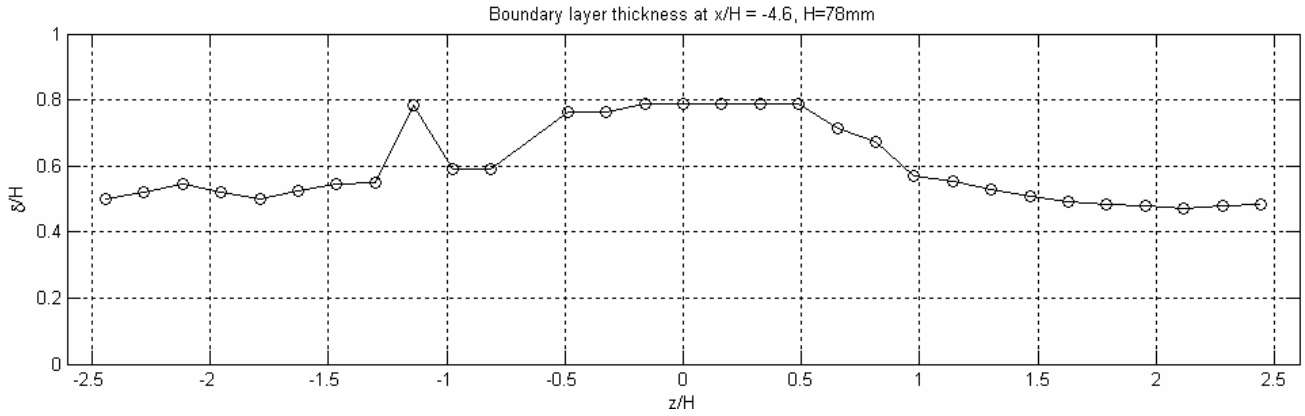

Figure 3.29: Variation of the boundary layer thickness δ_{99} with respect to the spanwise position at x/H = -4.6 upstream of large bump 3

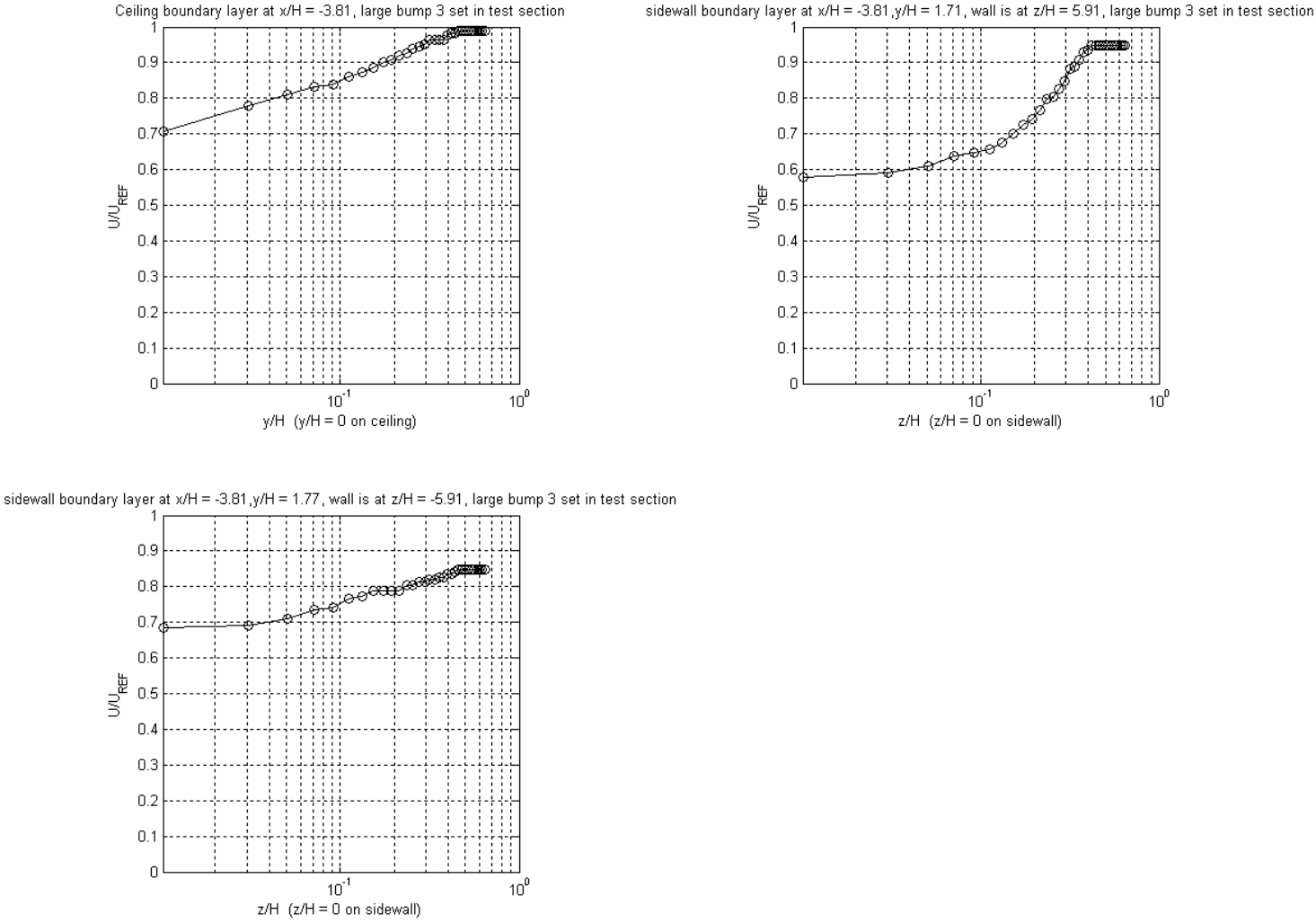

Figure 3.30: Ceiling and sidewalls boundary layer measurement using the sixteen-hole pressure rake

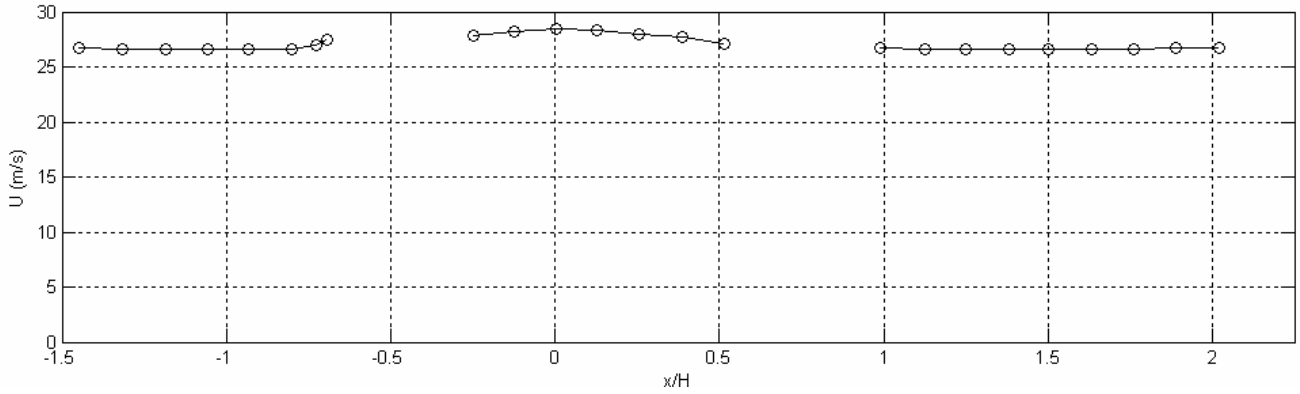

Figure 3.31: Centerline measurements (*y/H = 2.2*, *z/H = 0*) of the mean velocity magnitude measured by the Pitot-static probe when large bump 3 is set in the test-section

Table 3.2: Centerline measurements (*y/H = 2.2*, *z/H = 0*) of the mean velocity magnitude measured by the Pitot-static probe when large bump 3 is set in the test-section

position x/H	*U (m/s)*
-1.398429898	26.71796845
-1.265877301	26.63381715
-1.133324704	26.59164165
-1.007399737	26.59164165
-0.88147477	26.54939914
-0.748922173	26.54939914
-0.676018245	26.96884689
-0.642880095	27.4228303
-0.198828895	27.78875526
-0.072903928	28.18976813
0.053021039	28.46711616
0.178946006	28.34858498
0.304870973	27.98997987
0.43742357	27.66731802
0.563348537	27.13481059
1.037886834	26.75994486
1.175741535	26.63381715
1.297689924	26.59164165
1.430242521	26.59164165
1.552190911	26.54939914
1.684743508	26.54939914
1.811994001	26.59164165
1.939244494	26.67592598
2.071797091	26.71796845

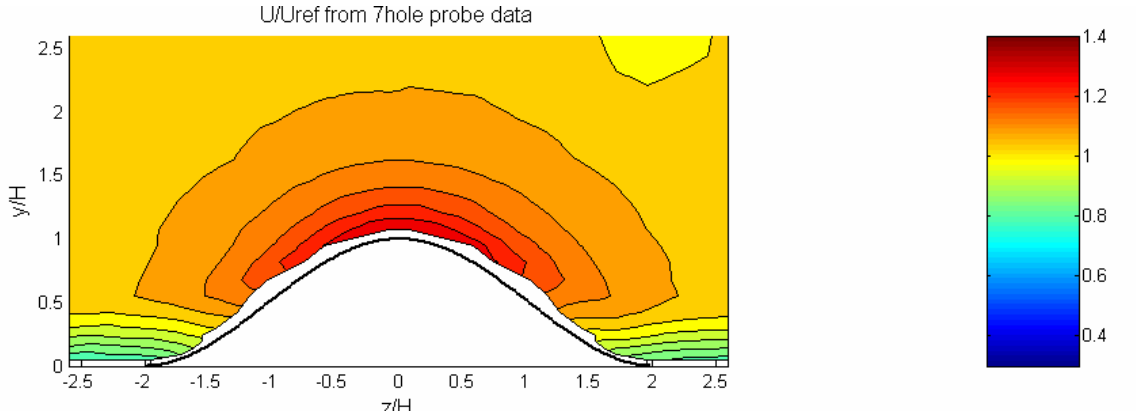

Figure 3.32: Normalized mean streamwise velocity component at x/H = 0 on large bump 3 measured with the seven-hole probe

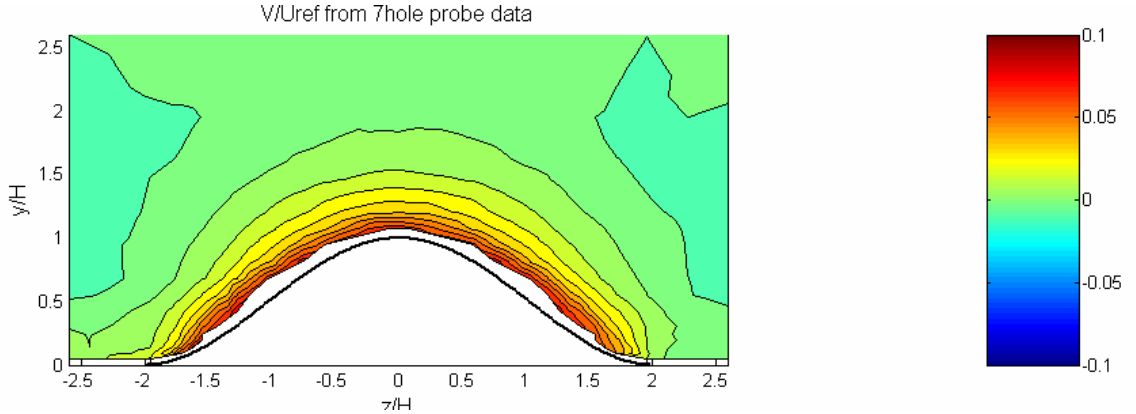

Figure 3.33: Normalized mean normal velocity component at x/H = 0 on large bump 3 measured with the seven-hole probe

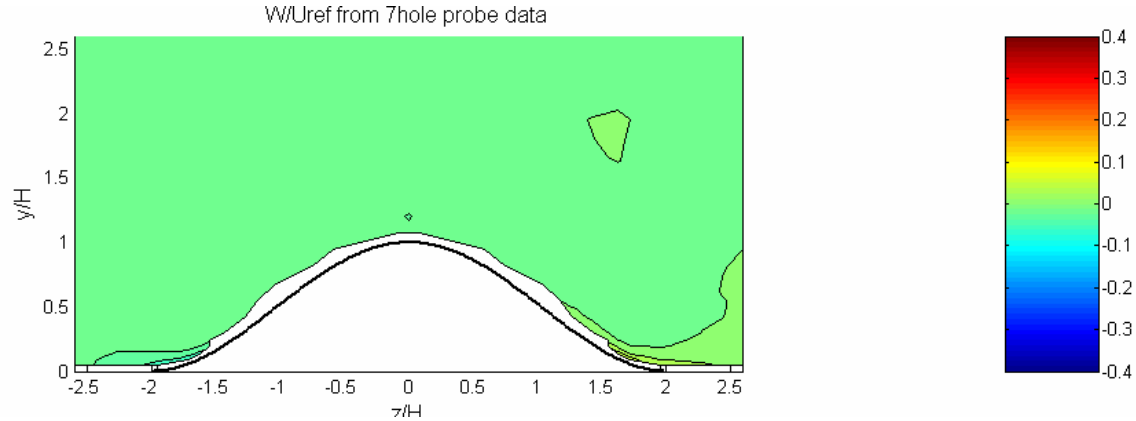

Figure 3.34: Normalized mean spanwise velocity component at x/H = 0 on large bump 3 measured with the seven-hole probe

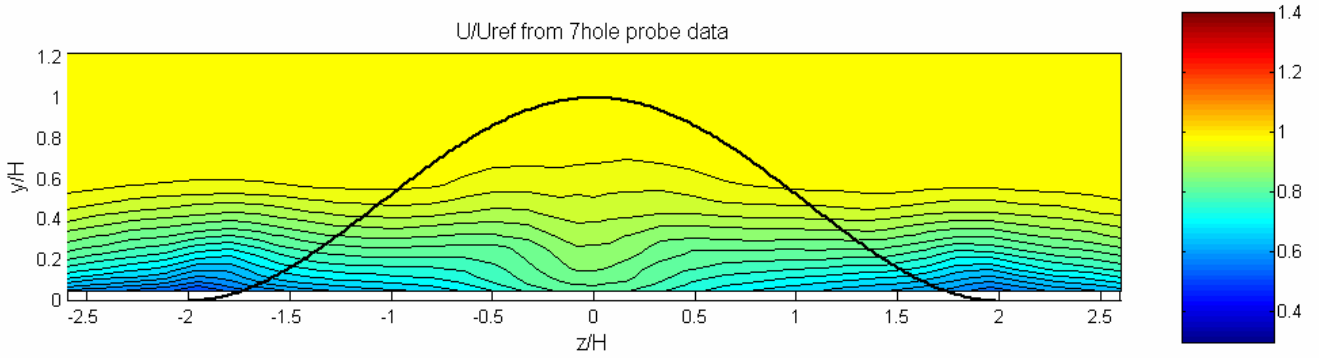

Figure 3.35: Normalized mean streamwise velocity component at x/H= 3.629 in the wake of large bump 3 measured with the seven-hole probe

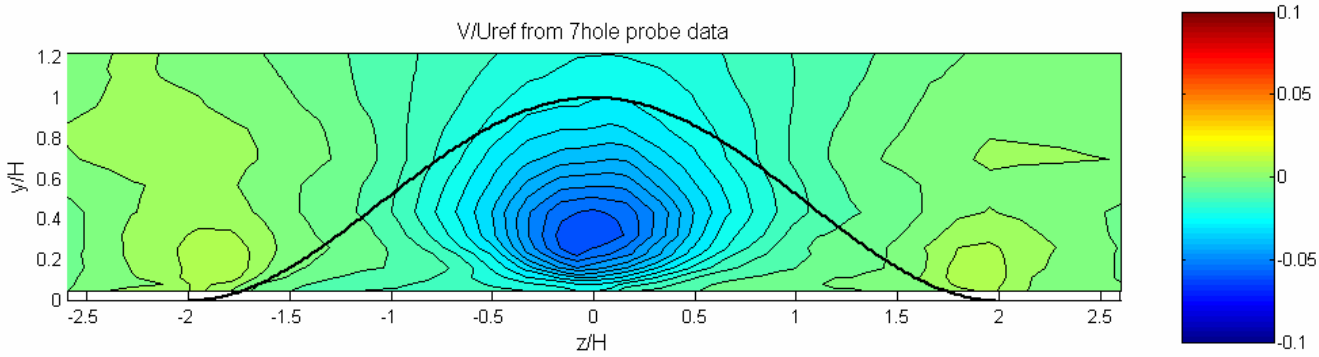

Figure 3.36: Normalized mean normal velocity component at x/H= 3.629 in the wake of large bump 3 measured with the seven-hole probe

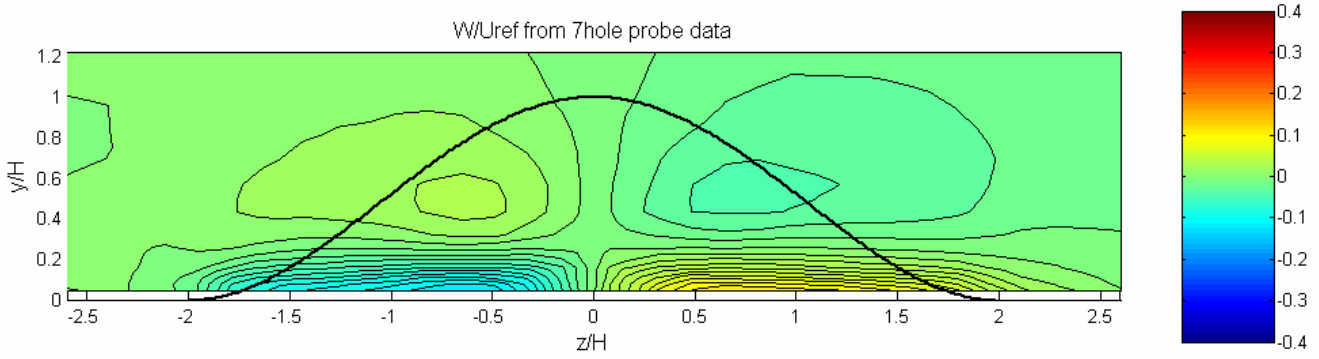

Figure 3.37: Normalized mean spanwise velocity component at x/H= 3.629 in the wake of large bump 3 measured with the seven-hole probe

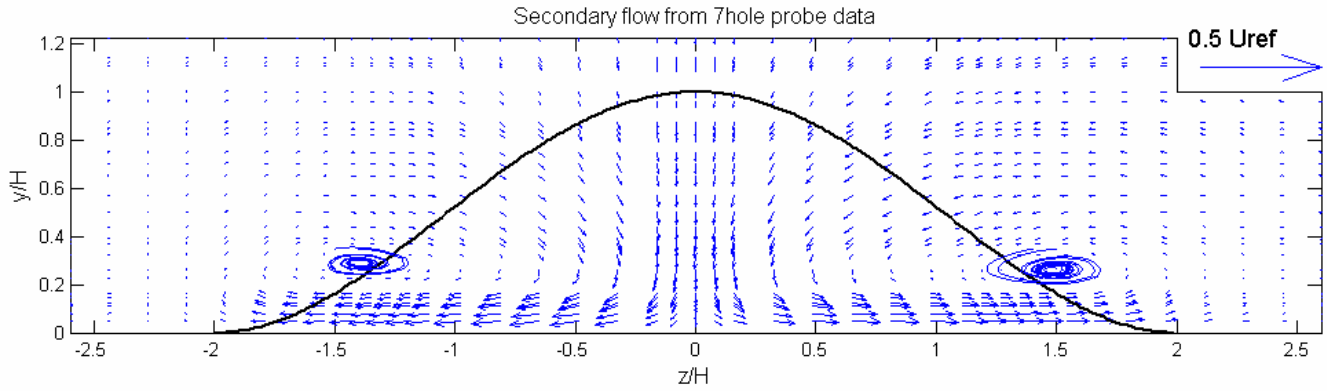

Figure 3.38: Secondary flow vector field at x/H= 3.629 in the wake of large bump 3 measured with the seven-hole probe

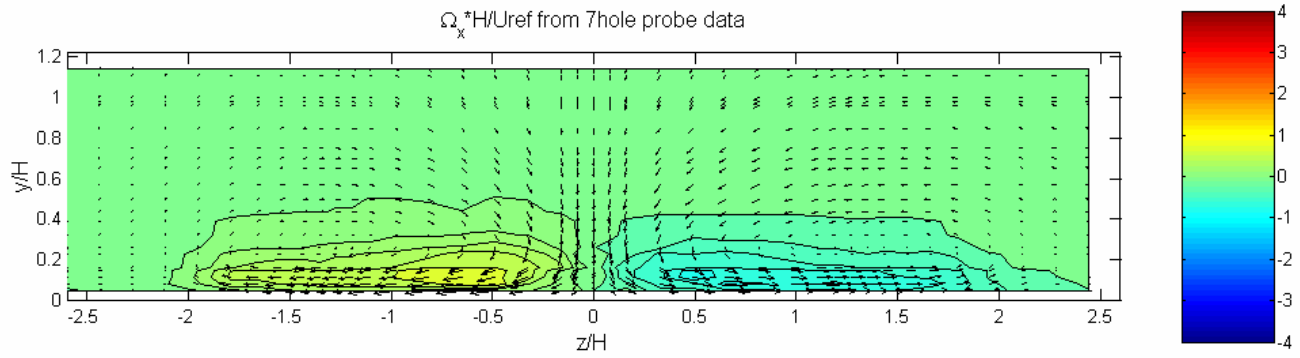

Figure 3.39: Normalized streamwise vorticity at x/H= 3.629 in the wake of large bump 3 measured with the seven-hole probe and secondary flow vectors

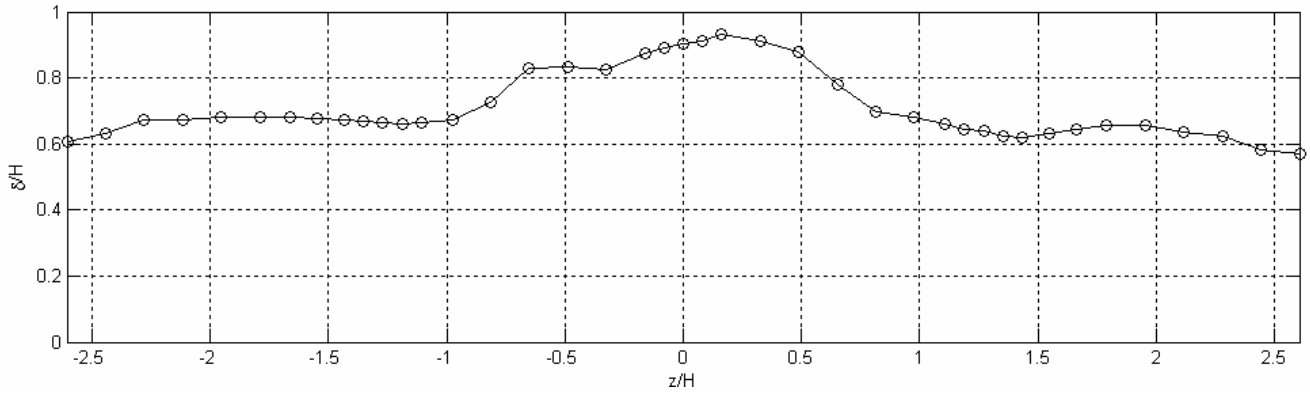

Figure 3.40: Variation of the boundary layer thickness on the span of the test section measured with the seven-hole probe in the wake of large bump 3 at x/H = 3.629

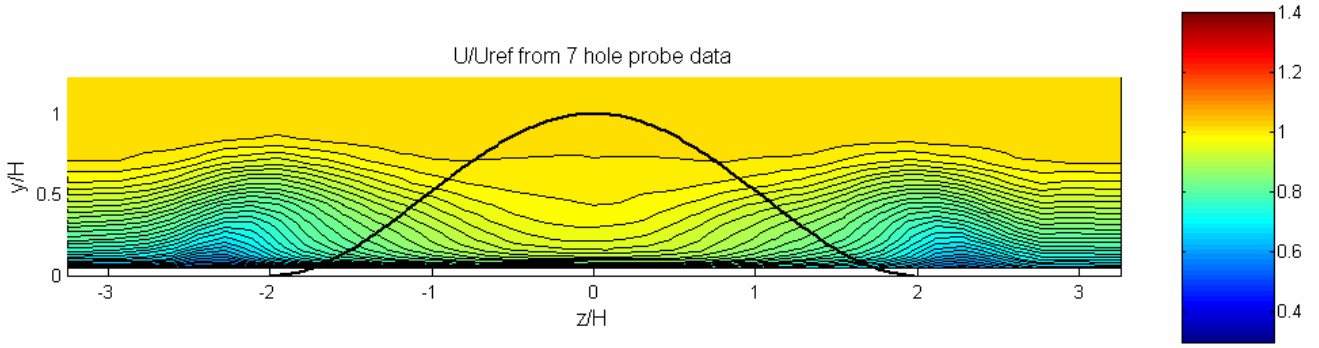

Figure 3.41: Normalized mean streamwise velocity component at x/H= 11.5 in the wake of large bump 3 measured with the seven-hole probe

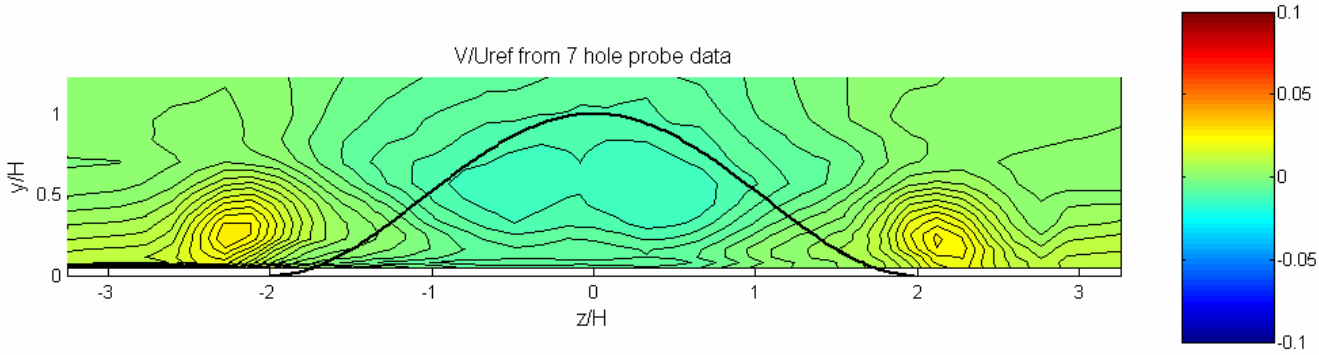

Figure 3.42: Normalized mean normal velocity component at x/H= 11.5 in the wake of large bump 3 measured with the seven-hole probe

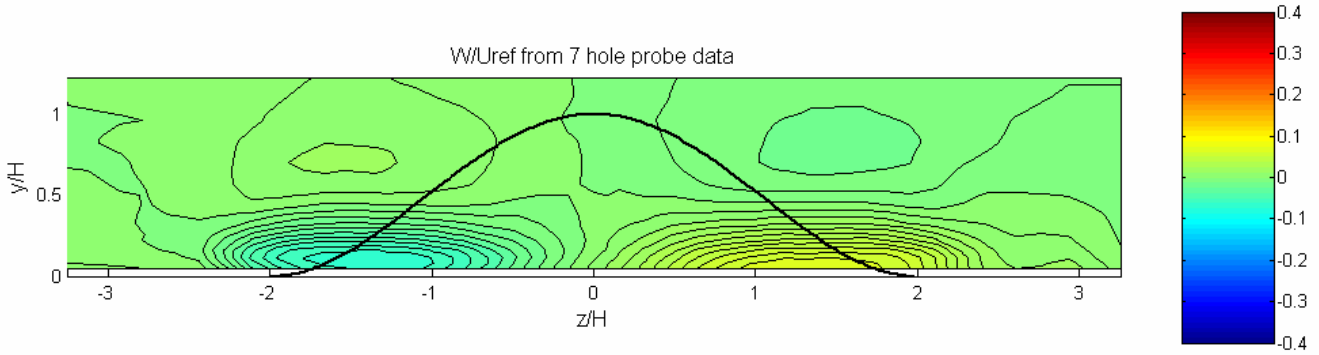

Figure 3.43: Normalized mean spanwise velocity component at x/H= 11.5 in the wake of large bump 3 measured with the seven-hole probe

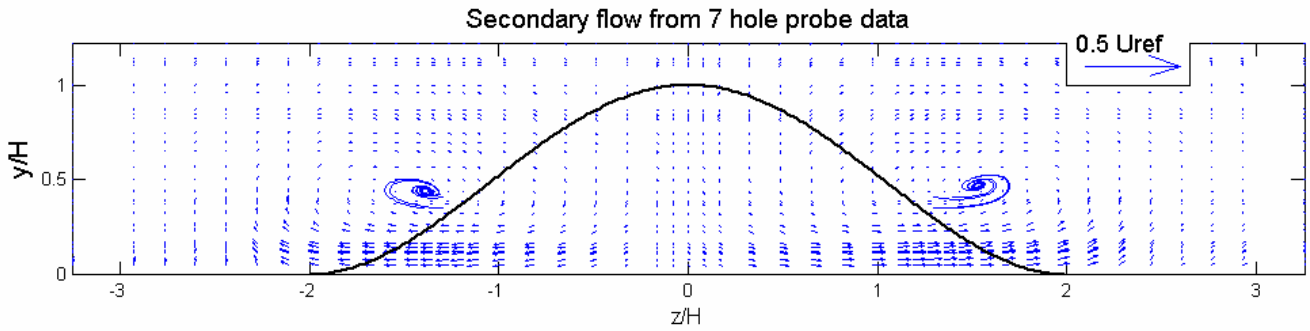

Figure 3.44: Secondary flow vector field at x/H= 11.5 in the wake of large bump 3 measured with the seven-hole probe

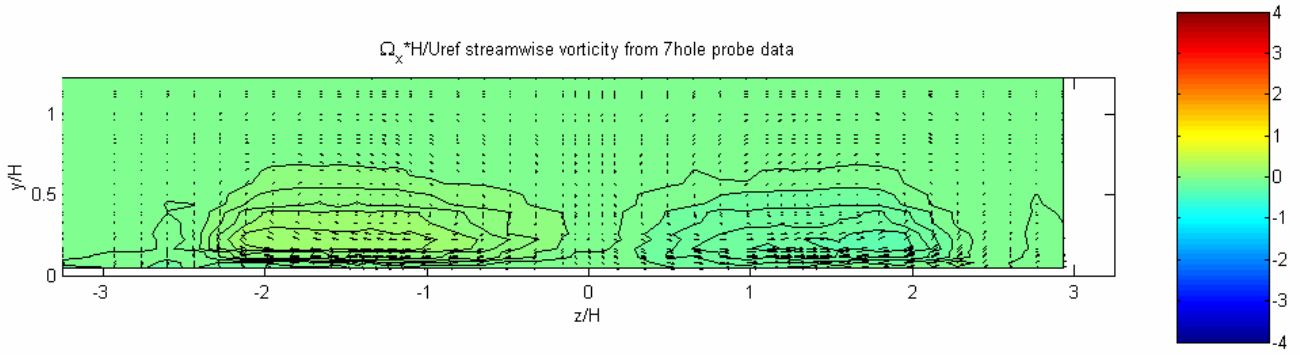

Figure 3.45: Normalized streamwise vorticity at x/H= 11.5 in the wake of large bump 3 measured with the seven-hole probe and secondary flow vectors

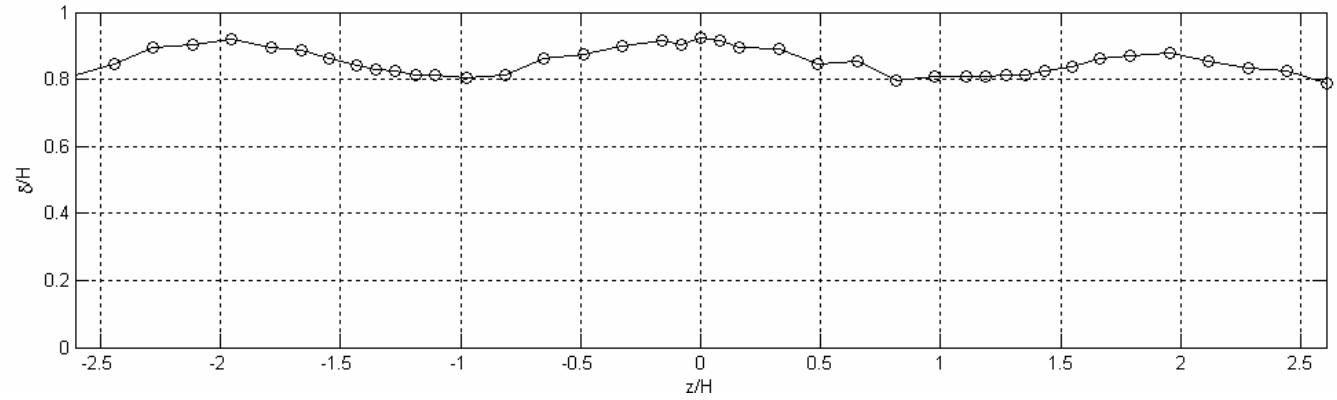

Figure 3.46: Variation of the boundary layer thickness on the span of the test section measured with the seven-hole probe in the wake of large bump 3 at x/H = 11.5

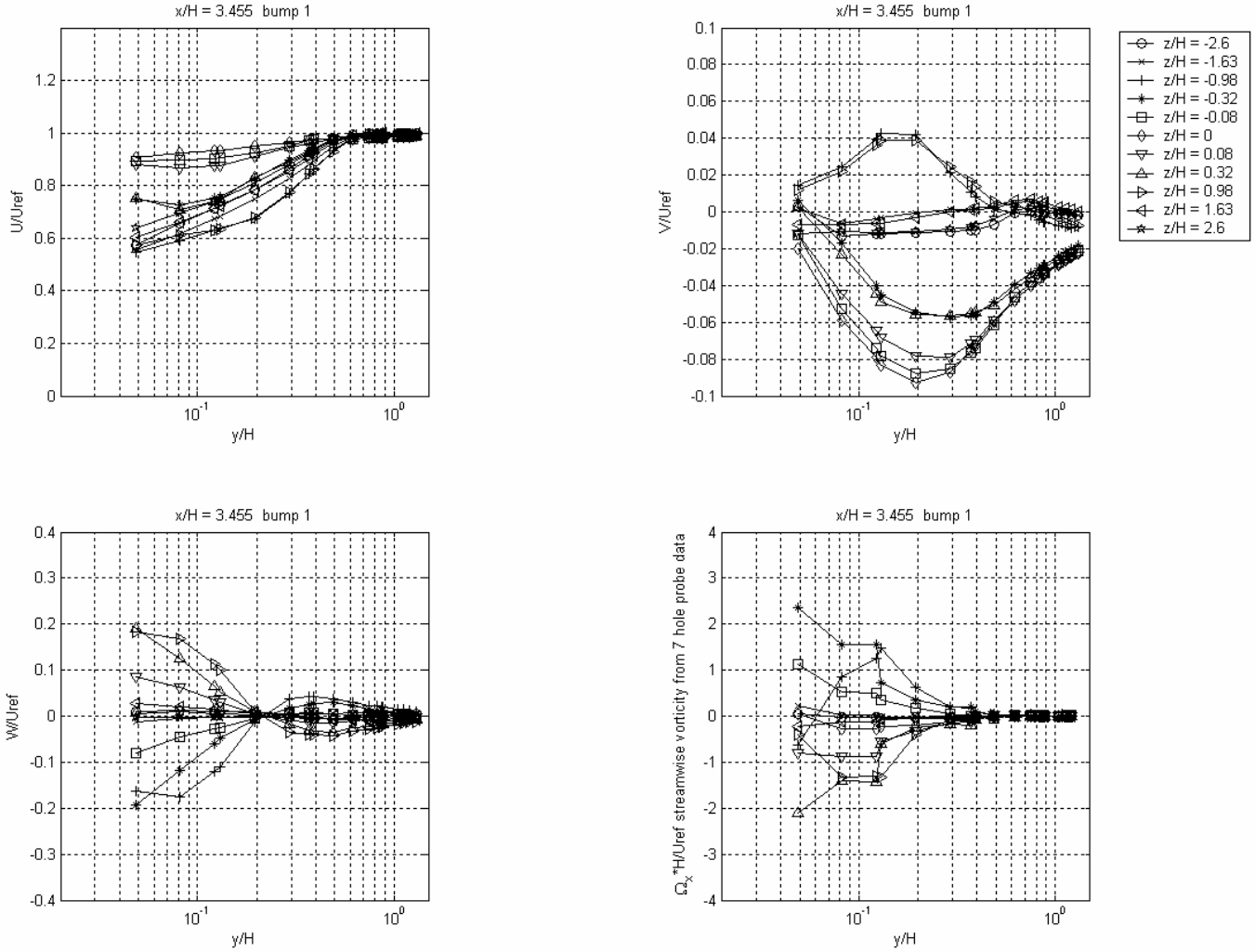

Figure 3.47: Components of the velocity vector and streamwise vorticity measured with the seven-hole probe in the wake of bump 1 at x/H = 3.455

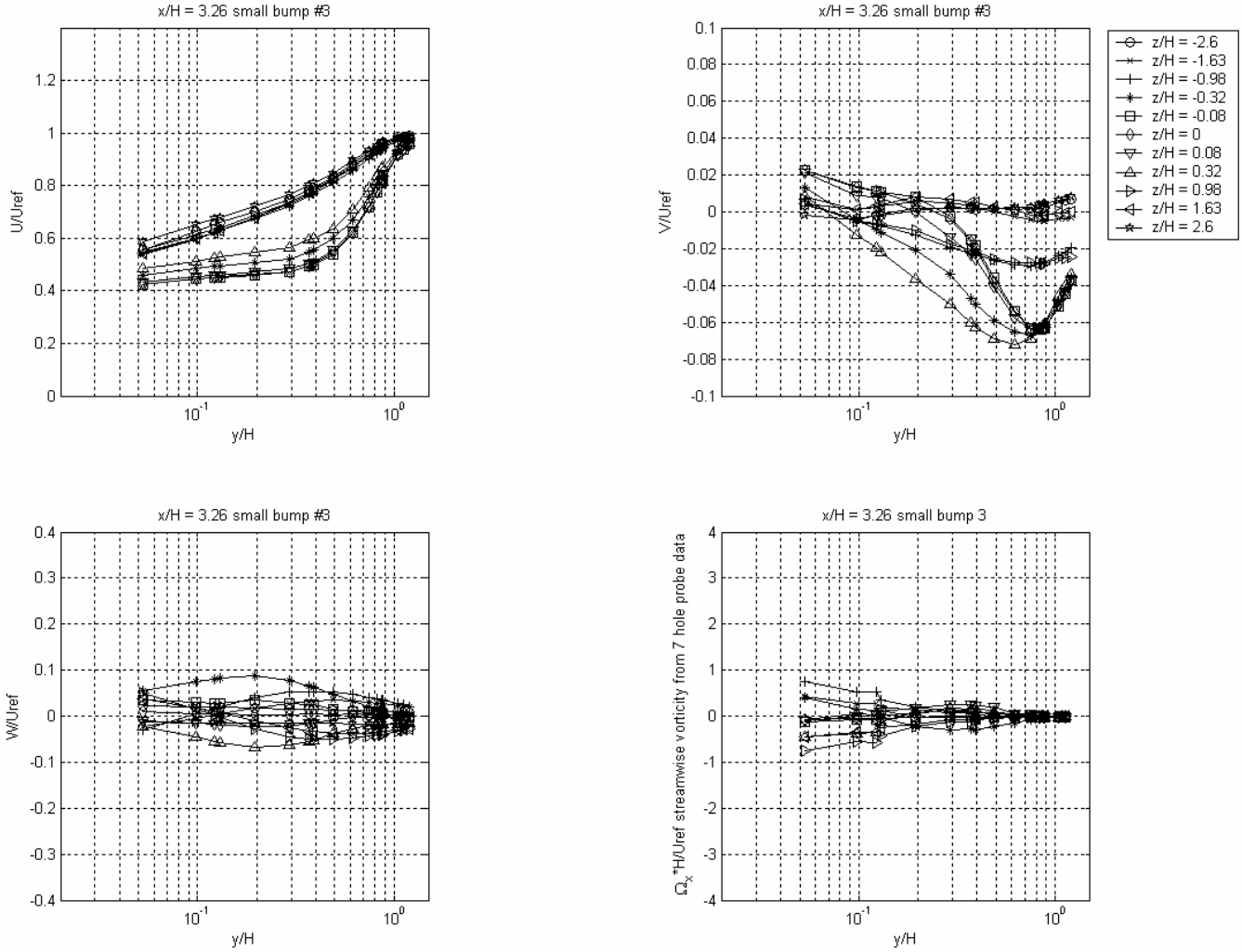

Figure 3.48: Components of the velocity vector and streamwise vorticity measured with the seven-hole probe in the wake of small bump 3 at x/H = 3.26

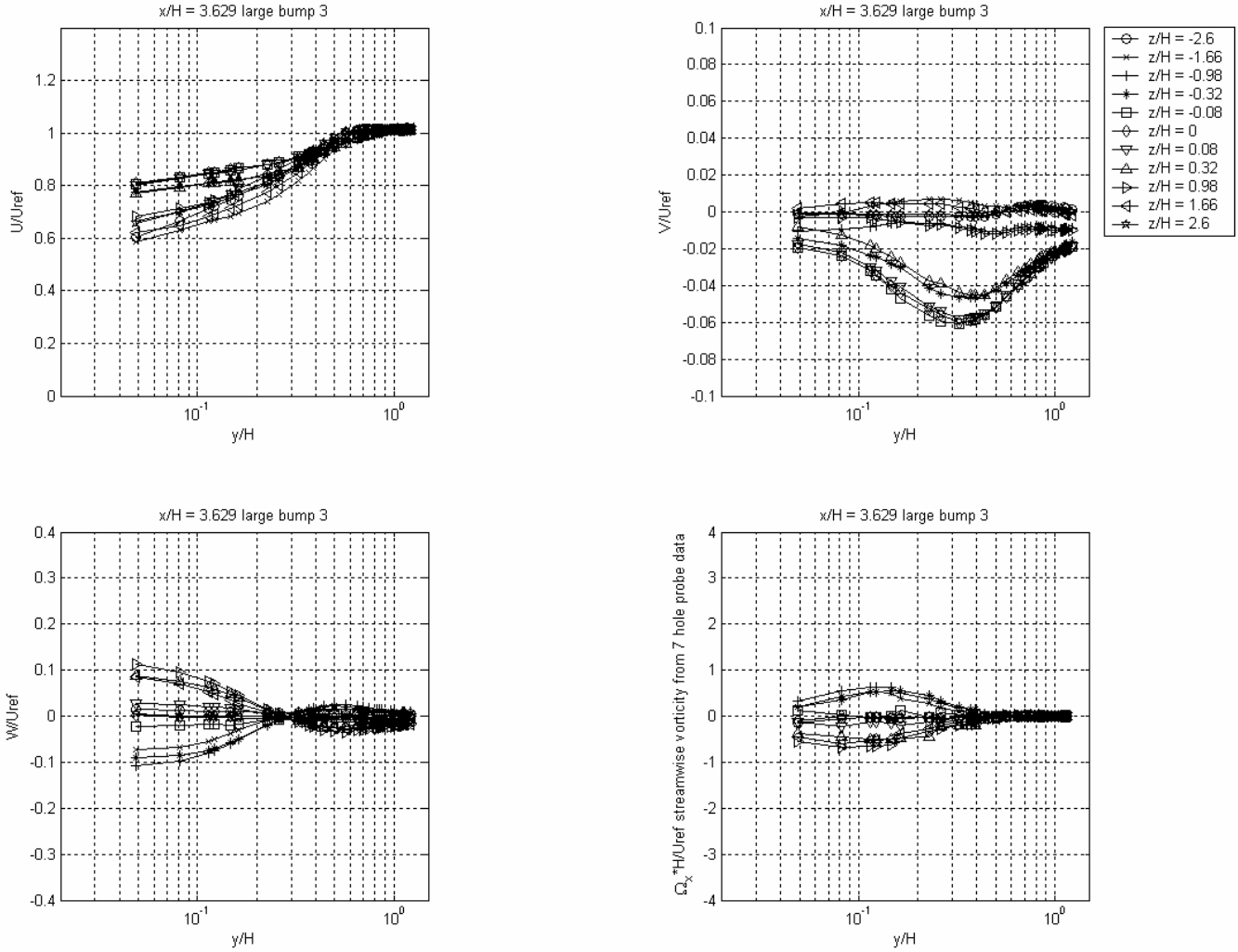

Figure 3.49: Components of the velocity vector and streamwise vorticity measured with the seven-hole probe in the wake of large bump 3 at x/H=3.629

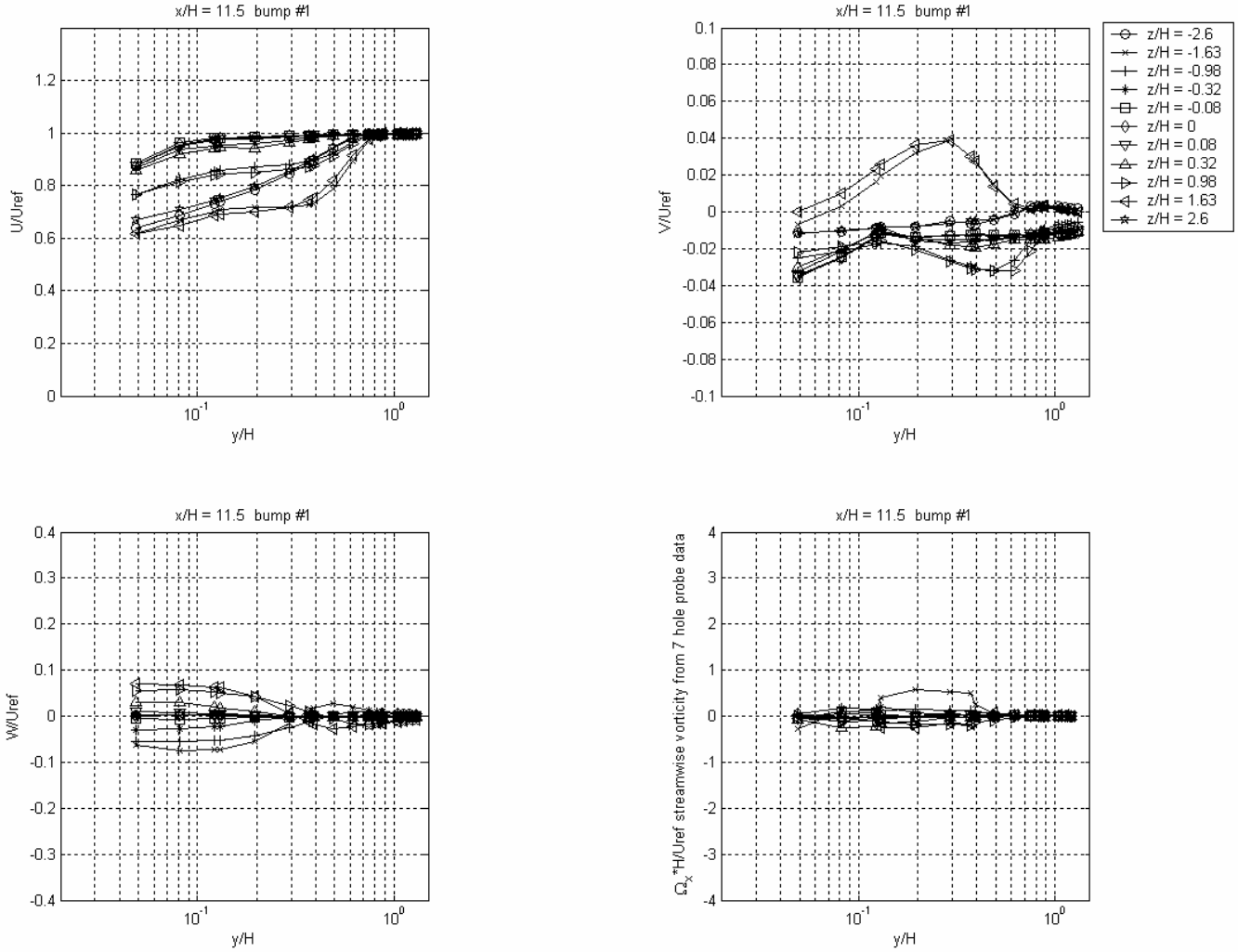

Figure 3.50: Components of the velocity vector and streamwise vorticity measured with the seven-hole probe in the wake of bump 1 at x/H = 11.5

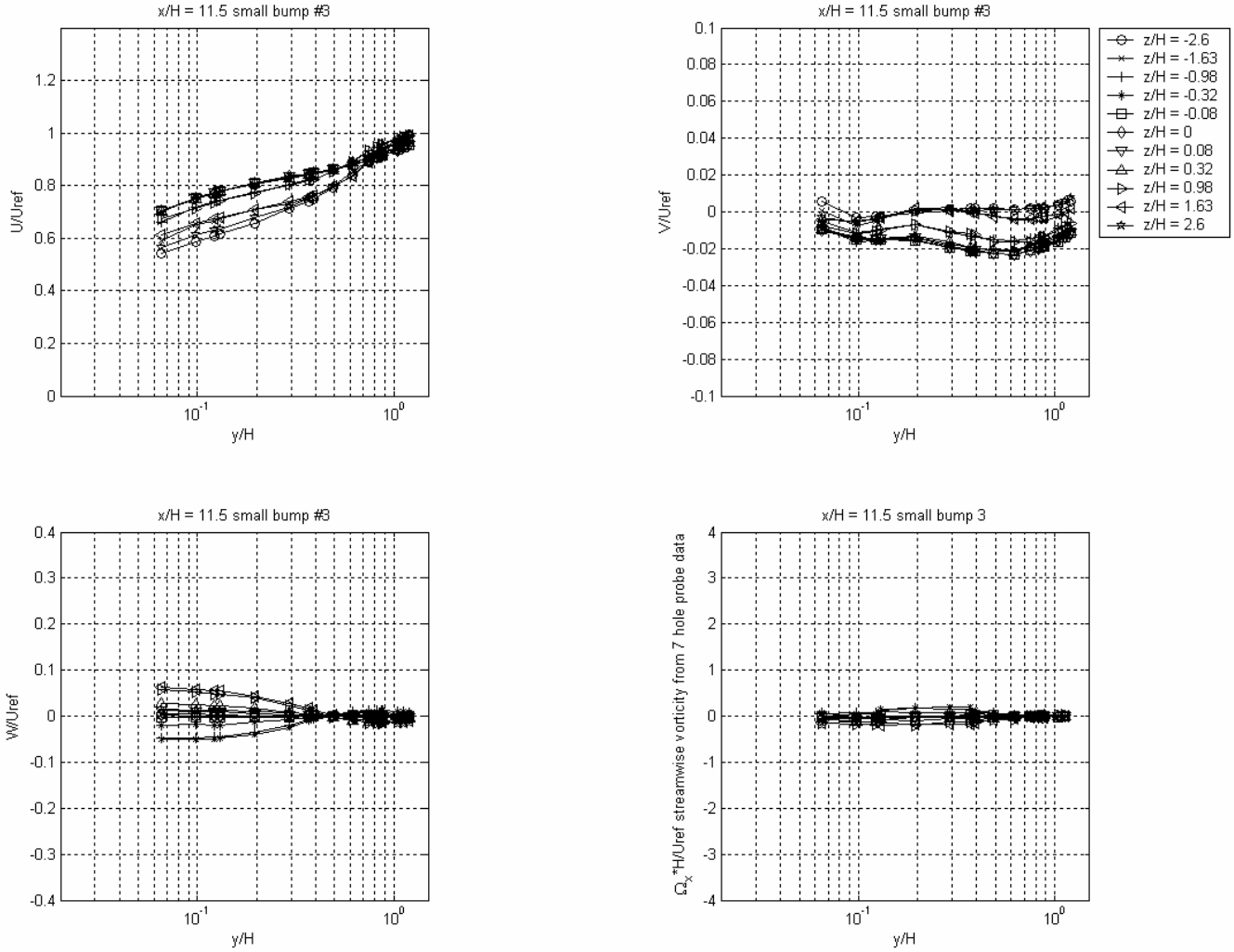

Figure 3.51: Components of the velocity vector and streamwise vorticity measured with the seven-hole probe in the wake of small bump 3 at x/H = 11.5

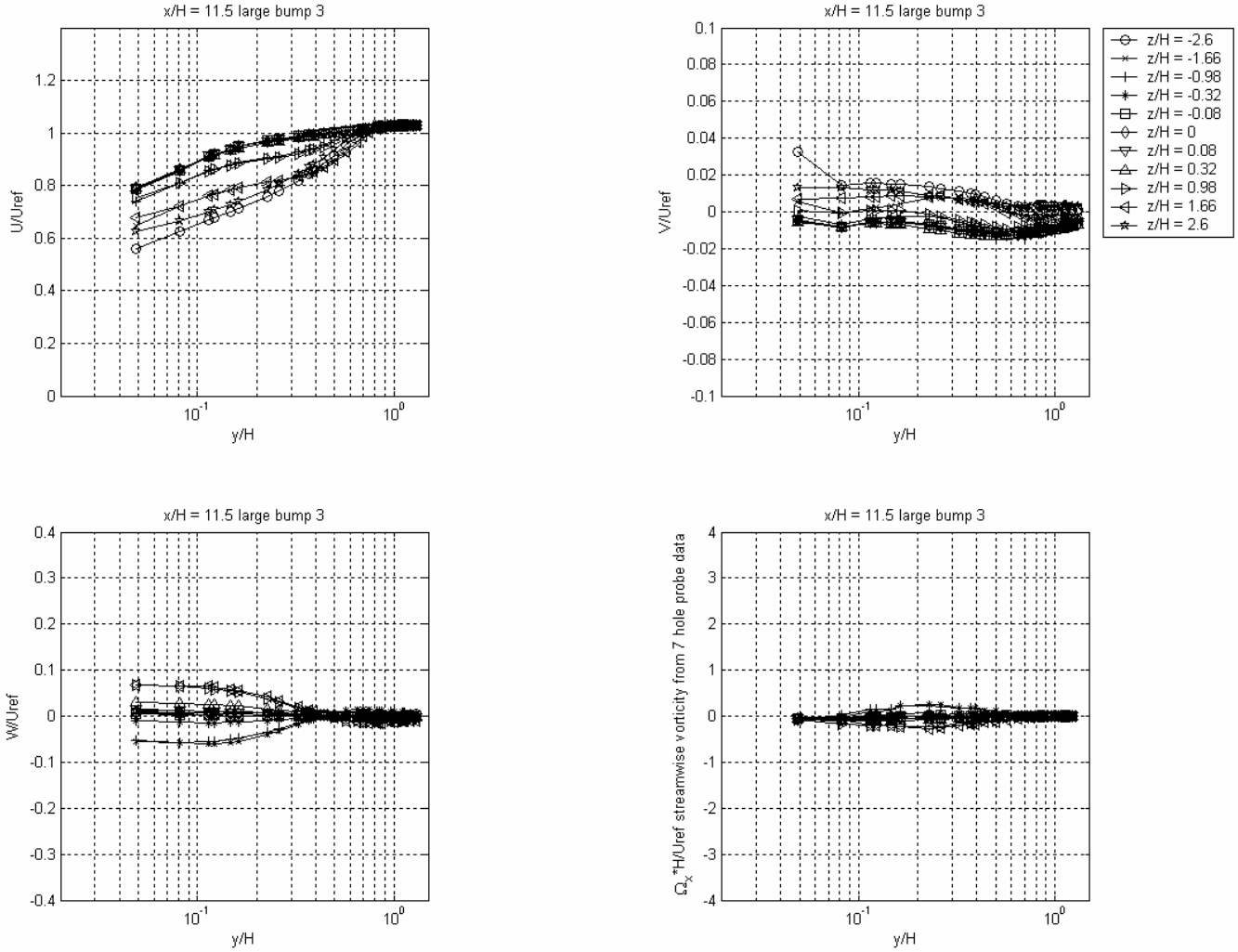

Figure 3.52: Components of the velocity vector and streamwise vorticity measured with the seven-hole probe in the wake of large bump 3 at x/H = 11.5

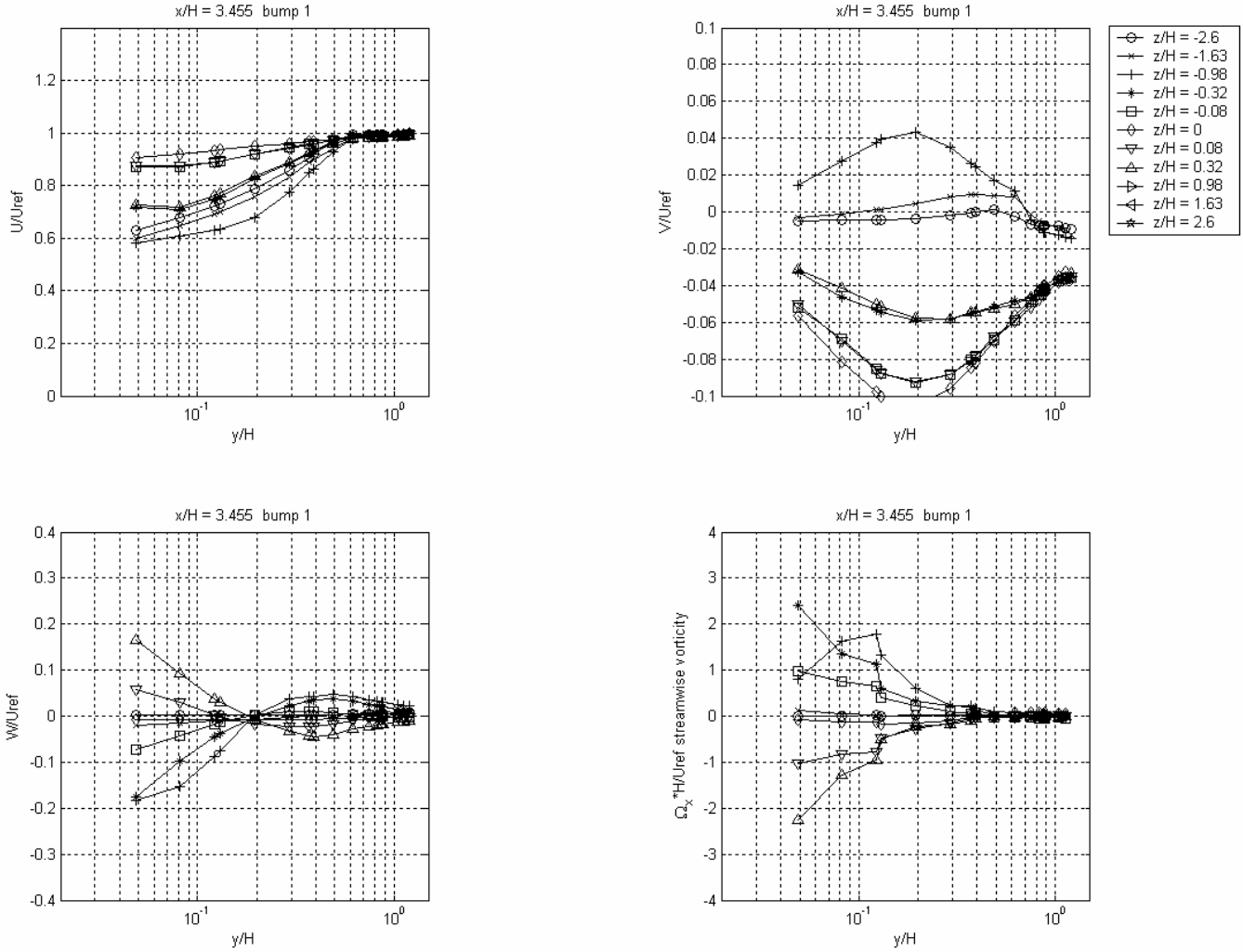

Figure 3.53: Components of the velocity vector and streamwise vorticity measured with LDV by Byun et *al.* (2004) in the wake of bump 1 at x/H = 3.455

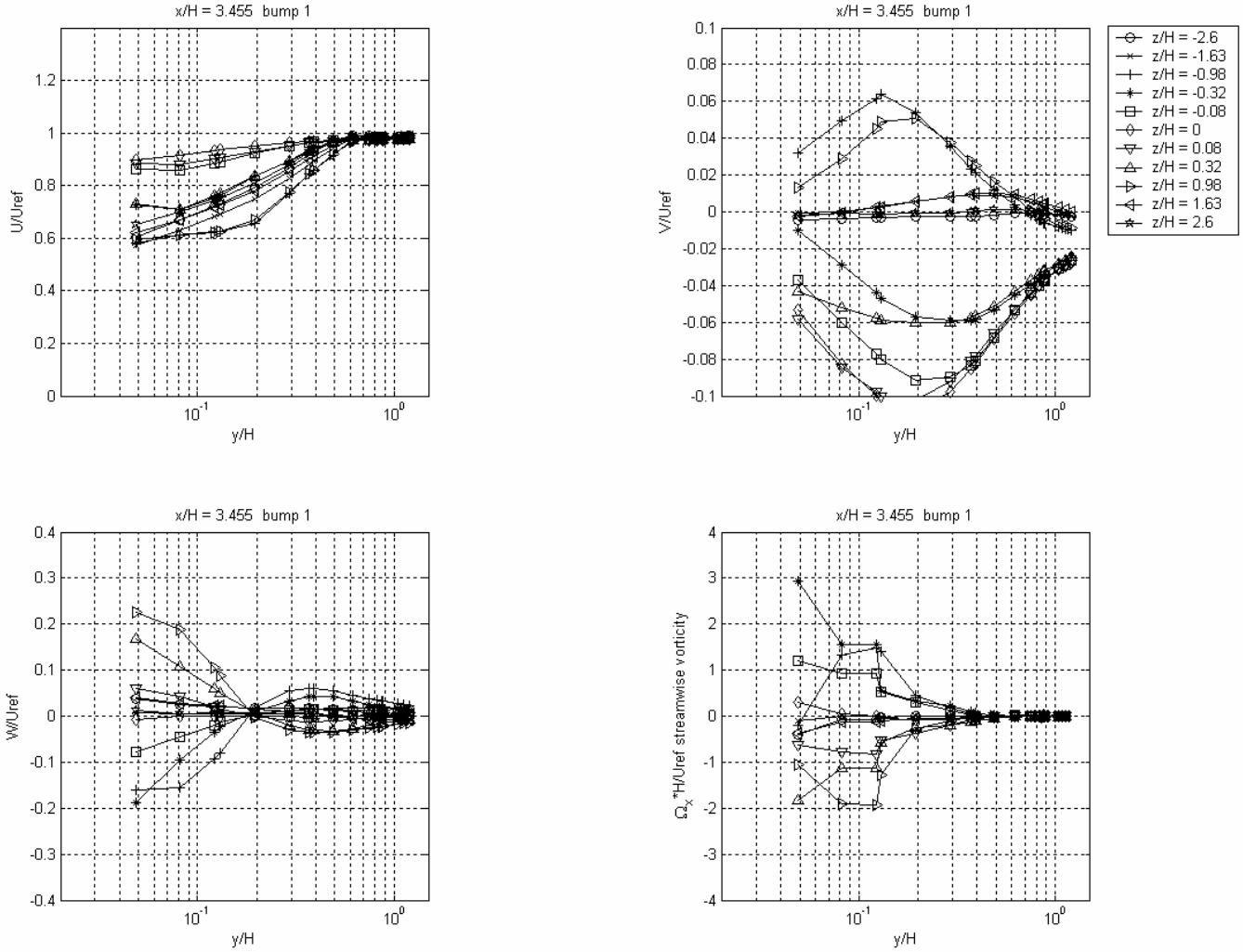

Figure 3.54: Components of the velocity vector and streamwise vorticity measured with quad-wire hot-wire by Ma and Simpson (2004) in the wake of bump 1 at x/H = 3.455

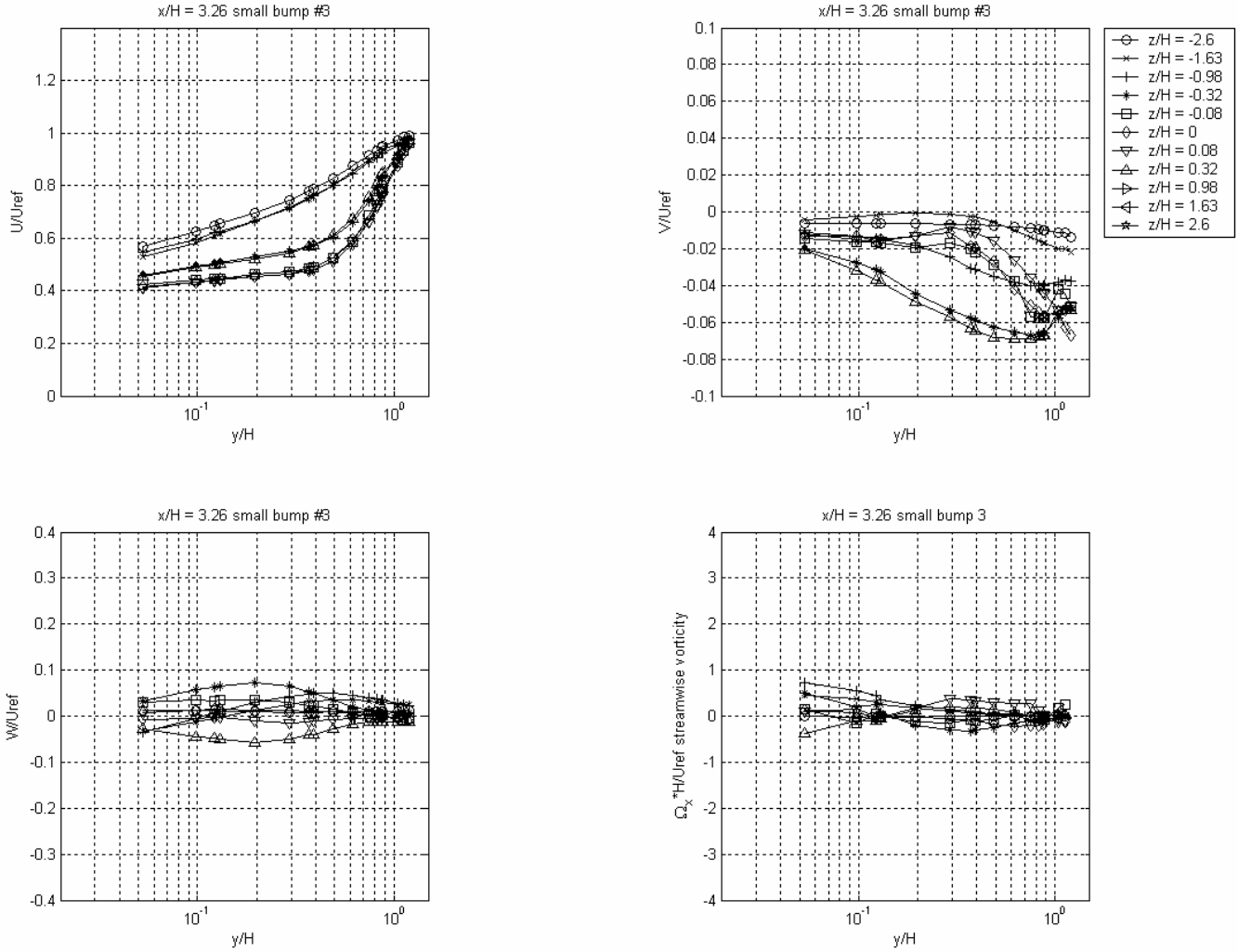

Figure 3.55: Components of the velocity vector and streamwise vorticity measured with LDV by Byun et *al.* (2004) in the wake of small bump 3 at x/H = 3.26

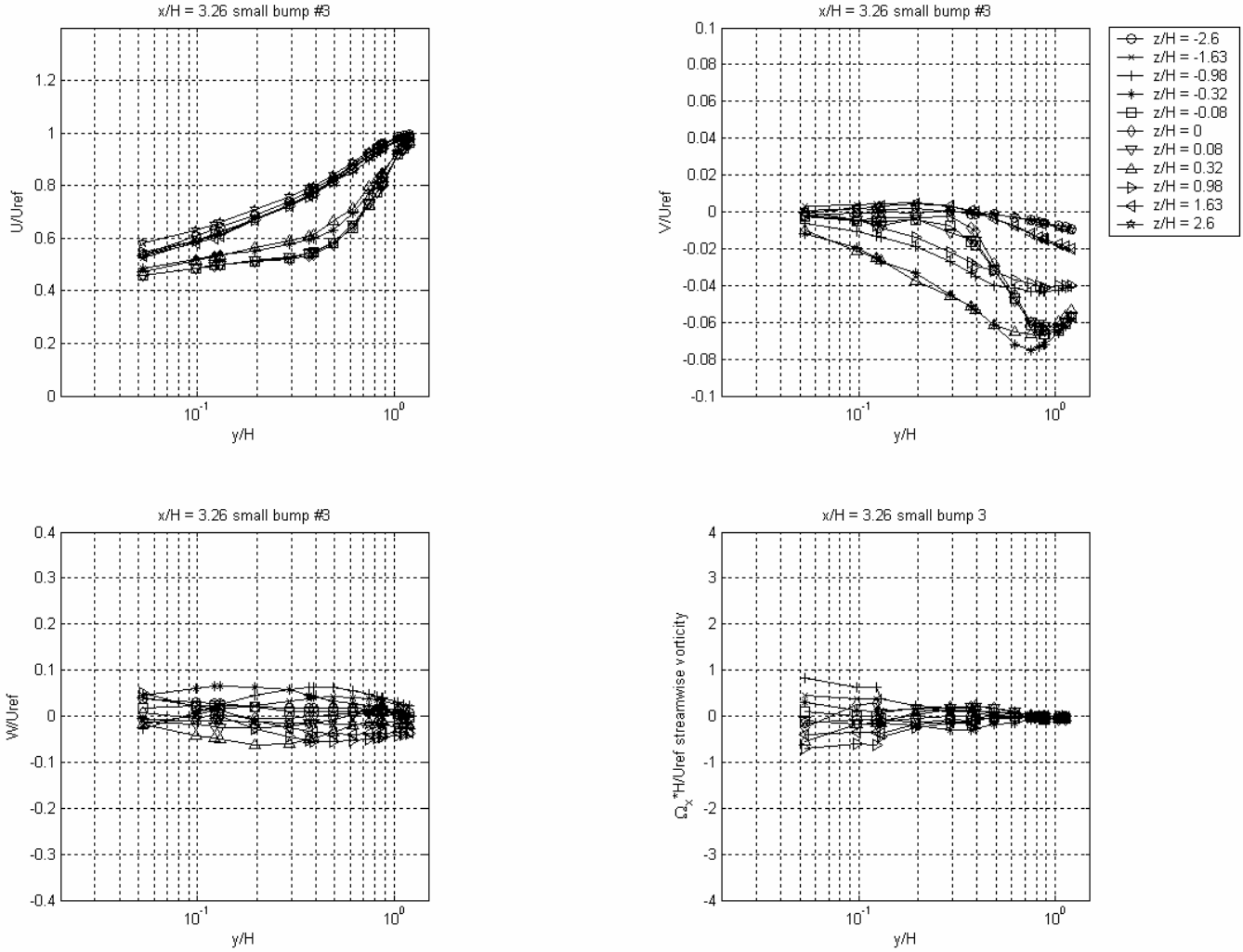

Figure 3.56: Components of the velocity vector and streamwise vorticity measured with quad-wire hot-wire by Ma and Simpson (2004) in the wake of small bump 3 at x/H = 3.26

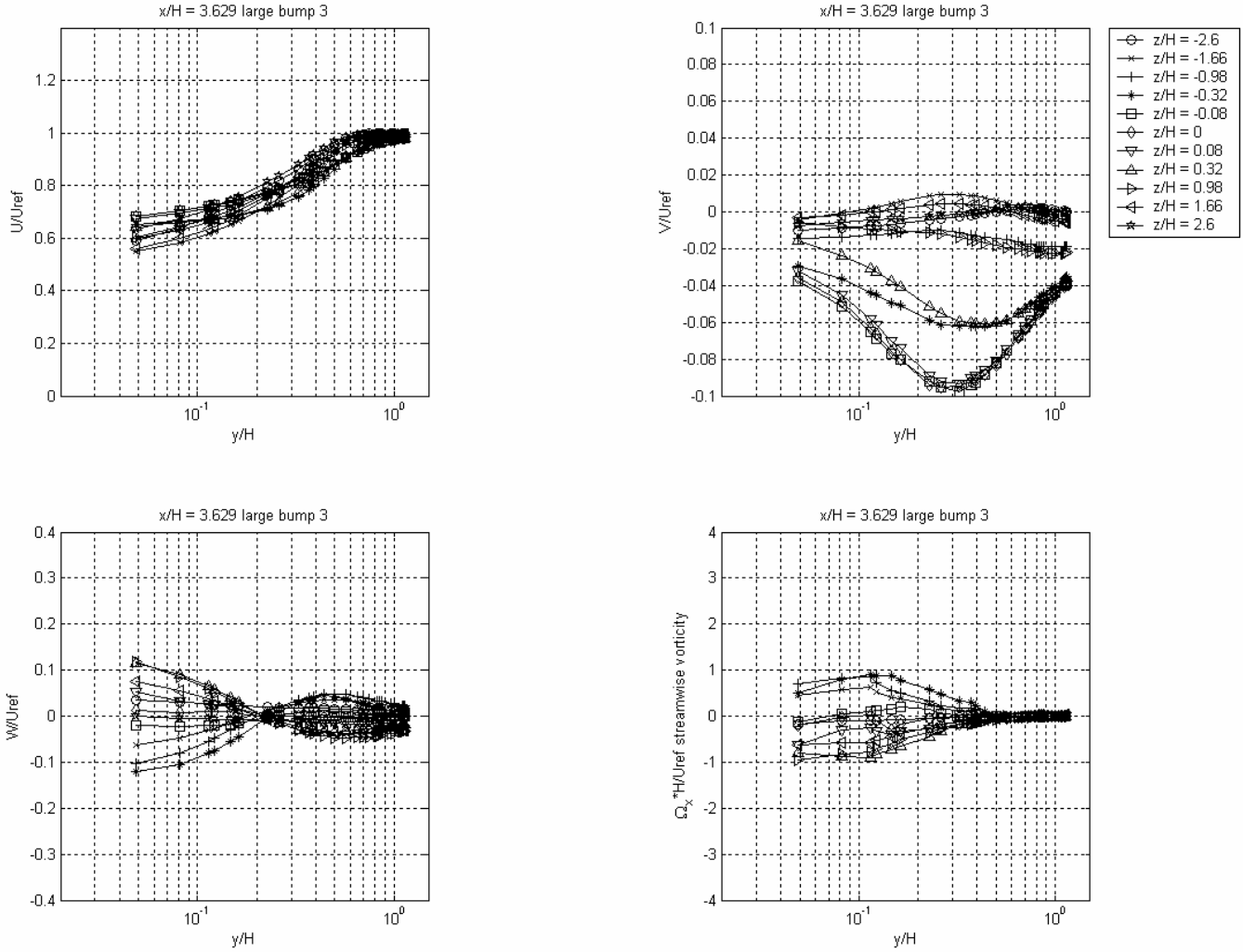

Figure 3.57: Components of the velocity vector and streamwise vorticity measured with quad-wire hot-wire by Ma and Simpson (2004) in the wake of large bump 3 at x/H = 3.629

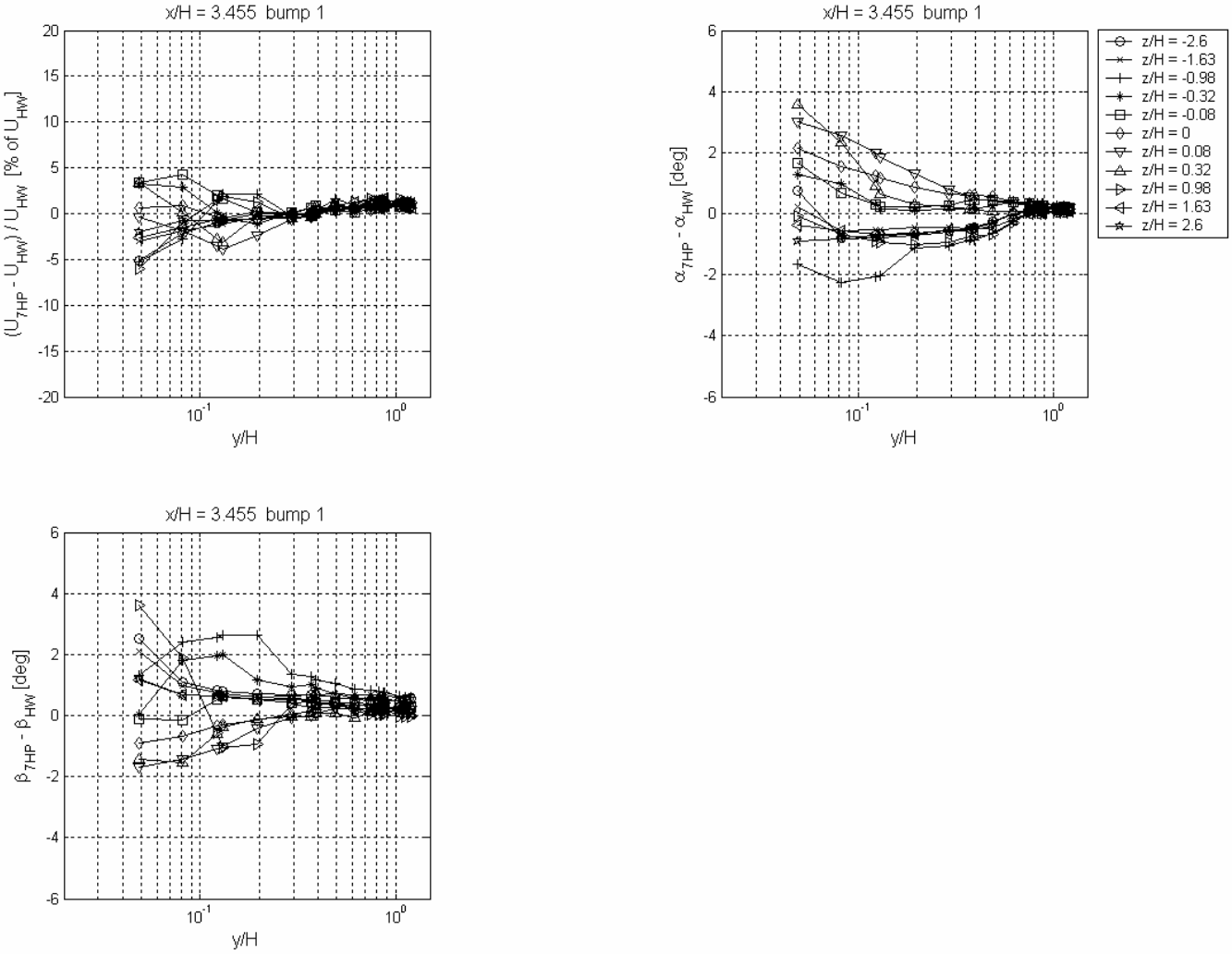

Figure 3.58: Bias-errors of the mean velocity magnitude (equation 3.6) and of the flow angles (equations 3.7) calculated with respect to hot-wire measurements by Ma and Simpson (2004) in the wake of bump 1 *at x/H* = 3.455

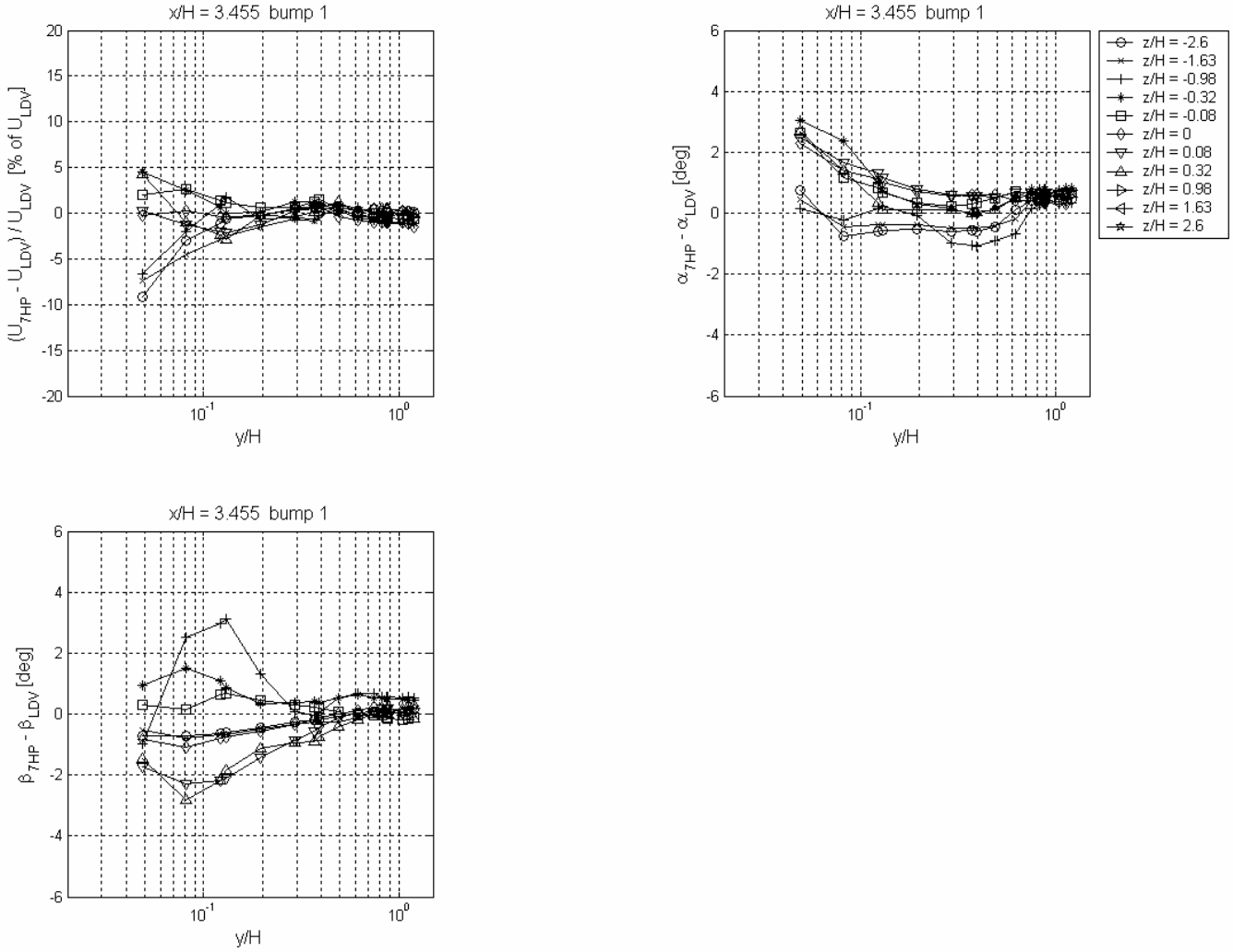

Figure 3.59: Bias-errors of the mean velocity magnitude (equation 3.6) and of the flow angles (equations 3.7) calculated with respect to LDV measurements by Byun et *al.* (2004) in the wake of bump 1 at x/H = 3.455

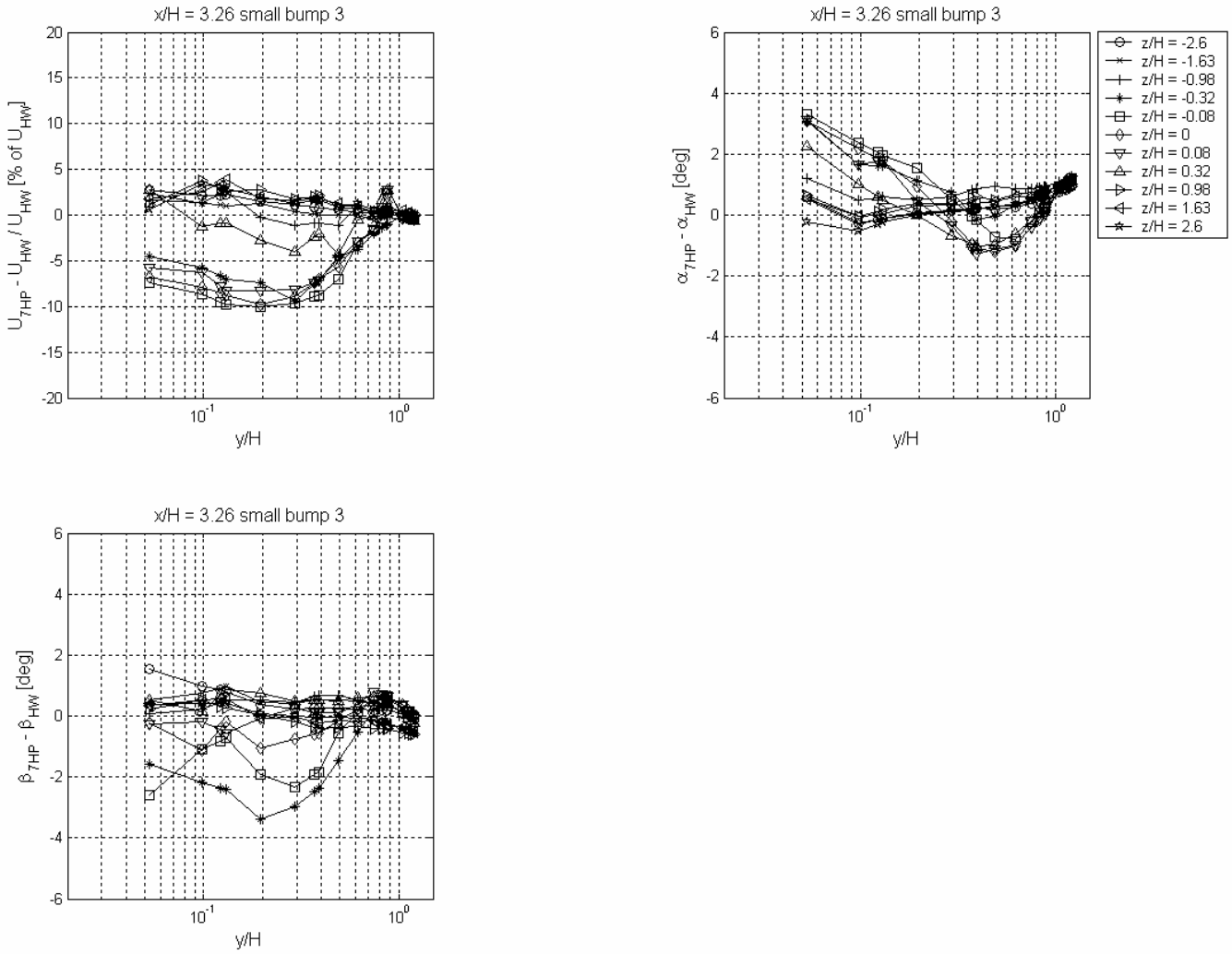

Figure 3.60: Bias-errors of the mean velocity magnitude (equation 3.6) and of the flow angles (equations 3.7) calculated with respect to hot-wire measurements by Ma and Simpson (2004) in the wake of small bump 3 at *x/H* = 3.26

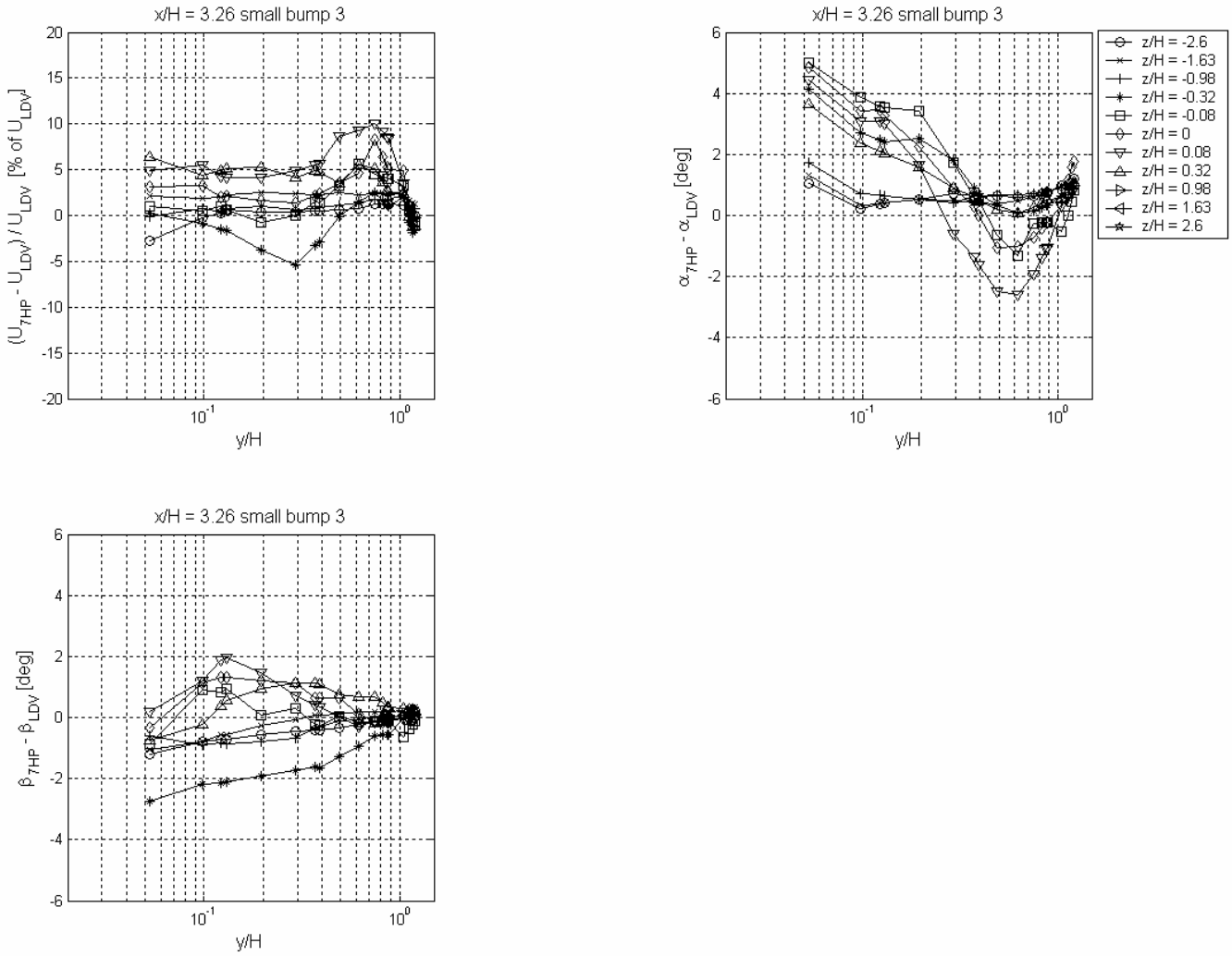

Figure 3.61: Bias-errors of the mean velocity magnitude (equation 3.6) and of the flow angles (equations 3.7) calculated with respect to LDV measurements by Byun et *al.* (2004) in the wake of small bump 3 at *x/H* = 3.26

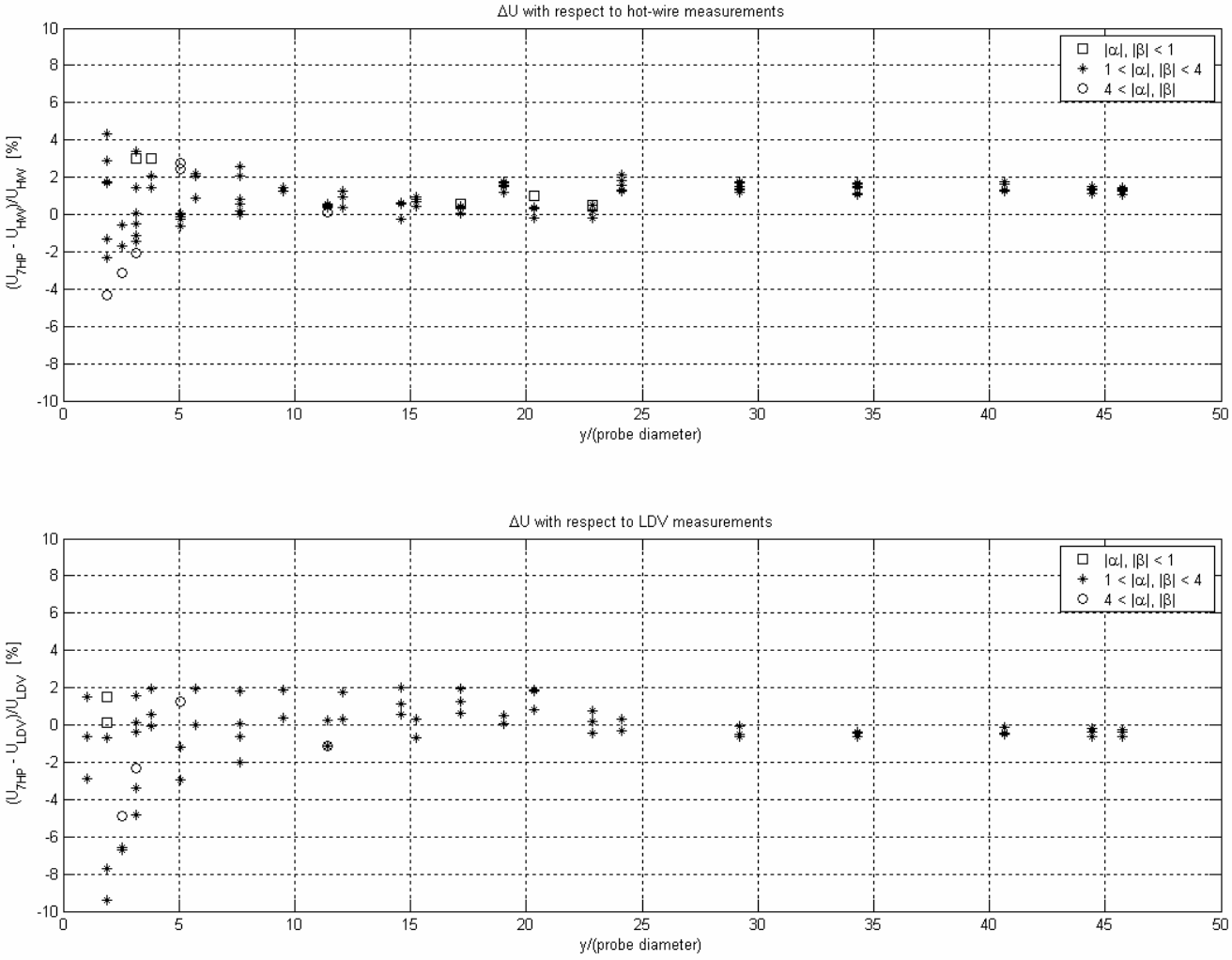

Figure 3.62: Bias-errors in the mean velocity magnitude calculated with respect to LDV and hot-wire measurements in the wakes of bump 1 and small bump 3 as a function of vertical position

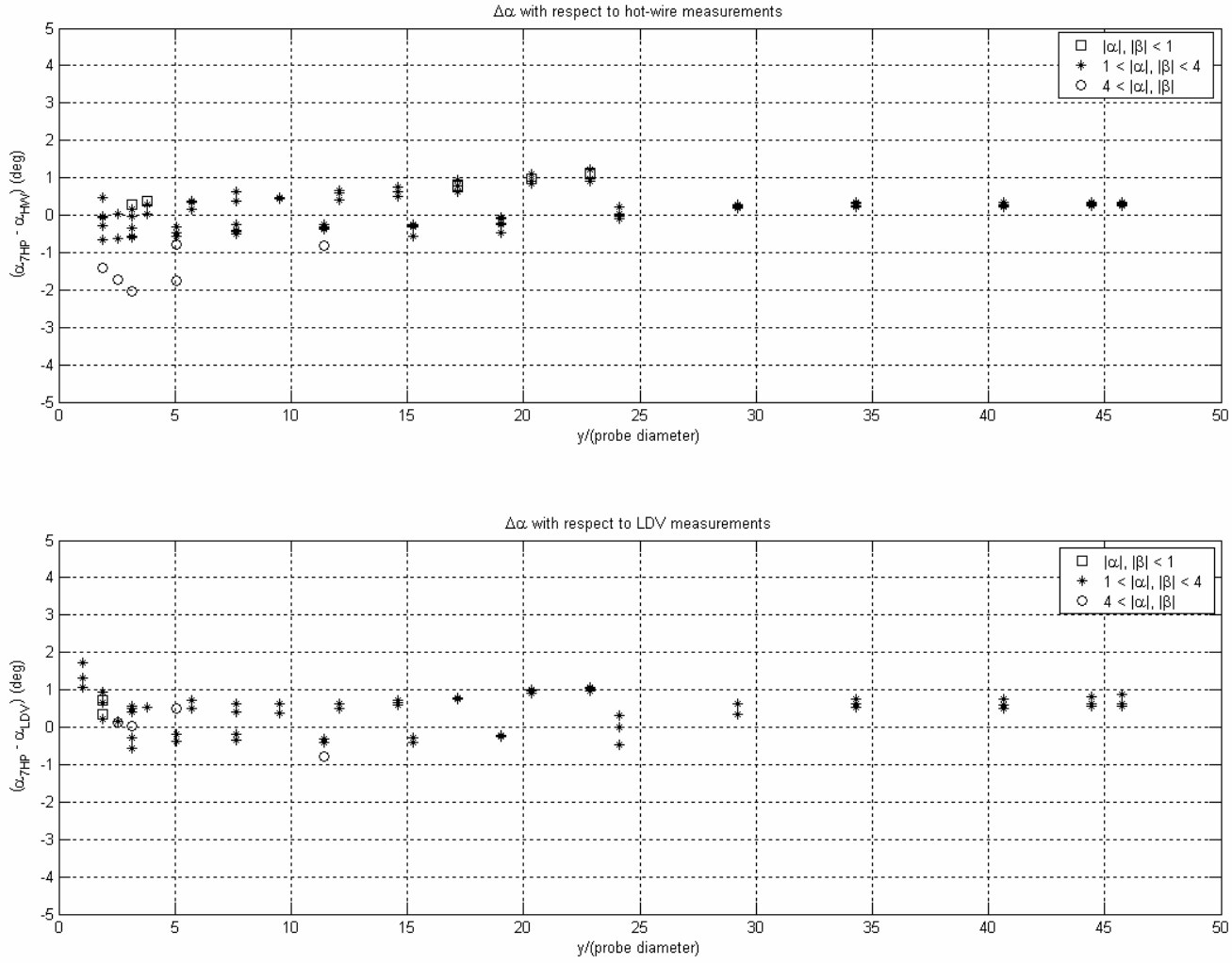

Figure 3.63: Bias-errors in the pitch angles calculated with respect to LDV and hot-wire measurements in the wakes of bump 1 and small bump 3 as a function of vertical position

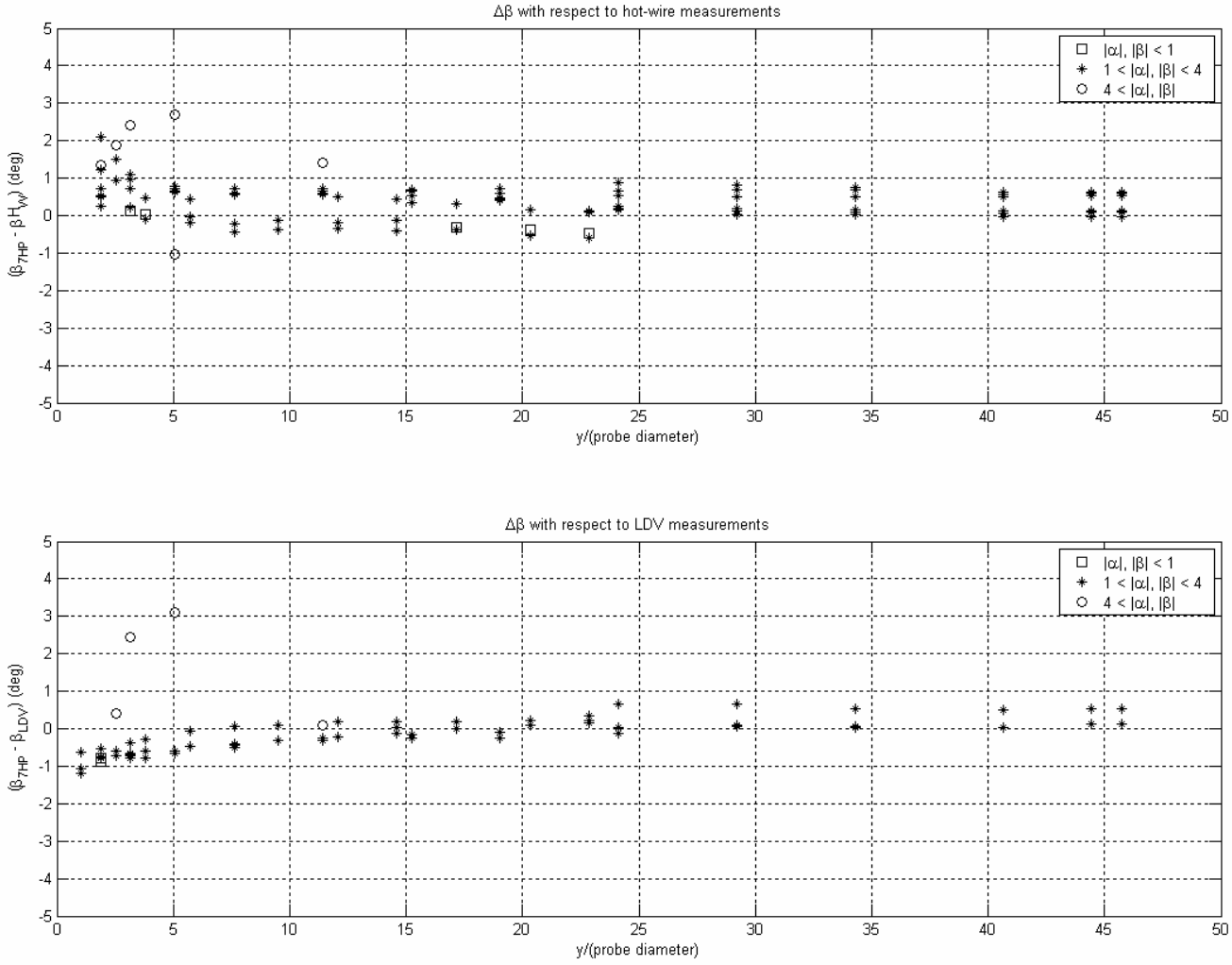

Figure 3.64: Bias-errors in the yaw angles calculated with respect to LDV and hot-wire measurements in the wakes of bump 1 and small bump 3 as a function of vertical position

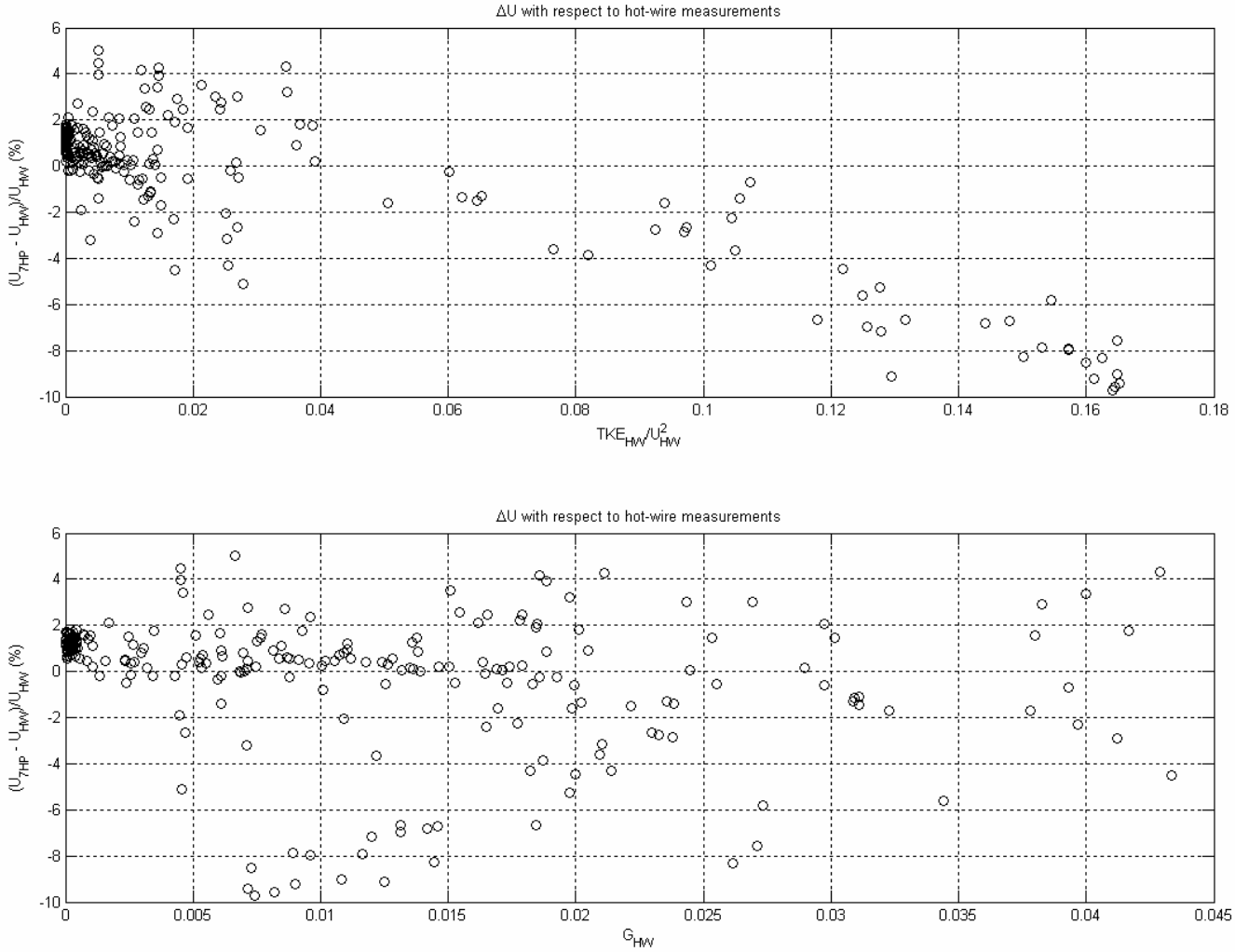

Figure 3.65: Bias-errors in mean velocity magnitude calculated with respect to hot-wire measurements as a function of TKE and the non-dimensional velocity gradient in the wakes of bump 1 and small bump 3

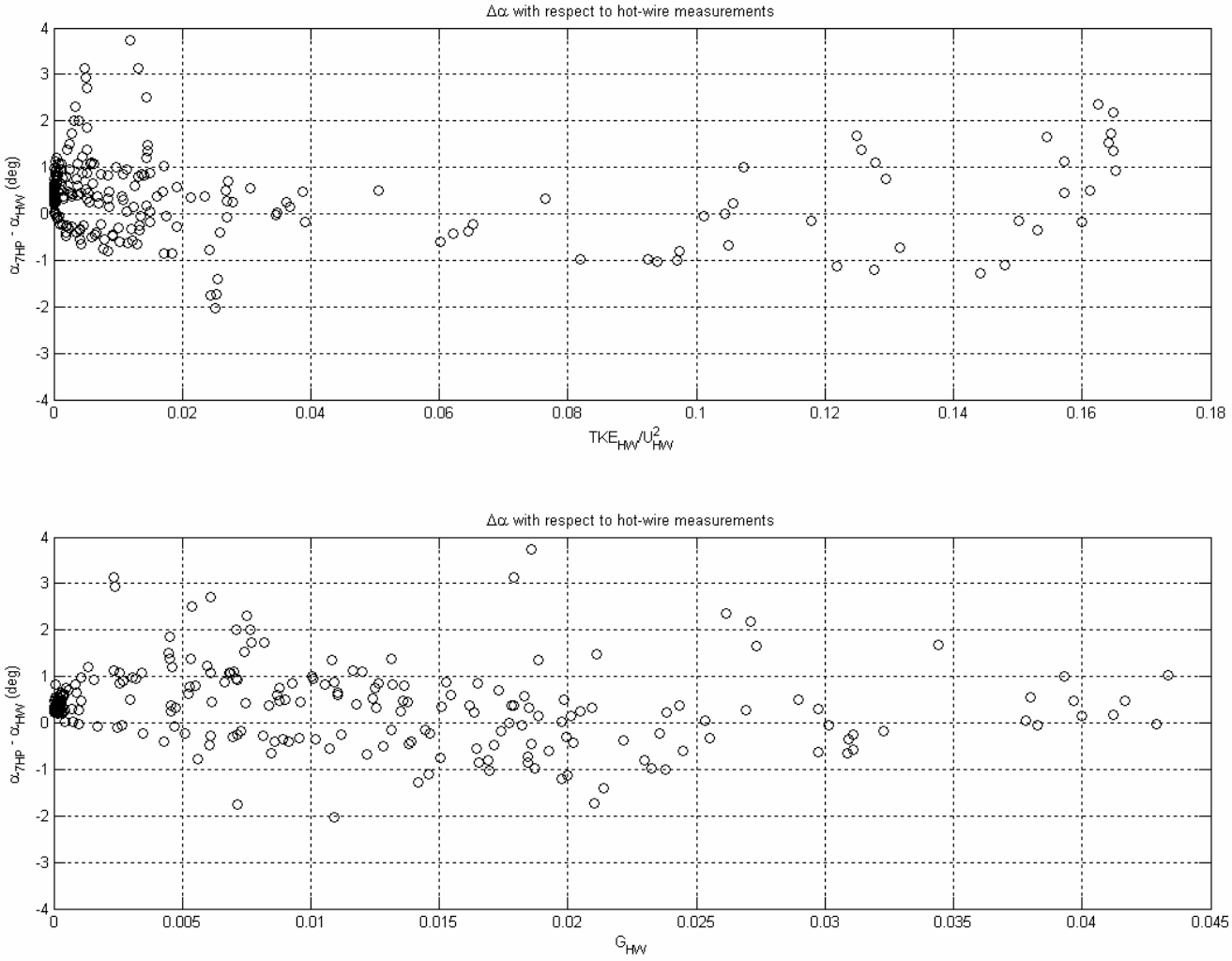

Figure 3.66: Bias-errors in pitch angles calculated with respect to hot-wire measurements as a function of TKE and the non-dimensional velocity gradient in the wakes of bump 1 and small bump 3 at *x/H* = 3.455 and *x/H* = 3.26, respectively

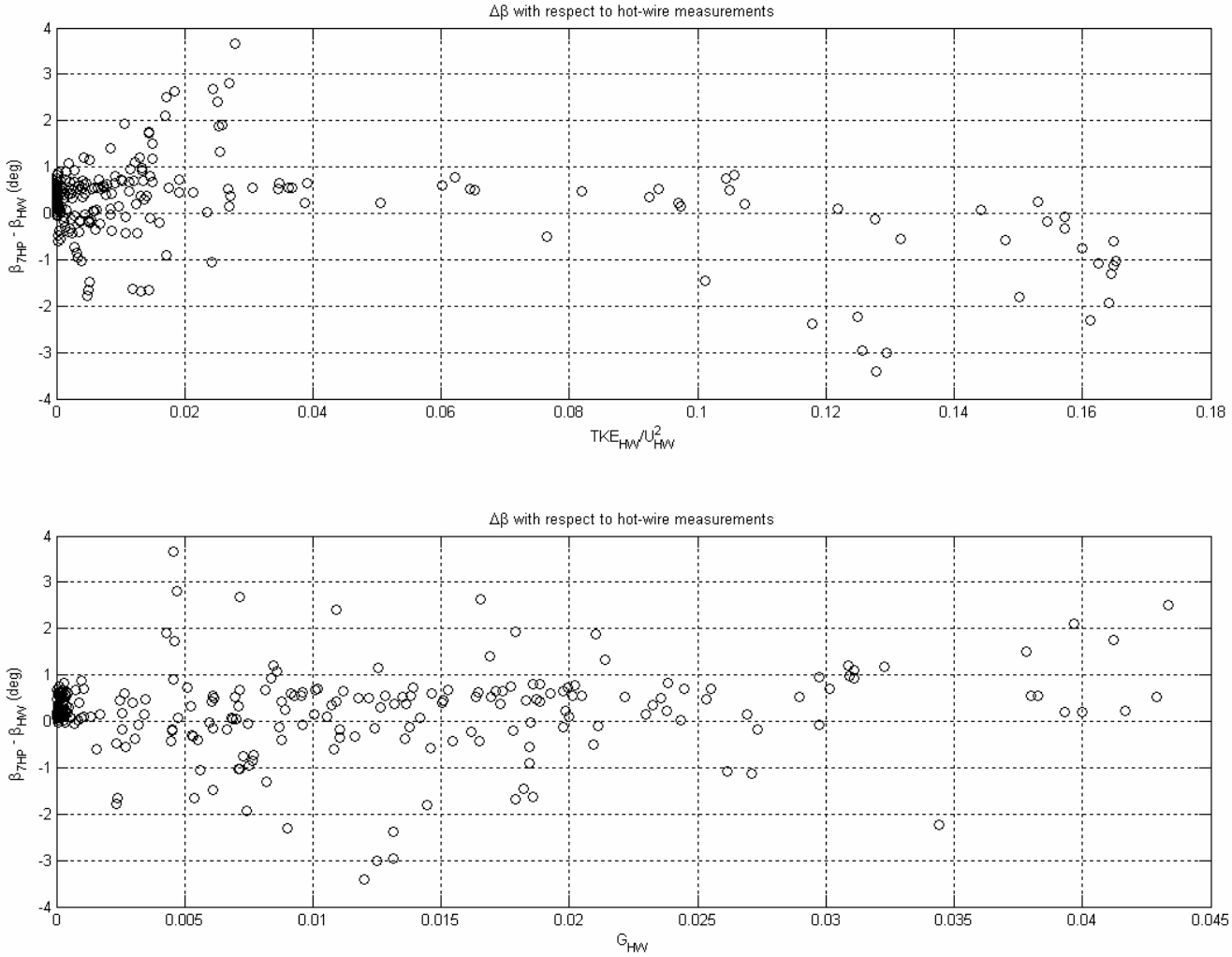

Figure 3.67: Bias-errors in yaw angles calculated with respect to hot-wire measurements as a function of TKE and the non-dimensional velocity gradient in the wakes of bump 1 and small bump 3 at *x/H* = 3.455 and *x/H* = 3.26, respectively

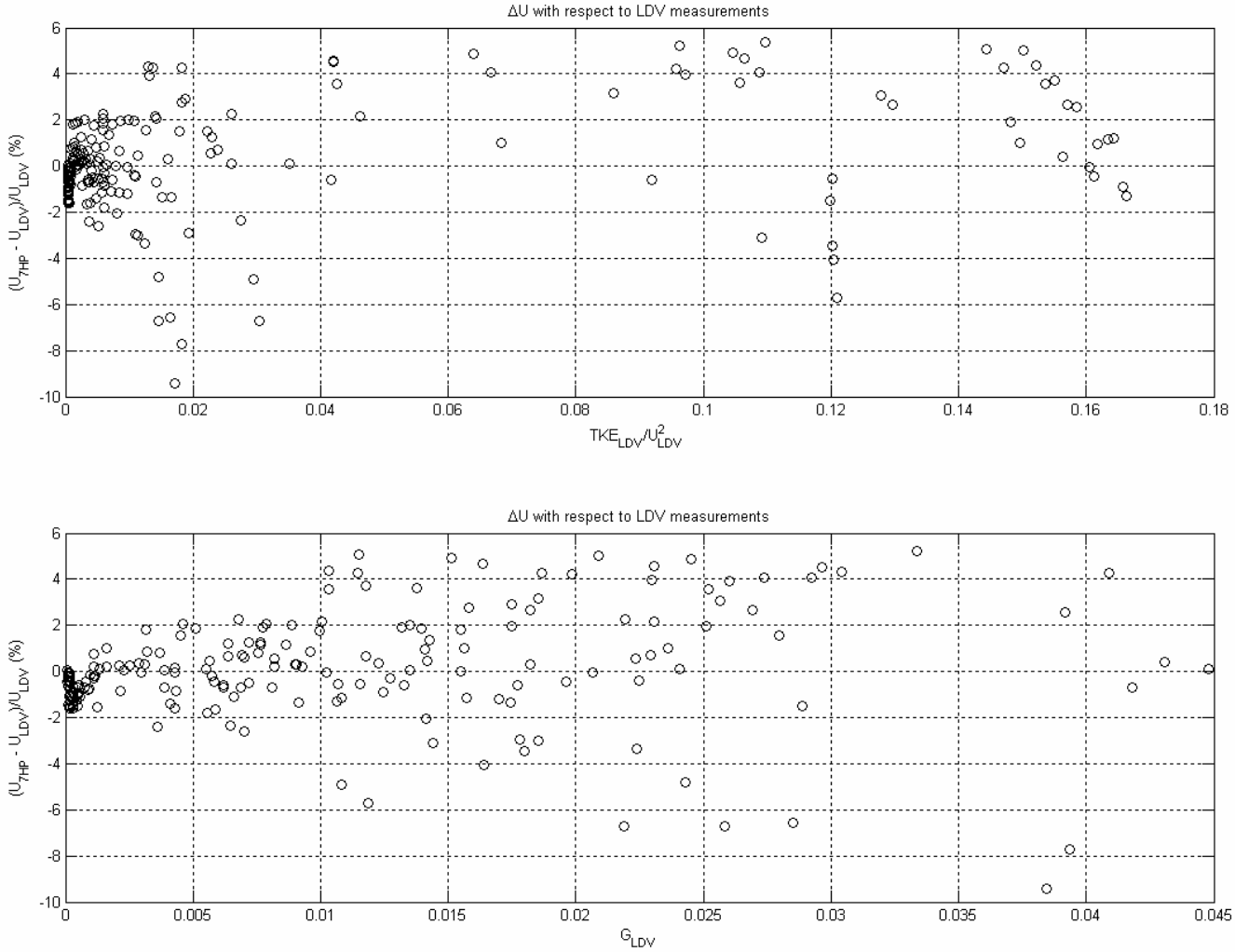

Figure 3.68: Bias-errors in mean velocity magnitude calculated with respect to LDV measurements as a function of TKE and the non-dimensional velocity gradient in the wakes of bump 1 and small bump 3 at *x/H* = 3.455 and *x/H* = 3.26, respectively

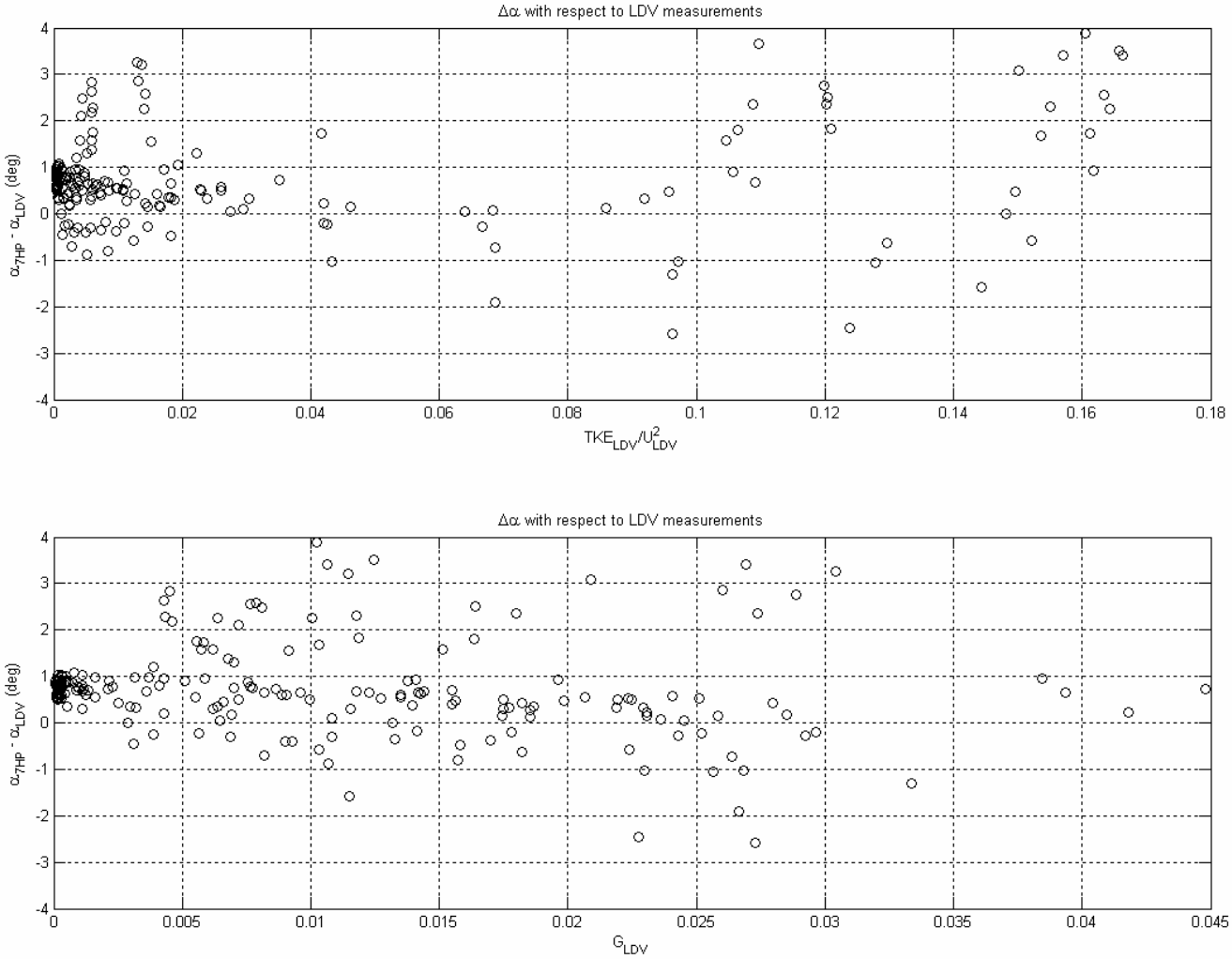

Figure 3.69: Bias-errors in pitch angles calculated with respect to LDV measurements as a function of TKE and the non-dimensional velocity gradient in the wakes of bump 1 and small bump 3 at *x/H* = 3.455 and *x/H* = 3.26, respectively

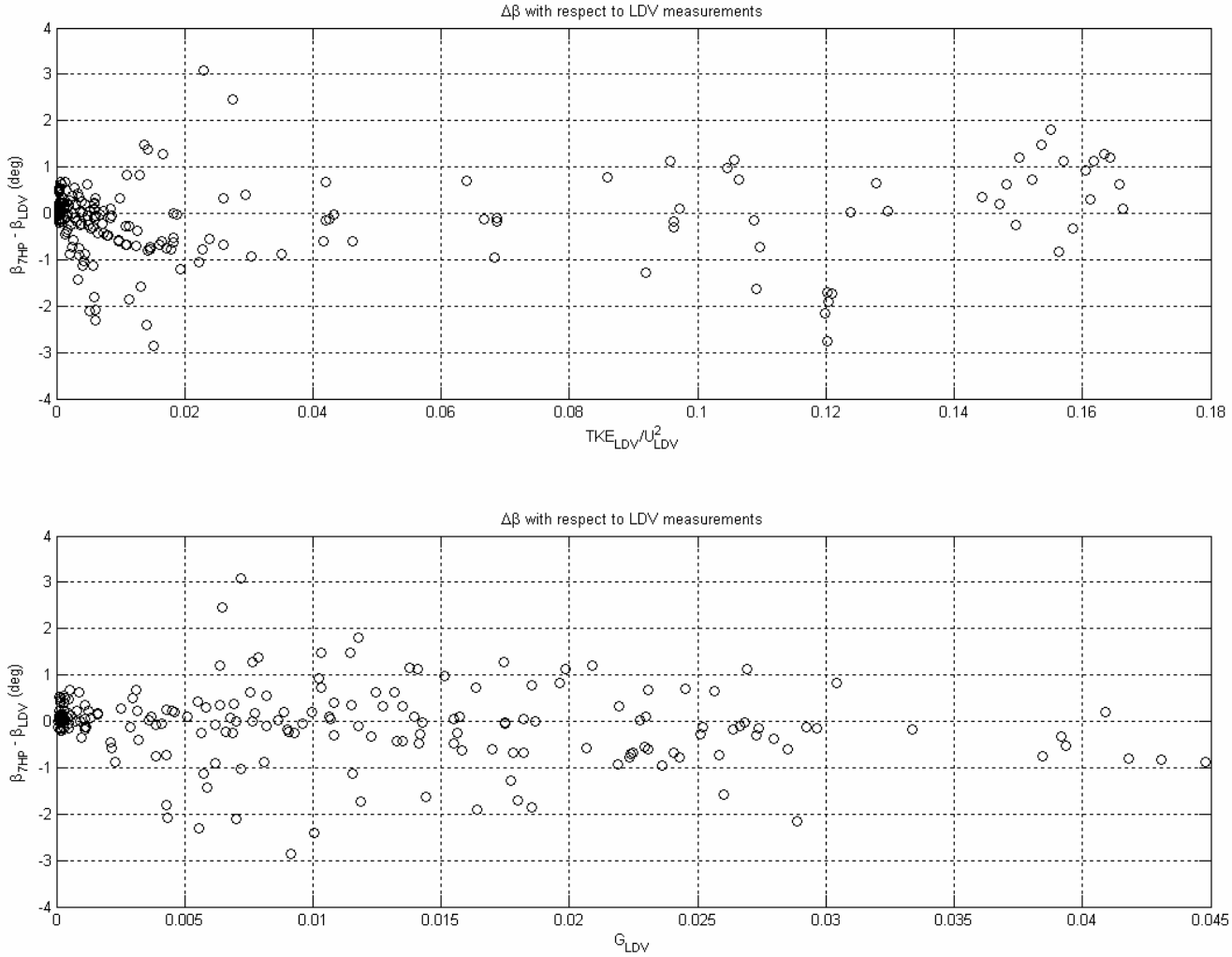

Figure 3.70: Bias-errors in yaw angles calculated with respect to LDV measurements as a function of TKE and the non-dimensional velocity gradient in the wakes of bump 1 and small bump 3 at *x/H* = 3.455 and *x/H* = 3.26, respectively

4 Sources of error in seven-hole probe measurements

The following chapter proposes to identify the sources of errors in the measurements performed by the seven-hole probe. To attain these objectives, the seven-hole probe measurements are compared to the measurements performed by the quad-wire hot-wire probe by Ma and Simpson (2004), and to the measurements performed by the LDV system by Byun et *al.* (2004). The range of Reynolds number based on the probe diameter was calculated in chapter 3 to be, $1470 \le \mathrm{Re}_d \le 3300$. Only the measurements performed in the wakes of bump 1 and small bump 3 at the streamwise locations $x/H = 3.455$ and $x/H = 3.26$, respectively, are utilized for the analyses conducted in this chapter since, as discussed sections 2.2.3.2 and 3.8.3, the seven-hole probe measurements in the wake of large bump 3 are not statistically ergodic.

To understand the how each source of errors affects the pressures measured by the seven-hole probe, a model for the seven pressures of each pressure port of the seven-hole probe is proposed and verified. Furthermore, using seven-hole probe measurements, a method is proposed to correct for the effects of velocity gradient.

4.1 Differences in incoming flow properties

It is obvious that small differences in the incoming flow properties exist between seven-hole probe data, hot-wire data, and LDV data in the wakes of the bumps since the measurements from these three methods were not obtained simultaneously. Consequently, a correction factor is defined to remove any possible errors due to different incoming flow conditions.

$$R_{LDV/hot-wire} = \frac{U_{7HP}}{U_{LDV/hot-wire}} \qquad \textbf{(4.1)}$$

In equation 4.1, U is the mean velocity magnitude measured by the seven-hole probe, the LDV system or the hot-wire probe. The correction factors calculated in the wakes of small bump 3 and bump 1 with respect to hot-wire measurements and LDV measurements are evaluated only in regions of low turbulent kinetic energy, low velocity gradient, and away from the wall. The results are presented in Table 4.1, as well as the uncertainties with 20:1 odds. The uncertainties with 20:1 odds are calculated by

obtaining the standard deviation of the correction factor and multiplying it by 1.96 ($\delta = 1.96 \cdot \sigma$, where σ is the standard deviation of the correction factor)

Table 4.1: Incoming flow properties correction factors (equation 4.1)

	Small bump 3	***Bump 1***
R_{LDV}	1.0053 ± 0.0134	0.9963 ± 0.0103
$R_{hot\text{-}wire}$	1.0034 ± 0.0053	1.0133 ± 0.0048

It can be seen that the correction factors calculated in the wakes of small bump 3 and bump 1 with respect to hot-wire measurements and LDV measurements are always close to unity indicating small variations of incoming flow properties in comparison to seven-hole probe measurements. The calculated uncertainties in the determination of the correction factor calculated with respect to LDV measurements are an order of magnitude larger than the ones calculated with respect of hot-wire measurements. The larger uncertainties in the determination of the correction factor calculated with respect to LDV measurements may be due to the fact that in regions of low turbulent kinetic energy, low velocity gradient, and away from the wall that is, at large vertical positions, the uncertainty in LDV measurements are larger due to a smaller concentration of the seeding particles.

In all the analyses conducted in chapter 4, the correction factor defined in equation 4.1 is used in order to remove any error from differences in incoming flow conditions.

4.2 Formulation for the calculations of the bias-errors

To quantify the differences between the mean velocity magnitude measured by the seven-hole probe and the mean velocity magnitude measured by the hot-wire probe or the LDV system, a bias-error is defined (equation 4.2).

$$\Delta U = \left| \frac{U_{7\,hole\ probe}}{U_{hot-wire\ or\ LDV}} - 1 \right| \qquad \textbf{(4.2)}$$

It is important to note that in this definition, the uncertainties associated with the LDV measurements, the hot-wire measurements and, the seven-hole probe measurements are not accounted for. As a reference, the uncertainties associated with hot-wire measurements and LDV measurements with 20:1 odds are $\delta U_{HW} = \pm 1\%$ (Ma and

Simpson (2004)) and $\delta U_{LDV} = \pm 0.26\%$ (Byun et *al.* (2004)), respectively. LDV measurements and hot-wire measurements of the mean velocity vector are assumed to be the true values of the mean velocity vector of the flow-field. Using the definition of the bias-error ΔU, the uncertainty of the bias-error with 20:1 odds is calculated as a percentage of the local velocity magnitude as follow,

$$\delta(\Delta U) = \pm 1.96\sigma \qquad \textbf{(4.3)}$$

In equation 4.3, σ is the standard deviation of the bias-error calculated in equation 4.2.

4.3 Performance of the seven-hole probe in a quasi-steady, non-turbulent flow field with low velocity gradients

To evaluate the performance of the seven-hole probe in a quasi-steady, non-turbulent flow with no velocity gradient, the bias-errors are evaluated between the seven-hole probe measurements and the hot-wire measurements or LDV measurements. Such regions of the flow are the same as the ones used for the calculations of the correction factors for the differences in incoming flow properties as discussed in section 4.1. Following the procedure defined in section 4.2, the bias-errors and their 20:1 odds uncertainties are calculated in the wakes of small bump 3 and bump 1 with respect to LDV and hot-wire measurements. The results of this analysis are presented in Table 4.2.

Table 4.2: Statistical analysis of the bias-errors between seven-hole probe measurements and hot-wire or LDV measurements in a quasi-steady, non-turbulent, low velocity gradient flow-field (procedure described in section 4.2)

	Small bump 3 & Bump
$\overline{\Delta U_{LDV}}$ *[% U_{LDV_local}]*	0.44 ± 0.68
$\overline{\Delta U_{hot-wire}}$ *[% $U_{hot\text{-}wire\_local}$]*	0.19 ± 0.29

It can be seen that the bias-errors between the mean velocity magnitude measured by the seven-hole probe and the mean velocity magnitude measured by the hot-wire probe or the LDV systems are relatively small, even within their uncertainties. In a similar way as the observations made in section 4.1, the bias-errors calculated with respect to LDV measurements are larger than the ones calculated with respect to hot-wire measurements. This may be due to the smaller concentration of seeding particles at large vertical positions inducing an increase of the uncertainties in the LDV measurements.

The low magnitudes of the bias-errors calculated with respect to hot-wire measurements and LDV measurements in regions of low turbulent kinetic energy, low velocity gradient, and away from the wall prove the efficiency of the techniques developed for acquiring data while minimizing the uncertainties due to the apparatus system.

4.4 Performance of the seven-hole probe in a complex flow field

The performance of the seven-hole probe in a complex flow that is, with large turbulent kinetic energy and velocity gradients is unknown. To answer this question, the bias-errors and their 20:1 odds uncertainties are calculated in the wakes of small bump 3 and bump 1 between the mean velocity magnitude measured by the seven-hole probe and the mean velocity magnitude measured by the hot-wire probe or the LDV system following the procedure defined in section 4.2. The results of this analysis are presented in Table 4.3.

Table 4.3: Statistical analysis of the bias-errors between seven-hole probe measurements and hot-wire or LDV measurements in a complex flow-field (procedure described in section 4.2)

	Small bump 3 & Bump 1
$\overline{\Delta U_{LDV}}$ *[% U_{LDV_local}]*	1.42 ± 3.31
$\overline{\Delta U_{hot-wire}}$ *[% $U_{hot\text{-}wire\_local}$]*	1.28 ± 3.48

It can be seen from Table 4.3 that the bias-errors calculated with respect to LDV measurements and hot-wire measurements in the complex flow-field are significantly larger than the ones calculated in the quasi-steady, non-turbulent, low velocity gradient flow-field. This observation indicates that as expected, the performance of the seven-hole probe in a complex flow-field significantly decreases. Consequently, the use of the uncertainties calculated in a quasi-steady, non-turbulent flow-field without velocity gradient (as the ones obtained from the calibration database) is inadequate for indicating the magnitude of the uncertainties in a complex flow-field.

4.5 Sources of uncertainty in seven-hole probe measurements and model for the pressures measured

As discussed in the previous sections, the performance of the seven-hole probe measurements in a flow-field with turbulent kinetic energy, velocity gradient, and

unsteadiness is significantly lower than in a flow-field with low turbulent kinetic energy, low velocity gradient, and quasi-steady. However, the direct influences of the turbulent kinetic energy and of the velocity gradients on the measurements performed by a seven-hole probe are not yet understood. Consequently, a model is proposed for the seven pressures read by each pressure port of the seven-hole probe to understand how the turbulent kinetic energy and the velocity gradients affect the seven-hole probe measurements in a complex flow field. It is important to note that the model developed in the following analyses are to be used **only** when the maximum pressure is read by the pressure port located on the tip of the probe. This limitation is due to the limited amount of data points where the circumferential pressure ports read the maximum pressure.

4.5.1 Alternative use of the seven-hole probe calibration database

As discussed in section 2.2.1, the calibration database was used to evaluate the mean flow properties in the unknown flow-field by calculating non-dimensional pressure coefficients, b_α and b_β defined in equation 2.4. Because the only flow angles used are the ones where the pressure port located on the tip of the probe reads the maximum pressure, the flow is assumed to be attached on the surface of the probe at all time. Furthermore, the pressures on the surface of the probe can be considered as those for a potential flow. Consequently, using the calibration database, where the true flow angles, velocities, static and total pressures are known, the pressures at each pressure port can be modeled as a function of the local velocity magnitude and the flow angles for a non-turbulent, uniform, and steady flow-field. Using a local dynamic pressure coefficient $K_i(\alpha,\beta)$ corresponding to the i^{th} pressure port, a relationship between the dynamic pressure and the pressure read at the i^{th} pressure port is obtained. Port 1, located on the tip of the probe reads a component of the total pressure. Consequently, K_1 is defined as follow,

$$\begin{aligned}\Delta P_{dynamic\_port\_1} &= P_{dynamic\_true} - P_{dynamic\_port\_1} \\ &= \left(P_{total} - P_{static}\right) - \left(p_1 - P_{static}\right) = P_{total} - p_1\end{aligned}$$

and **(4.4)**

$$P_{total} - p_1 = \frac{1}{2}\rho \cdot U_{true}^2 - \frac{1}{2}\rho \cdot K_1 \cdot U_{true}^2 = \frac{1}{2}\rho \cdot \left(1 - K_1\right) \cdot U_{true}^2$$

In equation 4.4, p_1 is the pressure read by the pressure port located on the tip of the probe and U_{true} is the true local velocity magnitude.

The circumferential i^{th} pressure ports ($i = 2 \rightarrow 7$) read a component of the static pressure and the K_i*'s* are defined as follow,

$$\begin{aligned}\Delta P_{dynamic\_port\_i} &= P_{dynamic\_true} - P_{dynamic\_port\_i} \\ &= \left(P_{total} - P_{static}\right) - \left(P_{total} - p_i\right) = p_i - P_{static}\end{aligned}$$

and **(4.5)**

$$p_i - P_{static} = \frac{1}{2}\rho \cdot U_{true}^2 - \frac{1}{2}\rho \cdot K_i \cdot U_{true}^2 = \frac{1}{2}\rho \cdot \left(1 - K_i\right) \cdot U_{true}^2$$

where $i = 2 \rightarrow 7$

In equation 4.5, p_i is the pressure read by the i^{th} circumferential pressure port and U_{true} is the true local velocity magnitude. Using the definitions for the K_i's in equations 4.4 and 4.5, with the data from the calibration file of the seven-hole probe, the K_i's are evaluated as a function of the pitch and yaw angle, α and β, respectively, and presented in Figure 4.2 for pressure ports 1 to 4 and in Figure 4.3 for pressure ports 5 to 7. It can be seen that the isobars representing K_1 are distributed as concentric circles as a function of the pitch and yaw angles. Furthermore, the K_i's calculated for the circumferential pressure ports ($i = 2 \rightarrow 7$) appear to have similar magnitudes and distributions when a coordinate rotation is performed. Consequently, two equations can be defined to model the magnitude of the K_i*'s* with respect to the pitch and yaw angles.

$$\begin{aligned}K_1 &= \sqrt{C_{11}\left(\left(\alpha - \alpha_0\right)^2 + \left(\beta - \beta_0\right)^2\right) + C_{12}} \\ K_i &= C_{i1} \cdot \alpha_i + C_{i2} \cdot \beta_i^2 + C_{i3} \quad \left(i = 2 \rightarrow 7\right)\end{aligned} \qquad \textbf{(4.6)}$$

In equation 4.6, C_{i1}, C_{i2}, C_{i3} ($i = 1 \rightarrow 7$) are coefficients experimentally determined to fit the data. The α_0 and β_0 are the offsets in pitch and yaw angle, respectively, that are observed in the concentric circles representing K_1 in Figure 4.2 and, α_i and β_i are the angles in the local coordinate system of the i^{th} pressure port defined in equation 4.7.

$$\begin{aligned}\alpha_2 &= \alpha \\ \beta_2 &= \beta \\ \\ \alpha_3 &= \alpha \cdot \cos(60) + \beta \cdot \sin(60) \\ \beta_3 &= -\alpha \cdot \sin(60) + \beta \cdot \cos(60) \\ \alpha_4 &= -\alpha \cdot \cos(30) + \beta \cdot \cos(30) \\ \beta_4 &= -\alpha \cdot \cos(30) - \beta \cdot \sin(30)\end{aligned} \qquad \textbf{(4.7)}$$

$$\alpha_5 = -\alpha$$
$$\beta_5 = \beta$$
$$\alpha_6 = -\alpha \cdot \cos(60) - \beta \cdot \sin(60)$$
$$\beta_6 = \alpha \cdot \cos(30) - \beta \cdot \sin(30)$$
$$\alpha_7 = \alpha \cdot \cos(60) - \beta \cdot \sin(60)$$
$$\beta_7 = \alpha \cdot \sin(60) + \beta \cdot \cos(60)$$

The offsets in pitch and yaw angles are evaluated to be, $\alpha_0 = -3.19\,\text{deg.}$ and $\beta_0 = 3.5\,\text{deg.}$, respectively.

Using a least square formula, the coefficients C_{i1}, C_{i2}, and C_{i3} are determined as well as the correlation coefficients between the polynomial fits and the measured data. These results are presented in Table 4.4.

Table 4.4: Coefficients and correlation coefficients of polynomial fits (equation 4.6) for the K_i's defined in equations 4.4 and 4.5

i^{th} port →	C_{i1}	C_{i2}	C_{i3}	*Correlation coefficient*
Port 1	-0.0007	1.0059	0	0.97988
Port 2	-0.02345	0.000574	0.59758	0.99945
Port 3	-0.02323	0.00055	0.59882	0.99931
Port 4	-0.02303	0.000552	0.59047	0.99893
Port 5	-0.02282	0.000569	0.58914	0.99916
Port 6	-0.02346	0.000632	0.58471	0.99884
Port 7	-0.02368	0.000594	0.58744	0.99873

The large correlation coefficients obtained for the circumferential pressure ports assert the validity of the models developed in equation 4.6. However, for the pressure port located on the tip of the probe, the correlation coefficient is significantly lower than the ones for the circumferential ports. As shown in equation 4.6 and in Figure 4.2, the center of the concentric circles is not located for zero flow angles. The first reaction would be to say that there is a bias angle in the calibration file itself. However, using the offset angles to determine the coefficients of the polynomial fit for the circumferential pressure ports significantly decreases the magnitude of the correlation coefficients. This observation indicates that there are no bias angles in the calibration file but that the geometry of the pressure port located on the tip of the probe is causing the bias angles. It is therefore impossible to obtain a model for K_1 as a function of the pitch and yaw angle

only, since defects in the geometry of pressure port 1 will induce significant differences from the model proposed. In this fashion, a look-up table is used to obtain the value of K_1 for specific flow angles.

Coefficients, K_i's for the i^{th} pressure port were defined to evaluate the pressures at each pressure ports through a model equation as a function of the flow angles. Models for the K_i's of the circumferential pressure ports were defined and their validity was asserted through the calculation of correlation coefficients. For the pressure port located on the tip of the probe, it was found that a model could not be obtained due to defects in the geometry of the center pressure port. Consequently, it was decided to use look-up table for determining K_1 as a function of the pitch and yaw angles.

4.5.2 Model for the pressures at each pressure port in a turbulent flow with velocity gradient

In section 4.5.1, a model was developed for the pressures at each pressure port of the seven-hole probe as a function of the flow angles for a steady, non-turbulent flow-field with no velocity gradient. As discussed in section 4.4, the performance of the seven-hole probe in such a flow is not a good indicator of the performance of the seven-hole probe in a flow with large turbulent kinetic energy and velocity gradient. Consequently, modified models to the ones defined in equation 4.4 and 4.5 have to be developed to account for the influence of the turbulent kinetic energy and for the influence of the velocity gradient.

4.5.2.1 Theoretical effect of the turbulent kinetic energy on pressure measurements

The instantaneous dynamic pressure in a turbulent flow-field without velocity gradients is described by the instantaneous Bernouilli's equation (Karamcheti (1996)).

$$P_{total}(t) - P_{static}(t) = \frac{1}{2}\rho U^2(t) + \frac{\partial \phi_p(t)}{\partial t} \qquad \textbf{(4.8)}$$

where $P_{total}(t)$, $P_{static}(t)$, ρ, $U(t)$ and, $\phi_p(t)$ are the instantaneous total pressure, static pressure, the incompressible density, the instantaneous magnitude of the velocity, and the velocity potential, respectively. Time averaging equation 4.8 leads to,

$$P_{total} - P_{static} = \frac{1}{2}\rho\left(U_{true}^2 + 2 \cdot TKE\right) = \frac{1}{2}\rho U_{indicated}^2 \quad \textbf{(4.9)}$$

where *TKE* is the turbulent kinetic energy, U_{true} is the true mean velocity magnitude, and $U_{indicated}$ is the mean velocity magnitude that would be indicated if a Pitot-static probe was reading the true mean and fluctuation dynamic pressure. From equation 4.8 and 4.9, it is obvious that any velocity measurements performed by a pressure probe are biased due to the influence of the turbulence in a flow-field. In a similar way, the pressures measured by the seven-hole probe should be biased under the influence of the turbulent kinetic energy.

Since the seven-hole probe measures components of the mean velocity vector in three-dimensions, it is going to be biased by the three components of the turbulent normal stresses, $\overline{u^2}, \overline{v^2}$, and $\overline{w^2}$ corresponding to the turbulent normal stresses in the streamwise, normal to the wall, and spanwise directions, respectively. Because the circumferential pressure ports are distributed evenly around the surface of the seven-hole probe, the normal to the wall, and spanwise turbulent normal stresses should influence the seven-hole probe pressure measurements in a similar way. Consequently, in the absence of velocity gradients, the indicated velocity read by the seven-hole probe can be written as,

$$U_{indicated}^2 = U_{true}^2 + C_u \cdot \overline{u^2} + C_{vw} \cdot \left(\overline{v^2} + \overline{w^2}\right) \quad \textbf{(4.10)}$$

In equation 4.10, C_u and C_{vw} are coefficients determining the influence of the normal stresses on seven-hole probe measurements.

4.5.2.2 Theoretical effect of velocity gradients on seven-hole probe pressure measurements

Assuming that the seven-hole probe is aligned with a non-turbulent flow-field, a velocity gradient (Figure 4.1) induces a change of the apparent angle at each pressure port.

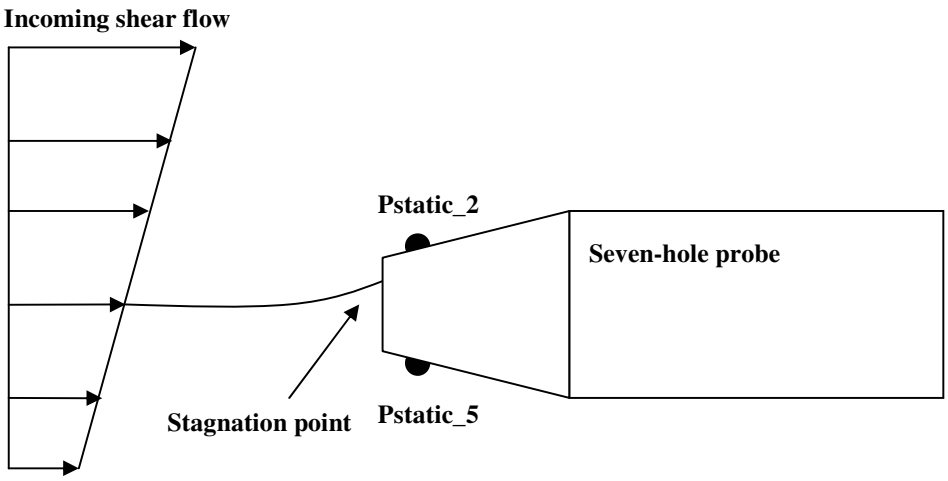

Figure 4.1: Representation of the seven-hole probe in a shear flow

For pressure port 1, located on the tip of the seven-hole probe, the change of the stagnation point location due to the velocity gradient induces a change of the apparent flow angle. Hall (1957) and Lighthill (1956) studied the effects of the velocity gradient on the location of the stagnation point on a blunt-nosed Pitot tube of circular cross-section. They derived similar relationships to model the change of location of the stagnation point due to a velocity gradient as a function of a non-dimensional velocity gradient *G*, (Hall (1957) and Lighthill (1956))

$$G = \frac{d}{2 \cdot U} \frac{\partial U}{\partial s}$$
$$\frac{\delta_{stagnation}}{d} = A_{stagnation} \cdot G - B_{stagnation} \cdot G^3 . \qquad \textbf{(4.11)}$$

In equation 4.11, d is the diameter of the probe, $\frac{\partial U}{\partial s}$ is the gradient of the mean velocity magnitude in the s direction, $\delta_{stagnation}$ is the displacement of the stagnation point from the location of the stagnation point without velocity gradients, $A_{stagnation}$, and $B_{stagnation}$ are coefficients analytically determined by Hall (1957) and Lighthill (1956).

Using the mean velocity measurements performed by the hot-wire probe or the LDV system, the non-dimensional velocity gradient G is calculated in the wakes of bump 1 and small bump 3 and, utilizing the equation determined by Lighthill (1956) ($A_{stagnation} = 0.45$, $B_{stagnation} = 3.05$), the displacement of the stagnation point due to the

velocity gradient is calculated. It is determined that the largest displacement of the stagnation point due to the velocity gradients observed in the wakes of bump 1 and small bump 3 is of the order of the tens of microns. Such a small displacement of the stagnation point location is within the uncertainty of the displacements of the probe provided by the traverse system. Consequently, the displacement of the stagnation point due to velocity gradient is considered to be negligible and, pressure port 1 located on the tip of the probe, can be considered to be insensitive to velocity gradients.

The velocity gradient was shown to have a negligible effect on pressure port 1, located on the tip of the seven-hole probe. However, the effect of the velocity gradient on the circumferential pressure ports (ports 2 to 7) is still unknown. Looking at Figure 4.1, the velocity gradient induces a higher velocity magnitude at the location of pressure port 2 and a lower velocity magnitude at the fifth pressure port. Consequently, the static pressure read by pressure port 2 is smaller than the one read by pressure port 5, and the apparent flow angles at pressure ports 2 and 5 are different from the true flow angles. In a similar manner, the apparent flow angles of the other circumferential pressure ports are going to vary under the influence of a velocity gradient. Note that only the component of the velocity gradient aligned with the line formed by two pressure ports at opposite locations on the probe (pressure ports 2 and 5, pressure ports 3 and 6, pressure ports 4 and 7) affects the two pressure ports.

The velocity gradient induces a change of the apparent flow angles felt by the circumferential pressure ports (ports 2 to 7). Consequently, directly using the definition for the K_i's $(i = 2 \rightarrow 7)$ in section 4.5.1 for evaluating the pressures at each circumferential pressure ports leads to significant errors since, as discussed in section 4.5.1, the K_i's are function of the flow angles only. In this fashion, another coefficient, κ_i $(i = 2 \rightarrow 7)$ is defined to take into account the change of apparent flow angle due to the velocity gradient by decomposing the *Ki*'s coefficients into a Taylor series with respect to the velocity gradient.

$$\kappa_i = K_i + \frac{\partial K}{\partial G} G_i \qquad \textbf{(4.12)}$$

In equation 4.12, $\frac{\partial K}{\partial G}$ is the change of rate of the K_i's with respect to the velocity gradient and is considered constant for all K_i's. G_i is the component of the velocity gradient aligned with the line formed by two pressure ports at opposite locations on the probe (G_{25}, G_{36}, and G_{47} corresponding to pressure ports 2 and 5, 3 and 6, and 4 and 7, respectively).

4.5.2.3 Model for the seven-hole probe in a turbulent shear flow

From the discussions of the previous sections, the influence of the turbulent normal stresses and of the velocity gradient on the seven pressures measured by the seven-hole probe was determined. Consequently, a model for the seven pressures measured by the seven-hole probe can now be defined as a function of the true local velocity magnitude, the turbulent normal stresses, the velocity gradients, the flow angles, the total, and static pressures. Under the influence of velocity gradient and turbulent normal stresses, equation 4.4 becomes,

$$P_{total} - p_1 = \frac{1}{2}\rho \cdot U_{indicated}^2 - \frac{1}{2}\rho \cdot \kappa_1 \cdot U_{indicated}^2 = \frac{1}{2}\rho \cdot (1-\kappa_1) \cdot U_{indicated}^2 \qquad \textbf{(4.13)}$$

In equation 4.13, $U_{indicated}$ is defined by equation 4.10. Since the influence of velocity gradients on pressure port 1 is negligible as discussed in section 4.5.2.2, $\kappa_1 = K_1$ and equation 4.13 can be reformulated as,

$$P_{total} - p_1 = \frac{1}{2}\rho \cdot (1-K_1) \cdot \left(U_{true}^2 + C_u \cdot \overline{u^2} + C_{vw} \cdot \left(\overline{v^2} + \overline{w^2}\right)\right) \qquad \textbf{(4.14)}$$

In a similar way, equation 4.5 can be reformulated as,

$$\begin{aligned} p_i - P_{static} &= \frac{1}{2}\rho \cdot (1-\kappa_i) \cdot U_{indicated}^2 \\ &= \frac{1}{2}\rho \cdot \left(1 - K_i - \frac{\partial K}{\partial G} G_i\right) \cdot \left(U_{true}^2 + C_u \cdot \overline{u^2} + C_{vw} \cdot \left(\overline{v^2} + \overline{w^2}\right)\right) \end{aligned} \qquad \textbf{(4.15)}$$

where $i = 2 \rightarrow 7$

In equation 4.15, G_i is the component of the velocity gradient aligned with the line formed by two pressure ports at opposite locations on the probe. Subtracting equation 4.14 and 4.15, and using the definition of the dynamic pressure in a turbulent flow-field in equation 4.9 leads to,

$$p_1 - p_i = \frac{1}{2}\rho \cdot \left(K_1 + K_i + \frac{\partial K}{\partial G} G_i \right) \cdot \left[U_{true}^2 + C_u \cdot \overline{u^2} + C_{vw} \cdot \left(\overline{v^2} + \overline{w^2} \right) \right] - \frac{1}{2}\rho \left(U_{true}^2 + 2 \cdot TKE \right) \quad \textbf{(4.16)}$$

where $i = 2 \rightarrow 7$

Using equation 4.16 in the definitions of q, b_α and, b_β (equation 2.4), leads to,

$$q = \frac{1}{2}\rho \left[U_{true}^2 + C_u \cdot \overline{u^2} + C_{vw} \cdot \left(\overline{v^2} + \overline{w^2} \right) \right] \cdot \left(K_1 + \frac{1}{6}\sum_{i=2}^{7} K_i + \frac{1}{3}\frac{\partial K}{\partial G}\left(G_{25} + G_{36} + G_{47} \right) \right) - \frac{1}{2}\rho \left(U_{true}^2 + 2 \cdot TKE \right) \quad \textbf{(4.17)}$$

$$b_{\alpha\_\text{model}} = \frac{\frac{1}{2}\rho \left[U_{true}^2 + C_u \cdot \overline{u^2} + C_{vw} \cdot \left(\overline{v^2} + \overline{w^2} \right) \right] \cdot \left(K_2 + K_7 - K_4 - K_5 \right)}{q\sqrt{3}} \quad \textbf{(4.18)}$$

$$b_{\beta\_\text{model}} = \frac{\frac{1}{2}\rho \left[U_{true}^2 + C_u \cdot \overline{u^2} + C_{vw} \cdot \left(\overline{v^2} + \overline{w^2} \right) \right] \cdot \left(\frac{K_5 + K_7 - K_2 - K_4}{2} + K_6 - K_3 \right)}{q} \quad \textbf{(4.19)}$$

In equation 4.17, G_{25}, G_{36} and, G_{47} are the components of the velocity gradient in the direction formed by a line along the second and fifth pressure port, the third and sixth pressure port, and the fourth and seventh pressure port, respectively.

4.5.2.4 Procedure for the determination of the model coefficients C_u, C_{vw} and $\frac{\partial K}{\partial G}$

Using the model developed for the pressures read by the seven-hole probe in a turbulent flow-field with velocity gradient, the coefficients C_u, C_{vw}, and $\frac{\partial K}{\partial G}$ can be calculated using seven-hole probe pressure measurements and velocity measurements from the hot-wire probe or the LDV system. The b_{α_model} and b_{β_model} (equation 4.17 to 4.19) are determined using the mean velocity magnitude, the turbulent normal stresses, the velocity gradient, and the flow angle from hot-wire measurements or LDV measurements in the wakes of bump 1 and small bump 3. The b_α and b_β are determined from equation 2.4 from the seven pressures measured by the seven-hole probe in the

wakes of bump 1 and small bump 3. As stated previously, the correction factor (equation 4.1) for correcting for the differences of incoming flow condition is used.

To reduce the uncertainties in the determination of the coefficients C_u, C_{vw}, and $\frac{\partial K}{\partial G}$, only large values of turbulent kinetic energy and of velocity gradients are used. Furthermore, only the measurements located for $y \geq 3 \cdot$ probe diameters are used due to the turbulence generated by the probe/flow interactions close to the wall as seen in Figure 4.4. The restrictions are chosen to be,

$$\frac{TKE}{U_{true}^2} \geq 0.02$$

$$G = \sqrt{G_y^2 + G_z^2} \geq 0.02 \qquad \textbf{(4.20)}$$

$$y \geq 3 \cdot (\text{probe diameter})$$

where G_y and G_z are the velocity gradients in the vertical and spanwise directions, respectively. The coefficients C_u, C_{vw}, and $\frac{\partial K}{\partial G}$ are optimized by minimizing the following equation only with the data points satisfying the conditions of equation 4.20,

$$\sum_{\substack{\text{data points} \\ \text{satisfying} \\ \text{equation 4.20}}} \left(\left| b_\alpha - b_{\alpha\_\text{model}} \right|^2 + \left| b_\beta - b_{\beta\_\text{model}} \right|^2 \right) \text{ is minimum} \qquad \textbf{(4.21)}$$

4.5.2.5 Results of model coefficients after optimization

The procedure defined in section 4.5.2.4 is used to obtain the coefficients C_u, C_{vw}, and $\frac{\partial K}{\partial G}$ with seven-hole probe pressure measurements, LDV measurements, and hot-wire measurements in the wakes of small bump 3 and bump 1. The results are presented in Table 4.5.

Table 4.5: Optimized model coefficients obtained using the procedure defined in section 4.5.2.4

	C_u	C_{vw}	$\frac{\partial K}{\partial G}$
Using LDV measurements	0	0.9	1.6
Using hot-wire measurements	4	-1	3.1

It can be seen that from the calculations of the model coefficients using LDV measurements, the streamwise turbulent normal stress appears to have no effects on seven-hole probe measurements. The fact that the streamwise turbulent normal stress has no effects on seven-hole probe measurements is quite unlikely since it was shown by Siddon (1959) that the component of the turbulent normal stresses normal to the pressure port induces the largest effects on the pressure read at this pressure port. Because the streamwise turbulent normal stress is aligned with the axis of the pressure ports of the seven-hole probe, it is expected that the streamwise turbulent normal stress induces significant effects on seven-hole probe measurements. Consequently, the results obtained with respect to LDV measurements appear to be doubtful. With respect to hot-wire measurements, it can be seen that the streamwise turbulent normal stress has significantly more influence on seven-hole probe measurements than the vertical and spanwise turbulent normal stresses. It is interesting to note that C_{vw} calculated with respect to LDV measurements and hot-wire measurements have relatively the same magnitude ($|C_{vw}| \approx 1$). However, the sign of C_{vw} is different depending on what set of measurements are used for its calculation. Similarly as what is observed in the calculations of C_u and C_{vw}, the calculation of $\frac{\partial K}{\partial G}$ with respect to LDV measurements and hot-wire measurements gives two significantly different results. However, the calculation of $\frac{\partial K}{\partial G}$ with respect to LDV measurements and to hot-wire measurements indicates a similar effect of the velocity gradient on the seven-hole probe measurements.

The significant differences observed in the determination of the model coefficients may be due to the uncertainties associated with the three measuring systems that are not accounted for in this analysis. In other words, the mean velocity magnitude, flow angles, and turbulent normal stresses indicated by the measurements performed by the LDV system or the hot-wire probe are not the true flow properties due to the uncertainties associated with the LDV measurements and the hot-wire measurements. Similarly, the seven pressures measured by the seven-hole probe are not the true seven pressures present at the pressure ports due to apparatus uncertainties.

4.5.2.6 Validation of the model (equation 4.16)

To validate the model developed in equations 4.16, a statistical analysis is performed between the b_α's and b_β's calculated from the seven pressures from the seven-hole probe measurements and, the b_{α_model}'s and b_{β_model}'s calculated using LDV measurements and hot-wire measurements with equations 4.17 to 4.19. All the data in the wakes of bump 1 and small bump 3 are used in this verification. The statistical analysis is performed on the following absolute bias-errors.

$$\Delta b_\alpha = \left| b_\alpha - b_{\alpha\_\text{model}} \right| \qquad \Delta b_\beta = \left| b_\beta - b_{\beta\_\text{model}} \right| \qquad \textbf{(4.22)}$$

The results of the statistical analysis of the bias-errors for the non-dimensional pressure coefficients b_α and b_β as well as the uncertainties with 20:1 odds are presented in Table 4.6, and the order of magnitude of the b_α's and b_β's measured by the seven-hole probe are presented in Table 4.7.

Table 4.6: Verification of the model developed through a statistical analysis of bias-errors defined in equation 4.22 in the wakes of bump 1 and small bump 3

Bias error statistical analysis	$\overline{\Delta b_\alpha}$	$\overline{\Delta b_\beta}$	***Correlation coefficient, b_α***	***Correlation coefficient, b_β***
With respect to LDV measurements	0.05 ± 0.085	0.084 ± 0.157	0.9508	0.9602
With respect to hot-wire measurements	0.043 ± 0.093	0.063 ± 0.106	0.9376	0.9824

Table 4.7: Order of magnitude of the non-dimensional pressure coefficients b_α and b_β measured by the seven-hole probe in the wakes of small bump 3 and bump 1

$\overline{\lvert b_\alpha \rvert}$	$\min(b_\alpha)$	$\max(b_\alpha)$	$\overline{\lvert b_\beta \rvert}$	$\min(b_\beta)$	$\max(b_\beta)$
0.152 ± 0.223	-1.006	0.851	0.234 ± 0.567	-2.807	2.242

In Table 4.6 and Table 4.7, the variations or uncertainties of the bias-errors are calculated with 20:1 odds ($\delta = 1.96 \cdot \sigma$, where σ is the standard deviation). It can be seen that the mean values of the bias-errors, within their uncertainties, are always an order of

magnitude lower than the mean values of the non-dimensional pressure coefficients, within their uncertainties. The low correlation coefficients calculated indicate significant scatter of the bias-errors. However, this scatter should be due to the uncertainties of the three measurement systems that are not accounted for in the model as discussed in section 4.5.2.5. The mean values of the bias-errors within their uncertainties, calculated with respect to hot-wire measurements are smaller than the ones calculated with respect to LDV measurements. It is important to note that hot-wire measurements and seven-hole probe measurements were obtained at the same time whereas LDV measurements were obtained more than a year earlier. Consequently, there is a high probability that some unaccounted parameters may have changed in the test-section that would be responsible for these differences.

The bias-errors of the non-dimensional pressure coefficients defined in equation 4.22 as a function of the magnitude of the non-dimensional velocity gradient and of the normalized turbulent kinetic energy are represented in Figure 4.5 and Figure 4.6, corresponding to the bias errors calculated with respect to hot-wire measurements and LDV measurements, respectively. It is interesting to note the bias-errors calculated with respect to LDV measurements and hot-wire measurements are usually within a range of 20%. The few points observed to be significantly larger may be attributed to erroneous data points from either of the three measurement systems. The fact that the bias-errors are usually within this range of 20% suggests that this scatter should be attributed to the uncertainties associated with the three measurement systems.

With respect to hot-wire measurements (Figure 4.5), the bias-errors stay relatively constant within the 20% range for increasing magnitudes of turbulent kinetic energy. With respect to LDV measurements (Figure 4.6), the bias-errors also stay relatively constant within the 20% range for increasing magnitudes of turbulent kinetic energy. However, for the larger magnitudes of turbulent kinetic energy, $TKE/U_{local}^2 \geq 0.1$, the bias-errors of the non-dimensional pressure coefficient b_β are observed to increase. This observation suggests that the coefficients C_u and C_{vw}, optimized with respect to LDV measurements are not well representing the influence of the turbulent normal stresses on the pressures measured by the seven-hole probe. This conclusion follows the remark

advanced in section 4.5.2.5 that the coefficient C_u optimized with respect to LDV measurements do not appear to be realistic.

For increasing magnitudes of the non-dimensional velocity gradient, the bias-errors calculated with respect to hot-wire measurements (Figure 4.5) significantly decrease. A significant decrease of the bias-errors is observed for $G \geq 0.025$. This observation indicates that for large velocity gradient $G \geq 0.025$, the uncertainties induced by the velocity gradient on the pressures measured by the seven-hole probe becomes significantly larger than the uncertainties associated with the three measurement systems and, the model developed in equation 4.15 manages to correct for the effects of large velocity gradient on the pressures measured by the seven-hole probe. With respect to LDV measurements (Figure 4.6), the bias-errors as a function of the non-dimensional velocity gradient appear to follow a similar trend than what is observed with respect to hot-wire measurements. However, the non-dimensional velocity gradients calculated from LDV measurements are smaller than the ones calculated from hot-wire measurements preventing to draw any conclusions from the LDV data.

From these observations, it appears that the model developed in section 4.5.2.3 is valid for explaining the influence of the velocity gradient on the pressures measured by the seven-hole probe since for large velocity gradients, the proposed model manages to decrease the magnitude of the bias-errors. To explain for the behavior of the bias-errors with respect to the turbulent kinetic energy, two explanations can be advanced. The first explanation would be that the model developed to explain the influence of the turbulent normal stresses on the seven-hole probe measurements is not valid. The second explanation would be that the uncertainties associated with the turbulent stresses are significantly lower than the uncertainties associated with the three measurement systems and the correction for the turbulent normal stresses could not be determined. From the results of the coefficients in Table 4.5, it was observed that the coefficients C_u and C_{vw} obtained from the optimization with respect to LDV measurements and hot-wire measurements are significantly different in sign and magnitude. This observation suggests that the determination of the coefficients C_u and C_{vw} is done within the uncertainties of the three measurement systems that explains for the inconsistency of the results calculated with respect to LDV measurements and hot-wire measurements.

Consequently, it is probable that the proposed model explains for the influence of the turbulent normal stresses on the pressure measurements by the seven-hole probe. However, no conclusions can be drawn in reason of the uncertainties of the three measurement systems larger than the uncertainties induced by the turbulences.

4.6 Figures

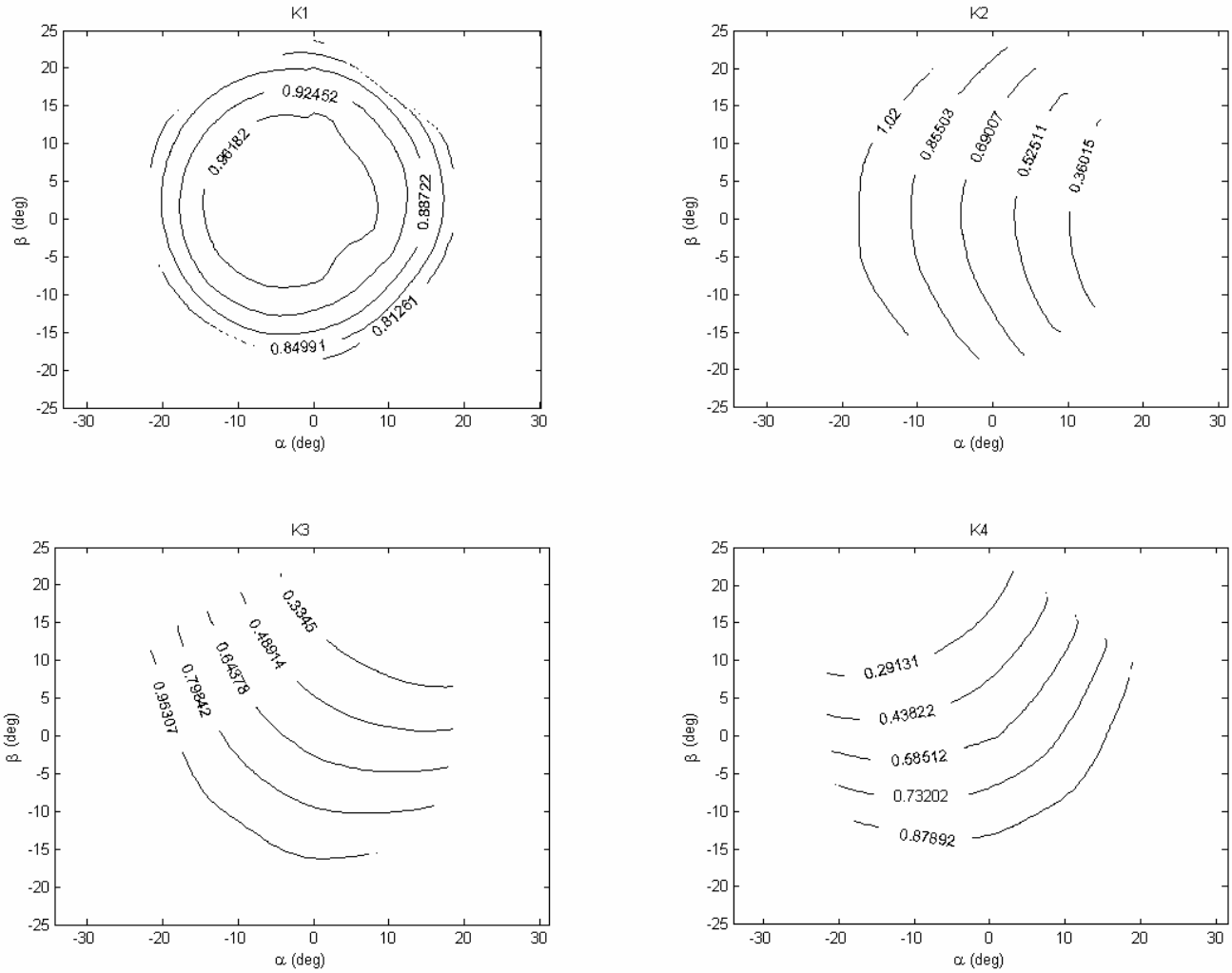

Figure 4.2: Local dynamic pressure coefficients K_i's defined in equation 4.4 and 4.5 for ports 1 to 4 (port 1 reading maximum pressure)

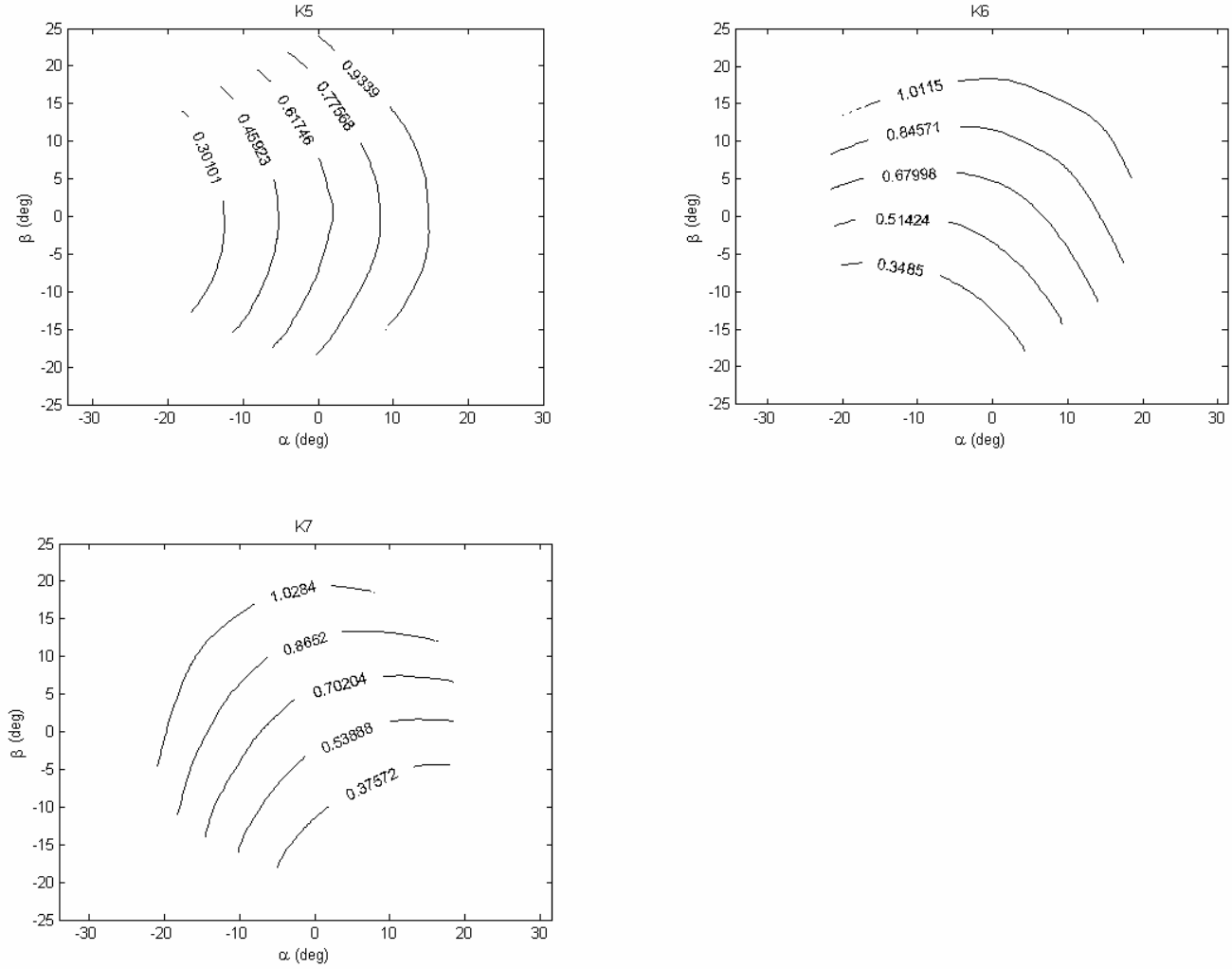

Figure 4.3: Local dynamic pressure coefficients K_i's defined in equation 4.4 and 4.5 for ports 5 to 7 (port 1 reading maximum pressure)

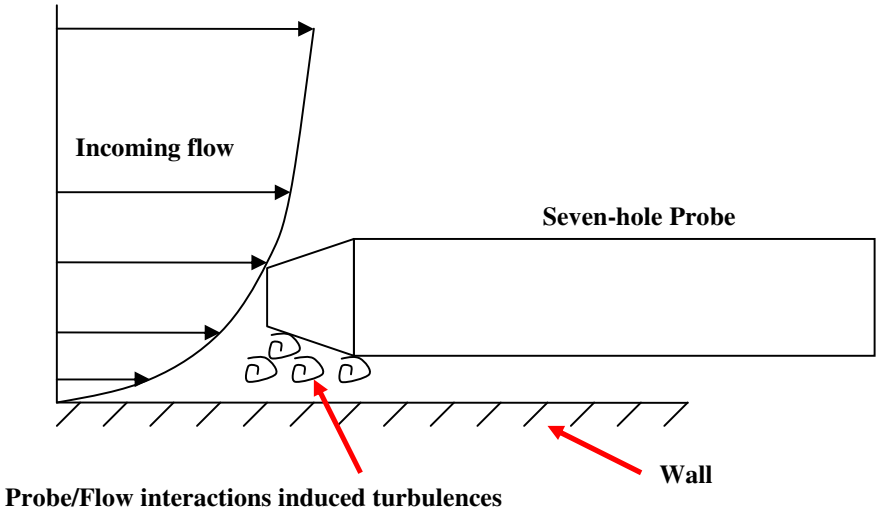

Figure 4.4: Representation the probe/flow interactions close to the wall (not on scale)

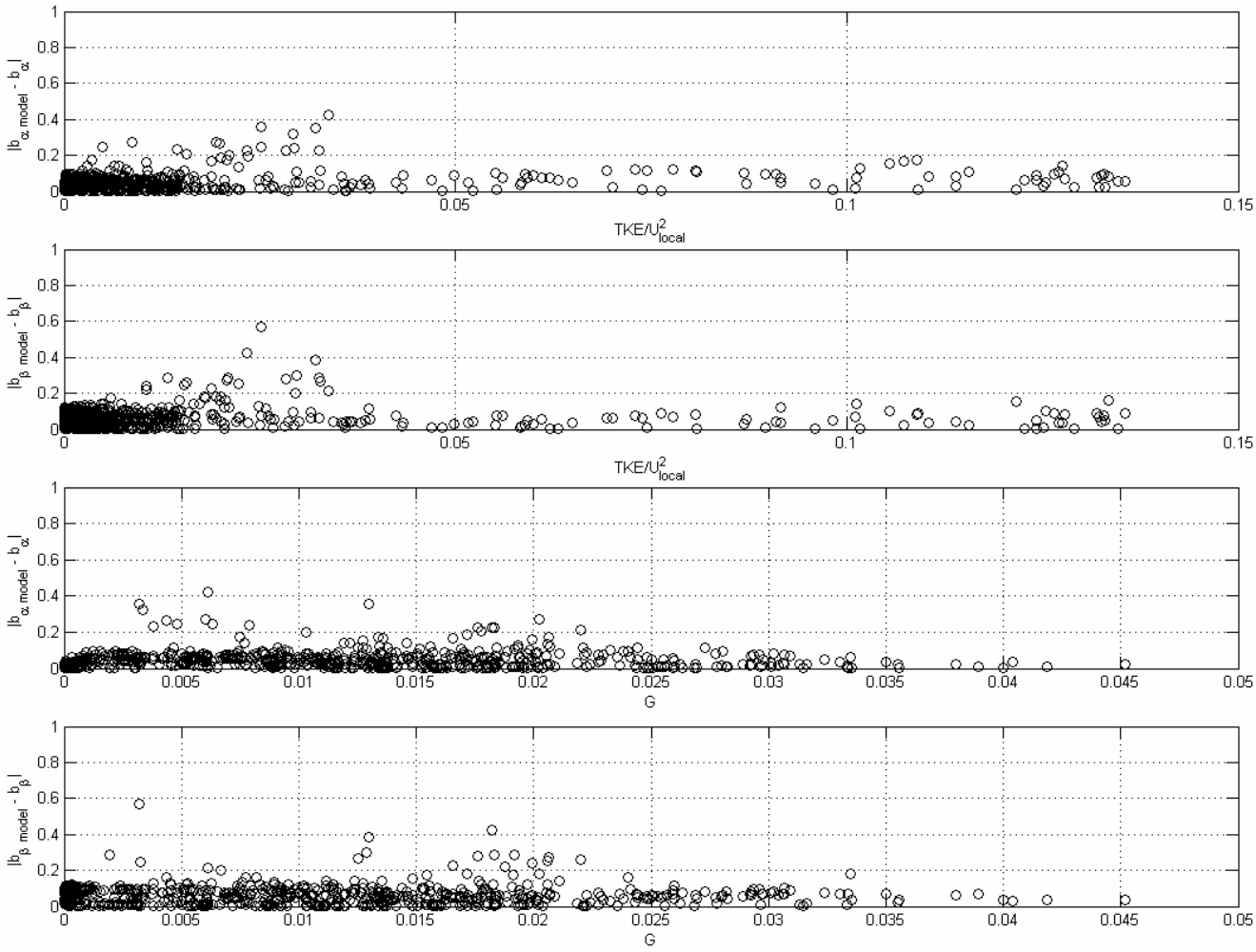

Figure 4.5: Bias-errors (defined in equation 4.22) calculated with respect to hot-wire measurements as a function of the turbulent kinetic energy and the magnitude of the non-dimensional velocity gradients (equation 4.11 and 4.20)

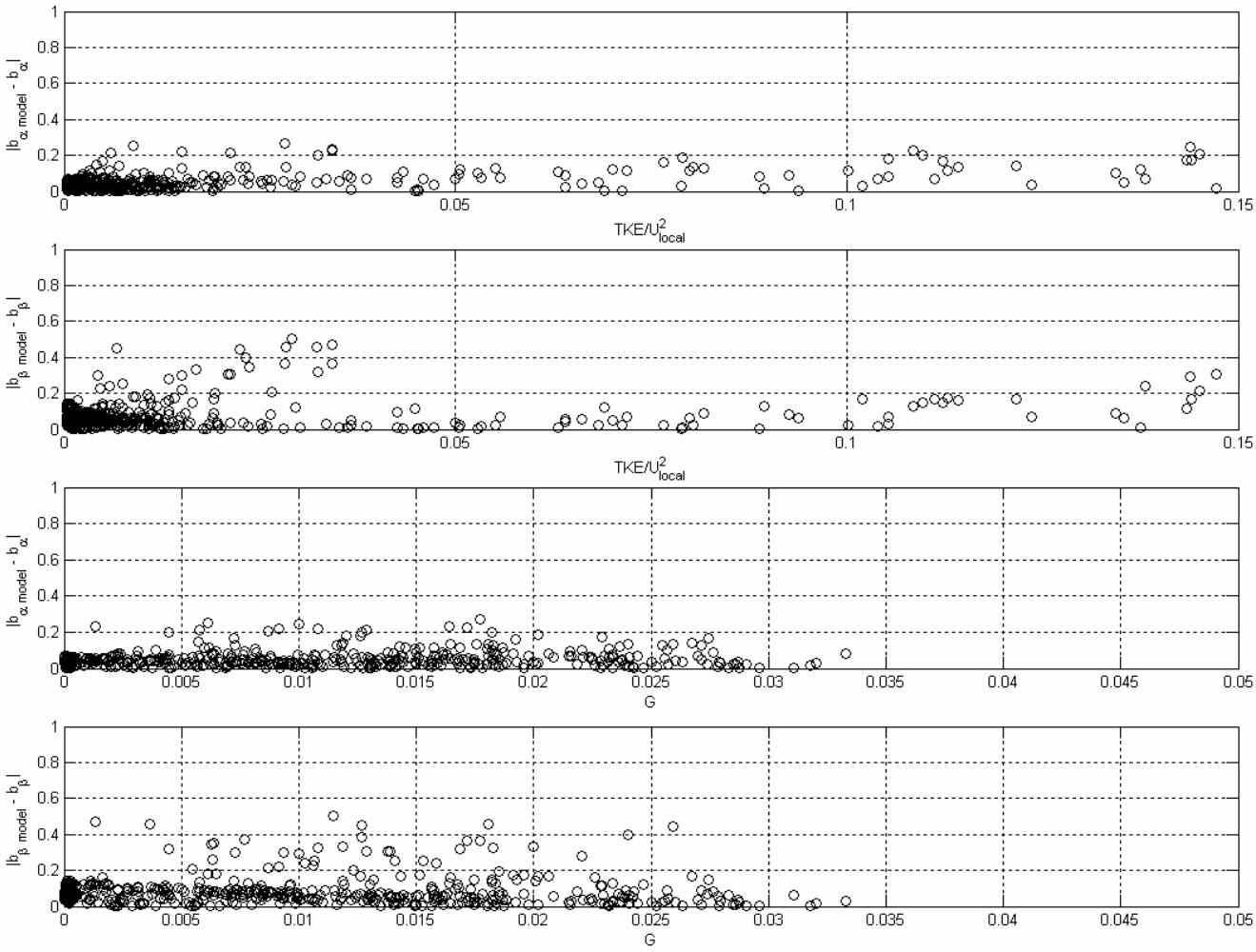

Figure 4.6: Bias-errors (defined in equation 4.22) calculated with respect to LDV measurements as a function of the turbulent kinetic energy and the magnitude of the non-dimensional velocity gradients (equation 4.11 and 4.20)

5 Conclusion

5.1 Summary of this study

Seven-hole probe, sixteen-hole pressure rake and Pitot - static tube measurements of the mean velocity flow were obtained in the Virginia Polytechnic Institute and State University Boundary Layer Wind Tunnel around three three-dimensional bumps. A technique allowing a minimization of the uncertainties due to the apparatus was developed and tested, and its efficacy was confirmed through a statistical analysis of bias-errors. The symmetry of the flow in the wakes of the bumps was obtained by shifting the position of the bumps in the test section and checking the symmetry of the mean velocity components measured by the seven-hole probe. It was found that the symmetry of the flow in the wake of bump 1 was not too sensitive to the position of the bump in the test section. However, the symmetry of the flow in the wake of small bump 3 was found to be significantly sensitive to the position of the bump in the test section and the asymmetry of the flow-field could not be eliminated. A good symmetry of the flow in the wake of bump 1 was observed. The position of large bump 3 in the test section for symmetry of the flow downstream of large bump 3 was studied by Ma and Simpson (2004). To test the statistical ergodicity of the data measured by the seven-hole probe in the wakes of the bumps, measurements were obtained with various sampling times. The sampling time for small bump 3 and bump 1 was sufficiently long for statistical ergodicity of the data. However, the sampling time chosen for the measurements in the wake of large bump 3 was found to be too small for statistical ergodicity, leading to erroneous velocity magnitudes.

In the wake of bump 1, measurements were obtained at $x/H = 3.455$ and at $x/H = 11.5$. It was found that a strong streamwise vorticity is created in the wake of bump 1 inducing a significant entrainment of high momentum close to the wall and a reduction of the boundary layer thickness around the centerline of the test section. This entrainment of high momentum fluid was found to increase significantly in the streamwise direction. A pair of counter rotating vortices were observed with their vortex

center increasing in vertical position and in spanwise position as the streamwise position increased.

Measurements in the wake of small bump 3 were obtained at $x/H = 3.26$ and $x/H = 11.5$. It was found that at $x/H = 3.26$, no high momentum fluid is entrained close to the wall but a strong negative normal velocity magnitude was observed around the centerline of the test section. At $x/H = 11.5$, small amounts of high momentum fluid were observed close to the wall however, no conclusions could be drawn on the state of the boundary layer due to a limited amount of data at high vertical positions. A pair of counter rotating vortices was observed in the wake of small bump 3 with their vortex center increasing in vertical position and in spanwise position as the streamwise position increased. The streamwise vorticity magnitude in the wake of small bump 3 was observed to be significantly smaller than the one observed in the wake of bump 1. It was observed that the asymmetry of the flow in the wake of small bump 3 decreased with increasing streamwise positions.

Around large bump 3, an extensive set of measurements was obtained. Upstream information of the state of the boundary layer was obtained on the sidewalls and on the ceiling of the test section at $x/H = -4.6$. At the same location, $x/H = -4.6$, information of the two-dimensional boundary layer at various spanwise locations were obtained as well as a profile at $x/H = -4.6$ upstream of large bump 3. A comparison of the upstream flow with and without large bump 3 set in place was examined and it was found that the presence of the bump significantly affected the incoming flow by increasing the boundary layer thickness. Measurements obtained at $x/H = 0$, $x/H = 3.629$, and $x/H = 11.5$ permitted observing the evolution of the flow in the wake of large bump 3. Large bump 3 showed some characteristics of both bump 1 and small bump 3, by entraining some high momentum fluid close to the wall at $x/H = 3.629$ and constraining the growth of the boundary layer thickness close to the centerline of the test section. The streamwise vorticity in the wake of large bump 3 was observed to be similar in magnitude than the one observed in the wake of small bump 3. A pair of counter rotating vortices was observed in the wake of large bump 3 with their vortex center increasing in vertical position but not in spanwise position as the streamwise position increased.

From a comparison between quad-wire hot-wire data by Ma and Simpson (2004) , LDV data by Byun et *al.* (2004) and the seven-hole probe data in the wakes of the three bumps at $x/H = 3.455$, $x/H = 3.26$, and $x/H = 3.629$ in the wakes of bump 1, small bump 3, and large bump 3, respectively, significant qualitative and quantitative discrepancies were observed. These discrepancies were found to be the largest in the wake of large bump 3 due to the bad choice of the sampling time. Analyses of the quantitative comparisons as a function of vertical positions, turbulent kinetic energy, and the velocity gradient revealed that large uncertainties in the mean velocity magnitude measured by the seven-hole probe are to be expected for $y \le 9 \cdot$ probe diameters, and large uncertainties in the pitch and yaw angles are to be expected for $y \le 6 \cdot$ probe diameters. The quantitative analyses with respect to turbulent kinetic energy and velocity gradients showed that turbulent kinetic energy and velocity gradients induced relatively large uncertainties in the mean velocity magnitude and in the flow angles measured by the seven-hole probe. For relatively large magnitudes of turbulent kinetic energy ($TKE/U^2 \ge 0.04$), bias-errors between seven-hole probe measurements and hot-wire or LDV measurements were found to be, $\Delta U \ge \pm 3\%$ of $U_{HW/LDV}$. For larger ranges of turbulent kinetic energy, the maximum bias-errors were found to be, $\Delta U \ge \pm 8\%$ of $U_{HW/LDV}$. For the flow angles, bias-errors of $\Delta U \ge \pm 1\,\mathrm{deg}.$ were observed in regions of large turbulent kinetic energy.

Using the calibration database from the seven-hole probe, a model was developed to evaluate the seven pressures at each pressure port measured by the seven-hole probe. It was found that the pressures measured by the seven-hole probe in a quasi-steady, non-turbulent, uniform flow-field are only a function of the mean velocity magnitude, and the pitch and yaw angles. To understand the effect of turbulence and of the velocity gradient on pressure measurements by the seven-hole probe, a theoretical framework for explanation of these effects was developed. It was found that the static and total pressures read by a pressure probe are biased under the influence of the turbulence. The velocity gradient was found to induce a change of the apparent flow angles at each

pressure port. Furthermore, it was established that the change of location of the stagnation point due to the shear flow was negligible.

Using the theoretical framework to understand the effects of turbulence and velocity gradient on the pressures measured by the seven-hole probe, the model developed for the seven pressures read by the seven-hole probe in a quasi-steady, non-turbulent, uniform flow was modified to account for the effects of turbulence and of velocity gradient. The model coefficients, C_u, C_{vw}, and $\frac{\partial K}{\partial G}$ were found to be significantly different when calculated with respect to LDV measurements or hot-wire measurements due to the uncertainties associated with the three measurement systems. The model results obtained from using LDV measurements were found to be doubtful since they indicated that the streamwise turbulent normal stress had no effects on the seven-hole probe measurements. Using the results obtained from hot-wire measurements, it was found that streamwise turbulent normal stress affected the seven-hole probe measurements more than cross-flow turbulent normal stress. It was observed that the significantly different values of the model coefficients obtained from LDV measurements and from hot-wire measurements were due to the uncertainties associated with the three measuring systems that induced large uncertainty in the determination of the model coefficients. By calculating absolute bias-errors of the non-dimensional pressure coefficients b_α and b_β, a scatter of the bias-errors in a range of 20% was observed that was explained by the uncertainties associated with the three measuring systems. By representing the bias-errors as a function of the turbulent kinetic energy and of the non-dimensional velocity gradient, it was found that the effect of the turbulent kinetic energy on the seven-hole probe measurements was smaller than the uncertainties associated with the three measuring systems. However, the effect of velocity gradient was found to be larger than the uncertainty associated with the three measuring systems. These observations indicated that the velocity gradient affected the seven-hole probe measurements more than the turbulent kinetic energy.

5.2 Prescription for use of the seven-hole probe in a shear flow

Using the proposed model in section 4.5.2.3, the effects of the turbulence and the velocity gradient can be theoretically corrected. However, from a practical point of view,

when seven-hole probe measurements are obtained in an unknown flow-field, the true velocity gradient and the turbulent normal stresses are unknown. Nevertheless, the velocity gradient in an unknown flow-field can be estimated using only seven-hole probe measurements. Consequently, using the model coefficient $\frac{\partial K}{\partial G}$ obtained from the data fit to hot-wire measurements and the non-dimensional velocity gradient G calculated from seven-hole probe measurements, the non-dimensional pressure coefficients, b_α and b_β can be re-evaluated to account for the effects of the velocity gradient on seven-hole probe measurements. Obviously, since the effects of turbulence cannot be accurately known, and the non-dimensional velocity gradient calculated with the seven-hole probe is not the true non-dimensional velocity gradient, some uncertainty in the calculations of the non-dimensional pressure coefficients will be present in the final results. However, as discussed in section 4.5.2.6, the effects of turbulence on seven-hole probe measurements are smaller than the effects of the velocity gradient. Thus, the main contribution to the uncertainties in seven-hole probe measurements due to the velocity gradient can be corrected that will allow smaller uncertainties in seven-hole probe measurements.

Reference

Akima, H., "A method of Bivariate Interpolation and Smooth Surface Fitting for Irregularly Distributed Data Points", ACM Trans., Math Software, vol. 2, pp. 148, 1978

Becker, H. A., Brown, A. P. G., "Response of Pitot Probes in Turbulent Streams", Journal of Fluid Mechanics, vol. 62, pp. 85-114, 1974

Becker, H. A., Cho, S. H., "Effect of Turbulence on Static Pressure Probe Responses: Applications of Old Probes to New Turbulence Studies", 7th Symposium on Turbulence, Rolla, MO, pp. 149-160, 1981

Byun, G., Simpson, R. L., Long, C. H., "A Study of Vortical Separation from Three-Dimensional Symmetric Bumps", AIAA paper 2003-641, 2003

Byun, G., Simpson, R. L., Long, C. H., "Study of Vortical Separation from Three-Dimensional Symmetric Bumps", AIAA journal, vol. 42, No. 4, 2004

Christiansen, T., Bradshaw, P., "Effect of Turbulence on Pressure Probes", J. Phys, E: Sci. Instrum., vol. 14, 1981

Devenport, W. J., Wenger, C. W., "A seven Hole Pressure Probe Measurement System and Calibration Method utilizing error Tables", AIAA-98-0202, 1998

Everett, K. N., Gerner, A. A., Durston, D. A., "Seven-Hole Cone Probes for High Angle Flow Measurement: Theory and Calibration", AIAA journal, vol. 21, No. 7, pp. 992-998, 1982

Fuchs, H. V., "Measurement of Pressure Fluctuations within Subsonic Turbulent Jets", Journal of Sound and Vibration, vol. 22 (3), pp. 361-378, 1972

Gallington, R. W., "Measurement of Very Large Flow Angles with Non-Nulling Seven-Hole Probes", USAFA-TR-80-17, 1980

George, J., Dissertation in progress, 2004

Guo, Y., Wood, D. H., "Instantaneous Velocity and Pressure Measurements in Turbulent Mixing Layers", Experimental Thermal and Fluid Science, vol. 24, pp. 139-150, 2001

Hall, I. M., Journal of Fluid Mechanic, vol. 2, 497, 1957

Hooper, J. D., Musgrove, A. R., " Multi-Hole Pressure Probes for the Determination of the Total Velocity Vector in turbulent Single-Phase Flow", Transport Phenomena in Heat and Mass Transfer, pp. 1274-1284, 1992

Hooper, J. D., Musgrove, A. R., "Pressure Probe Measurement of the Turbulent Stress Distribution in a Swirling Jet", Experimental Heat Transfer, Fluid Mechanics and Thermodynamics, pp. 172-179, 1993

Hooper, J. D., Musgrove, A. R., "Reynolds Stress, Mean Velocity, and Dynamic Static Pressure Measurements by a Four-Hole Pressure Probe", Journal of Experimental Thermal and Fluid Science, vol. 15, pp.375-383, 1997

Jenkins, R. C., "Effect of Pitot Probe Shape on Measurement of Flow Turbulence", AIAA Journal, vol. 25, No. 6, pp. 879-892, 1984

Johansen, E. S., Rediniotis, O. K., Jones, G., "The Compressible Calibration of Miniature Multi-Hole Probes", Journal of Fluid Engineering, vol. 123, pp. 128-138, 2001

Johansen, E. S., Rediniotis, O. K., "Development of Unsteady Calibration Facilities and Techniques for Fast-Response Pressure Probes", AIAA paper 2002-0689, 2002

Johansen, E. S., Allen, R. D., Rediniotis, O. K , Zeiger, M. D., "Embedded-Sensor, Fast-Response, Multi-Hole Probes", AIAA paper 2003-1091, 2003

Johansen, E. S. , Rediniotis, O. K., Tsao, T., Seifert, A., Pack, L. G., "MEMS-Based Probes for Velocity and Pressure Measurements in Unsteady and Turbulent Flowfields", AIAA paper, 99-0521, 1999

Karamcheti ,K., "Principles of Ideal-Fluid Aerodynamics", Krieger Publishing companies, pp 281-291, 1996

Kays, W. M., "Convective Heat and Mass Transfer", McGraw-Hill Book Company, pp. 92-95, 1966

Lighthill, M. J., Journal of Fluid Mechanic, vol. 2, 493, 1956

Long, C. H., "A Study of vortical separation from symmetric bumps" MS thesis, Aerospace and Ocean Engineering, VPI&SU, 2002 (in progress)

Ma, R., Simpson, R. L., "Vortical Flow Downstream of Three-Dimensional Symmetric Bumps", (In Progress), 2004

Pisasale, A. J., Ahmed, N. A., "Examining the Effects of Flow Reversal on Seven-Hole Probe Measurements", AIAA journal, vol. 14, No. 12, pp. 2460-2467, 2003

Rediniotis, O. K., Hoang, N. T., Telionis, D. P., "The Seven-Hole Probe: Its Calibration and Use", Instructional Fluid Dynamic Experiments, vol. 152, pp. 21-26, 1993

Schetz, J. A., "Boundary Layer Analysis", Prentice Hall, 1993

Siddon, T. E., "On the Response of Pressure Measuring Instrumentation in Unsteady Flow (An Investigation of Errors Induced by Probe-Flow Interaction)", UTIAS Report No. 136, 1969

Takahashi, T. T., "Measurement of Air Flow Characteristics Using Seven Hole Cone Probes", AIAA paper 97-0600, 1997

Vijayagopal, R., Pathak, M. M., Rediniotis, O. K., "Miniature Multi-Hole Pressure Probes – Their Neural Network Calibration and Frequency Response Enhancement", AIAA paper, 1998-204, 1998

Willits, S. M., Boger, D. A., "Measured and Predicted Flows behind a Protuberance Mounted on a Flat Plate", Applied Research Laboratory, Penn State Univ., State College, 1999

Zeiger, M. D., Chalmeta, L. P., Telionis, D. P., "Tip Geometry Effects on Calibration and Performance of Seven-Hole Probes", AIAA paper 98-2810, 1998

Zeiger, M. D., Rediniotis, O. K., "Embedded-Sensor Air-Data Systems for UAVs", AIAA conference paper, AIAA 2002-3496, 2002

Zeiger, M. D., Schaeffler, N. W., "Correcting Multi-Hole Probe Alignment Bias Errors Post-Calibration", AIAA conference paper 2001-0900, 2001

Zilliac, G.G., "Calibration of Seven-Hole Pressure Probes for Use in Fluid Flows with Large Angularity", N90-15399, 1989

Zilliac, G. G., "Modeling, Calibration, and Error Analysis of Seven-Hole Probes". Experiments in Fluids, vol. 14, pp. 104-120, 1993

Vita

Kevin Pisterman started the curriculum for his B.S. degree in Aerospace Engineering in 1998 at the E.A.I. tech. at Sophia-Antipolis, France. He then transferred in 2000 to the Aerospace and Ocean Engineering Department of Virginia Polytechnic Institute and State University in Blacksburg, USA, and completed his B.S. degree in Aerospace Engineering in May 2002. After graduation, he entered the graduate program in the Aerospace and Ocean Engineering Department of Virginia Polytechnic Institute and State University in Blacksburg, USA, for his Master of Science degree. He completed his work in July 2004.